Multiphase Fluid-Material Interaction: Efficient Solution Algorithms and Shock-Dominated Applications

Wentao Ma

Dissertation submitted to the Faculty of the
Virginia Polytechnic Institute and State University
in partial fulfillment of the requirements for the degree of

Doctor of Philosophy
in
Aerospace Engineering

Kevin G. Wang, Chair
Christine M. Gilbert
Rakesh K. Kapania
Christopher J. Roy

August 8, 2023
Blacksburg, Virginia

Keywords: Multiphase flow, Fluid-structure interaction, Compressible flow, Bimaterial Riemann problem, Bubble dynamics, Structural collapse, Shock wave

Copyright 2023, Wentao Ma

Multiphase Fluid-Material Interaction: Efficient Solution Algorithms and Shock-Dominated Applications

Wentao Ma

(ABSTRACT)

This dissertation focuses on the development and application of numerical algorithms for solving compressible multiphase fluid-material interaction problems. The first part of this dissertation is motivated by the extraordinary shock-resisting ability of elastomer coating materials (e.g., polyurea) under explosive loading conditions. Their performance, however, highly depends on their dynamic interaction with the substrate (e.g., metal) and ambient fluid (e.g., air or liquid); and the detailed interaction process is still unclear. Therefore, to certify the application of these materials, a fluid-structure coupled computational framework is needed. The first part of this dissertation developes such a framework. In particualr, the hyper-viscoelastic constitutive relation of polyurea is incorporated into a high-fidelity computational framework which couples a finite volume compressible multiphase fluid dynamics solver and a nonlinear finite element structural dynamics solver. Within this framework, the fluid-structure and liquid-gas interfaces are tracked using embedded boundary and level set methods. Then, the developed computational framework is applied to study the behavior a bilayer coating–substrate (i.e., polyurea-aluminum) system under various loading conditions. The observed two-way coupling between the structure and the bubble generated in a near-field underwater explosion motivates the next part of this dissertation.

The second part of this dissertation investigates the yielding and collapse of an underwater thin-walled aluminum cylinder in near-field explosions. As the explosion intensity varies

by two orders of magnitude, three different modes of collapse are discovered, including one that appears counterintuitive (i.e., one lobe extending towards the explosive charge), yet has been observed in previous laboratory experiments. Because of the transition of modes, the time it takes for the structure to reach self-contact does not decrease monotonically as the explosion intensity increases. Detailed analysis of the bubble-structure interaction suggests that, in addition to the incident shock wave, the second pressure pulse resulting from the contraction of the explosion bubble also has a significant effect on the structure's collapse. The phase difference between the structural vibration and the bubble's expansion and contraction strongly influences the structure's mode of collapse.

The third part focuses on the development of efficient solution algorithms for compressible multi-material flow simulations. In these simulations, an unresolved challenge is the computation of advective fluxes across material interfaces that separate drastically different thermodynamic states and relations. A popular class of methods in this regard is to locally construct bimaterial Riemann problems, and to apply their exact solutions in flux computation, such as the one used in the preceding parts of the dissertation. For general equations of state, however, finding the exact solution of a Riemann problem is expensive as it requires nested loops. Multiplied by the large number of Riemann problems constructed during a simulation, the computational cost often becomes prohibitive. This dissertation accelerates the solution of bimaterial Riemann problems without introducing approximations or offline precomputation tasks. The basic idea is to exploit some special properties of the Riemann problem equations, and to recycle previous solutions as much as possible. Following this idea, four acceleration methods are developed. The performance of these acceleration methods is assessed using four example problems that exhibit strong shock waves, large interface deformation, contact of multiple (> 2) interfaces, and interaction between gases and condensed matters. For all the problems, the solution of bimaterial Riemann problems is accelerated by

37 to 87 times. As a result, the total cost of advective flux computation, which includes the exact Riemann problem solution at material interfaces and the numerical flux calculation over the entire computational domain, is accelerated by 18 to 81 times.

Multiphase Fluid-Material Interaction: Efficient Solution Algorithms and Shock-Dominated Applications

Wentao Ma

(GENERAL AUDIENCE ABSTRACT)

This dissertation focuses on the development and application of numerical methods for solving multiphase fluid-material interaction problems. The first part of this dissertation is motivated by the extraordinary shock-resisting ability of elastomer coating materials (e.g., polyurea) under explosive loading conditions. Their performance, however, highly depends on their dynamic interaction with the underlying structure and the ambient water or air; and the detailed interaction process is still unclear. Therefore, the first part of this dissertation developes a fluid-structure coupled computational framework to certify the application of these materials. In particular, the special material property of the coating material is incorparated into a state-of-the-art fluid-structure coupled computational framework that is able to model large deformation under extreme physical conditions. Then, the developed computational framework is applied to study how a thin-walled aluminum cylinder with polyurea coating responds to various loading conditions. The observed two-way coupling between the structure and the bubble generated in a near-field underwater explosion motivates the next part of this dissertation.

The second part of this dissertation investigates the failure (i.e., yielding and collapse) of an underwater thin-walled aluminum cylinder in near-field explosions. As the explosion intensity varies by two orders of magnitude, three different modes of collapse are discovered, including one that appears counterintuitive (i.e., one lobe extending towards the explosive

charge), yet has been observed in previous laboratory experiments. Via a detailed analysis of the interaction between the explosion gas bubble, the aluminum cylinder, and the ambient liquid water, this dissertation elucidated the role of bubble dynamics in the structure's different failure behaviors and revealed the transition mechanism between these behaviors.

The third part of this dissertation presents efficient solution algorithms for the simulations of compressible multi-material flows. Many problems involving bubbles, droplets, phase transitions, and chemical reactions fall into this category. In these problems, discontinuities in fluid state variables (e.g., density) and material properties arise across the material interfaces, challenging numerical schemes' accuracy and robustness. In this regard, a promising class of methods that emerges in the recent decade is to resolve the exact wave structure at material interfaces, such as the one used in the preceding parts of the dissertation. However, the computational cost of these methods is prohibitive due to the nested loops invoked at every mesh edge along the material interface. To address this issue, the dissertation develops four efficient solution methods, following the idea of exploiting special properties of governing equations and recycling previous solutions. Then, the acceleration effect of these methods is assessed using various challenging multi-material flow problems. In different test cases, significant reduction in computational cost (acceleration of 18 to 81 times) is achieved, without sacrificing solver robustness and solution accuracy.

Dedication

To my family.

Acknowledgments

First, I would like to express my heartfelt gratitude to my advisor, Professor Kevin Wang. Without his unwavering encouragement, support, and guidance over the past four years, the accomplishment in this work would never have been possible. Throughout this journey, I have been profoundly grateful for his mentorship, which has allowed me to delve into the realm of developing state-of-the-art computational tools to solve challenging scientific and engineering problems. Professor Wang's kindness, enthusiasm, and commitment to excellence have shaped the person I aspire to be in my future career and beyond.

In addition, I extend my sincere gratitude to other members of my dissertation committee, Professor Christine Gilbert, Professor Rakesh Kapania, and Professor Christopher Roy. Their invaluable insights, thoughtful feedback, and dedicated review of this work have undoubtedly enhanced its quality and depth.

Furthermore, my appreciation goes out to my labmates in the Multiphysics Modeling and Computation (M2C) Lab, along with my colleagues and friends. Their camaraderie and encouragement have made this journey truly joyful and memorable. Special thanks to my wonderful labmates, Ms. Xuning Zhao, Mr. Shafquat Islam, Mr. Aditya Narkhede, and Mr. Timothy Ozenkoski, for all their help and support duing my Ph.D. journey.

Lastly, I would like to thank my family for their unconditional love and support. Their belief in me has been a constant source of motivation. I am deeply grateful to them for being a steadfast source of strength during difficult times.

Contents

List of Figures **xiii**

List of Tables **xx**

1 Introduction **1**

1.1 Compressible multi-material flow simulations 1

1.1.1 Computational challenges 1

1.1.2 Recent progress: Bimaterial Riemann problem solver at material interfaces 3

1.1.3 Computational efficiency issue 4

1.2 Bubble-structure interaction in near-field underwater explosions 6

1.3 Objectives 8

1.4 Dissertation accomplishments and outline 10

1.4.1 Dissertation accomplishments 10

1.4.2 Outline 11

Bibliography 12

2 A Fluid-Structure Coupled Computational Model for the Certification of Shock-Resistant Elastomer Coatings **22**

2.1 Introduction . . . 24

2.2 Physical model and numerical methods . . . 28

2.3 Numerical experiments . . . 34

2.4 Concluding remarks . . . 42

Bibliography . . . 43

3 Computational Analysis of Bubble-Structure Interactions in Near-Field Underwater Explosion: A Counter-Intuitive Mode of Structural Collapse 49

3.1 Introduction . . . 50

3.2 Physical model and numerical methods . . . 52

3.3 Results and discussion . . . 53

3.4 Conclusion . . . 57

Bibliography . . . 58

4 Computational Analysis of Bubble-Structure Interactions in Near-Field Underwater Explosion: Mode Transitions in Structural Collapse 60

4.1 Introduction . . . 62

4.2 Physical models and numerical methods . . . 66

4.2.1 Physical models . . . 66

4.2.2 Numerical methods . . . 71

4.2.3 Simulation setup . . . 74

4.3 Mesh convergence analysis . . . 76
4.4 Bubble-structure interaction and different collapse modes . . . 81
4.4.1 $p_0 = 8.0$ MPa (enthalpy: 0.5498 J/mm) . . . 81
4.4.2 $p_0 = 12.5$ MPa (enthalpy 0.8590 J/mm) . . . 84
4.4.3 $p_0 = 25.0$ MPa (enthalpy 1.7181 J/mm) . . . 87
4.4.4 $p_0 = 50.0$ MPa (enthalpy 3.4361 J/mm) . . . 90
4.4.5 $p_0 = 100.0$ MPa (enthalpy 6.8722 J/mm) . . . 93
4.4.6 Summary . . . 95
4.5 Transition of collapse modes . . . 98
4.5.1 Different collapse behaviors . . . 98
4.5.2 Discussion . . . 99
4.6 Conclusion . . . 102
Bibliography . . . 105

5 Efficient Solution of Bimaterial Riemann Problems for Compressible Multi-Material Flow Simulations 113

5.1 Introduction . . . 115
5.2 Governing equations and solution framework . . . 120
5.2.1 Navier-Stokes equations with general equations of state . . . 120
5.2.2 Formulation of bimaterial Riemann problems at material interfaces . . . 123
5.2.3 Interface tracking and discretization of governing equations . . . 127

5.3 Efficient solution of bimaterial Riemann problems . . . 129
5.3.1 Conventional solution procedure and its efficiency issues . . . 129
5.3.2 Change of integration variable . . . 135
5.3.3 Storing and reusing integration trajectory data . . . 137
5.3.4 Adaptive step size . . . 140
5.3.5 Obtaining initial guesses using R-tree data structure . . . 146
5.4 Numerical experiments . . . 150
5.4.1 One-dimensional benchmark problem . . . 151
5.4.2 Underwater explosion . . . 154
5.4.3 Laser-induced cavitation . . . 159
5.4.4 Hypervelocity impact in a fluid environment . . . 164
5.5 Summary . . . 170
Bibliography . . . 173

6 Conclusions and Perspectives for Future Work **182**

6.1 Conclusion . . . 182
6.2 Perspectives for future work . . . 186

List of Figures

1.1 Examples of compressible multi-material flow: Underwater explosion. Left: A gas bubble generated in an underwater explosion [1]. Right: Massive underwater explosion in navy aircraft carrier test [2]. 2

1.2 Examples of compressible multi-material flow: Shock-wave lithotripsy. Left: Extracorporeal shock wave lithotripsy [9]. Right: Contour plot of sound speed from a shock wave lithotripsy simulation, in which the human tissue (including kidney (red), fat (blue), general soft tissue (dark yellow) and unclassified tissue (yellow)) and water (green) are modeled as compressible fluid [39]. . . 2

1.3 Examples of compressible multi-material flow: Hypervelocity imapct. Left: Hypervelocity impact flash captured in a laboratory experiment [7]. Right: Pressure contour plot from a hypervelocity impact simulation, in which the copper projectile and the soda lime glass target are both modeled as compressible fluid due to the extreme physical condition (i.e., high velocity, high pressure) [47]. 3

2.1 Certification of shock-resistant elastomer coatings: A model problem. 29

2.2 Setup of numerical experiment: A finite element model of an aluminum cylinder coated with polyurea on its inner surface (top), and an unstructured, non-interface-conforming finite volume fluid mesh for fluid-structure coupled analysis (bottom). 35

2.3 Collapse of the aluminum-polyurea structure under a constant pressure load. (The upper half of the structure is shown.) 36

2.4 A close-up view of the self-contact. 37

2.5 Fluid-structure coupled analysis of collapse due to hydrostatic pressure: Time-history of fluid and structural results, before the structure reaches self-contact. 38

2.6 Fluid-structure coupled analysis of collapse due to hydrostatic pressure: Time-history of fluid and structural results after the structure reaches self-contact. (The upper half of the structure is shown.) 39

2.7 Comparison of "dry" and coupled analysis: Time-history of displacement at two sensor points on the inner surface of the structure (see Fig. 2.2). 40

2.8 Comparison of "dry" and coupled analysis: Time-history of velocity at a sensor point on the inner surface of the structure (see Fig. 2.2). 40

2.9 Result of the fluid-structure coupled analysis of a near-field explosion. 41

4.1 A two-dimensional model of an underwater aluminum cylinder subjected to a near-field explosion. (The z axis is aligned with the longitudinal direction of the cylinder.) 67

4.2 Physical models adopted in this work and their dependencies. 70

4.3 Illustration of the discretization methods in space (a) and time (b). 71

4.4 Setup of numerical experiment. 75

4.5 Example fluid and structural meshes (Pair 8): the entire computational domain (a) and a zoom-in snapshot around the fluid-structure interface (b). . . 77

4.6 Results obtained using mesh pair 8 at four different time instants: The fluid pressure field and the plastic deformation of the structure (top row), and the fluid velocity field (bottom row). 79

4.7 Experimental result of the collapse of an aluminum 6061 tube due to a near-field explosion (Ikeda [23], test AE05r01). (a)-(e) A sequence of images from the high-speed movie obtained from this test. (f) Schematic drawing of the collapsed cylinder (a cross-sectional view). 80

4.8 Mesh convergence analysis: Vertical displacement at the sensor marked in Figure 4.6 (red) and bubble size (radius equivalent, blue) at 3.259 ms, obtained using different pairs of meshes. (Pair 1: coarsest, Pair 8: finest) . . . 80

4.9 Snapshots of the fluid and structural results in the case of $p_0 = 8.0$ MPa. . . 82

4.10 Time history of selected quantities of interest in the case of $p_0 = 8.0$ MPa. (a) The distances between the top and bottom points (i.e. vertical width)and the left and right points (i.e. horizontal width) of the cylinder. (b) The bubble size (radius equivalent) and the fluid pressure at a sensor location. The time instants shown in Figure 4.9 are marked on these curves. 82

4.11 Snapshots of the fluid and structural results in the case of $p_0 = 12.5$ MPa. . 85

4.12 Time history of selected quantities of interest in the case of $p_0 = 12.5$ MPa. (a) The distances between the top and bottom points and the left and right points of the cylinder. (b) The bubble size (radius equivalent) and the fluid pressure at a sensor location. The time instants shown in Figure 4.11 are marked on these curves. 86

4.13 Snapshots of the fluid and structural results in the case of $p_0 = 25.0$ MPa. . 88

4.14 Time history of selected quantities of interest in the case of $p_0 = 25.0$ MPa. (a) The distances between the top and bottom points and the left and right points of the cylinder. (b) The bubble size (radius equivalent) and the fluid pressure at a sensor location. The time instants shown in Figure 4.13 are marked on these curves. 89

4.15 Snapshots of the fluid and structural results in the case of $p_0 = 50.0$ MPa. . 91

4.16 Time history of selected quantities of interest in the case of $p_0 = 50.0$ MPa. (a) The distances between the top and bottom points and the left and right points of the cylinder. (b) The bubble size (radius equivalent) and the fluid pressure at a sensor location. The time instants shown in Figure 4.15 are marked on these curves. 92

4.17 Snapshots of the fluid and structural results in the case of $p_0 = 100.0$ MPa. The sensor location P1 is marked in the first two sub-figures. 94

4.18 Time history of selected quantities of interest in the case of $p_0 = 100.0$ MPa. (a) The distances between the top and bottom points and the left and right points of the cylinder. (b) The bubble size (radius equivalent) and the fluid pressure at a sensor location. The time instants shown in Figure 4.17 are marked on these curves. 95

4.19 Comparison of the evolution of the bubble and the cylinder in the five (5) representative cases. One image is generated for each half cycle (expansion or contraction) of the bubble. Within each image, results at different time instants are superimposed, and the increase of opacity indicates the time evolution. 97

4.20 The transition of collapse modes as p_0 increases from 1 MPa to 100 MPa. . . 98

4.21 The time to collapse (t_{co}) for (a) 8 MPa $<$ $p_0 \leq$ 100.0 MPa and (b) 8 MPa $<$ $p_0 \leq$ 25 MPa. 99

4.22 Effective plastic strain at the (a) top point and (b) bottom point of the cylinder's inside wall. 100

4.23 Effective plastic strain at the cylinder inside wall's (a) top and (b) bottom points when the cylinder's vertical width reaches minimum for the first time (i.e. when the cylinder completes the first half-cycle of vibration). 101

4.24 Vertical width of the cylinder when the bubble contracts to its minimum size. 102

5.1 Construction and solution of a bimaterial Riemann problem at material interface. 124

5.2 Interface tracking and discretization of governing equations: The level set method and FIVER. 128

5.3 The conventional procedure for solving bimaterial Riemann problems. 131

5.4 Integration trajectories through the 1-wave of the example Riemann problem in three successive outer loop iterations. 139

5.5 Integration trajectories in three successive outer loop iterations, with Algorithm 1. 140

5.6 Algorithm 2: One step of numerical integration through a rarefaction fan with adaptive step size. 142

5.7 Repetition of iteration 1 in Fig. 5.4 with adaptive step size. 145

5.8 Visualization of the bimaterial Riemann problems solved in the simulation presented in Sec. 5.4.3 during 10 time steps. This 5D data set is displayed with p_l, p_r, and $u_r - u_l$ as the three spatial coordinates. The color of each data point indicates the value of ρ_r, and the size of the point indicates the value of ρ_l. "Point 1" is used to demonstrate the initial guess improvement from the nearest neighbor search. 147

5.9 Improved solution procedure for bimaterial Riemann problems in multi-material flow simulaitons. 150

5.10 A 1D bimaterial Riemann problem: Density, pressure, and velocity distributions at $t = 0.15$ μs. 153

5.11 A 1D bimaterial Riemann problem: Comparison of the flux computation time of different simulations. 154

5.12 A 1D bimaterial Riemann problem: Effect of R-tree on the total number of integration steps. 154

5.13 Underwater explosion: simulation results at $t = 0.058$. (a) density filed, (b) pressure filed, (c) density along the horizontal symmetric axis, (d) pressure along the horizontal symmetric axis. 156

5.14 Underwater explosion: Computational cost of exact Riemann problem solutions in the first 200 time steps. 157

5.15 Underwater explosion: Comparison of the flux computation time of different simulations. 158

5.16 Underwater explosion with the JWL EOS: Simulation result at $t = 0.058$, along the horizontal centerline of the computational domain. 159

5.17 Underwater explosion with the JWL EOS: Comparison of the flux computation time of different simulations. 160

5.18 Laser-induced cavitation: Laser radiation, bubble formation, and the fluid velocity field. 162

5.19 Laser-induced cavitation: The pressure field. 163

5.20 Laser-induced cavitation: Comparison of the flux computation time of different simulations. 164

5.21 Simulation of flow around a copper projectile before collision: Pressure and velocity fields at $t = 8.87$ μs. Velocity of projectile: 1 km/s. 165

5.22 Simulation of flow around a copper projectile before collision: Comparison of the flux computation time. 167

5.23 Hypervelocity impact in a fluid environment: pressure, velocity, and temperature fields. Velocity of projectile: 4 km/s. 168

5.24 Hypervelocity impact in a fluid environment: the time history of the pressure at the marked sensor location. The pressure field is from $t = 0.825$ μs. . . . 169

5.25 Hypervelocity impact in a fluid environment: Comparison of the flux computation time of different simulations. 170

List of Tables

4.1 Material and geometric properties of the cylinder (Aluminum 6061-T6) . . . 75

4.2 Bubble properties . . . 75

4.3 Properties of the ambient water and the air inside the cylinder . . . 75

4.4 Fluid and structural meshes used in the mesh convergence analysis. . . . 77

5.1 Number of EOS evaluations required by exact and approximate Riemann problem solvers. . . . 134

5.2 Comparison of the state variables at Point 1 in Fig. 5.8 and its nearest neighbor in the R-tree. . . . 149

Chapter 1

Introduction

1.1 Compressible multi-material flow simulations

Fluid flows involving multiple materials or phases arise in many scientific and engineering disciplines. This dissertation considers a class of problems in which different materials (or phases) are separated by sharp interfaces, and the flow needs to be treated as being compressible. Many fluid dynamics problems involving bubbles, droplets, phase transitions, and chemical reactions fall into this category (e.g., [27, 64, 66]). Some problems in solid and soft matter mechanics also belong to this category, when the material behaves like a compressible fluid due to some special loading condition (e.g., [31, 39]). Figures 1.1 to 1.3 demonstrate three examples of compressible multi-material flow. Because of compressibility, the physical model typically involves a thermodynamic equation of state (EOS) for each material. Across a material interface, discontinuity arises not only in some state variables (e.g. density, internal energy), but also in the EOS. These discontinuities can be quite significant, if the interface separates gaseous and condensed phases.

1.1.1 Computational challenges

Different numerical methods have been developed to represent material interfaces. In Lagrangian [59, 60] and Arbitrary Lagrangian-Eulerian (ALE) [44, 49] frameworks, the compu-

Figure 1.1: Examples of compressible multi-material flow: Underwater explosion. Left: A gas bubble generated in an underwater explosion [1]. Right: Massive underwater explosion in navy aircraft carrier test [2].

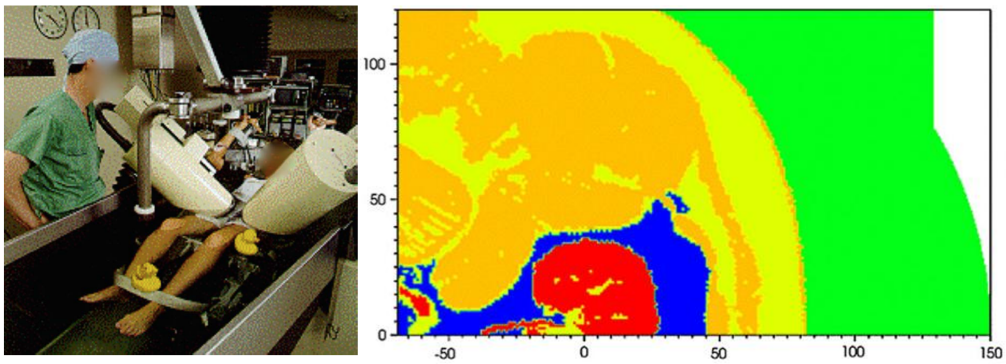

Figure 1.2: Examples of compressible multi-material flow: Shock-wave lithotripsy. Left: Extracorporeal shock wave lithotripsy [9]. Right: Contour plot of sound speed from a shock wave lithotripsy simulation, in which the human tissue (including kidney (red), fat (blue), general soft tissue (dark yellow) and unclassified tissue (yellow)) and water (green) are modeled as compressible fluid [39].

tational mesh is updated to conform to the material interface. In the Eulerian framework, the material interface is tracked using numerical methods such as interface capturing [5, 38], level set [23], volume of fluid [10], and front tracking [56]. Regardless of the method used to represent interfaces, the spatial discretization of the governing equations (e.g. Navier-Stokes equations) at an interface presents new challenges not encountered in single-phase flow simulations. Many popular numerical flux functions (e.g. Roe, HLLC, HLLE) assume a single EOS. Therefore, they cannot be directly applied at material interfaces. It is also well known

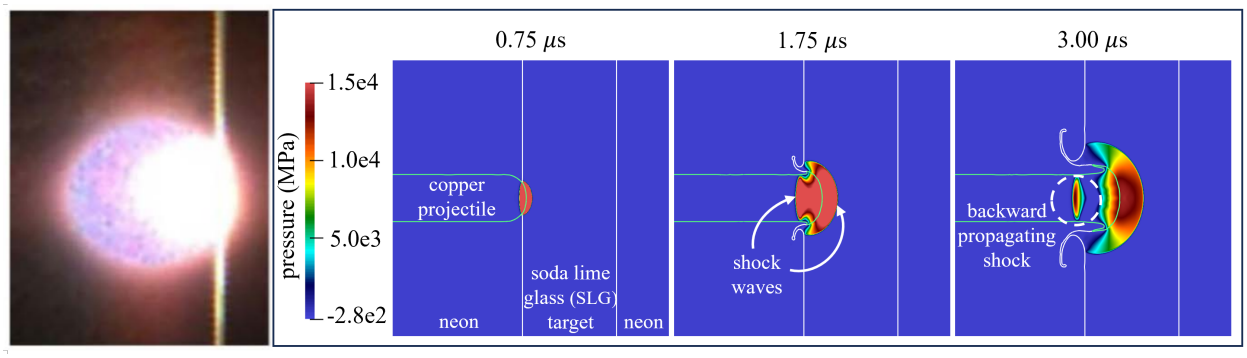

Figure 1.3: Examples of compressible multi-material flow: Hypervelocity imapct. Left: Hypervelocity impact flash captured in a laboratory experiment [7]. Right: Pressure contour plot from a hypervelocity impact simulation, in which the copper projectile and the soda lime glass target are both modeled as compressible fluid due to the extreme physical condition (i.e., high velocity, high pressure) [47].

that spurious oscillations often occur near material interfaces, even if the applied numerical scheme performs well for single-phase flows (e.g., [35, 43]). For example, Brummelen *et al.* showed that when an interface capturing method is used, spurious pressure oscillation may occur due to the loss of pressure-invariance property in discretization [58]. Fedkiw *et al.* developed the ghost fluid method, in which ghost states on both sides of a material interface are constructed [22]. In order to suppress an "overheating" phenomenon, one needs to apply the "isobaric fixing" technique that requires solving another auxiliary partial differential equation [21, 22]. Some authors have also reported that the original ghost fluid method may produce inaccurate results when an interface is hit by a shock wave, or the density or EOS jumps significantly across it [42, 43, 53].

1.1.2 Recent progress: Bimaterial Riemann problem solver at material interfaces

In the past two decades, many authors have proposed the idea of constructing bimaterial Riemann problems across material interfaces, and applying their exact solutions in flux

computation [4, 11, 15, 19, 20, 27, 28, 32, 38, 43, 53, 54, 61]. For example, Liu *et al.* incorporated exact Riemann solvers in their ghost fluid method, in order to correctly predict the double rarefaction waves in nearly cavitating flow conditions [43] . Later, Wang *et al.* used the exact Riemann solutions to populate not only ghost cells but also the real fluid cells near material interfaces, thereby eliminating the need of isobaric fix [61]. Cocchi and Saurel developed a prediction-correction scheme in which the solutions of exact Riemann problems are used to correct flow states near contact discontinuities [15]. Igra and Takayama modified this method to make it work in conjunction with the level-set method [28]. Also, Kitamura *et al.* conducted a comparative study of the AUSM (Advection Upstream Splitting Method) family of schemes, and found that when combined with the exact Riemann problem solver, AUSM schemes are applicable to more challenging problems with larger pressure ratios [38] . Recently, Farhat *et al.* developed the FIVER (FInite Volume method with Exact multiphase Riemann solvers) method, in which the exact solutions of bimaterial Riemann problems are used directly to compute advective fluxes, instead of populating ghost or real fluid cells [19, 20, 26, 48, 62]. FIVER has been applied to study several shock-dominated multiphase flow and fluid-structure interaction problems, including underwater explosion and implosion [18, 46], pipeline explosion [62], cavitation erosion [12, 13, 63, 65], laser-induced vaporization [66], and hypervelocity impact [31]. Furthermore, some authors have proposed to extend exact Riemann problem solvers to account for additional interfacial physics, such as surface tension and phase transition [11, 27, 32].

1.1.3 Computational efficiency issue

A unique advantage of the constructed bimaterial Riemann problems is that they account for not only the discontinuity of state variables (e.g. density, internal energy) across a material interface, but also the change of thermodynamic EOS. With this in mind, one may expect

this idea to be more impactful for problems that require sophisticated, highly nonlinear EOS. In reality, however, most of the efforts reviewed above deal with simple EOS, such as perfect and stiffened gases. For general EOS, computational cost becomes a major issue, as finding the exact solution of a Riemann problem requires nested loops [36, 55]. In particular, when the solution contains a rarefaction fan, each iteration in the outer loop requires numerically integrating two state variables through the fan, with the upper bound of the integral being an unknown variable [36]. As a result, finding the exact solution of a Riemann problem often requires evaluating the EOS thousands of times. In contrast, approximate Riemann solvers (e.g. Roe, HLLC) only call the EOS a few times. Therefore, although the exact Riemann problem solver is only applied within a lower-dimensional subset (i.e., material interfaces) of the computational domain, its cost can be much higher than the approximate Riemann solver that is applied in the entire domain. This dramatic increase of computational cost often makes the simulation unfeasible.

Previously, Colella and Glaz accelerated single-material Riemann problem solvers by developing a local parametrization for the EOS [16]. This method assumes slow variation of the thermodynamic state, which may not be true in challenging multi-material flow problems. Liu *et al.* found that their ghost fluid method equipped with a specifically designed approximate two-phase Riemann problem solver cannot provide correct solutions under nearly cavitating flow conditions [43]. Exact solutions of Riemann problems were thus employed to address the two strong rarefaction waves in this situation. Farhat *et al.* avoided online numerical integration by tabulating and interpolating the Riemann invariants on sparse grids [20, 51]. For the problem they considered, which involves the stiffened gas EOS and the Jones-Wilkins-Lee (JWL) EOS, only one two-dimensional sparse grid needs to be constructed. But for arbitrary EOS, two three-dimensional sparse grids need to be constructed for each material. This offline precomputation can be expensive. It also requires a high level

of expertise from the user, who is expected to specify, before the simulation, the resolution of the sparse grids as well as the lower and upper bounds of each tabulated variable.

1.2 Bubble-structure interaction in near-field underwater explosions

One important application of the compressible multi-material flows discussed in Sec. 1.1 is underwater explosion, which threatens marine vehicles, pipelines, and platforms. If the explosion occurs near a structure (i.e., near-field underwater explosion), the problem becomes more complicated, as the bubble formed by the gaseous explosion products expands and contracts rapidly near the structure. Previous studies have demonstrated that the bubble dynamics, the dynamics of the surrounding liquid water, and the transient deformation of the structure depend on each other, leading to a fluid-structure interaction (FSI) process that involves a multiphase flow, shock waves, complex bubble geometry, large structural deformation, and nonlinear material behaviors (e.g., yielding, fracture) [24, 25, 29, 33, 41, 45]. For thin-walled underwater structures, a primary failure mechanism is instability in the form of implosion. Although extensive research efforts have been devoted towards understanding the implosion of cylindrical shell structures (e.g., underwater pipelines, deep-sea submersibles) induced by high hydrostatic pressure [17, 30, 37, 40, 57], knowledge about the response of this type of structures to a near-field explosion is still far from complete. Because of the complexity of the problem, high-fidelity fluid-structure coupled computational analysis becomes a promising tool to fully understand the implosion mechanism of the structure that is strongly coupled with surrounding multiphase flow.

To protect structures from underwater and air explosions, the design and application of shock

mitigation materials and methods has been a long-standing active research area. Recent studies have revealed some extraordinary properties of several phase-separated elastomers (e.g., polyureas), which indicates a promising approach for mitigating shock-induced damage and failure [6, 14, 34, 50, 52]. Specifically, the elastomers can be applied to the surface of various structures as shock (and ballistic impact) mitigation coatings.

As an example, the effectiveness of polyurea coatings for mitigating shock-induced deformation and fracture has been demonstrated at different scales (e.g., [3, 6, 8]). These studies have also shown that the performance of the coating under shock loading depends not only on their material properties, but also on the complex dynamic interaction of the coating material with the underlying substrate and the surrounding fluid medium (e.g., water, air). For example, it has been shown that the effectiveness of the coating depends on the material of the substrate, and on which side of it (i.e., inner or outer surface) the coating is applied [8]. Also, the effect of the same polyurea coating under underwater and aerial shock loadings are different [8]. Furthermore, it has been found that increasing the coating thickness continuously does not translate to a continuous increase in its performance, and the optimal thickness depends sensitively on both the shock loading condition and the substrate [6].

Despite the recent progresses reviewed above, the dynamic process of shock wave impacting on the bilayer coating-substrate structure is still unclear, which involves the propagation and attenuation of shock waves within multiple solid (e.g., elastomer coating and substrate) and fluid (e.g., water and air) materials, as well as the dynamic interaction of these materials at fluid-structure and coating-substrate interfaces. Because of these complexities, the design and practical use of high strain-rate sensitive elastomer coatings require improved knowledge and predictive capability regarding a challenging shock-dominated multi-material fluid-structure interaction problem, featuring

- shock wave transmission, reflection, and attenuation through the solid and fluid ma-

terials and at their interfaces (i.e., fluid-coating, coating-substrate, and substrate-fluid interfaces); and

- large deformation, hyper-elastic and viscoelastic behaviors of the coating materials.

1.3 Objectives

The order of the dissertation objectives listed in this section follows the chronological progression of the author's Ph.D. research experience. It starts with the application and modification of a state-of-the-art computational tool for multiphase fluid-material interaction problems. In this process, the author gained firsthand experience to understand the methodology's strengths in terms of robustness and accuracy. However, a notable drawback emerges in the form of computational efficiency, when complex equations of state are considered (see Section 1.1). This limitation motivates the development of more efficient algorithms.

In particular, the first objective is motivated by the shock-resisting performance of elastomer coating materials as well as its dependence on the interaction with the substrate and surrounding fluid medium. Correspondingly, the first part of the dissertation aims at developing a fluid-structure coupled computational framework that enables the certification of coating materials using fluid-structure coupled analysis. Particular focus will be placed on:

- modeling and simulating the special material properties (e.g., hyperelasticity and viscoelasticity) of elastomer coatings;
- modeling and predicting the dynamic response of bilayer elastomer coating–substrate systems (e.g., polyurea-aluminum) to underwater shock loadings.

The second objective of this dissertation is motivated by the complex and highly coupled

structural and fluid dynamics in near-field underwater explosions. In this dissertation, we focus on the interactions between an underwater thin-walled structure, a gas bubble generated by the explosion, and the ambient liquid water. This leads to the second part of the dissertation, which aims to understand the role of bubble dynamics in the structural collapse induced by near-field underwater explosions. Particular focus will be placed on:

- modeling and simulating the structural instability (e.g., collapse) caused by the two-way interaction between the structure and the bubble;
- explaining the causal relation between the magnitude of the explosion and the structure's modes of collapse;
- revealing the mechanism of mode transitions as the magnitude of the explosion varies.

The compressible multi-material flow in the first two parts features strong discontinuity in both the fluid state variable and material property (e.g., equations of state). A popular class of methods to overcome the associated numerical challenge is constructing local bimaterial Riemann problems at material interfaces and solve them exactly, such as the FIVER method used in this dissertation. Despite the robustness and accuracy of this class of methods, their computational cost is prohibitive when complex equations of state are involved. To mitigate this issue, the third objective of the dissertation is to develop solution algorithms that improve the computational efficiency of the exact bimaterial Riemann problem solvers involved in compressible multi-material flow simulations. This leads to the third part of this dissertation. The new solution algorithms should:

- significantly accelerate the solution of bimaterial Riemann problems;
- not introduce new approximations;
- not require additional offline precomputation procedures.

1.4 Dissertation accomplishments and outline

1.4.1 Dissertation accomplishments

Corresponding to the objectives listed in Sec. 1.3, the major accomplishments of this dissertation are summarized as follows.

- Development of a fluid-structure coupled computational model for the certification of shock-resistant elastomer coatings. Hyperelasticity and viscoelasticity of the coating material are integrated into the model by implementing corresponding constitutive relations. Then, the model is applied to the prediction of dynamic response of bilayer elastomer coating–substrate systems (e.g., polyurea-aluminum) to various loading conditions. Obvious evidence of a two-way coupling between the structure and the surrounding fluid is observed in a near-filed underwater explosion. In particular, instead of collapsing monotonically as in hydrostatic collapse, the structure oscillates before completely collapse. This observation inspired an investigation of the bubble's role in the collapse of the structure, which is the next accomplishment of this dissertation.

- Computational analysis of the interactions between an underwater thin-walled structure and a gas bubble generated by a near-field explosion. In particular,

  (a) three different modes of structural collapse are observed under different magnitudes of the explosion. These modes include one that appears to be counterintuitive, but has been observed in previous laboratory experiments;

  (b) a parametric study is performed to understand the effect of explosion magnitude on the bubble-structure interaction, and on the structure's collapse behaviors/modes;

  (c) the mechanism of mode transitions is discussed in detail, featuring the interaction between the thin-walled structure, the gas bubble, and the ambient liquid water.

- Significant acceleration of compressible multi-material flow simulations by the development of a new, efficient bimaterial Riemann problem solver. By exploiting some special properties of the Riemann problem equations and recycling previous solution as much as possible, four methods are proposed. These methods are able to accelerate the solution of bimaterial Riemann problem significantly (37 to 87X speedup in different test cases) without introducing approximations or offline precomputation tasks. As a result, the total cost of advective flux computation, which includes the exact Riemann problem solution at material interfaces and the numerical flux calculation over the entire computational domain, is accelerated by 18 to 81 times. In particular, the four methods are:

  (a) a change of integration variable through rarefaction fans;

  (b) storing and reusing integration trajectory data;

  (c) integration step size adaptation;

  (d) constructing an R-tree on the fly to generate initial guesses.

1.4.2 Outline

This dissertation is organized in the manuscript (multi-paper) format. Each of the main chapter is in the format of a journal or conference article. The arrangement of the chapters follows the chronological progression of the author's Ph.D. research experience. In particular, the reminder of this dissertation is organized as follows.

Chapter 2 presents the development of a fluid-structure coupled computational framework for the certification of shock-resistant elastomer coatings. The simulation results about the dynamic response of bilayer elastomer coating–substrate systems (e.g., polyurea-aluminum) to various loading conditions are included. In particular, the observed two-way coupling

between the structure and the bubble motivates the work presented in the next two chapters.

Chapters 3 and 4 are two articles about a high-fidelity computational analysis of bubble-structure interactions in near-field underwater explosions. Specifically, Chapter 3 presents a mode of structural collapse that appears counterintuitive but has been previously observed in laboratory experiments. In Chapter 4, a comprehensive study is presented to understand the relation between explosion magnitude and different modes of structural collapse. The mechanism of mode transitions is revealed and discussed in detail.

Chapter 5 presents the efficient solution of bimaterial Riemann problems for the simulation of compressible multi-material flows. The solution procedure of off-the-shelf Riemann problem solvers and the corresponding computational cost are discussed. Then, four acceleration methods are developed and presented in detail. Finally, the acceleration effects and accuracy of the developed methods are evaluated by challenging test cases involving underwater explosion, laser-induced cavitation, and hypervelocity impact.

Finally, a conclusion and a summary of future work are presented in Chapter 6.

Bibliography

[1] Underwater explosions at 120,000 fps - the slow mo guys, . URL https://www.youtube.com/watch?v=E5rGFZWQfzk.

[2] Us navy detonate a massive explosion in the atlantic ocean to test their warships, . URL https://www.youtube.com/watch?app=desktop&v=ziVUumtxNuU.

[3] MR Amini, J Isaacs, and S Nemat-Nasser. Investigation of effect of polyurea on response of steel plates to impulsive loads in direct pressure-pulse experiments. *Mechanics of Materials*, 42(6):628–639, 2010.

[4] Tariq D. Aslam. A level set algorithm for tracking discontinuities in hyperbolic conservation laws ii: Systems of equations. *Journal of Scientific Computing*, 19(1-3):37 – 62, 2003.

[5] J.W. Banks, D.W. Schwendeman, A.K. Kapila, and W.D. Henshaw. A high-resolution godunov method for compressible multi-material flow on overlapping grids. *Journal of Computational Physics*, 223(1):262–297, 2007. ISSN 0021-9991.

[6] GS Barsoum and PJ Dudt. The fascinating behaviors of ordinary materials under dynamic conditions. *Ammtiac Quarterly*, 4:11–14, 2010.

[7] Roshdy G Barsoum. Shockwave compression physics of condensed matter lattice boltzmann method with application to glass under hypervelocity impact. 2019.

[8] Roshdy George S Barsoum. *Elastomeric Polymers with High Rate Sensitivity: Applications in Blast, Shockwave, and Penetration Mechanics*. William Andrew, 2015.

[9] Darren Beiko, R. John D'A. Honey, Kenneth T. Pace, John D. Denstedt, Hassan Razvi, Denis H. Hosking, Richard W. Norman, and James W.L. Wilson. The history of endourology in canada. *Canadian Urological Association Journal*, 14(2):12–6, Feb. 2019.

[10] David J Benson. Volume of fluid interface reconstruction methods for multi-material problems. *Applied Mechanics Reviews*, 55(2):151–165, 04 2002. ISSN 0003-6900.

[11] Wurigen Bo, Xingtao Liu, James Glimm, and Xiaolin Li. A robust front tracking method: Verification and application to simulation of the primary breakup of a liquid jet. *SIAM Journal on Scientific Computing*, 33(4):1505–1524, 2011.

[12] S Cao, G Wang, O Coutier-Delgosha, and K Wang. Shock-induced bubble collapse near solid materials: Effect of acoustic impedance. *Journal of Fluid Mechanics*, 907, 2021.

[13] Shunxiang Cao, Ying Zhang, Defei Liao, Pei Zhong, and Kevin G Wang. Shock-induced damage and dynamic fracture in cylindrical bodies submerged in liquid. *International journal of solids and structures*, 169:55–71, 2019.

[14] Taeyi Choi, Daniel Fragiadakis, C Michael Roland, and James Runt. Microstructure and segmental dynamics of polyurea under uniaxial deformation. *Macromolecules*, 45 (8):3581–3589, 2012.

[15] Jean-Pierre Cocchi and Richard Saurel. A Riemann problem based method for the resolution of compressible multimaterial flows. *Journal of Computational Physics*, 137 (2):265–298, 1997. ISSN 0021-9991.

[16] Phillip Colella and Harland M Glaz. Efficient solution algorithms for the riemann problem for real gases. *Journal of Computational Physics*, 59(2):264–289, 1985. ISSN 0021-9991.

[17] C. Farhat, K.G. Wang, A. Main, S. Kyriakides, L.-H. Lee, K. Ravi-Chandar, and T. Belytschko. Dynamic implosion of underwater cylindrical shells: experiments and computations. *International Journal of Solids and Structures*, 50(19):2943–2961, 2013. ISSN 0020-7683.

[18] C. Farhat, K.G. Wang, A. Main, S. Kyriakides, L.-H. Lee, K. Ravi-Chandar, and T. Belytschko. Dynamic implosion of underwater cylindrical shells: Experiments and computations. *International Journal of Solids and Structures*, 50(19):2943–2961, 2013.

[19] Charbel Farhat, Arthur Rallu, and Sriram Shankaran. A higher-order generalized ghost fluid method for the poor for the three-dimensional two-phase flow computation of underwater implosions. *Journal of Computational Physics*, 227(16):7674–7700, 2008. ISSN 0021-9991.

[20] Charbel Farhat, Jean-Frédéric Gerbeau, and Arthur Rallu. Fiver: A finite volume method based on exact two-phase riemann problems and sparse grids for multi-material flows with large density jumps. *Journal of Computational Physics*, 231(19):6360–6379, 2012. ISSN 0021-9991.

[21] Ronald Fedkiw, Antonio Marquina, and Barry Merriman. An isobaric fix for the overheating problem in multimaterial compressible flows. *Journal of Computational Physics*, 148:545–578, 1999.

[22] Ronald P Fedkiw, Tariq Aslam, Barry Merriman, and Stanley Osher. A non-oscillatory eulerian approach to interfaces in multimaterial flows (the ghost fluid method). *Journal of Computational Physics*, 152(2):457–492, 1999.

[23] Frederic Gibou, Ronald Fedkiw, and Stanley Osher. A review of level-set methods and some recent applications. *Journal of Computational Physics*, 353:82–109, 2018. ISSN 0021-9991.

[24] Sachin Gupta, Helio Matos, James M LeBlanc, and Arun Shukla. Shock initiated instabilities in underwater cylindrical structures. *Journal of the Mechanics and Physics of Solids*, 95:188–212, 2016.

[25] Emily L Guzas, Sachin Gupta, Joseph M Ambrico, James M LeBlanc, and Arun Shukla. Computational modeling of dynamically initiated instabilities and implosion of underwater cylindrical structures in a confined environment. *Journal of Applied Mechanics*, 86(2), 2019.

[26] Jonathan Ho and Charbel Farhat. Discrete embedded boundary method with smooth dependence on the evolution of a fluid-structure interface. *International Journal for Numerical Methods in Engineering*, 122(19):5353–5383, 2021.

[27] Ryan W. Houim and Kenneth K. Kuo. A ghost fluid method for compressible reacting flows with phase change. *Journal of Computational Physics*, 235:865–900, 2013. ISSN 0021-9991.

[28] D. Igra and K. Takayama. A high resolution upwind scheme for multi-component flows. *International Journal for Numerical Methods in Fluids*, 38(10):985–1007, 2002.

[29] C. Ikeda. *Fluid-structure interactions: implosions of shell structures and wave impact on a flat plate*. PhD thesis, University of Maryland, College Park, 2012.

[30] CM Ikeda, J Wilkerling, and JH Duncan. The implosion of cylindrical shell structures in a high-pressure water environment. *Proceedings of the Royal Society A: Mathematical, Physical and Engineering Sciences*, 469(2160):20130443, 2013.

[31] Shafquat T. Islam, Wentao Ma, John G. Michopoulos, and Kevin Wang. Plasma formation in ambient fluid from hypervelocity impacts. *Extreme Mechanics Letters*, 58: 101927, 2023. ISSN 2352-4316.

[32] Ali Jafarian and Ahmadreza Pishevar. An exact multiphase riemann solver for compressible cavitating flows. *International Journal of Multiphase Flow*, 88:152–166, 2017. ISSN 0301-9322.

[33] Carlos Javier, Michael Galuska, Michael Papa, James LeBlanc, Helio Matos, and Arun Shukla. Underwater explosive bubble interaction with an adjacent submerged structure. *Journal of Fluids and Structures*, 100:103189, 2021.

[34] T Jiao and RJ Clifton. Measurement of the response of an elastomer at pressures up to 9 gpa and shear-rates of 105–106s- 1. In *Journal of Physics: Conference Series*, volume 500, page 112036. IOP Publishing, 2014.

[35] Eric Johnsen and Frank Ham. Preventing numerical errors generated by interface-capturing schemes in compressible multi-material flows. *Journal of Computational Physics*, 231(17):5705–5717, 2012. ISSN 0021-9991.

[36] James Russell Kamm. An exact, compressible one-dimensional riemann solver for general, convex equations of state. Technical report, Los Alamos National Lab.(LANL), Los Alamos, NM (United States), 2015.

[37] Shyamal Kishore, P Naik Parrikar, Nicholas DeNardo, and Arun Shukla. Underwater dynamic collapse of sandwich composite structures. *Experimental Mechanics*, 59(5): 583–598, 2019.

[38] Keiichi Kitamura, Meng-Sing Liou, and Chih-Hao Chang. Extension and comparative study of ausm-family schemes for compressible multiphase flow simulations. *Communications in Computational Physics*, 16(3):632–674, 2014.

[39] Jeff Krimmel, Tim Colonius, and Michel Tanguay. Simulation of the effects of cavitation and anatomy in the shock path of model lithotripters. *Urological research*, 38:505–518, 2010.

[40] Stelios Kyriakides and Edmundo Corona. *Mechanics of offshore pipelines: volume 1 buckling and collapse*, volume 1. Elsevier, 2007.

[41] James LeBlanc, Christopher Shillings, Erin Gauch, Frank Livolsi, and Arun Shukla. Near field underwater explosion response of polyurea coated composite plates. *Experimental Mechanics*, 56(4):569–581, 2016.

[42] T.G. Liu, B.C. Khoo, and K.S. Yeo. Ghost fluid method for strong shock impacting on material interface. *Journal of Computational Physics*, 190(2):651–681, 2003. ISSN 0021-9991.

[43] T.G. Liu, B.C. Khoo, and C.W. Wang. The ghost fluid method for compressible gas–water simulation. *Journal of Computational Physics*, 204(1):193–221, 2005. ISSN 0021-9991.

[44] Raphaël Loubère, Pierre-Henri Maire, Mikhail Shashkov, Jérôme Breil, and Stéphane Galera. Reale: A reconnection-based arbitrary-lagrangian–eulerian method. *Journal of Computational Physics*, 229(12):4724–4761, 2010. ISSN 0021-9991.

[45] Wentao Ma, Xuning Zhao, and Kevin Wang. A fluid-structure coupled computational model for the certification of shock-resistant elastomer coatings. In *Proceedings of 39th International Conference on Offshore Mechanics and Arctic Engineering*, volume 2A: Structures, Safety, and Reliability. ASME, 08 2020. V02AT02A024.

[46] Wentao Ma, Xuning Zhao, Christine Gilbert, and Kevin Wang. Computational analysis of bubble–structure interactions in near-field underwater explosion. *International Journal of Solids and Structures*, 242:111527, 2022.

[47] Wentao Ma, Xuning Zhao, Shafquat Islam, Aditya Narkhede, and Kevin Wang. Efficient solution of bimaterial riemann problems for compressible multi-material flow simulations, 2023.

[48] Alex Main, Xianyi Zeng, Philip Avery, and Charbel Farhat. An enhanced fiver method for multi-material flow problems with second-order convergence rate. *Journal of Computational Physics*, 329:141–172, 2017.

[49] Alexis Marbœuf, Alexandra Claisse, and Patrick Le Tallec. Conservative and entropy controlled remap for multi-material ale simulations with space-staggered schemes. *Journal of Computational Physics*, 390:66–92, 2019. ISSN 0021-9991.

[50] AD Mulliken and MC Boyce. Mechanics of the rate-dependent elastic–plastic deformation of glassy polymers from low to high strain rates. *International journal of solids and structures*, 43(5):1331–1356, 2006.

[51] Arthur Rallu. *A multiphase fluid-structure computational framework for underwater imploison problems*. PhD thesis, Stanford University, 2009.

[52] CM Roland, JN Twigg, Y Vu, and PH Mott. High strain rate mechanical behavior of polyurea. *Polymer*, 48(2):574–578, 2007.

[53] Shiv Kumar Sambasivan and H. S. UdayKumar. Ghost fluid method for strong shock interactions part 1: Fluid-fluid interfaces. *AIAA Journal*, 47(12):2907–2922, 2009.

[54] Hiroshi Terashima and Grétar Tryggvason. A front-tracking method with projected interface conditions for compressible multi-fluid flows. *Computers & Fluids*, 39(10): 1804–1814, 2010. ISSN 0045-7930.

[55] Eleuterio F Toro. *Riemann solvers and numerical methods for fluid dynamics: a practical introduction*. Springer Science & Business Media, 2013.

[56] G. Tryggvason, B. Bunner, A. Esmaeeli, D. Juric, N. Al-Rawahi, W. Tauber, J. Han, S. Nas, and Y.-J. Jan. A front-tracking method for the computations of multiphase flow. *Journal of Computational Physics*, 169(2):708–759, 2001. ISSN 0021-9991.

[57] Stephen E Turner and Joseph M Ambrico. Underwater implosion of cylindrical metal tubes. *Journal of Applied Mechanics*, 80(1), 2013.

[58] E.H. van Brummelen and B. Koren. A pressure-invariant conservative godunov-type method for barotropic two-fluid flows. *Journal of Computational Physics*, 185(1):289–308, 2003. ISSN 0021-9991.

[59] François Vilar, Chi-Wang Shu, and Pierre-Henri Maire. Positivity-preserving cell-centered lagrangian schemes for multi-material compressible flows: From first-order to high-orders. part ii: The two-dimensional case. *Journal of Computational Physics*, 312:416–442, 2016. ISSN 0021-9991.

[60] J. VonNeumann and R. D. Richtmyer. A Method for the Numerical Calculation of Hydrodynamic Shocks. *Journal of Applied Physics*, 21(3):232–237, 04 1950. ISSN 0021-8979.

[61] C. W. Wang, T. G. Liu, and B. C. Khoo. A real ghost fluid method for the simulation of multimedium compressible flow. *SIAM Journal on Scientific Computing*, 28(1):278–302, 2006.

[62] K. G. Wang, P. Lea, and C. Farhat. A computational framework for the simulation of high-speed multi-material fluid-structure interaction problems with dynamic fracture. *International Journal for Numerical Methods in Engineering*, 104(7):585–623, 2015.

[63] Kevin G. Wang. Multiphase fluid-solid coupled analysis of shock-bubble-stone interaction in shockwave lithotripsy. *International Journal for Numerical Methods in Biomedical Engineering*, 33(10), 2017. doi: 10.1002/cnm.2855.

[64] Gaoming Xiang and Bing Wang. Numerical study of a planar shock interacting with a cylindrical water column embedded with an air cavity. *Journal of Fluid Mechanics*, 825:825–852, 2017.

[65] Gaoming Xiang, Xiaojian Ma, Cosima Liang, Hongyang Yu, Defei Liao, Georgy Sankin, Shunxiang Cao, Kevin Wang, and Pei Zhong. Variations of stress field and stone fracture produced at different lateral locations in a shockwave lithotripter field. *The Journal of the Acoustical Society of America*, 150(2):1013–1029, 2021. doi: 10.1121/10.0005823.

[66] Xuning Zhao, Wentao Ma, and Kevin Wang. Simulating laser-fluid coupling and laser-induced cavitation using embedded boundary and level set methods. *Journal of Computational Physics*, 472:111656, 2023. ISSN 0021-9991.

Chapter 2

A Fluid-Structure Coupled Computational Model for the Certification of Shock-Resistant Elastomer Coatings

(Published in *Proceedings of the ASME 2020 39th International Conference on Offshore Mechanics and Arctic Engineering*, OMAE2020-18501, V02AT02A024, 2020.)

W. Ma[a], X. Zhao[a], K. Wang[a]

[a] Department of Aerospace and Ocean Engineering, Virginia Tech

Blacksburg, VA 24061, United States

Abstract

Shock waves from underwater and air explosions are significant threats to surface and underwater vehicles and structures. Recent studies on the mechanical and thermal properties of various phase-separated elastomers indicate the possibility of applying these materials as a coating to mitigate shock-induced structural failures. To demonstrate this approach and investigate its efficacy, this paper presents a fluid-structure coupled computational model capable of predicting the dynamic response of air-backed bilayer (i.e. elastomer coating – metal substrate) structures submerged in water to hydrostatic and underwater explosion loads. The model couples a three-dimensional multiphase finite volume computational fluid dynamics model with a nonlinear finite element computational solid dynamics model using the FIVER (FInite Volume method with Exact multi-material Riemann solvers) method. The kinematic boundary condition at the fluid-structure interface is enforced using an embedded boundary method that is capable of handling large structural deformation and topological changes. The dynamic interface condition is enforced by formulating and solving local, one-dimensional fluid-solid Riemann problems, which is well-suited for transferring shock and impulsive loads. The capability of this computational model is demonstrated through a numerical investigation of hydrostatic and shock-induced collapse of aluminum tubes with polyurea coating on its inner surface. The thickness of the structure is resolved explicitly by the finite element mesh. The nonlinear material behavior of polyurea is accounted for using a hyper-viscoelastic constitutive model featuring a modified Mooney-Rivlin equation and a stress relaxation function in the form of prony series. Three numerical experiments are conducted to simulate and compare the collapse of the structure in different loading conditions, including a constant pressure, a fluid environment initially in hydrostatic equilibrium, and a two-phase fluid flow created by a near-field underwater explosion.

2.1 Introduction

Shock waves from underwater and air explosions are major threats to ocean vehicles and structures. The design and application of shock mitigation materials and methods has been a long-standing active research area. Within this area, recent studies have revealed some extraordinary properties of several phase-separated elastomers (e.g., polyureas), which indicates a promising approach for mitigating shock-induced damage and failure [3, 8, 22, 28, 30]. Specifically, these copolymers with separated glassy and rubbery domains at nm to µm scales can be tailored chemically to achieve a combination of energy dissipation, resilience, and stiffness under high pressure, high strain-rate loading. Therefore, they can be applied to the surface of various structures as a shock (and ballistic impact) mitigation coating.

As an example, the effectiveness of polyurea coatings for mitigating shock-induced deformation and fracture has been demonstrated at different scales (e.g., [1, 3, 4]). These studies have also shown that the performance of the coating under shock loading depends not only on their material properties, but also on the complex dynamic interaction of the coating material with the underlying substrate and the surrounding fluid media (e.g., water, air). For example, it has been shown that the effectiveness of the coating depends on the material of the substrate, and on which side of it (i.e. inner or outer surface) the coating is applied [4]. Also, the effect of the same polyurea coating under underwater and aerial shock loadings are different [4]. Furthermore, it has been found that increasing the coating thickness continuously does not translate to a continuous increase in its performance, and the optimal thickness depends sensitively on both the shock loading condition and the substrate [3].

Because of these complexities, the design and practical use of high strain-rate sensitive elastomer coatings for specific engineering applications require improved knowledge and predictive capability regarding a challenging shock-dominated multi-material fluid-structure

interaction problem, featuring

- three-dimensional (3D) shock wave transmission, reflection, and attenuation through the solid and fluid materials and at their interfaces (i.e. fluid-coating, coating-substrate, and substrate-fluid interfaces);
- large deformation, hyper-elastic, and viscoelastic/viscoplastic behaviors of the coating material; and
- shock-induced material damage and dynamic fracture under high strain-rate loading.

In the past, extensive research has been devoted towards understanding the mechanical behaviors of elastomer coatings under high pressure, high strain-rate loading (e.g., [1, 3, 4, 16, 17, 19, 22, 23, 25, 29, 30, 31, 32, 40]). Several fundamental mechanisms by which elastomer coatings protect the substrate have been identified through laboratory experiments (e.g., Barsoum and Dudt [3], Amini *et al.* [1]) and numerical analysis (e.g., Heyden *et al.* [19], Filonova *et al.* [16]). Several research teams have tested elastomer material coupons to measure their properties and dynamics under high strain-rate and high pressure loading. For example, using a high-speed drop weight tensile test instrument, Roland *et al.* [30] carried out stress-strain measurements for polyureas with strain rate varying from 10^{-2} s^{-1} to 10^{2} s^{-1}. Using the Split-Hopkinson Pressure Bar with various modifications, a few teams (e.g., Yi *et al.* [40], *Sarva et al.* [31], Song *et al.* [32], Nemat-Nasser *et al.* [29]) have conducted compression tests for polyureas (and other elastomers) with strain rate varying from 10^{2} s^{-1} to 10^{3} s^{-1}. It has been discovered that as strain rate increases to 10^{3} s^{-1}, its elastic modulus can increase by up to three orders of magnitude. Using a sandwiched Pressure-Shear Plate Impact (PSPI) facility, Jiao *et al.* [22, 23] have conducted pressure-shear tests on polyurea, and found that at a strain rate of 10^{5} to 10^{6} s^{-1}, the response (e.g., shear resistance, shear wave speed) of polyurea also depends sensitively on the impact pressure. For example,

they found that when the impact pressure increases from 1 to 10 GPa, the plateau-level (saturation) shear resistance of polyurea P-1000 increases also by one order of magnitude, from 0.1 GPa to 1.0 GPa.

These studies have shown that the response of elastomeric polyurea under high pressure and high strain-rate loading, such as in the scenarios of underwater and aerial explosions, is closely related to the material's highly nonlinear properties and behaviors, including (1) large strain nonlinear elasticity, (2) asymmetric stress-strain behavior in compression and tension, (3) rate- and pressure-dependent viscoelasticity and viscoplasticity, (4) substantial hysteresis during unloading, and (5) stretch-induced softening [4, 7]. Based on the experimental data obtained, several constitutive models have been developed and calibrated to account for these features. For example, Amirkhizi *et al.* [2] developed and calibrated a viscoelastic constitutive model for polyurea, where the viscoelastic relaxation is modeled using a 4-term Prony series, which is then scaled to account for the impacts of temperature and pressure. Cho *et al.* [7] developed and calibrated a viscoelastic-viscoplastic constitutive model for polyurea (PU1000), in which the nonlinear strain-rate dependence is captured using separate micro-rheological linear spring-and-dashpot models for the soft (rubbery) and hard (glassy) domains of polyurea. Clifton *et al.* [10] have developed and calibrated a quasi-linear viscoelastic constitutive model for polyurea, featuring a continuous distribution of viscoelastic relaxation times. The model also generalizes the Mooney-Rivlin hyperelasticity model with an additional multiplicative factor that accounts for the (experimentally observed) dependence of shear wave speed on pressure.

Despite the recent progresses reviewed above, the dynamic process of shock wave impacting on the bilayer coating-substrate structure is still unclear, which involves the propagation and attenuation of shock waves within multiple solid (elastomer coating and substrate) and fluid (e.g., water, air) materials, as well as the dynamic interaction of these materi-

als at fluid-structure and coating-substrate interfaces. In this paper, we present a three-dimensional CFD (computational fluid dynamics) – CSD (computational solid dynamics) coupled computational model, referred to as FIVER (FInite Volume method with Exact multi-material Riemann solvers), for predicting the dynamic response of bilayer elastomer coating – substrate systems (e.g., polyurea-aluminum) to underwater shock loading. The key components of FIVER relevant to this study include (1) a parallel nonlinear (both material-wise and geometry-wise) finite element CSD solver, equipped with a modified Mooney-Rivlin hyperelasticity model [10] and a prony series viscoelastic relaxation function [2] for polyurea, (2) a parallel finite volume, multiphase compressible Navier-Stokes CFD solver, equipped with a level-set method for tracking fluid-fluid interfaces (e.g., UNDEX bubble) [14, 35]; (3) a second-order, numerically stable partitioned time-integrators for coupling the CFD and CSD solvers [12]; and (4)a second-order embedded boundary method with multi-material Riemann problem solvers for enforcing the transmission conditions at fluid-structures interfaces, particularly designed for problems involving large deformation and fracture [15, 20, 26, 27, 34, 35, 36]. Over the past decade, FIVER has been applied to study several fluid-structure interaction problems in ocean, aerospace, and biomedical engineering applications, including underwater hydrostatic implosion [13, 38], pipeline explosion [24, 39], shock wave lithotripsy [5, 6, 37], bio-mimetic propulsors [9], and supersonic parachute deployment [21].

We demonstrate the computational model through a numerical investigation of hydrostatic and shock-induced collapse of an aluminum cylinder with polyurea coating on its inner surface. The thickness of the structure is resolved explicitly by the finite element mesh. The nonlinear material behavior of polyurea is accounted for using a hyper-viscoelastic constitutive model featuring a modified Mooney-Rivlin equation [10] and a stress relaxation function in the form of prony series [2]. Three numerical tests are presented, in which the structure

is subjected to different loading conditions, including a constant pressure (i.e. without consideration of fluid-structure interaction), an ambient fluid initially at rest, and a two-phase fluid flow created by a near-field underwater explosion.

2.2 Physical model and numerical methods

We consider a model problem shown in Figure 2.1, which involves a cylindrical metal structure submerged in water. The elastomer coating can be applied on either side of the metal. This figure illustrates the secenario of a near-field explosion, that is, the distance between the explosive charge and the structure is relatively small, such that the dynamics of the gaseous explosion product — sometimes referred to as the "bubble" — should also be considered. Therefore, the problem involves three fluid subdomains: the ambient fluid (i.e. water), the gas inside the structure (e.g., air), and the explosion product. If instead the explosion occurs at a large distance from the structure, it can be modeled as a pressure wave, with profile and amplitude determined by experimental data and similitude equations (cf. [11, 33]).

Due to the presence of shock waves, the fluid in all the subdomains are modeled as compressible flows, governed by the Navier-Stokes equations,

$$\frac{\partial W(x,t)}{\partial t} + \nabla \cdot F(W) = \nabla \cdot G(W, \nabla W), \tag{2.1}$$

with

$$W = \begin{bmatrix} \rho \\ \rho V \\ \rho e_t \end{bmatrix}, \quad F = \begin{bmatrix} \rho V^T \\ \rho V \otimes V + p\boldsymbol{I} \\ (\rho e_t + p)V^T \end{bmatrix}, \quad G = \begin{bmatrix} 0 \\ \boldsymbol{\tau} \\ V^T\boldsymbol{\tau} - Q^T \end{bmatrix}, \tag{2.2}$$

where we have used lower case, upper case, and bold letters to denote scalars, vectors, and

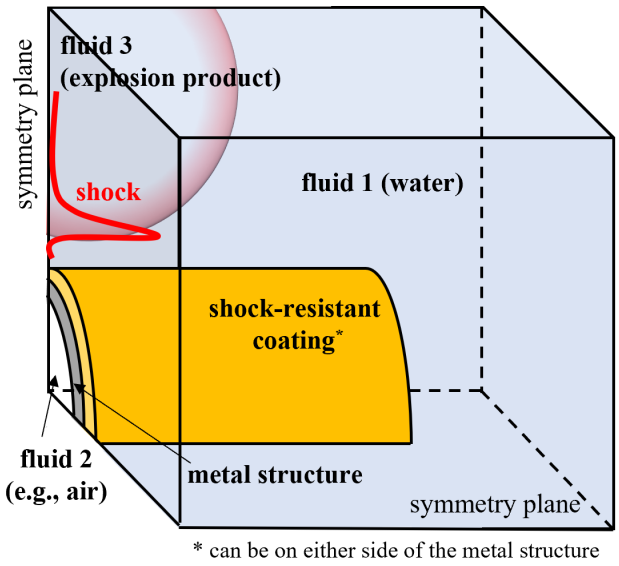

Figure 2.1: Certification of shock-resistant elastomer coatings: A model problem.

second-order tensors, respectively. Specifically, ρ, V, e_t, p, and $\boldsymbol{\tau}$ denote fluid density, velocity, total energy per unit mass, pressure, and the viscous stress tensor, respectively. $\boldsymbol{I}$ is the 3×3 identity matrix. Q denotes the heat flux. Equations (2.1) and (2.2) have already neglected any body forces (in particular, gravity) and heat sources. In this paper, for simplicity we also neglect the effects of viscosity and heat diffusion, which reduces Equation (2.1) to the Euler equations, i.e.

$$\frac{\partial W(x,t)}{\partial t} + \nabla \cdot F(W) = 0, \tag{2.3}$$

Following Wang *et al.* [39], we adopt the Tait equation of state (EOS) for the liquid water, and the perfect gas EOS for the gas inside the cylinder. For simplicity, in this paper we model the gaseous explosion product as a high pressure air bubble, also using the perfect gas EOS. The level-set equation is solved to track the evolution of the bubble.

To solve the multi-material fluid-structure interaction problem, we apply the method of FIVER (Finite Volume method with Exact multi-material Riemann solvers). In an augmented fluid domain that includes all the fluid subdomains and the region occupied by

the solid structure, the fluid governing equations are semi-discretized by an unstructured, node centered, non-interface-conforming finite volume mesh. Then, for an arbitrary control volume C_i, the Euler equations are integrated, which gives

$$\frac{\partial W_i}{\partial t} + \frac{1}{\|C_i\|} \sum_{j \in N(i)} \int_{\partial C_{ij}} F(W) \cdot \boldsymbol{n_{ij}} dS = 0, \tag{2.4}$$

where W_i denotes the average W in control volume C_i; $\|C_i\|$ denotes the volume of C_i; $N(i)$ is the set of nodes that are connected to node i by an edge; $\partial C_{ij} = \partial C_i \cap \partial C_j$ is the boundary faces of the two control volume; and $\boldsymbol{n}_{ij}$ is the unit normal to ∂C_{ij}. Then, we compute the flux in different ways, depending on the location of nodes i and j — specifically, which fluid or structural subdomain does it belong to. Additional details of FIVER have been presented in previous publications, including [15, 27, 39].

The dynamic equilibrium of a structure undergoing finite deformation is modeled in the Lagrangian setting using the following equations

$$\rho_s \frac{\partial^2 u_j}{\partial t^2} = \frac{\partial}{\partial x_i} \left(\tau_{ij} + \tau_{im} \frac{\partial u_j}{\partial x_m} \right) + b_j, \tag{2.5}$$

where the subscripts i, j, and m vary from 1 to 3 and designate the (x, y, z) coordinate system. ρ_s denotes structure density in the undeformed configuration, u the displacement vector, and τ the second Piola–Kirchoff stress tensor[1]. b denotes the body force vector, which is set to 0 in this paper. The dynamic response of polyurea is modeled as an instantaneous elastic response followed by a viscoelastic stress relaxation process. Accordingly, the constitutive model for polyurea consists of two parts, namely a hyperelastic model and a stress relaxation model.

When modeling the instantaneous elastic response, polyurea is considered as an isotropic

[1] to be distinguished from the fluid viscous stress tensor.

hyperelastic material undergoing finite deformation. The hyperelastic model used in this paper is the one proposed by Clifton *et al.* [10]. In this model, the strain energy density function has the form

$$\bar{W} = f(J)\hat{W}(\bar{I}_1, \bar{I}_2), \tag{2.6}$$

where $\hat{W}(\bar{I}_1, \bar{I}_2)$ is the strain energy associated with distortion, and $f(J)$ is a factor that depicts the effect of volumetric change. This multiplicative decomposition of strain energy, in contrast to the traditional addictive decomposition, was designed to better describe the shear wave speed's strong dependence on pressure.

Following Clifton *et al.* [10], the factor $f(J)$ takes the form

$$f(J) = \left(J^{-M} - 2J^{-N}\right) + 2, \tag{2.7}$$

where J is the volume ratio after and before deformation. It can be computed as the square root of the determinant of right Cauchy-Green deformation tensor. M and N are material constants, and $M = 2N$. The "+2" in Equation (2.7) allows $f(J)$ to satisfy the requirement of $f(1) = 1$.

The distortional strain energy, $\hat{W}(\bar{I}_1, \bar{I}_2)$, has the Mooney Rivlin form,

$$\hat{W}(\bar{I}_1, \bar{I}_2) = C_{00} + C_{01}(\bar{I}_2 - 3) + C_{02}(\bar{I}_1 - 3), \tag{2.8}$$

where $\bar{I}_1$ and $\bar{I}_2$ are given by

$$\bar{I}_1 = J^{-2/3} I_1, \tag{2.9}$$

$$\bar{I}_2 = J^{-4/3} I_2, \tag{2.10}$$

where I_1 and I_2 are the first and second invariant of the right Cauchy-Green deformation tensor.

The right Cauchy-Green deformation tensor, C, has the following relation with the Green-Lagrangian strain tensor E:

$$\boldsymbol{C} = 2\boldsymbol{E} + \boldsymbol{I}, \tag{2.11}$$

where I is the 3×3 identity matrix.

The second Piola–Kirchoff stress tensor $\boldsymbol{\tau}$ is given by

$$\boldsymbol{\tau} = \frac{\partial \bar{W}}{\partial \boldsymbol{E}}, \tag{2.12}$$

and the Cauchy stress tensor T is given by

$$T = \frac{1}{\det(\boldsymbol{F})} \boldsymbol{F}\boldsymbol{\tau}\boldsymbol{F}^T, \tag{2.13}$$

where F is the deformation gradient tensor.

The stress relaxation model addresses the deviatoric and the hydrostatic (dilatational) stress components in different ways. The reason is that, in many cases, the dilatational response of polyurea can be effectively modeled as elastic. Amirkhizi *et al.* [2] and Clifton and Jiao [4] also showed that the effect of hydrostatic stress relaxation is small. Therefore, in this work, the viscoelastic stress relaxation process is only applied to deviatoric stresses. The deviatoric and hydrostatic parts of the instantaneous Cauchy stresses have the relation given by

$$\sigma^e_{ij} = T_{ij} - \sigma^e_{\text{hyd}} \delta_{ij}, \tag{2.14}$$

where σ^e_{ij} is the instantaneous elastic deviatoric stress, T_{ij} is the instantaneous elastic Cauchy

stress, δ_{ij} is the Kronecker delta, and σ^e_{hyd} is the hydrostatic stress, given by

$$\sigma^e_{\text{hyd}} = \frac{\text{tr}(\boldsymbol{T})}{3}, \tag{2.15}$$

where tr denotes the trace operator.

The deviatoric stress after relaxation, $\sigma(t)$, may be expressed in the form of the convolution integral as shown by Goh *et al.* [18], i.e.

$$\sigma(t) = \int_0^t g(t-s)\frac{d\sigma^e}{ds}ds, \tag{2.16}$$

where $g(t)$ is the relaxation function, which can be written in the form of Prony series,

$$g(t) = g_\infty + \sum_{i=1}^{N} g_i \exp\Big(-\frac{t}{\tau_i}\Big), \tag{2.17}$$

where τ_i (not the stress tensor) are relaxation times, g_∞ and g_i $(i = 1, \cdots, N)$ are dimensionless constants.

$$g_\infty + \sum_{i=1}^{N} g_i = 1. \tag{2.18}$$

Substituting Equation (2.17) into (2.16) yields

$$\sigma(t) = g_\infty \sigma^e(t) + \sum_{i=1}^{N} g_i \int_0^t \exp\Big(-\frac{t-s}{\tau_i}\Big)\frac{d\sigma^e}{ds}ds. \tag{2.19}$$

One benefit of the exponential form in Equation (2.17) (the Prony series) is that the convolution integral can be evaluated using a finite time increment formulation which, instead of storing the entire stress history, only needs to store the information from last time step. Thus, the computational expense is significantly reduced.

Specifically, when implementing the stress relaxation model (in particular, Equation (2.19)), the following property of the exponential function is utilized:

$$\exp\Big(-\frac{t_{n+1}}{\tau_i}\Big) = \exp\Big(-\frac{t_n}{\tau_i}\Big)\exp\Big(-\frac{\Delta t}{\tau_i}\Big), \tag{2.20}$$

where the subscripts n and $n+1$ denote two consecutive time steps, and Δt the time step size.

Substituting Equation (2.20) into (2.19), we obtain the recursive formula

$$\begin{aligned}\sigma(t_{n+1}) = g_\infty \sigma^e(t_{n+1}) + \sum_{i=1}^{N}\Big(&\exp\big(-\frac{\Delta t}{\tau_i}\big)h_i(t_n) \\ &+ g_i\tau_i\frac{\sigma^e(t_{n+1})-\sigma^e(t_n)}{\Delta t}\big(1-\exp\big(-\frac{\Delta t}{\tau_i}\big)\big)\Big),\end{aligned} \tag{2.21}$$

where

$$h_i(t_n) = \int_0^t g_i \exp\big(-\frac{t-s}{\tau_i}\big)\frac{d\sigma^e}{ds}ds. \tag{2.22}$$

Using Equation (2.21), the computation of stress at any time step only requires information from the previous step. This is an important advantage as it simplifies implementation and significantly reduces memory requirement.

2.3 Numerical experiments

The structure investigated is a circular aluminum shell with polyurea coating applied on its inner surface. The axial thickness of the shell is 0.4 mm. The radius and the radial thickness of the aluminum shell are 19.1 mm and 0.711 mm, respectively. The radial thickness of polyurea coating is 0.2 mm. The entire structure is discretized with hexahedron grids.

The aluminum shell and polyurea coating have 5 and 4 layers of grid in radial direction respectively. In circumferential direction, the structure is divided into 400 elements. Since there is no force or motion in axial direction (i.e. the x-axis), only one layer of grid is used in axial direction. Figure 2.1 (top) shows the geometry and the finite element grid of the structural model, including both the aluminum shell and the polyurea coating.

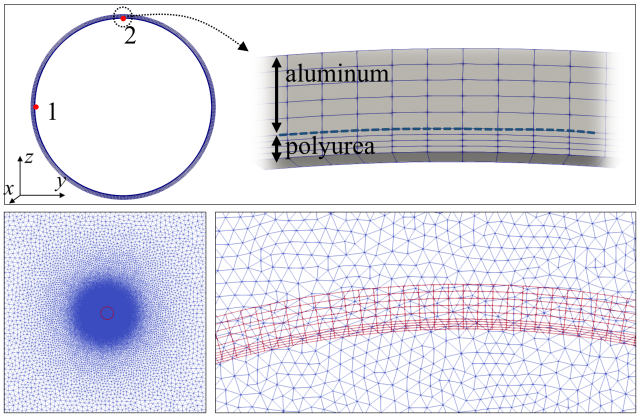

Figure 2.2: Setup of numerical experiment: A finite element model of an aluminum cylinder coated with polyurea on its inner surface (top), and an unstructured, non-interface-conforming finite volume fluid mesh for fluid-structure coupled analysis (bottom).

In the numerical experiments, aluminum has a Young's modulues of 70.8 GPa, Poisson's ratio of 0.33, and a density of 2.78×10^{-3} g/mm^3. The constitutive model of the aluminum shell is a finite strain plastic material law, in which the yielding stress is 30.4 GPa, tangent modulus is 66.74 GPa, and the hardening is pure isotropic. The constitutive models of polyurea coating have been discussed in the previous section. The parameters in hyperelasticity model are identical to those in Clifton *et al.* [10]: density is 1.07×10^{-3}g/mm^3, $C_{00} = 0.2684$ GPa, $C_{01} = C_{02} = 0.1098$ GPa, and $M = 4.4$. The stress relaxation model uses a two-term Proney series, in which the parameters are acquired through simplifying the four-term Proney series from Amirkhizi *et al.* [2]. Based on the time scale of the current problem (of the order of milliseconds), we adopt the two terms in the relaxation function with $\tau = 0.064$ ms and 1.163×10^{-4} ms. Therefore, the parameters are $g_\infty = 0.26$, $g_1 = 0.237$, $g_2 = 0.503$, $\tau_1 = 0.064$

ms, and $\tau_2 = 1.163 \times 10^{-4}$ ms. In the structural model, a 0.1% ovality is introduced as a geometric imperfection to drive the structure to collapse in mode 2.

Figure 2.2 also shows a top view of the unstructured non-interface-conforming fluid mesh, which has 0.21 million nodes and 0.64 million tetrahedron elements. In the most refined region, that is, where the structure and the bubble are located, the characteristic element size is 0.3 mm.

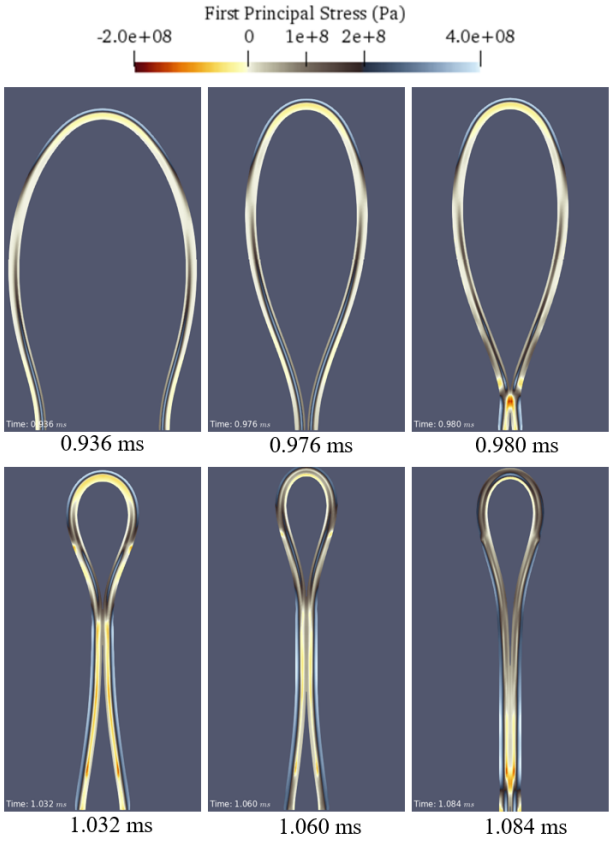

Figure 2.3: Collapse of the aluminum-polyurea structure under a constant pressure load. (The upper half of the structure is shown.)

Next, we present three numerical tests in which the structure is placed in different loading conditions. Specifically, we present

- a "dry" simulation in which the outer surface of the structure is subjected to a constant

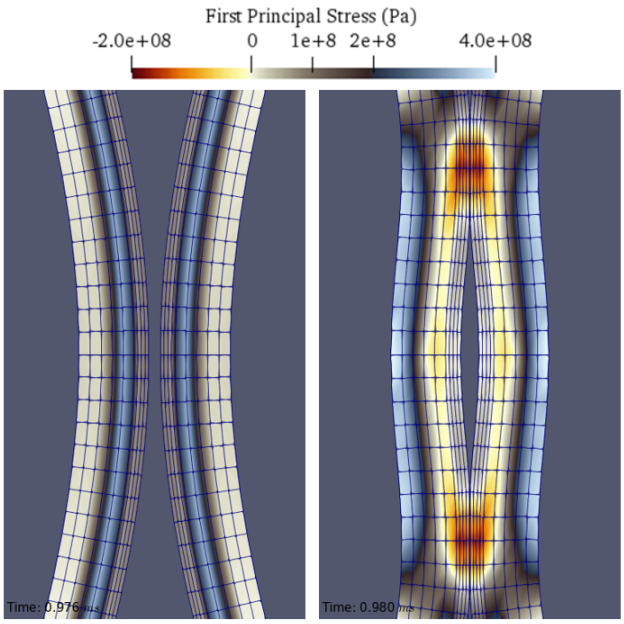

Figure 2.4: A close-up view of the self-contact.

pressure, 1.8 MPa. As the structure deforms, the direction of the pressure load at any point changes accordingly (as a follower force). Nonetheless, the magnitude of pressure is fixed. This setup effectively decouples the dynamics of the structure from that of the surrounding fluid. Therefore, the fluid dynamics solver is not involved in the simulation.

- A fluid-structure coupled analysis of the collapse of the structure due to hydrostatic pressure. In this case, the fluid pressure is initially set to 1.8 MPa, in consistency with the dry simulation.

- A fluid-structure coupled analysis of the a near-field explosion. The explosion bubble is modeled as a spherical bubble with an initial radius of 2.5 mm, centered at approximately 11 mm from the outer surface of the structure. The pressure and density inside the bubble are set to 50.0 MPa and 5.0×10^{-5} g/mm^3. The hydrostatic pressure is set to 1.0 MPa, which is lower than the (hydrostatic) collapse pressure of the structure.

Figures 2.3 and 2.4 present the time-history of the structural deformation and stress predicted by the dry simulation, with Figure 2.4 showing the moment of self-contact. The process of collapse takes about 0.98 ms until the middle points (in z-axis) reach in contact. Afterwards, the region of contact moves towards the upper and lower ends, until approximately 1.08 ms, the structure is roughly in static equilibrium (but still with high frequency, low amplitude oscillations).

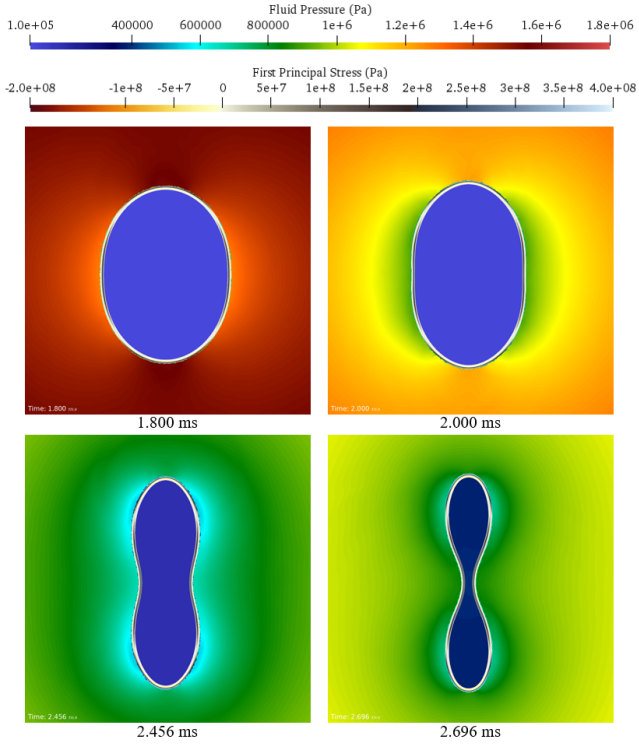

Figure 2.5: Fluid-structure coupled analysis of collapse due to hydrostatic pressure: Time-history of fluid and structural results, before the structure reaches self-contact.

Figures 2.5 and 2.6 present the time-history of fluid pressure and structural dynamics predicted by the second simulation, which accounts for the fluid-structure interaction during the collapse of the structure. As the boundary of the structure moves inward, it gives the surrounding water a non-zero velocity, which leads to the reduction of pressure. This in turn reduces the pressure load on the structural surface, thereby decreasing the speed of its collapse. Figure 2.6 presents a sequence of images showing the pressure variation after the

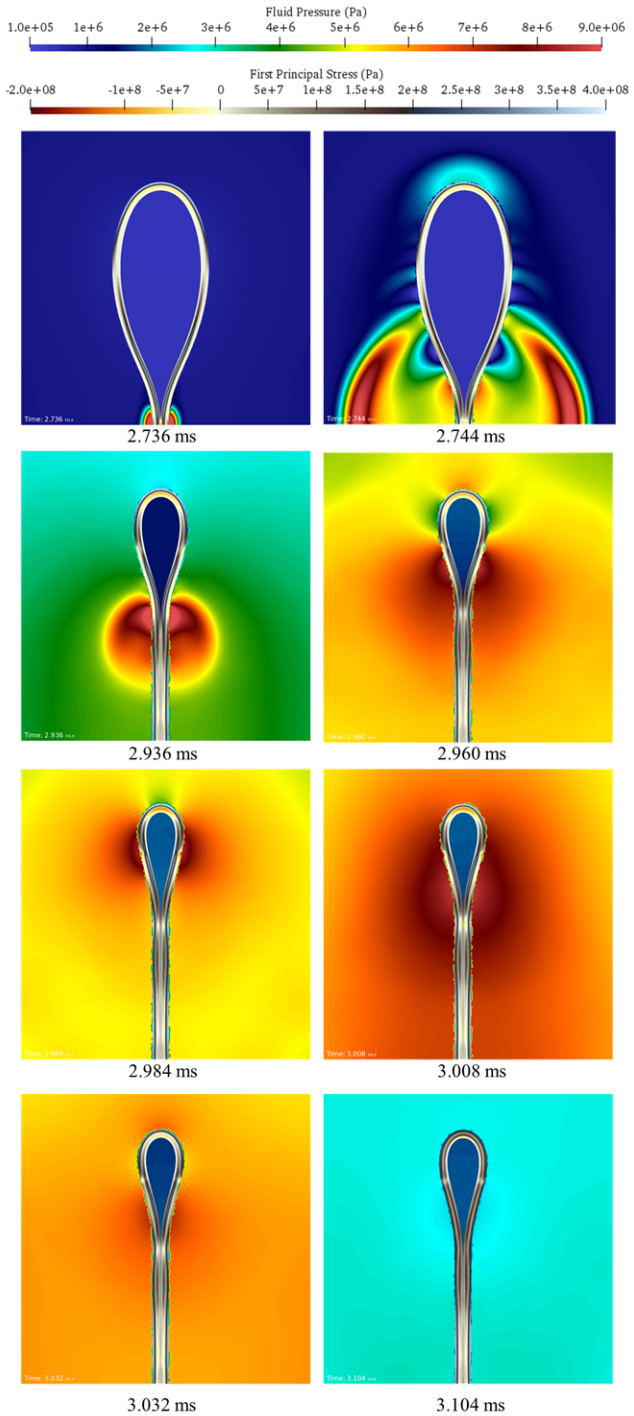

Figure 2.6: Fluid-structure coupled analysis of collapse due to hydrostatic pressure: Time-history of fluid and structural results after the structure reaches self-contact. (The upper half of the structure is shown.)

structure reaches self-contact. To the surrounding fluid flow, the contact of the structure means a sudden drop of velocity (to approximately 0), which leads to a sudden rise of pressure. Figure 2.6 shows that as the region of contact spreads out, the region of high pressure follows its front.

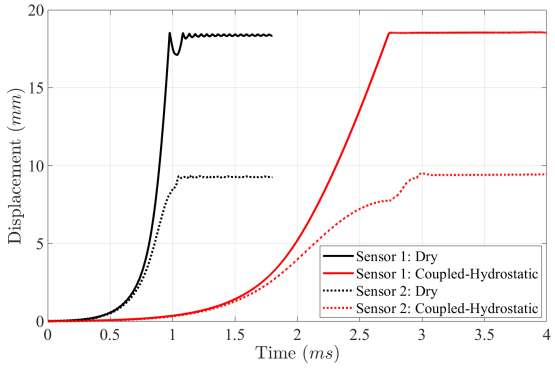

Figure 2.7: Comparison of "dry" and coupled analysis: Time-history of displacement at two sensor points on the inner surface of the structure (see Fig. 2.2).

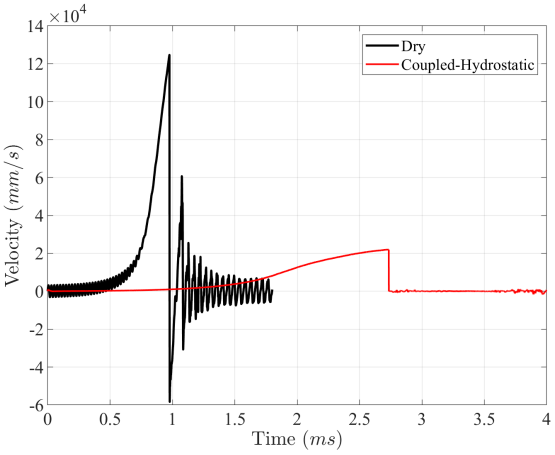

Figure 2.8: Comparison of "dry" and coupled analysis: Time-history of velocity at a sensor point on the inner surface of the structure (see Fig. 2.2).

Comparing the results obtained from the dry and coupled simulations, it is clear that the former significantly overpredicts the speed of the structure's collapse, as it ignores the decrease of pressure in the surrounding flow during the course. Figure 2.7 compares the local displacement at two sensors on the inner surface of the structure (i.e. in the region of polyurea).

The time of collapse, measured up to the time instance the structure reaches self-contact, is found to be 0.98 ms in the dry simulation, compared to 2.7 ms in the coupled simulation. In addition, Figure 2.8 compares the structural velocity at one of the two sensors. It can be observed that in both the dry and the coupled simulations, the velocity increases monotonically throughout the duration of the collapse. The maximum velocity is found to be around 125 m/s in the dry simulation, which is about 6 times higher than that in the coupled simulation.

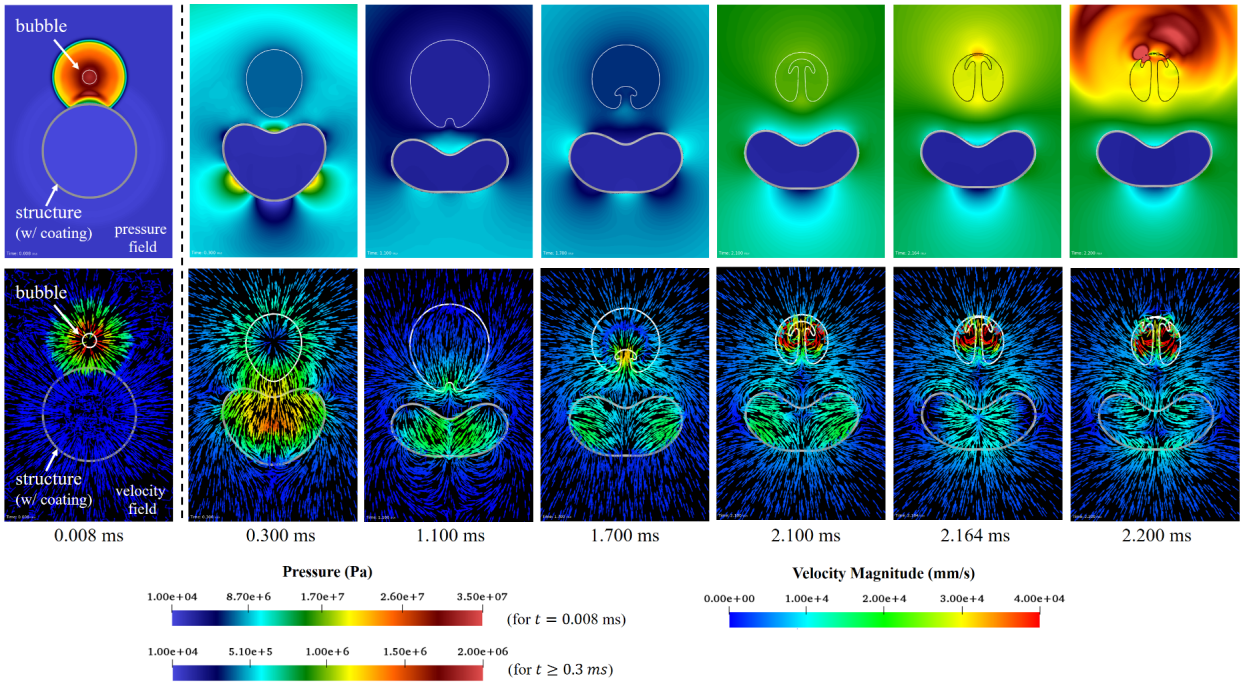

Figure 2.9: Result of the fluid-structure coupled analysis of a near-field explosion.

Figure 2.9 shows a sequence of solution snapshots obtained from the third test, which features a near-field explosion. Specifically, the two images taken at 0.008 ms shows the spherical shock wave impacting on the top of the structure, which drives the structure to collapse. The structure's deformation is different from, and more complex than, that observed in the previous two test cases. At 0.3 ms, the upper side of the structure is moving inward, whereas the lower side is moving outward. As the upper side of the structure moves inward, it also

pulls the bubble towards it. Gradually the bubble deforms from a perfect sphere to an oval. Between 0.3 ms and 2.1 ms, it can be observed that the structure vibrates instead of immediately flattens as found in the previous two cases. Interestingly, as the upper side of the structure bounces back (from 1.1 ms to 1.7 ms), it produces a liquid jet that penetrates into the bubble. As the jet moves inside the bubble, it generates two vortices, and gradually deforms into a mushroom shape. The last two columns of image, taken at 2.164 ms and 2.2 ms, shows that when the liquid jet reaches the upper side of the bubble, it leads to a sudden increase of pressure at the point of contact.

2.4 Concluding remarks

By adopting and implementing several recently developed constitutive models of polyurea, we have extended the FIVER framework to model and simulate the dynamic response of structures with polyurea coating to hydrostatic and underwater explosion loads. We have presented a numerical experiment that compares the response of a coated aluminum cylinder in different loading conditions, which also demonstrates the capabilities of the computational framework. Additional studies are being performed to validate the computational model, and applying it to simulate more realistic structures and test cases.

Acknowledgment

The authors gratefully acknowledge the support of the Office of Naval Research (ONR) under Awards N00014-19-1-2102, and the support of the National Science Foundation (NSF) under Awards CBET-1751487.

Bibliography

[1] MR Amini, J Isaacs, and S Nemat-Nasser. Investigation of effect of polyurea on response of steel plates to impulsive loads in direct pressure-pulse experiments. *Mechanics of Materials*, 42(6):628–639, 2010.

[2] AV Amirkhizi, J Isaacs, J McGee, and S Nemat-Nasser. An experimentally-based viscoelastic constitutive model for polyurea, including pressure and temperature effects. *Philosophical magazine*, 86(36):5847–5866, 2006.

[3] GS Barsoum and PJ Dudt. The fascinating behaviors of ordinary materials under dynamic conditions. *Ammtiac Quarterly*, 4:11–14, 2010.

[4] Roshdy George S Barsoum. *Elastomeric Polymers with High Rate Sensitivity: Applications in Blast, Shockwave, and Penetration Mechanics*. William Andrew, 2015.

[5] Shunxiang Cao, Ying Zhang, Defei Liao, Pei Zhong, and Kevin G Wang. Assessing the effect of lithotripter focal width on the fracture potential of stones in shockwave lithotripsy. *The Journal of the Acoustical Society of America*, 141(5):3718–3718, 2017.

[6] Shunxiang Cao, Ying Zhang, Defei Liao, Pei Zhong, and Kevin G Wang. Shock-induced damage and dynamic fracture in cylindrical bodies submerged in liquid. *International Journal of Solids and Structures*, 169:55–71, 2019.

[7] Hansohl Cho, Renaud G Rinaldi, and Mary C Boyce. Constitutive modeling of the rate-dependent resilient and dissipative large deformation behavior of a segmented copolymer polyurea. *Soft Matter*, 9(27):6319–6330, 2013.

[8] Taeyi Choi, Daniel Fragiadakis, C Michael Roland, and James Runt. Microstructure

and segmental dynamics of polyurea under uniaxial deformation. *Macromolecules*, 45 (8):3581–3589, 2012.

[9] Howard Chung, Shunxiang Cao, Michael Philen, Philip S Beran, and Kevin G Wang. Cfd-csd coupled analysis of underwater propulsion using a biomimetic fin-and-joint system. *Computers & Fluids*, 172:54–66, 2018.

[10] Rodney J Clifton, Xinjie Wang, and Tong Jiao. A physically-based, quasilinear viscoelasticity model for the dynamic response of polyurea. *Journal of the Mechanics and Physics of Solids*, 93:8–15, 2016.

[11] Robert Hugh Cole. *Underwater explosions*. Dover Publications, 1965.

[12] C Farhat, A Rallu, K Wang, and T Belytschko. Robust and provably second-order explicit–explicit and implicit–explicit staggered time-integrators for highly non-linear compressible fluid–structure interaction problems. *International Journal for Numerical Methods in Engineering*, 84(1):73–107, 2010.

[13] C Farhat, KG Wang, A Main, Stelios Kyriakides, L-H Lee, Krishnaswa Ravi-Chandar, and T Belytschko. Dynamic implosion of underwater cylindrical shells: experiments and computations. *International Journal of Solids and Structures*, 50(19):2943–2961, 2013.

[14] Charbel Farhat, Arthur Rallu, and Sriram Shankaran. A higher-order generalized ghost fluid method for the poor for the three-dimensional two-phase flow computation of underwater implosions. *Journal of Computational Physics*, 227(16):7674–7700, 2008.

[15] Charbel Farhat, Jean-FréDéRic Gerbeau, and Arthur Rallu. Fiver: A finite volume method based on exact two-phase riemann problems and sparse grids for multi-material

flows with large density jumps. *Journal of Computational Physics*, 231(19):6360–6379, 2012.

[16] Vasilina Filonova, Yang Liu, and Jacob Fish. Generalized viscoplasticity based on overstress (gvbo) for large strain single-scale and multiscale analyses. In *Numerical Simulations of Coupled Problems in Engineering*, pages 3–27. Springer, 2014.

[17] Erin Gauch, James LeBlanc, and Arun Shukla. Near field underwater explosion response of polyurea coated composite cylinders. *Composite Structures*, 202:836–852, 2018.

[18] SM Goh, MN Charalambides, and JG Williams. Determination of the constitutive constants of non-linear viscoelastic materials. *Mechanics of Time-Dependent Materials*, 8(3):255–268, 2004.

[19] Stefanie Heyden, B Li, Kerstin Weinberg, Sergio Conti, and M Ortiz. A micromechanical damage and fracture model for polymers based on fractional strain-gradient elasticity. *Journal of the Mechanics and Physics of Solids*, 74:175–195, 2015.

[20] Daniel Z Huang, Dante De Santis, and Charbel Farhat. A family of position- and orientation-independent embedded boundary methods for viscous flow and fluid–structure interaction problems. *Journal of Computational Physics*, 365:74–104, 2018.

[21] Daniel Z Huang, Philip Avery, Charbel Farhat, Jason Rabinovitch, Armen Derkevorkian, and Lee D Peterson. Modeling, simulation and validation of supersonic parachute inflation dynamics during mars landing. In *AIAA Scitech 2020 Forum*, page 0313, 2020.

[22] T Jiao and RJ Clifton. Measurement of the response of an elastomer at pressures up to 9 gpa and shear-rates of 105–106s- 1. In *Journal of Physics: Conference Series*, volume 500, page 112036. IOP Publishing, 2014.

[23] Tong Jiao and Rodney Clifton. Experimental and computational investigation of the shearing resistance of an elastomer at pressures up to 18 gpa and strain rates of 105-106s-1. In *APS Shock Compression of Condensed Matter Meeting Abstracts*, 2015.

[24] Patrick D Lea, Charbel Farhat, and Kevin G Wang. A fluid-structure coupled computational framework for fluid-induced failure and fracture. In *ASME 2015 34th International Conference on Ocean, Offshore and Arctic Engineering*. American Society of Mechanical Engineers Digital Collection, 2015.

[25] James LeBlanc and Arun Shukla. Response of polyurea-coated flat composite plates to underwater explosive loading. *Journal of Composite Materials*, 49(8):965–980, 2015.

[26] Alex Main and Charbel Farhat. A second-order time-accurate implicit finite volume method with exact two-phase riemann problems for compressible multi-phase fluid and fluid–structure problems. *Journal of Computational Physics*, 258:613–633, 2014.

[27] Alex Main, Xianyi Zeng, Philip Avery, and Charbel Farhat. An enhanced fiver method for multi-material flow problems with second-order convergence rate. *Journal of Computational Physics*, 329:141–172, 2017.

[28] AD Mulliken and MC Boyce. Mechanics of the rate-dependent elastic–plastic deformation of glassy polymers from low to high strain rates. *International journal of solids and structures*, 43(5):1331–1356, 2006.

[29] S Nemat-Nasser. Experimental characterization of polyurea with constitutive modeling and simulation. In *Proceedings of ONR, ERC, ACTD Workshop, MIT, Cambridge, Massachusetts*, 2004.

[30] CM Roland, JN Twigg, Y Vu, and PH Mott. High strain rate mechanical behavior of polyurea. *Polymer*, 48(2):574–578, 2007.

[31] Sai S Sarva, Stephanie Deschanel, Mary C Boyce, and Weinong Chen. Stress–strain behavior of a polyurea and a polyurethane from low to high strain rates. *Polymer*, 48 (8):2208–2213, 2007.

[32] B Song and W Chen. Dynamic compressive behavior of epdm rubber under nearly uniaxial strain conditions. *J. Eng. Mater. Technol.*, 126(2):213–217, 2004.

[33] Michael M Swisdak Jr. Explosion effects and properties. part ii. explosion effects in water. Technical report, Naval Surface Weapons Center White Oak Lab, Silver Spring, MD, 1978.

[34] Kevin Wang, Jon Gretarsson, Alex Main, and Charbel Farhat. Computational algorithms for tracking dynamic fluid-structure interfaces in embedded/immersed boundary methods. In *20th AIAA Computational Fluid Dynamics Conference*, page 3385, 2011.

[35] Kevin Wang, Arthur Rallu, J-F Gerbeau, and Charbel Farhat. Algorithms for interface treatment and load computation in embedded boundary methods for fluid and fluid–structure interaction problems. *International Journal for Numerical Methods in Fluids*, 67(9):1175–1206, 2011.

[36] Kevin Wang, J Grétarsson, A Main, and C Farhat. Computational algorithms for tracking dynamic fluid–structure interfaces in embedded boundary methods. *International Journal for Numerical Methods in Fluids*, 70(4):515–535, 2012.

[37] Kevin G Wang. Multiphase fluid-solid coupled analysis of shock-bubble-stone interaction in shockwave lithotripsy. *International journal for numerical methods in biomedical engineering*, 33(10):e2855, 2017.

[38] Kevin G Wang, Patrick Lea, Alex Main, Owen McGarity, and Charbel Farhat. Predictive simulation of underwater implosion: Coupling multi-material compressible fluids

with cracking structures. In *ASME 2014 33rd International Conference on Ocean, Offshore and Arctic Engineering*, pages V08AT06A028–V08AT06A028. American Society of Mechanical Engineers, 2014.

[39] KG Wang, P Lea, and C Farhat. A computational framework for the simulation of high-speed multi-material fluid–structure interaction problems with dynamic fracture. *International Journal for Numerical Methods in Engineering*, 104(7):585–623, 2015.

[40] J Yi, MC Boyce, GF Lee, and E Balizer. Large deformation rate-dependent stress–strain behavior of polyurea and polyurethanes. *Polymer*, 47(1):319–329, 2006.

Chapter 3

Computational Analysis of Bubble-Structure Interactions in Near-Field Underwater Explosion: A Counter-Intuitive Mode of Structural Collapse

(Published in *Proceedings of the ASME 2021 International Mechanical Engineering Congress and Exposition*, IMECE2021-72854, V012T12A004, 2022.)

W. Ma[a], T. Ozenkoski[a], K. Wang[a]

[a] Department of Aerospace and Ocean Engineering, Virginia Tech

Blacksburg, VA 24061, United States

The coauthor Mr. Timothy Ozenkoski contributed to the writing of this conference article.

A COMPUTATIONAL ANALYSIS OF BUBBLE-STRUCTURE INTERACTION IN NEAR-FIELD UNDERWATER EXPLOSION

Wentao Ma, Timothy Ozenkoski, Kevin Wang*
Department of Aerospace and Ocean Engineering
Virginia Polytechnic Institute and State University
Blacksburg, Virginia 24061

ABSTRACT

Underwater explosion poses a significant threat to the structural integrity of ocean vehicles and platforms. Accurate prediction of the dynamic loads from an explosion and the resulting structural response is crucial to ensuring safety without overconservative design. When the distance between the explosive charge and the structure is relatively small (i.e., near-field explosion), the dynamics of the gaseous explosion product, i.e., the "bubble", comes into play, rendering a multiphysics problem that features the interaction of the bubble, the surrounding liquid water, and the solid structure. The problem is highly nonlinear, as it involves shock waves, large deformation, yielding, contact, and possibly fracture. This paper investigates the two-way interaction between the cyclic expansion and collapse of an explosion bubble and the deformation of a thin-walled elastoplastic cylindrical shell in its vicinity. Intuitively, when a shock wave impinges on a thin cylindrical shell, the shell would collapse in the direction of shock propagation. However, some recent laboratory experiments have shown that under certain conditions the shell collapsed in a counter-intuitive mode in which the direction of collapse is perpendicular to that of shock propagation. In other words, the nearest point on the structural surface moved towards the explosion charge, despite being impacted by a compressive shock. This paper focuses on replicating this phenomenon through numerical simulation and elucidating the underlying mechanisms. A recently developed computational framework ("FIVER") coupling a nonlinear finite element structural dynamics solver and a finite volume compressible fluid dynamics solver is used to complete this study. The solver utilizes an embedded boundary method to track the wetted surface of the structure (i.e. the fluid-structure interface), which is capable of handling large structural deformation and topological changes (e.g., fracture). The solver also adopts the level set method for tracking the bubble surface (i.e. the liquid-gas interface). The fluid-structure and liquid-gas interface conditions are enforced by constructing and solving one-dimensional multi-material Riemann problems, which naturally accommodates the propagation of shock waves across the interfaces. In this paper, mesh refinement study is made to examine the sensitivity of the results to various meshing parameters. The results show that the intermediate level of refinement is appropriate in terms of both the accuracy and the computation costs. Next, the deformation history of both the bubble and the structure are presented and analyzed to provide a detailed view of the counter-intuitive collapse mode mentioned above. We show that timewise, the structural collapse spans multiple cycles of bubble oscillation. Additional details about the time-histories of fluid pressure, structure displacement, and bubble size are presented to elucidate this dynamic bubble-structure interaction and the resulting structural failure.

Keywords: fluid-structure interaction, underwater explosion, bubble dynamics, collapse, simulation

1. INTRODUCTION

Submerged structures and vehicles are susceptible to damage and collapse induced by both near-field and far-field underwater explosions. These explosions typically consist of two primary parts: the bubble located at the origin of the explosion, and the shock wave that is formed from the explosion. In free field, the shock wave profile can be readily described using a combination of experimentally determined data and an exponentially decaying function, such as Cole's Model [1]. The fluid-structure interaction induced by both the shock wave and the bubble dynamics, however, is more complex and generally requires a coupled simulation or laboratory experiment to fully and accurately describe the phenomena. When dealing with near-

* Corresponding author. E-mail address: kevinwgy@vt.edu

field and far-field explosions, the loading effects can generally be broken down into three different conditions.

1. The explosion is a far-field explosion and the only loading the structure undergoes is the planar shockwave from the explosion (e.g., [2-4]).
2. The explosion is an extreme near-field explosion in which the bubble is close enough to the structure that it pulls towards it and merges on the structure's wetted surface (e.g., [5,6]).
3. The explosion is a near-field explosion in which the bubble is sufficiently far away from the structure that it does not merge with the structure, but the structure undergoes loading from the pulsation of the bubble (e.g., [7-9]).

In condition 1, the bubble created is far enough away from the structure that the two do not interact, and the effects of bubble pulsation can be ignored. As a result, the primary effect from the explosion that should be considered is a shock wave that can often be assumed to be planar. The dynamic response and failure of structures under shock waves produced by far-field explosions have been studied extensively in the past. For example, various studies (e.g., [2-4]) have shown how explosions can cause damage or collapse on various structures, including ship hulls, underwater pipelines, and submarines. These large pressure waves can cause large plastic deformations in a structure and can easily cause severe damaging. Bartolini *et al.* discusses how varying the distance between the explosion origin and structure can impact whether a thin cylindrical shell would collapse under a specific loading condition [10]. Of the three conditions mentioned above, this is probably the simplest to model.

In the case of a near-field explosion, conditions 2 and 3 are both possible. In condition 2, if the bubble is adjacent to the structure, the bubble will pull towards it and merge with the structure's surface. This can have catastrophically damaging effects as when the bubble expands, it may have a pressure much lower than the hydrostatic pressure of the surrounding fluid. When the bubble is initially formed, the pressure inside is much higher than the hydrostatic pressure of the medium surrounding it. As the bubble expands, the bubble pressure can decrease below the hydrostatic pressure of the fluid, creating a region on the surface of the structure where the pressure distribution varies significantly. For example, Brett and Yiannakopolous discusses this phenomenon and highlights how this interaction is largely more damaging than the pulsation of the bubble and even the initial contact of the shock wave [11].

The third condition is one where the bubble is close enough to the structure that the pulsation can have an influence on its deformation but is sufficiently far away so that the bubble does not merge with the structure. This condition is less severe than the other near-field condition but is still potentially more damaging than the far-field alternative. Due to the close proximity of the explosion to the structure, the shock wave from a weaker explosion can be just as impactful as a larger explosion much farther away. Additionally, if the structure is deformed from the initial shock wave, then the following pulsations can act to further deform and damage it. These pulsations are typically lower in magnitude than the initial load but can act to increase the damage on an already damaged structure. Various numerical studies have been used to show this phenomena, and multiple experiments have been performed in [12,13].

In an underwater explosion, it is shown that the bubble formed does not purely expand and then disperse. Due to the explosion, the bubble initially has a small radius and an internal pressure much higher than that of the surrounding fluid. As the radius of the bubble increases, the internal pressure of the bubble decreases until the hydrostatic pressure of the surrounding fluid is then higher than the pressure of the bubble, which in turn causes for the bubble's radius to decrease until the internal pressure is once again higher than that of the surrounding fluid. Depending on the loading conditions and boundary conditions, the bubble will continue this oscillation in size until it initially disperses. For every oscillation of the bubble, a pressure pulse is propagated through the surrounding medium and significant energy is taken out of the system. After enough energy has been taken out, the bubble will finally collapse, and the pulsation will stop.

Although the bubble is initially shaped spherically, throughout its pulsation multiple forces interact with it to cause shape deformation [14]. As the bubble pulsates, a jet stream may form around it, pushing into the center of the bubble. If this stream is powerful enough, it can perturb through the bubble and cause it to break into two separate bubbles. Other factors, such as the materials used to cause the explosion, the shape of the initial charge, and the style of detonation can also influence the initial shape of the bubble and its collapse. Zhang *et al.* refers to this as "*the memory effect*" as the bubbles "remembers" the conditions it was initially created under and is influenced by those conditions as well [14].

In this paper, we investigate the two-way interaction between the dynamics of an explosion bubble and the deformation and collapse of a thin-walled elastoplastic cylindrical shell, in the context of near-field explosion in which the bubble is close to the structural surface but does not merge with it. Although a thin-walled cylindrical shell is a broad term, it has a number of practical applications, and results from its collapse can be related to structural applications on both submarines and underwater pipelines. In both of these cases, the collapse condition of the structure is dependent on a number of variables, including material properties, ovality, eccentricity, the length/thickness ratio, and the diameter/thickness ratio [15].

While most research on submarines is classified, several applicable papers have been published regarding the collapse of cylindrical tubes under hydrostatic loading, shock-induced loading, and the combined loading of both these conditions. Ikeda presented a study that discussed how the length/diameter ratio influenced the mode of collapse of a cylindrical shell and found that models with a larger length/diameter ratio collapsed in mode 2, whereas models with a smaller ratio collapsed in a higher mode [16]. Kyriakides *et al.* also performed multiple investigations on how imperfections and characteristics of the geometry of a cylindrical shell would influence collapse,

including studies on denting [17], localization of collapse on finite-length shells [18], and the collapse of long cylindrical shells under the combined loads of external hydrostatic pressure and bending [19].

While the dimensions of a manufactured cylindrical shell have been shown to impact the collapse pressure of the structure, imperfections caused by manufacturing processes can also have a significant impact as well. During manufacturing, these shells (i.e., pipelines) commonly undergo a cold-form manufacturing process that typically leave a pipeline with an ovality < 1.0% and rarely exceeding 2% [20-22]. Even an ovality of 1% can have a significant impact on the critical pressure of a cylindrical shell, potentially reducing the collapse pressure of a thick-walled pipeline by over 25% [23]. An ovality of 10% would have even more drastic influence on the critical pressure of a cylinder, reducing it to 50% that of a cylindrical shell that had no ovality [16].

The dynamics of collapse for a bubble work in tandem with the geometric properties, material properties, and imperfections of the cylindrical shell to influence collapse. In the case of this numerical experiment, the complex behaviors of bubble pulsation are paired with hydrostatic pressure, physical properties, and the imperfections of ovality to create an atypical collapse behavior where the structure is pulled towards the bubble instead of collapsing in the direction of the initial shock wave. This complex study is performed using a three-dimensional CFD (computational fluid dynamics) – CSD (computational structural dynamics) coupled model, in which information such as a fluid velocity field, structural nodal displacement, fluid pressure, and structural strain can all be determined. This includes a Navier-Stokes CFD solver, which is capable of tracking fluid-fluid interfaces between the bubble and the surrounding water. A second-order embedded boundary method capable of handling large deformations is incorporated as well.

This numerical experiment details the collapse of a thin-walled aluminum cylindrical shell under the combined loading from a near-field explosion and from hydrostatic pressure. It holds geometric imperfections, such as initial ovality, and there is no eccentricity on the shell. This solver produces a time-history of collapse, which is analyzed, and the phenomena inducing atypical collapse behavior are discussed.

2. PHYSICAL MODEL AND NUMERICAL METHODS

Figure 1 details the model used to demonstrate the collapse of the thin cylindrical shell. The cylindrical shell has a thickness of 0.711 mm and an outer diameter of 38.911 mm. Numbers 1-4 denote multiple sensors. Sensor 1 detects pressure in fluid and sensor 2-4 measure the displacement of the points on the shell. The reference positions of sensors 2-4 are measured from the center of the undeformed cylinder, but still account for ovality.

This diagram features three unique fluid domains: two gaseous domains and one liquid domain. The liquid domain is the ambient fluid, or water surrounding the cylindrical shell. The other two gaseous domains include the explosion byproduct in the bubble on the top portion of the figure and the air located inside the empty cylindrical shell on the bottom part of the figure.

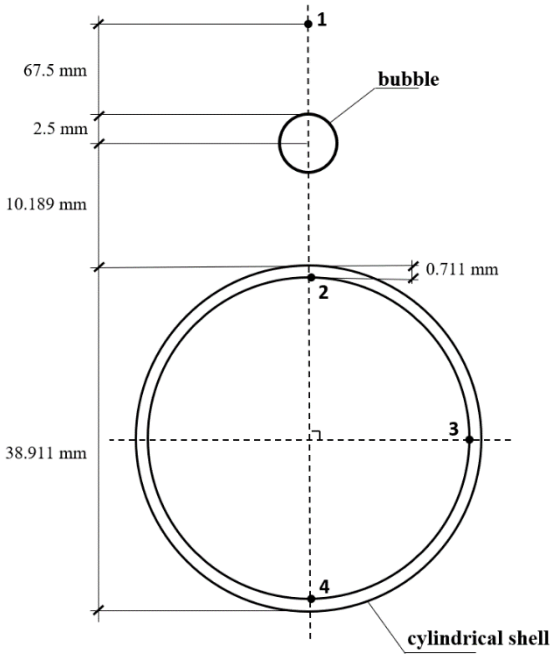

FIGURE 1: Experimental model diagram and dimensions.

Because there is a large variation in pressure due to the shock waves created from the explosion, the medium's behavior is modeled with the Navier-Stokes equations, *Equation (1)* and the fluid is treated as compressible.

$$\frac{\partial W(x,t)}{\partial \mathrm{t}} + \nabla \cdot F(W) = \nabla \cdot G(W, \nabla W) \tag{1}$$

The terms *W, F,* and *G* are described as follows.

$$W = \begin{bmatrix} \rho \\ \rho \mathrm{V} \\ \rho \mathrm{e}_t \end{bmatrix}, F = \begin{bmatrix} \rho \mathrm{V}^T \\ \rho \mathrm{V} \otimes V + \mathrm{p}\mathbf{I} \\ (\rho \mathrm{e}_t + p)V^T \end{bmatrix}, G = \begin{bmatrix} 0 \\ \boldsymbol{\tau} \\ V^T \boldsymbol{\tau} - Q^T \end{bmatrix} \tag{2}$$

In these equations, capitalized letters correspond to vector quantities, lowercase letters correspond scalar quantities, and bolded letters correspond to second-order tensors. ρ is the fluid's density, V is the velocity, e_t is the total energy per unit mass in the system, p is the pressure, $\boldsymbol{\tau}$ is the viscous stress tensor, $\mathbf{I}$ is the 3×3 identity matrix, the superscript T denotes the transpose of the given vector, and Q is the heat flux.

It should be noted that body forces such as gravity are neglected in *Equations (1) and (2)*, and sources of heat have been neglected as well. To simplify the calculations in the solver, viscosity and heat diffusion are also ignored, which reduces *Equation (1)* to the Euler equations, *Equation (3).* This simplified equation models inviscid flow and allows the solver to utilize fewer resources.

$$\frac{\partial W(x,t)}{\partial t} + \nabla \cdot F(W) = 0 \quad (3)$$

The Tait equation of state (EOS) is utilized for the liquid water surrounding both the bubble and cylindrical shell. This equation establishes a relationship between the pressure of the fluid and the density of the fluid, allowing for the liquid water to be treated as compressible. This is necessary due to the extreme loading conditions and large pressure variations produced by the shock waves. The air inside the cylindrical shell follows the ideal gas law.

To simplify modelling farther, the explosion from the detonation of a charge is modeled as a small, high-pressure air bubble following the ideal gas law. To track the progression of the bubble, the level-set equation, *Equation (4)*, is solved where ϕ denotes a function that tracks the interface between exactly two constituents. v is the velocity vector of the fluid.

$$\frac{\partial \phi}{\partial t} + v \cdot \nabla \phi = 0 \quad (4)$$

The simulation in this paper utilized the FIVER method (Finite Volume method with Exact multi-material Riemann solvers) to resolve the collapse of the cylindrical shell. This solver is able to account for the interactions between the fluid domain and the structural body and will deform the body as is appropriate. The fluid mesh is entirely rigid throughout the simulation and does not deform. Instead, an imbedded boundary method tracks the wetted surface of the submerged cylinder and interfaces the interactions between the two meshes, overlaying the continuously deforming cylindrical mesh over the fixed fluid mesh. This method allows for large deformations of the structural mesh and does not require the large computational power another solver might require to deform the fluid mesh along with the structural mesh. This finite volume mesh is unstructured, node-centered, and is non-interface-conforming.

An augmented fluid domain is used, which includes all the subdomains as well as the fluid domain inside of the cylinder and the fluid domain inside of the bubble. The Euler equations are integrated across C_i, an arbitrary control volume, to produce *Equation (5)*.

$$\frac{\partial W_i}{\partial t} + \frac{1}{||C_i||} \sum_{j \in N(i)} \int_{\partial C_{\mathrm{ij}}} F(W) \cdot \boldsymbol{n}_{\mathrm{ij}} \, dS = 0 \quad (5)$$

In *Equation (5)* W_i is the average fluid state vector W in the total control volume C_i. $N(i)$ is the vector of nodes that are connected to the i[th] node by their edge. $\partial C_{\mathrm{ij}} = \partial C_i \cap C_j$ is the boundary faces for the two control volumes. $\boldsymbol{n}_{\mathrm{ij}}$ is the unit tensor that faces normal to the boundary faces ∂C_{ij}. From this information, the flux can be calculated in unique ways which are dependent on the locations of nodes i and j. These unique ways are dependent on the subdomain that the node belongs to.

Equation 6 describes a structure undergoing finite deformation, and it is modeled in the Lagrangian setting.

$$\rho_s \frac{\partial^2 u_j}{\partial t^2} = \frac{\partial}{\partial x_i}(\tau_{\mathrm{ij}} + \tau_{\mathrm{im}} \frac{\partial u_j}{\partial x_m}) + b_j \quad (6)$$

In *Equation (6)*, the subscripts *i*, *j*, and *m* are used to denote values between 1 and 3 and designate a direction in the cartesian (x, y, z) coordinate system. The density of the undeformed structure is denoted by ρ_s, the second Piola-Kirchoff stress is denoted by τ, the nodal displacement vector is denoted by u, and *b* denotes the body force vector. The body force *b* is 0 in this paper as external forces directly acting on any internal portion of the cylindrical shell are neglected.

Geometric and material nonlinearities of aluminum is properly described by a constitutive model based on Green's second-order strain tensor and second Piola-Kirchhoff stress tensor. Plasticity of aluminum follows the J2 yield criterion with isotropic hardening.

Additional details of the FIVER framework can be found in references [24-32]. Over the past decades, FIVER has been applied to several fluid-structure interaction problems including underwater hydrostatic implosion [33-35], pipeline explosion [36,37], shock wave lithotripsy [38-41], bio-mimetic propulsors [42], and supersonic parachute deployment [43]. Several verification and validation studies have also been conducted. For example, Farhat *et al*. [33] showed that for an underwater implosion problem the structural dynamics and fluid pressure predicted by FIVER match closely with the experimental data. Main *et al*. [31] showed that for another implosion experiment, FIVER is able to accurately capture the shock wave resulting from bubble collapse. More recently, Cao et al. [41] validated FIVER and the level set method for the collapse of a bubble in free field and near different solid materials.

3. RESULTS AND DISCUSSION

This numerical experiment investigates a thin cylindrical aluminum shell with material properties detailed in *Table 1* and geometric/finite element properties detailed in *Table 2*. This model assumes the cylindrical shell has infinite length, however for modelling purposes an axial thickness must be prescribed. In this experiment, the finite element mesh is only one element deep and has a thickness of 0.4 mm. The material properties correspond with Aluminum 6061-T6. The ovality of the cylinder was established based off of a sinusoidal function that would modify a perfect cylinder to have two modes of imperfection. These two modes of imperfection will work to push the structure to collapse in mode 2. Although difficult to see in *Figure 1*, the direction of the ovality occurs so that the left- and right-hand sides of the structure are slightly closer to each other, and the bottom and top sides of the structure are slightly farther away.

Table 1: Cylindrical Shell Material Properties

Young's Modulus	Poisson's Ratio	Density	Yield Stress	Tangent Modulus
69.6 GPa	0.33	2779 kg/m^3	292 MPa	674 MPa

Table 2: Cylindrical Shell Geometric / Element Properties				
Outer Diameter	Thickness	Ovality	# Layers	# elements per layer
38.911 mm	0.711 mm	0.1%	5	400

Table 3 denotes information regarding both the bubble's geometry and the fluid medium's properties. Besides, the initial pressure of the air inside the shell is 0.1 MPa with an initial density of 1.225 kg/m^3. It should be noted that the bubble distance is the distance from the center of the bubble to the outer wall of the cylinder. These dimensions can be seen in *Figure 1*.

Table 3: Bubble/Fluid Characteristics and Geometry				
Bubble Distance	Bubble Radius	Bubble Pressure	Fluid Speed of Sound	Hydrostatic Pressure
10.189 mm	2.5 mm	12.5 MPa	1,513.4 m/s	1.0 MPa

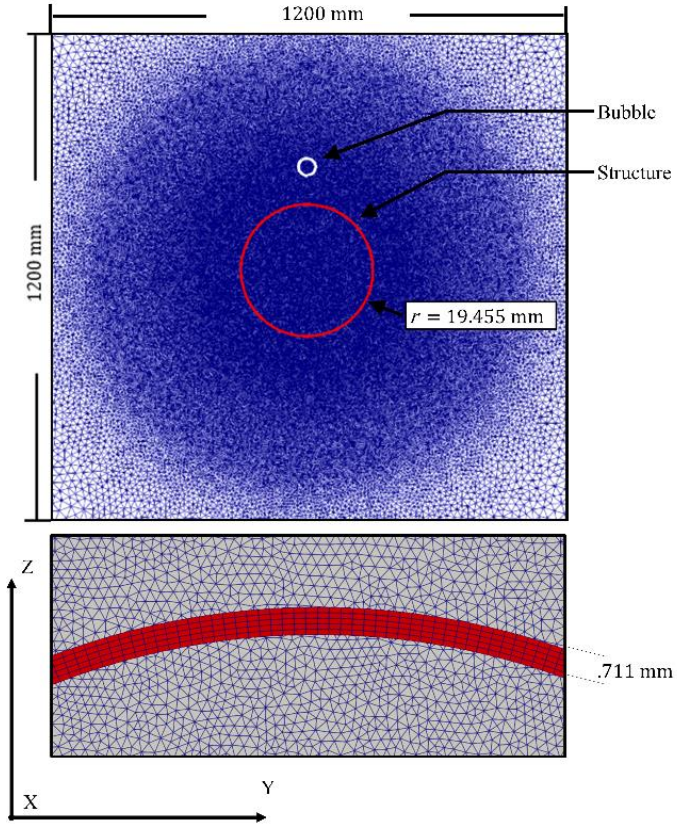

Figure 2: A visual overlay of the non-conforming fluid mesh and the thin cylindrical shell structural mesh. Note that the overall fluid mesh dimension (*1200 mm*) is not to scale as the entire fluid mesh was too large to be encapsulated in the image.

Figure 2 shows the fluid mesh (blue) and structural mesh (red). The inside of the cylinder is meshed to model the air there. To increase the accuracy of the results and the stability of the simulation, the size of one element of the fluid mesh is approximately the same as the size of a structural mesh element at the interface between the two. The centermost portion of the meshes has the highest element density, as most of the interactions occur in that region. As seen in the top subfigure, the mesh resolution decreases as the distance from the structure increases.

Table 4 presents three different computation grids for a mesh refinement study. Solid element density is the number of elements in circumferential and radial directions in the cylindrical shell, e.g., Grid 2 has 5 brick elements through the thickness and 400 elements in one revolution of the cylinder. Finest fluid cell size is the grid size at the interface of fluid mediums and the aluminum cylinder.

Table 4: Computation Grids			
	Solid Element Density	# Fluid Cells	Finest Fluid Cell Size (mm)
Grid 1	200 × 3	0.607×10^6	0.6
Grid 2	400 × 5	0.689×10^6	0.3
Grid 3	600 × 5	4.537×10^6	0.2

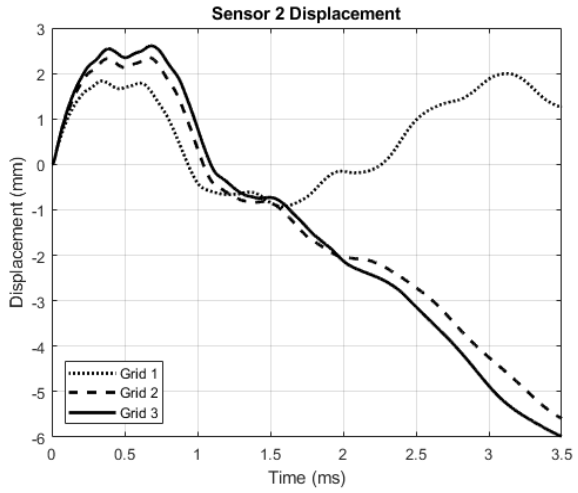

Figure 3: Displacement of sensor 2 for three different element densities

Figure 3 shows the displacement at sensor 2 (the one directly facing the bubble in *Figure 1*) for the three grids listed in Table 4. Results from Grid 2 and the much finer Grid 3 agree reasonably well. The maximum difference between the two curves is about 10% occurring near the end of the curves. Because of the significantly less computation resource required by Grid 2, the following results in this paper are from the simulation on Grid 2.

Figure 4 features a time-history of the collapse of the submerged cylinder paired with the oscillation number of the bubble. Each image in the figure corresponds with one half-cycle of bubble expansion or compression, where lighter shades are earlier time steps and darker shades are later time steps. In each cycle, the left figure showcases the expansion of the bubble, and the right figure showcases the collapse of the bubble. The bubble is located towards the top of the figure, and the cylindrical shell is the larger body towards the bottom of the figure. As observed in Figure 4, the cylindrical shell collapses in a counter-intuitive mode/orientation in which the point facing the explosion moves

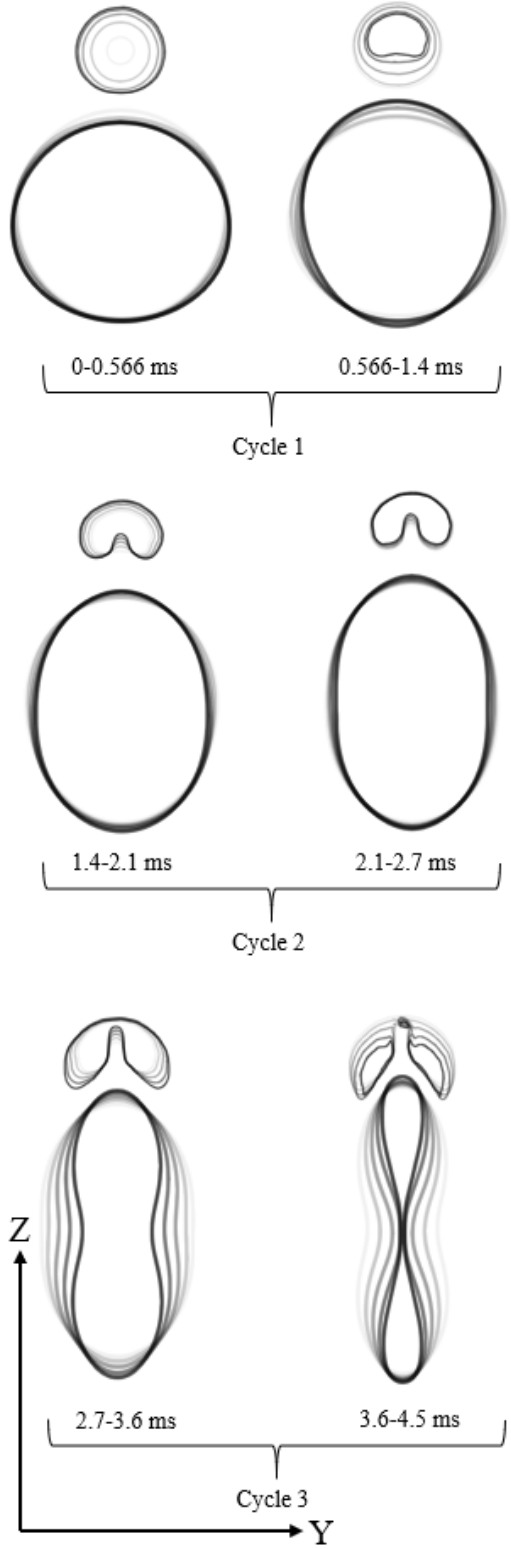

Figure 4: Collapse cycle of the bubble paired with motion of the cylindrical shell. Each image in the figure corresponds with one half-cycle of bubble expansion or compression, where lighter shades are earlier time steps and darker shades are later time steps.

toward the explosive bubble. Ikeda [44] observed similar collapse behavior on Aluminum shells with similar geometry under similar experiment setup.

Cycle 1 is the initial formation of the bubble, where the expansion of the bubble lasts 0.566 ms and the compression of the bubble lasts 0.834 ms. During the first half of the cycle, the bubble maintains an almost purely circular shape as it expands, and the structure begins to ovalize with the longer axis corresponding to the y-axis (denoted at the bottom of *Figure 3*). During the second half of cycle 1, the bubble compresses again and begins to lose its circular shape. A dent is formed along its bottom side and protrudes towards the center of the bubble. During this process, the structure does not continue to be compressed in z-direction and instead begins to be compressed in the y-direction at ~0.4 ms, near the end of the first half cycle. The top of the structure appears to deform in the same direction the dent is forming inside the bubble and undergoes a larger magnitude of deformation than in the first half of the cycle. Before ~0.4 ms, the structure is deformed against the initial ovality, and after that the structure is deformed with the initial ovality. This deformed configuration could be described as an exaggeration of the initially prescribed ovality.

The first half of cycle 2 lasts 0.7 ms, and the second half of cycle 2 lasts 0.6 ms. During both the expansion and the collapse of this cycle, the structure continues to collapse symmetrically about the z-axis. The dent in the bottom side of the bubble continues to perturb through it and increases in magnitude.

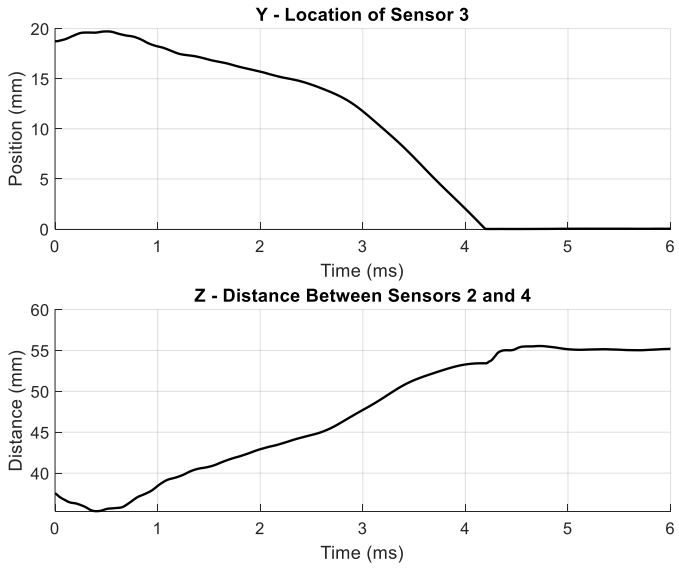

Figure 5: The y-directional location of sensor 3 and the absolute z-directional distance between sensors 2 and 4.

The first half of cycle 3 last 0.9 ms and the second half of cycle 3 also lasts 0.9 ms. It is during this cycle that the bubble splits into two smaller bubbles and the structure collapses. During the expansion, the dent in the bubble almost perturbs through the top of it and the structure undergoes the largest magnitude of deformation. During the second half of the cycle,

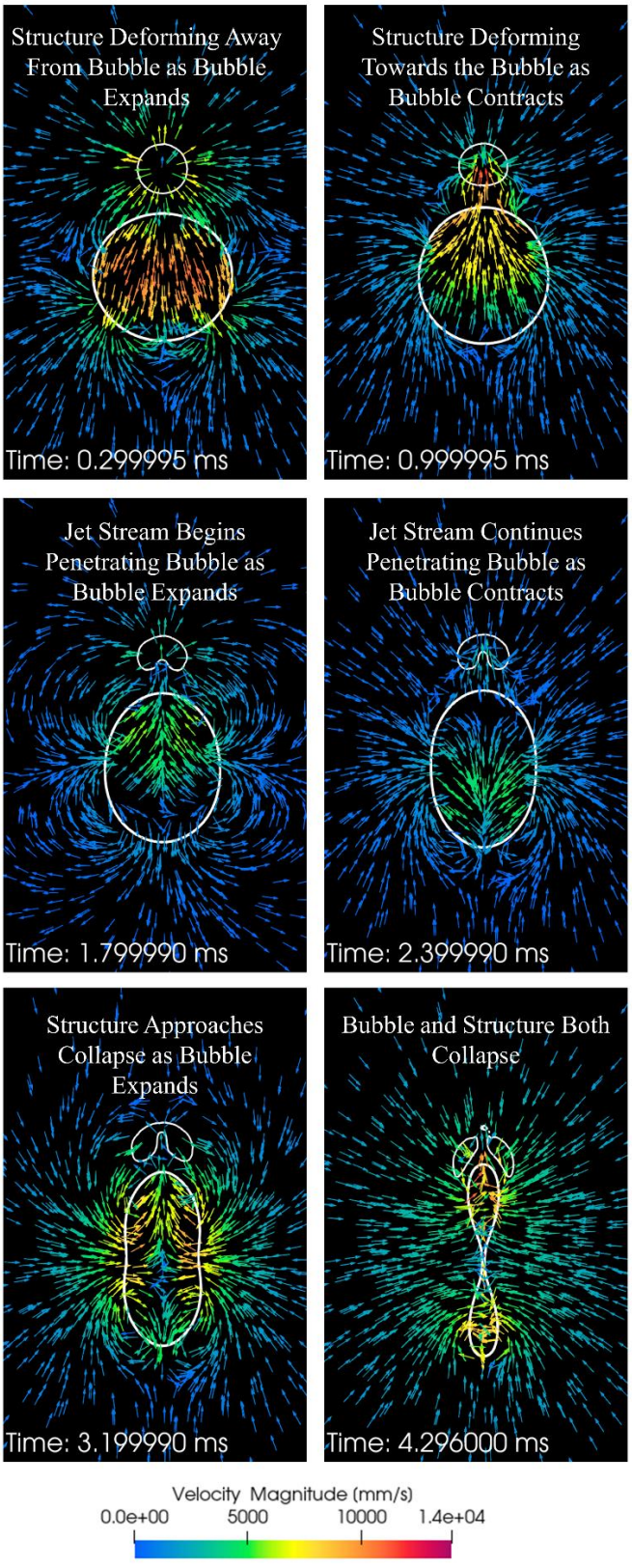

Figure 6: Velocity field of the fluid medium for each half-cycle oscillation of the bubble.

the bubble finally splits through the middle and breaks into two smaller primary bubbles, with a third smallest bubble located above and in-between the two. During this stage, the structure also reaches its final collapse where the left and right sides meet.

Figure 5 shows the displacement at each of the sensors shown in *Figure 1*. The top figure features the y-directional position of the sensor 90 degrees clockwise around the structure from the bubble (origin is at the centroid of cylinder), and the bottom figure features the absolute z-directional distance between sensors 2 and 4. These figures give a better insight towards the motions of the cylindrical shell during collapse.

During the most time of the first bubble half-cycle since explosion, sensor 3 travels farther away from the center of the cylindrical shell, while sensors 2 and 4 move closer together. However, near the end of the first bubble half-cycle, sensor 3 begins approaching the centroid of the shell, while sensors 2 and 4 grow farther apart. The cylindrical shell finally collapses at 4.192 ms where sensor 3 touches the opposite side of the wall. There is a brief period where the collided sections of the structure flatten in the z-direction, but this motion quickly stops, leaving two bulges at either end of the cylinder. After the structure has collapsed at 4.192 ms, sensors 2, 3, and 4 remain primarily stationary and only move a few fractions of a millimeter as residual forces interact with the structure.

Figures 6 and *7* show the velocity field and the pressure field of the fluid medium, respectively. The first image in *Figure 7* shows the initial state of the system, and the remaining images correspond with an instance of time approximately midway through each half-oscillation of the bubble. Although the maximum value of the pressure scale in *Figure 7* is 2.0 MPa, the maximum pressure inside the bubble is 12.5 MPa. This scale range was chosen as most of the interesting behavior occurs in this range, and the initial pressure inside of the bubble dissipates quickly. In *Figure 7*, the structure is colored by the effective plastic strain. As the shell collapses, plastic deformation first occurs at the top and bottom portion of the shell and then at the left and right. *Figure 8* includes a pair of plots that include (in descending order) the pressure detected at sensor 1 from the shock wave and bubble oscillation, as well as the bubble's average radius.

During the first half-cycle of the bubble's oscillation, the initial shock wave from the bubble's expansion hits the structure with a strength of 3.276 MPa detected at sensor 1. A lower pressure region can be seen enveloping the bubble and the entire cylindrical shell, which has pressures much lower than the hydrostatic pressure of 1.0 MPa. Throughout this period, water flows away from the bubble in all directions.

When the bubble begins to collapse in the second half-cycle of its oscillation, the outward flow from the bubble begins to turn inward and the pressure above the shell reaches a minimum. The cylinder begins to collapse about the z-axis instead of the y-axis. Although the bubble has flows coming from all directions, the flow directly between the structure and the bubble is the largest

in magnitude, and a jet can be seen forming between them in the second frame of *Figure 6*.

At the beginning of the second bubble cycle, the pressure around the bubble and cylindrical shell is at a local maximum and begins to decrease (at 1.4 ms in *Figure 8*). Due to this, the bubble begins to expand again, and the flow diverges from the bubble (shown in the third frame of *Figure 6*). Despite this divergence, there is still a mild jet stream between the shell and the bubble that causes for the dent in the bubble to increase. This corresponds with the top point of the shell continuing to travel upwards while the bottom point moves downwards. During the second portion of the second cycle (the fourth frame of *Figure 6*), the bubble shrinks again, and the jet stream becomes slightly stronger. The structure continues to deform in the same motion as previously discussed.

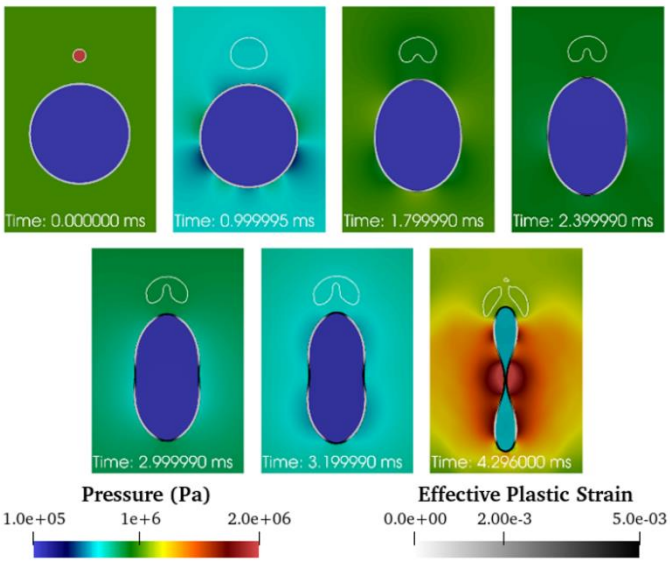

Figure 7: Pressure field time-history starting with the initial conditions, and then showing one instance of time from each half-oscillation of the bubble.

When the bubble begins to expand again at the beginning of cycle 3, the fifth frame of *Figure 6* shows the flow diverging from the bubble in all directions except for the jet stream between the structure, which continues to flow towards the bubble. This flow pattern continues to facilitate the upward motion of the shell's top point and the downward motion of the shell's bottom point. At ~3.3 ms, the water around the upper section of the bubble reverses direction and begins to flow downwards, towards the bubble. The water around the lower-left and lower-right portions of the bubble continues to flow away, but at a higher velocity. This flow is accompanied by growth in the left and right lobes of the bubble, causing for them to become more pronounced.

Once the bubble undergoes the second part of its third cycle, the jet in the last frame of *Figure 6* penetrates through to the other side and the two lobes of the bubble separate at ~3.8 ms. The structure continues to collapse until ~4.2 ms, when the two edges in the middle meet. When these edges meet, a shock wave is emitted from the contact point as the water around it was suddenly stopped.

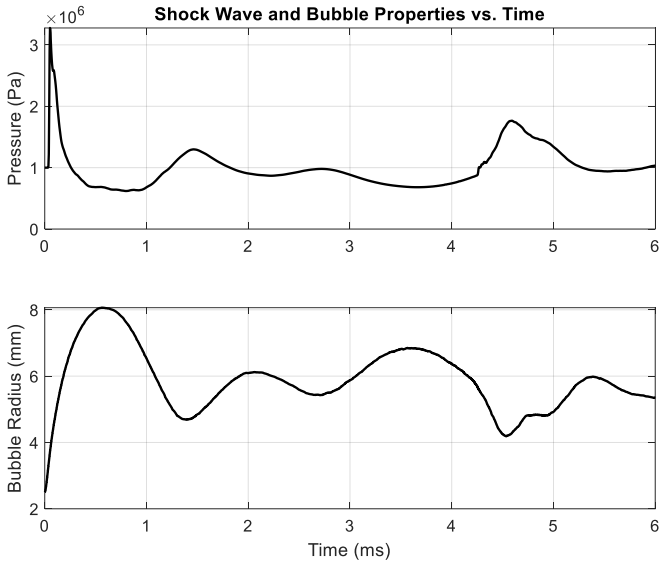

Figure 8: Time-history of overpressure delivered from the shock wave and the average bubble radius.

These findings can be all be visually seen by comparing results from *Figures 4-8*, which encapsulate the full behavior of collapse. *Figure 4* is broken down into six sub-images, which each shows the structure's time-history about a half-cycle of the bubble's oscillation. The top 2 images show (in tandem with *Figure 5*) that the cylindrical shell begins to be compressed in the z-direction and then resists the initial deformation. After this first half-cycle, *Figure 5* shows that the structure continues to separate between sensors 2 and 4 until the entire body collapses. *Figure 6* details the fluid dynamics surrounding the structure, which illustrates how a jet stream was formed to penetrate the bubble. *Figure 8* can then be viewed in tandem with *Figure 6* to visualize the bubble's change in average radius, and the pressure pulses' history. *Figure 7* then serves as a broad overview of how the pressure field fluctuates around the shell at various instances of time, and farther illustrates influences on the collapse of the structure.

4. CONCLUSION

In this paper, we applied a fluid-structure coupled computational framework to model and simulate the interaction between an underwater cylindrical shell and an explosive bubble generated by a near-field underwater explosion. The motion of both the explosive bubble and cylindrical shell, as well as the dynamics of flow field were analyzed. Under certain situation like the one presented in this paper, the cylindrical shell collapses in a counter-intuitive mode/orientation in which the point facing the explosion moves toward the explosive bubble. The moving direction of this collapse mode/orientation is consistent with the liquid jet that diverges from the structure and penetrates through the bubble during the bubble pulsations. Both the collapse mode

and the liquid jet occur under the effects of the interaction between the explosive bubble, the cylindrical shell, and the surrounding liquid. Additional studies are being performed to understand the underlying mechanisms.

ACKNOWLEDGEMENTS

The authors gratefully acknowledge the support of the Office of Naval Research (ONR) under Awards N00014-19-1-2102, and the support of the National Science Foundation (NSF) under Awards CBET-1751487.

REFERENCES

[1] Michael M Swisdak. Explosion Effects and Properties. Part II. Explosion Effects in Water. Technical Report NSWC/WOL TR 76-116, Naval Surface Weapons Center, White Oak, Silver Spring, MD 20910, USA, 1978.

[2] Young S. Shin. Ship Shock Modeling and Simulation for Far-Field Underwater Explosion. *Computers and Structures*, 82(23-26):2211–2219, 2004.

[3] L. Loureiro Silva, and T. A. Netto. On the Dynamic Collapse of Cylindrical Shells Under Hydrostatic and Impulsive Pressure Loadings: Experimental and Numerical Analysis. In *ASME 2011 30th International Conference on Ocean, Offshore and Arctic Engineering*, ASME Paper No. OMAE2011-49361, pp. 299-306, 2011.

[4] Jianyu Wu, Ji Chong, Yuan Long, You Zhou, Yang Yu, and Jianfeng Liu. Experimental Study on the Deformation and Damage of Cylindrical Shell-Water-Cylindrical Shell Structures Subjected to Underwater Explosion. *Thin-Walled Structures*, 127:654–65, 2018.

[5] E. Klaseboer, B.C. Khoo, and K.C. Hung. Dynamics of an Oscillating Bubble near a Floating Structure. *Journal of Fluids and Structures*, 21(4):395–412, 2005.

[6] Shuai Li, A-Man Zhang, Rui Han, and Qingwei Ma. 3D Full Coupling Model for Strong Interaction between a Pulsating Bubble and a Movable Sphere. *Journal of Computational Physics*, 392:713–731, 2019.

[7] A.M. Zhang, X.L. Yao, and J. Li. The Interaction of an Underwater Explosion Bubble and an Elastic–Plastic Structure. *Applied Ocean Research*, 30(3):159–171, 2008.

[8] Jian Li, and Ji-Li Rong. Experimental and Numerical Investigation of the Dynamic Response of Structures Subjected to Underwater Explosion. *European Journal of Mechanics - B/Fluids*, 32:59–69, 2012.

[9] Jia-Xia Wang, Zhi Zong, Kun Liu, and Jie Cui. Simulations of the Dynamics and Interaction between a Floating Structure and a near-Field Explosion Bubble. *Applied Ocean Research*, 78:50–60, 2018.

[10] Lorenzo Maria Bartolini, Lorenzo Marchionni, Caterina Molinari, and Antonio Parrella. Effects of Underwater Explosion on Pipeline Integrity. In *ASME 2015 34th International Conference on Ocean, Offshore and Arctic Engineering*, ASME Paper No. OMAE2015-41092, V05AT04A004, 2015.

[11] John M. Brett, and George Yiannakopolous. A Study of Explosive Effects in Close Proximity to a Submerged Cylinder. *International Journal of Impact Engineering*, 35(4):206–25, 2008.

[12] Ching-Yu Hsu, Cho-Chung Liang, Anh-Tu Nguyen, and Tso-Liang Teng. A Numerical Study on the Underwater Explosion Bubble Pulsation and the Collapse Process. *Ocean Engineering*, 81:29–38, 2014.

[13] Nu Zhang, Zhi Zong, and Wenpeng Zhang. Dynamic Response of a Surface Ship Structure Subjected to an Underwater Explosion Bubble. *Marine Structures*, 35:26–44, 2014.

[14] A-Man Zhang, Shi-Ping Wang, Chao Huang, and Bin Wang. Influences of Initial and Boundary Conditions on Underwater Explosion Bubble Dynamics. *European Journal of Mechanics - B/Fluids*, 42:69–91, 2013.

[15] Stelios Kyriakides and Edmundo Corona. Mechanics of Offshore Pipelines, Volume 1: Buckling and Collapse. Elsevier Science, 2007.

[16] C. M. Ikeda, J. Wilkerling, and J. H. Duncan. The Implosion of Cylindrical Shell Structures in a High-Pressure Water Environment. *Proceedings of the Royal Society A: Mathematical, Physical and Engineering Sciences*, 469(2160):20130443, 2013.

[17] T.-D. Park and S. Kyriakides. On the Collapse of Dented Cylinders under External Pressure. *International Journal of Mechanical Sciences*, 38(5): 557–578, 1996.

[18] J.Y. Dyau and S. Kyriakides. On the Localization of Collapse in Cylindrical Shells under External Pressure. *International Journal of Solids and Structures*, 30(4):463–482, 1993.

[19] Wendell B. Stephens, James H. Starnes, and B. O. Almroth. Collapse of Long Cylindrical Shells under Combined Bending and Pressure Loads. *AIAA Journal*, 13(1):20–25, 1975.

[20] Muntaseer Kainat, J. J. Roger Cheng, Michael Martens, and Samer Adeeb. Measurement and Characterization of the Initial Geometric Imperfections in High Strength U-ing, O-ing and Expanding Manufactured Steel Pipes. *Journal of Pressure Vessel Technology*, 138(2):021201, 2015.

[21] Muntaseer Sarwar-E-Kainat. Initial Imperfections of High Strength UOE Manufactured Steel Pipes and Their Effects on Pipe Buckling. Ph.D. dissertation, University of Alberta, Canada, 2014.

[22] Konstantinos Antoniou, Giannoula Chatzopoulou, Spyros A. Karamanos, Athanasios Tazedakis, Christos Palagas, and Efthimios Dourdounis. Numerical Simulation of JCO-E Pipe Manufacturing Process and Its Effect on the External Pressure Capacity of the Pipe1. *Journal of Offshore Mechanics and Arctic Engineering*, 141(1):011704, 2019.

[23] Jian-Xing Yu, Meng-Xue Han, Jing-Hui Duan, Yang Yu, and Zhen-Zhou Sun. A Modified Numerical Calculation Method of Collapse Pressure for Thick-Walled Offshore Pipelines. *Applied Ocean Research*, 91:101884, 2019.

[24] Charbel Farhat, Jean-Frédéric Gerbeau, and Arthur Rallu. FIVER: A Finite Volume Method Based on Exact Two-Phase Riemann Problems and Sparse Grids for Multi-

Material Flows with Large Density Jumps. *Journal of Computational Physics*, 231(19):6360–6379, 2012.

[25] Alex Main, Xianyi Zeng, Philip Avery, and Charbel Farhat. An Enhanced FIVER Method for Multi-Material Flow Problems with Second-Order Convergence Rate. *Journal of Computational Physics*, 329:141–172, 2017.

[26] Kevin Wang, Arthur Rallu, J-F Gerbeau, and Charbel Farhat. Algorithms for Interface Treatment and Load Computation in Embedded Boundary Methods for Fluid and Fluid–structure Interaction Problems. *International Journal for Numerical Methods in Fluids*, 67(9):1175–1206, 2011.

[27] Charbel Farhat, Arthur Rallu, and Sriram Shankaran. A Higher-order Generalized Ghost Fluid Method for the Poor for the Three-dimensional Two-phase Flow Computation of Underwater Implosions. *Journal of Computational Physics*, 227(16):7674–7700, 2008.

[28] C Farhat, A Rallu, K Wang, and T Belytschko. Robust and Provably Second-order Explicit–explicit and Implicit–explicit Staggered Time-integrators for Highly Non-linear Compressible Fluid–structure Interaction Problems. *International Journal for Numerical Methods in Engineering*, 84(1):73–107, 2010.

[29] Kevin Wang, J Gretarsson, A Main, and C Farhat. Computational Algorithms for Tracking Dynamic Fluid–structure Interfaces in Embedded Boundary Methods. *International Journal for Numerical Methods in Fluids*, 70(4):515–535, 2012.

[30] Kevin Wang, Jon Gretarsson, Alex Main, and Charbel Farhat. Computational Algorithms for Tracking Dynamic Fluid-structure Interfaces in Embedded/immersed Boundary Methods. In *20th AIAA Computational Fluid Dynamics Conference*, page 3385, 2011.

[31] Alex Main and Charbel Farhat. A Second-order Time Accurate Implicit Finite Volume Method with Exact Two-phase Riemann Problems for Compressible Multi-phase Fluid and Fluid–structure Problems. *Journal of Computational Physics*, 258:613–633, 2014.

[32] Daniel Z Huang, Dante De Santis, and Charbel Farhat. A Family of Position-and Orientation-independent Embedded Boundary Methods for Viscous Flow and Fluid–structure Interaction Problems. *Journal of Computational Physics*, 365:74–104, 2018.

[33] C Farhat, KG Wang, A Main, Stelios Kyriakides, L-H Lee, Krishnaswa Ravi-Chandar, and T Belytschko. Dynamic Implosion of Underwater Cylindrical Shells: Experiments and Computations. *International Journal of Solids and Structures*, 50(19):2943–2961, 2013.

[34] Kevin G Wang, Patrick Lea, Alex Main, Owen McGarity, and Charbel Farhat. Predictive Simulation of Underwater Implosion: Coupling Multi-material Compressible Fluids with Cracking Structures. In *ASME 2014 33rd International Conference on Ocean, Offshore and Arctic Engineering*, ASME Paper No. OMAE2014-23341, V08AT06A028, 2020.

[35] Wentao Ma, Xuning Zhao, and Kevin Wang. A Fluid-Structure Coupled Computational Model for the Certification of Shock-Resistant Elastomer Coatings. In *ASME 2020 39th International Conference on Ocean, Offshore and Arctic Engineering*, ASME Paper No. OMAE2020-18501, V02AT02A024, 2020.

[36] Kevin G Wang, Patrick Lea, and Charbel Farhat. A Computational Framework for the Simulation of High-Speed Multi-Material Fluid-Structure Interaction Problems with Dynamic Fracture. *International Journal for Numerical Methods in Engineering*, 104(7): 585–623, 2015.

[37] Patrick D Lea, Charbel Farhat, and Kevin G Wang. A Fluid-structure Coupled Computational Framework for Fluid Induced Failure and Fracture. In *ASME 2015 34th International Conference on Ocean, Offshore and Arctic Engineering*. American Society of Mechanical Engineers Digital Collection, 2015.

[38] Shunxiang Cao, Ying Zhang, Defei Liao, Pei Zhong, and Kevin G Wang. Assessing the Effect of Lithotripter Focal Width on the Fracture Potential of Stones in Shockwave Lithotripsy. *The Journal of the Acoustical Society of America*, 141(5):3718–3718, 2017.

[39] Kevin G Wang. Multiphase Fluid-solid Coupled Analysis of Shock-bubble-stone Interaction in Shockwave Lithotripsy. *International Journal for Numerical Methods in Biomedical Engineering*, 33(10):e2855, 2017.

[40] Shunxiang Cao, Ying Zhang, Defei Liao, Pei Zhong, and Kevin G Wang. Shock-induced Damage and Dynamic Fracture in Cylindrical Bodies Submerged in Liquid. *International Journal of Solids and Structures*, 169:55–71, 2019.

[41] Shunxiang Cao, Guangyao Wang, Olivier Coutier-Delgosha, and Kevin Wang. Shock-induced Bubble Collapse near Solid Materials: Effect of Acoustic Impedance. *Journal of Fluid Mechanics*, 907:A17, 2021.

[42] Howard Chung, Shunxiang Cao, Michael Philen, Philip S Beran, and Kevin G Wang. CFD-CSD Coupled Analysis of Underwater Propulsion Using a Biomimetic Fin-and-joint System. *Computers & Fluids*, 172:54–66, 2018.

[43] Daniel Z Huang, Philip Avery, Charbel Farhat, Jason Rabinovitch, Armen Derkevorkian, and Lee D Peterson. Modeling, Simulation and Validation of Supersonic Parachute Inflation Dynamics during Mars Landing. In *AIAA Scitech 2020 Forum*, page 0313, 2020.

[44] Christine M. Ikeda. Fluid Structure Interactions: Implosions of Shell Structures and Wave Impact on a Flat Plate. Ph.D. dissertation, University of Maryland, College Park, 2012.

Chapter 4

Computational Analysis of Bubble-Structure Interactions in Near-Field Underwater Explosion: Mode Transitions in Structural Collapse

(Published in *International Journal of Solids and Structures*, 242, 111527, 2022.)

W. Ma[a], X. Zhao[a], C. Gilbert[a], K. Wang[a]

[a] Department of Aerospace and Ocean Engineering, Virginia Tech

Blacksburg, VA 24061, United States

Abstract

The response of underwater structures to a near-field explosion is coupled with the dynamics of the explosion bubble and the surrounding water. This multiphase fluid-structure interaction process is investigated in the paper using a two-dimensional model problem that features the yielding and collapse of a thin-walled aluminum cylinder. A recently developed computational framework that couples a finite volume compressible fluid dynamics solver with a finite element structural dynamics solver is employed. The fluid-structure and liquid-gas interfaces are tracked using embedded boundary and level set methods. The conservation of mass and momentum across the interfaces is enforced by solving one-dimensional bimaterial Riemann problems. The initial pressure inside the explosion bubble is varied by two orders of magnitude in different test cases. Three different modes of collapse are discovered, including an horizontal collapse (i.e. with one lobe extending towards the explosive charge) that appears counterintuitive, yet has been observed in previous laboratory experiments. Because of the transition of modes, the time it takes for the structure to reach self-contact does not decrease monotonically as the explosion magnitude increases. The fluid pressure and velocity fields, the bubble dynamics, and the transient structural deformation are visualized to elucidate the cause of each collapse mode and the mode transitions. The result suggests that, in addition to the incident shock wave, the second pressure pulse resulting from the contraction of the explosion bubble also has significant effect on the structure's collapse. The phase difference between the structural vibration and the bubble's expansion and contraction influences the structure's mode of collapse. Furthermore, the transient structural deformation has clear effect on the bubble dynamics, leading to a two-way interaction. A counter-jet that points away from the structural surface is observed. Compared to the liquid jets produced by bubbles collapsing near a rigid wall, this counter-jet is in the opposite direction.

Keywords

fluid-structure interaction, collapse, bubble dynamics, shock wave, underwater explosion, simulation

4.1 Introduction

Underwater explosions pose a significant threat to the structural integrity of marine vehicles, pipelines, and platforms. Accurate prediction of a structure's response to an underwater explosion event is crucial to ensuring safety while reducing the costs associated with overconservative design requirements. If the explosion occurs at a long distance from the structure (i.e. far-field explosion), the load on the structure is dominated by the incident shock wave, which can be captured using one-dimensional hydrodynamics models [8, 33, 37, 41]. If the explosion occurs near the structure (i.e. near-field explosion), the problem becomes more complicated, as the bubble formed by the gaseous explosion products expands and contracts rapidly near the structure. Previous studies have demonstrated that the bubble dynamics, the dynamics of the surrounding liquid water, and the transient deformation of the structure depend on each other, leading to a fluid-structure interaction (FSI) process that involves a multiphase flow, shock waves, complex bubble geometry, large structural deformation, and nonlinear material behaviors (e.g., yielding, fracture) [17, 18, 23, 25, 29, 34].

For thin-walled underwater structures, a primary failure mechanism is instability in the form of collapse. In the past, extensive research efforts have been devoted towards understanding the collapse of cylindrical shell structures (e.g., underwater pipelines, deep-sea submersibles) due to high hydrostatic pressure [11, 24, 26, 28, 43]. In comparison, knowledge about the response of this type of structures to a near-field explosion is still far from complete. A few

recent studies suggest that the pulsation of the explosion bubble may have a substantial effect on the structure's collapse. For example, Gupta *et al.* conducted laboratory experiments on the collapse of aluminum 6061-T6 tubes in a confined environment, in which the tubes are subjected to the combined loading from a prescribed hydrostatic pressure and an explosion that strikes the tubes in the longitudinal direction [17]. Their measurement shows that the magnitude of the first bubble pulse — that is, the increase of pressure due to the first contraction of the explosion bubble — is lower than the incident shock wave, but not negligible. When the hydrostatic pressure is relatively low, the tube starts collapsing after the impact of this bubble pulse, which arrives much later than the incident shock wave. Later, Guzas *et al.* confirmed these findings using fluid-structure coupled simulations [18]. They also showed that the structural collapse may initiate after two to four cycles of bubble expansion and contraction, depending on the hydrostatic pressure. Ikeda conducted implosion experiments using the same type of aluminum tubes within a large pressure chamber, in which the tubes are subjected to a side-on explosion [23]. In these experiments, the initiation of structural collapse also occurs after the arrival of the first bubble pulse. The tubes collapse in mode 2 as expected. But surprisingly, the two lobes are aligned with the loading direction. In other words, the closest point on the cylinder to the explosive charge moves towards the charge. It is hypothesized that this counterintuitive phenomenon is related to the pulsation of the explosion bubble. Although the papers reviewed above (i.e. [17, 18, 23]) do not include details on the explosion bubble dynamics, the results presented therein indicate that the frequency of the bubble's pulsation can be similar to the first few vibration frequencies of the structure. Moreover, some other studies suggest that the dynamics of a bubble pulsating near a deformable surface can be significantly different from that of the same bubble near a rigid wall, which indicates a two-way interaction between the bubble and the structure. For example, Cao *et al.* investigated shock-induced bubble collapse near different types of solid and soft materials, showing that the material's acoustic impedance

has an obvious effect [5]. Several previous studies (e.g., [1, 9, 14, 15, 31]) have investigated bubbles pulsating near a deformable boundary, showing a liquid jet that forms in a direction away from the boundary, that is, in the opposite direction compared to the jets formed by bubbles near a rigid wall.

In this work, we investigate the response of an underwater, thin-walled aluminum cylinder to a near-field explosion, focusing on the interaction between the pulsation of the explosion bubble and the deformation and collapse of the cylinder. Clearly, the magnitude of the explosion is a key parameter. A specific objective in this study is to sweep this parameter through a broad range bounded by two extreme values: a very low magnitude that does not trigger the collapse of the cylinder, and a very high magnitude that causes the cylinder to collapse immediately upon the arrival of the incident shock wave. Based on the research findings mentioned above, we expect to discover transitions between different types of structural and bubble behaviors.

A recently developed fluid-structure coupled computational framework is employed in this study [13, 19, 36, 46, 47]. The framework couples a finite volume compressible fluid dynamics solver with a nonlinear finite element structural dynamics solver using a partitioned time-integration procedure [10]. An embedded boundary method is utilized to track the wetted surface of the structure (i.e. the fluid-structure interface), which is capable of handling large structural deformation and topological changes [45, 46]. A level set method is utilized to track the bubble surface (i.e. the liquid-gas interface) [12, 36]. The fluid-structure and liquid-gas interface conditions are enforced by the FInite Volume method with Exact two-material Riemann problems (FIVER), which naturally accommodates the propagation of shock waves across the interfaces [13, 36, 47]. This computational framework has been verified and validated for several multiphase flow and FSI problems that are closely related to the current application [5, 7, 11, 36, 47, 49, 51]. For example, Farhat *et al.* simulated

the collapse of aluminum 6061-T6 tubes in modes 2 and 4 due to hydrostatic pressure [11]. They showed that the simulation result is in close agreement with the experimental data in both the transient structural deformation and the pressure pulse generated by the structure's self-contact. Cao *et al.* simulated the collapse of a bubble in free field and near different solid and soft materials [5]. They showed that the simulated bubble dynamics in free field matches closely the experimental data, and the pressure time-history obtained from a bubble collapsing near a rigid wall agrees well with earlier simulations conducted using a different solver.

In this work, we consider aluminum 6061-T6 as the structural material. To properly account for geometric and material nonlinearities, the computational structural model is based on Green-Lagrange strain tensor and the J_2 flow theory with isotropic hardening. The elastic and plastic properties of the aluminum material are set to be the same as in the validation study presented in Farhat *et al.* [11]. To capture the progressive yielding through the wall of the aluminum cylinder, we resolve the wall thickness explicitly in the finite element mesh. We analyze a two-dimensional model that contains one cross section of the cylinder. This geometric simplification is adopted in many studies on cylinder instabilities (e.g., [20, 21, 22, 30]). In this work, it allows us to perform the aforementioned parameter sweep with mesh convergence at reasonable computational cost. The detonation process is not simulated explicitly. Instead, we initiate the simulations with a small bubble that models the state of the explosion bubble at the end of the detonation process. By varying the pressure (and hence, enthalpy) inside this bubble, we model explosions of different magnitudes. For each simulation, we visualize the fluid pressure and velocity fields, the bubble dynamics, and the transient deformation of the structure. Results from different test cases are contrasted to investigate the impact of the explosion magnitude on the dynamics of the structure and the bubble.

The remainder of this paper is organized as follows. Section 4.2 presents the physical models and numerical methods employed in this work, and the setup of our simulations. Section 4.3 presents a mesh convergence analysis that allowed us to determine the mesh resolution for this study. It also shows that upon convergence, the mode of collapse reported in Ikeda [23] is replicated. In Section 4.4, we present five representative test cases with different initial pressures inside the bubble, which led to drastically different structural behaviors ranging from cyclic elastic vibration to an immediate collapse without vibration. In Section 4.5, we categorize the different collapse behaviors observed in the parametric study into three modes, and discuss the cause of each mode as well as the mechanisms underlying the mode transitions. Finally, a few concluding remarks are provided in Section 4.6.

4.2 Physical models and numerical methods

4.2.1 Physical models

Figure 4.1 presents an illustration of the problem investigated in this work. A thin-walled, air-filled circular cylinder is submerged in water. An underwater explosion occurs in the close proximity of the cylinder, and is modeled as a gas bubble with high internal pressure and density. Let Ω_S, Ω_L, Ω_A, and Ω_B denote the subdomains occupied by the aluminum material, the liquid water, the air inside the cylinder, and the gas bubble, respectively. The multiphase fluid flow is dominated by shock waves and high pressure. In comparison, viscous stresses and heat diffusion can be neglected. Therefore, the following Euler equations are solved in Ω_L, Ω_A, and Ω_B.

$$\frac{\partial \boldsymbol{W}(x,t)}{\partial t} + \nabla \cdot \mathcal{F}(\boldsymbol{W}) = \boldsymbol{0}, \quad \forall\ \boldsymbol{x} \in \Omega_L(t)\ \cup\ \Omega_A(t)\ \cup\ \Omega_B(t),\ t > 0, \tag{4.1}$$

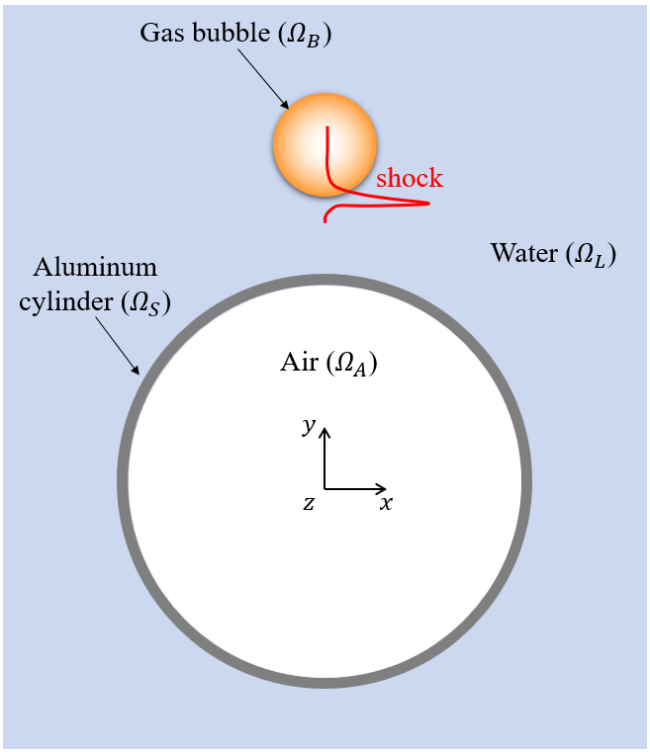

Figure 4.1: A two-dimensional model of an underwater aluminum cylinder subjected to a near-field explosion. (The z axis is aligned with the longitudinal direction of the cylinder.)

with

$$\boldsymbol{W} = \begin{bmatrix} \rho \\ \rho \boldsymbol{V} \\ \rho e_t \end{bmatrix}, \quad \mathcal{F} = \begin{bmatrix} \rho \boldsymbol{V}^T \\ \rho \boldsymbol{V} \otimes \boldsymbol{V} + p\boldsymbol{I} \\ (\rho e_t + p)\boldsymbol{V}^T \end{bmatrix}. \tag{4.2}$$

Here, ρ, e_t, and p denote the mass density, total energy per unit mass, and pressure, respectively. $\boldsymbol{V}$ is the velocity vector. $\boldsymbol{I}$ denotes the the 3×3 identity matrix.

$$e_t = e + \frac{1}{2}|V|^2, \tag{4.3}$$

where e is the internal energy per unit mass.

Equation (4.1) is closed by an equation of state (EOS) for each fluid material. For the gas

inside the bubble and the air inside the cylinder, we apply the perfect gas EOS, i.e.

$$p = (\gamma - 1)\rho e, \tag{4.4}$$

where γ is the heat capacity ratio. For the liquid water, we apply the Tait EOS,

$$p = p_c + \alpha \left(\left(\frac{\rho}{\rho_c} \right)^{\beta} - 1 \right), \tag{4.5}$$

where $\alpha = 3.5291 \times 10^8$ Pa and $\beta = 6.4762$ [46]. (ρ_c, p_c) is a reference state, which is set by $\rho_c = 1.0 \times 10^3$ kg/m^3 and $p_c = 1.0 \times 10^5$ Pa in this work. For each equation of state $p(\rho, e)$, the speed of sound, c, is given by

$$c = \sqrt{\left.\frac{\partial p}{\partial \rho}\right|_e + \frac{p}{\rho^2} \left.\frac{\partial p}{\partial e}\right|_\rho}. \tag{4.6}$$

Within the solid subdomain, Ω_S, the dynamic equilibrium of the cylinder undergoing finite deformation is modeled in the Lagrangian setting [6], i.e.

$$\rho_s \ddot{\boldsymbol{u}}(\boldsymbol{X}, t) - \nabla \cdot \left(J^{-1} \boldsymbol{F} \cdot \boldsymbol{S} \cdot \boldsymbol{F}^T \right) = \boldsymbol{b}, \quad \forall\ \boldsymbol{X} \in \Omega_S(0),\ t > 0. \tag{4.7}$$

Here, ρ_s denotes the solid material's density, $\boldsymbol{u}$ the displacement vector, $\boldsymbol{X}$ the material coordinates, $\boldsymbol{S}$ the second Piola-Kirchhoff stress tensor, $\boldsymbol{F}$ the deformation gradient, and $J = \det \boldsymbol{F}$. $\boldsymbol{b}$ is the body force vector acting on the cylinder, which is assumed to be zero in this study. The dots above $\boldsymbol{u}$ indicate its partial derivative with respect to time.

The cylinder is assumed to be made of aluminum alloy 6061-T6, and can undergo yielding and plastic deformation. Following Farhat *et al.* [11], it is modeled as an elastic-plastic

material, using the J_2 flow theory with isotropic hardening. The yield criterion is defined by

$$\sqrt{2J_2\left(\boldsymbol{s}\right)} = \left(\frac{3}{2}\boldsymbol{s}\cdot\boldsymbol{s}\right)^{1/2} = \sigma_e, \tag{4.8}$$

where $\boldsymbol{s}$ is the deviator of the second Piola-Kirchhoff stress tensor, and σ_e the von Mises effective stress.

The fluid-structure interface is given by

$$\Gamma_{FS} = \partial\Omega_S(t) \ \cap \ \left(\partial\Omega_L(t) \ \cup \ \partial\Omega_A(t) \ \cup \ \partial\Omega_B(t)\right). \tag{4.9}$$

Across the fluid-structure interface, the normal velocity and the surface traction are continuous, i.e.

$$\begin{array}{c}(\boldsymbol{V}-\dot{\boldsymbol{u}})\cdot\boldsymbol{n}=0,\\ -p\boldsymbol{n}=\boldsymbol{\sigma}\cdot\boldsymbol{n},\end{array} \quad \text{on } \Gamma_{FS}, \tag{4.10}$$

where $\boldsymbol{n}$ denotes the unit normal to Γ_{FS}, $\boldsymbol{\sigma}$ the Cauchy stress tensor, which is related to the second Piola-Kirchhoff stress by $\boldsymbol{\sigma} = J^{-1}\boldsymbol{F}\cdot\boldsymbol{S}\cdot\boldsymbol{F}^T$.

The bubble surface (i.e. liquid-gas interface) is given by

$$\Gamma_{FF} = \partial\Omega_L(t) \ \cap \ \partial\Omega_B(t). \tag{4.11}$$

We assume that the two fluid materials across Γ_{FF} are immiscible. In addition, surface tension is negligible compared to the hydrodynamic pressure. Therefore, normal velocity and pressure are assumed to be continuous across Γ_{FF}, i.e.

$$\begin{array}{c}\left(\lim\limits_{\boldsymbol{x}'\to\boldsymbol{x},\ \boldsymbol{x}'\in\Omega_L}\boldsymbol{V}(\boldsymbol{x}') \ - \lim\limits_{\boldsymbol{x}'\to\boldsymbol{x},\ \boldsymbol{x}'\in\Omega_B}\boldsymbol{V}(\boldsymbol{x}')\right)\cdot\boldsymbol{n}=0,\\ \lim\limits_{\boldsymbol{x}'\to\boldsymbol{x},\ \boldsymbol{x}'\in\Omega_L}p(\boldsymbol{x}') \ = \lim\limits_{\boldsymbol{x}'\to\boldsymbol{x},\ \boldsymbol{x}'\in\Omega_B}p(\boldsymbol{x}')\end{array} \quad \forall\boldsymbol{x}\in\Gamma_{FF}. \tag{4.12}$$

To track the evolution of the liquid-gas interface, we solve the level-set equation,

$$\frac{\partial \phi(\boldsymbol{x},t)}{\partial t} + \boldsymbol{V}\cdot\nabla\phi = 0, \quad \forall\, \boldsymbol{x} \in \Omega_L \cup \Omega_A \cup \Omega_B \cup \Omega_S, \tag{4.13}$$

where $\phi(\boldsymbol{x},t)$ denotes the level set function, initialized to be the signed shortest distance from $\boldsymbol{x}$ to the interface. In this way, the large deformation and topological changes (e.g. splitting and merging) of the bubble surface are accommodated without the need of any special treatment.

In summary, Figure 4.2 presents an overview of the model equations solved in this work, as well as their dependencies.

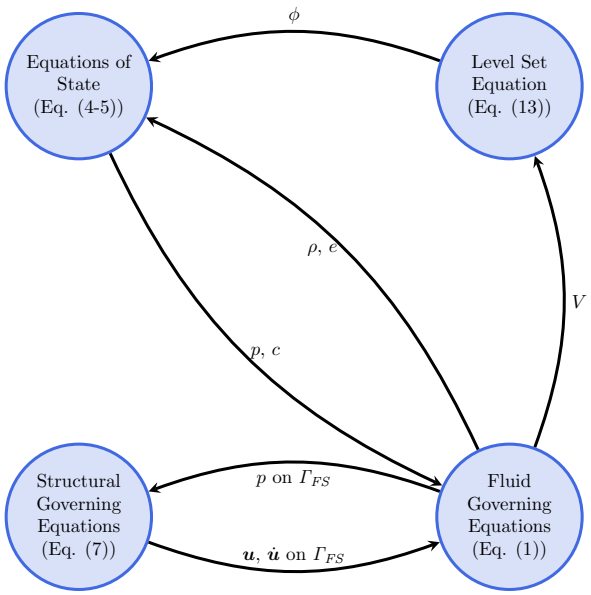

Figure 4.2: Physical models adopted in this work and their dependencies.

4.2.2 Numerical methods

A recently developed multiphase fluid-structure coupled computational framework is applied to solve the aforementioned governing equations [13, 36, 45, 47]. This framework couples a nonlinear finite element solid dynamics solver with a finite volume fluid dynamics solver using a partitioned procedure.

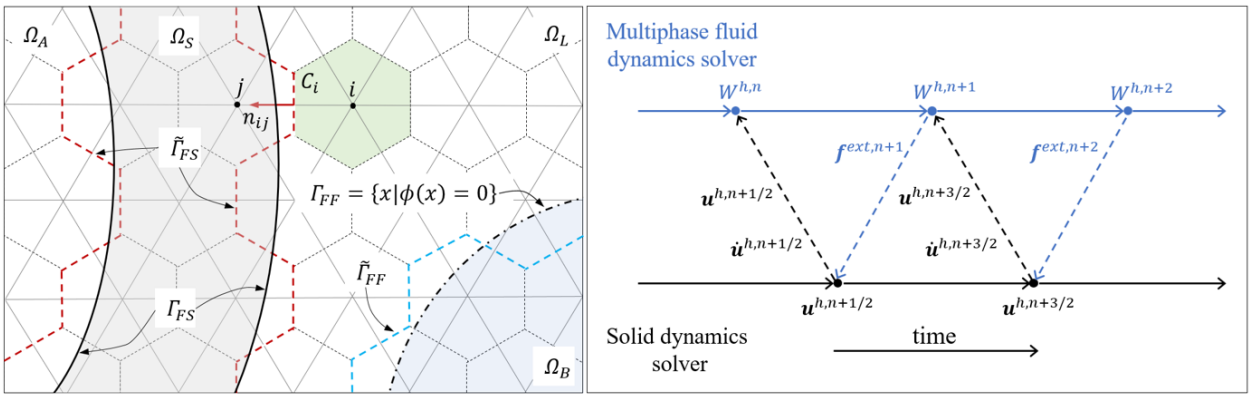

Figure 4.3: Illustration of the discretization methods in space (a) and time (b).

As shown in Figure 4.3(a), an augmented fluid domain $\tilde{\Omega}$ is defined to include the space occupied by the liquid, the gas bubble, the cylinder, and the air inside, i.e.

$$\tilde{\Omega} = \Omega_L \cup \Omega_B \cup \Omega_S \cup \Omega_A. \tag{4.14}$$

In $\tilde{\Omega}$, a node-centered, unstructured, and non-interface-conforming finite volume mesh is used to semi-discretize the fluid governing equations. Around each node (e.g. Node i in Figure 4.3(a)), a control volume C_i is constructed. Integrating Eq. (4.1) within C_i gives the semi-discrete form,

$$\frac{\partial \boldsymbol{W}_i}{\partial t} + \frac{1}{\|C_i\|} \sum_{j \in N(i)} \int_{\partial C_{ij}} \mathcal{F}(\boldsymbol{W}) \cdot \boldsymbol{n_{ij}} dS = 0, \tag{4.15}$$

where $\boldsymbol{W}_i$ denotes the average of $\boldsymbol{W}$ in C_i. $\|C_i\|$ denotes the volume of C_i. $N(i)$ is the

set of neighboring nodes that are connected to node i by an edge. $\partial C_{ij} = \partial C_i \cap \partial C_j$ is the interface between C_i and C_j. $\boldsymbol{n}_{ij}$ is the unit vector normal to ∂C_{ij}. We compute the surface integral over ∂C_{ij} in different ways, depending on the location of nodes i and j — specifically, which fluid or solid subdomain they belong to. The following four scenarios are considered.

(1) Nodes i and j are both located in the same fluid subdomain (Ω_L or Ω_A or Ω_B). In this case, the method of monotonic upwind scheme conservation law (MUSCL) [44] and Roe's flux [39] are used to calculate the flux $\mathcal{F}(\boldsymbol{W})$ across ∂C_{ij}.

(2) Nodes i and j belong to different fluid subdomains. In this scenario, a one-dimensional (1-D) two-fluid Riemann problem is constructed along the edge i-j, that is,

$$\frac{\partial \boldsymbol{w}}{\partial \tau} + \frac{\partial \mathcal{F}(\boldsymbol{w})}{\partial \xi} = 0, \quad \text{with } \boldsymbol{w}(\xi, 0) = \begin{cases} \boldsymbol{w}_i & \text{if } \xi \leq 0, \\ \boldsymbol{w}_j & \text{if } \xi > 0, \end{cases} \tag{4.16}$$

where τ denotes the time coordinate, and ξ the local spatial coordinate aligned with $\boldsymbol{n}_{ij}$ and centered at the midpoint between i and j. The initial states $\boldsymbol{w}_i$ and $\boldsymbol{w}_j$ are projections of $\boldsymbol{W}_i$ and $\boldsymbol{W}_j$ on the ξ axis. This 1-D Riemann problem is solved exactly. Its solution is supplied to Roe's flux function to calculate the flux across ∂C_{ij}, thereby enforcing the interface conditions (Eq. (4.12)) [13].

(3) One of the two nodes belongs to a fluid subdomain, while the other node belongs to the solid subdomain, Ω_S. In this case, a 1-D fluid-structure Riemann problem with a moving wall boundary is constructed. For example, if node i is the one in a fluid subdomain, the Riemann problem is

$$\frac{\partial \boldsymbol{w}}{\partial \tau} + \frac{\partial \mathcal{F}(\boldsymbol{w})}{\partial \xi} = 0, \quad \tau > 0, \ \xi < v_S \tau, \tag{4.17}$$

$$\boldsymbol{w}(\xi, 0) = \boldsymbol{w}_i, \quad \xi < 0, \tag{4.18}$$

$$v(v_S\tau, \tau) = v_S, \quad \tau > 0, \tag{4.19}$$

where ξ is the local spatial coordinate along $\boldsymbol{n}_{ij}$, centered at the midpoint between i and j. The initial state $\boldsymbol{w}_i$ is reconstructed by the fluid state $\boldsymbol{W}_i$. v_S denotes the normal velocity of the structure at its intersection with edge $i-j$, which is computed by the structural dynamics solver. Similar to the previous scenario, the exact solution of this 1-D Riemann problem is supplied to Roe's flux function to calculate the flux across ∂C_{ij} [45, 47].

(4) Both nodes i and j belong to the solid subdomain. In this case, the flux across ∂C_{ij} is set to 0.

The algorithm above is referred to as FIVER, which stands for FInite Volume method with Exact two-material Riemann problems [12, 13, 19, 35, 36, 45, 46, 47]. It has been employed in the past to simulate the collapse of underwater structures due to hydrostatic pressure [11, 34, 50], as well as bubble dynamics in free field and near different material boundaries [5, 48]. FIVER requires tracking the fluid-structure and liquid-gas interfaces in the non-interface-conforming, unstructured mesh $\tilde{\Omega}^h$. A collision-based computational geometry algorithm [45, 46] is applied to track the fluid-solid interface.

The liquid-gas interface is tracked implicitly by solving the level set equation (4.13). In this study, (4.13) is first rearranged to obtain

$$\frac{\partial \phi(\boldsymbol{x}, t)}{\partial t} + \nabla \cdot (\phi \boldsymbol{V}) = \phi \nabla \cdot \boldsymbol{V}. \tag{4.20}$$

Equation (4.20) is solved using a finite volume method on the same fluid mesh. Specifically, the convection term, $\nabla \cdot (\phi \boldsymbol{V})$, is discretized using the same MUSCL scheme, but without a

slope limiter. The term $\phi \nabla \cdot \boldsymbol{V}$ on the right-hand-side is treated as a source term. Additional details can be found in [36].

A Galerkin finite element method is applied to semi-discretize the weak form of Equation (4.7), which yields

$$\boldsymbol{M} \frac{\partial^2 \boldsymbol{u}^h}{\partial t^2} + \boldsymbol{f}^{int} \left(\boldsymbol{u}^h, \frac{\partial \boldsymbol{u}^h}{\partial t} \right) = \boldsymbol{f}^{ext}, \tag{4.21}$$

where $\boldsymbol{M}$ denotes the mass matrix, $\boldsymbol{u}^h$ denotes the discrete displacement vector; $\boldsymbol{f}^{int}$ and $\boldsymbol{f}^{ext}$ denote the discrete internal force and external force vector, respectively.

The staggered fluid-structure time integrator presented in [10] is used in this work to integrate the coupled fluid and structural governing equations. The fluid equations are integrated in time using an explicit fourth-order Runge–Kutta method, while the structural equations are integrated using the second-order central difference scheme. Notably, the fluid and solid time steps are offset by half a step (Figure 4.3(b)). This is a designed feature to achieve second-order accuracy in time while maintaining optimal numerical stability.

4.2.3 Simulation setup

The setup of the numerical simulations is shown in Figure 4.4, including the dimensions of the cylinder and the bubble. A fluid pressure sensor, P1, is placed in the subdomain of liquid water at a location that is close to both the cylinder and the bubble. Also, three displacement and strain sensors are placed on the inner wall of the cylinder. The material and geometric properties of the cylinder are listed in Table 4.1. In particular, the aluminum material properties are set to be the same as in [11]. The properties of the bubble are listed in Table 4.2. Here, the stand-off distance is defined as the shortest distance between the bubble's center and the cylinder's outer surface. The bubble's initial pressure in this study is varied from 1.0 MPa to 100.0 MPa in different test cases. The properties of the ambient

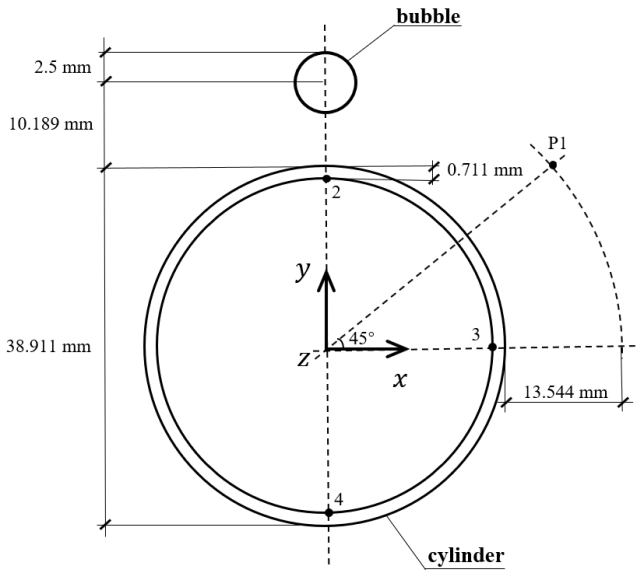

Figure 4.4: Setup of numerical experiment.

water and the air inside the cylinder are listed in Table 4.3.

Table 4.1: Material and geometric properties of the cylinder (Aluminum 6061-T6)

Young's modulus	Poisson's ratio	Density	Yield stress	Tangent modulus	Outer diameter	Thickness
69.6 GPa	0.33	2779 kg/m^3	292 MPa	674 MPa	38.911 mm	0.711 mm

Table 4.2: Bubble properties

Stand-off distance	Initial radius	Initial density	Initial pressure	Heat capacity ratio
10.189 mm	2.5 mm	50.0 kg/m^3	1.0 to 100.0 MPa	1.4

Table 4.3: Properties of the ambient water and the air inside the cylinder

Water pressure	Water density	Air pressure	Air density	Air heat capacity ratio
1.0 MPa	1000.39 kg/m^3	0.1 MPa	1.225 kg/m^3	1.4

4.3 Mesh convergence analysis

A test case with initial pressure, $p_0 = 12.5$ MPa, inside the bubble is selected as an example problem to demonstrate the capability of achieving mesh convergence and to find appropriate mesh resolutions for the parametric study presented in Sections 4.4 and 4.5. Eight (8) pairs of fluid and structural meshes were created for this test case, with resolution varying by a factor of 10. All the fluid meshes are unstructured and nonuniform, mostly refined in a circular region that contains both the structure and the bubble (at its maximum size). Table 4.4 summarizes the important parameters of these meshes. As an example, Figure 4.5 shows the fluid and structural meshes in Pair 8. The fluid domain is a square with a length of $1,200$ mm, which is approximately 30 times the diameter of the structure. Figure 4.5(b) highlights the fact that the fluid mesh does not conform to the boundary of the structure. The embedded boundary method described in Section 4.2.2 is employed to track the structure within this fluid mesh.

All the computations are performed using the Tinkercliffs computer cluster at Virginia Tech. The fluid dynamics solver is parallelized using MPI. As an example, for mesh pair 8, the fluid mesh is divided into $2,047$ subdomains, each one assigned to an AMD EPYC 7702 processor core. The time step size is 3.5×10^{-6} ms. To advance the physical time by 1.0 ms, 28.3 hours of wall-clock time are needed, i.e. 5.8×10^4 core-hours. The total computational cost for the simulation on mesh pair 8 is 2.3×10^5 core-hours.

Figure 4.6 presents four solution snapshots obtained using the finest meshes (i.e. Pair 8). As soon as the simulation begins, the bubble generates a strong outgoing shock wave because of the high internal pressure. The first snapshot ($t = 0.022$ ms) captures the impact of this shock wave on the cylinder as well as the reflection. At the same time, the bubble starts to expand, which can be observed from the fluid velocity field. The second snapshot

Table 4.4: Fluid and structural meshes used in the mesh convergence analysis.

	Structural Mesh	Fluid Mesh	
	Resolution*	Num. of Nodes	Element Size** (mm)
Pair 1	100×1	4.29×10^4	1.2
Pair 2	200×3	1.71×10^5	0.6
Pair 3	260×4	2.99×10^5	0.45
Pair 4	336×4	4.66×10^5	0.36
Pair 5	400×5	6.74×10^5	0.3
Pair 6	600×5	6.74×10^5	0.3
Pair 7	600×5	1.51×10^6	0.2
Pair 8	1000×10	4.19×10^6	0.12

* The first/second number is the number of elements to resolve the circumference/thickness of the cylinder.

** In the most refined region.

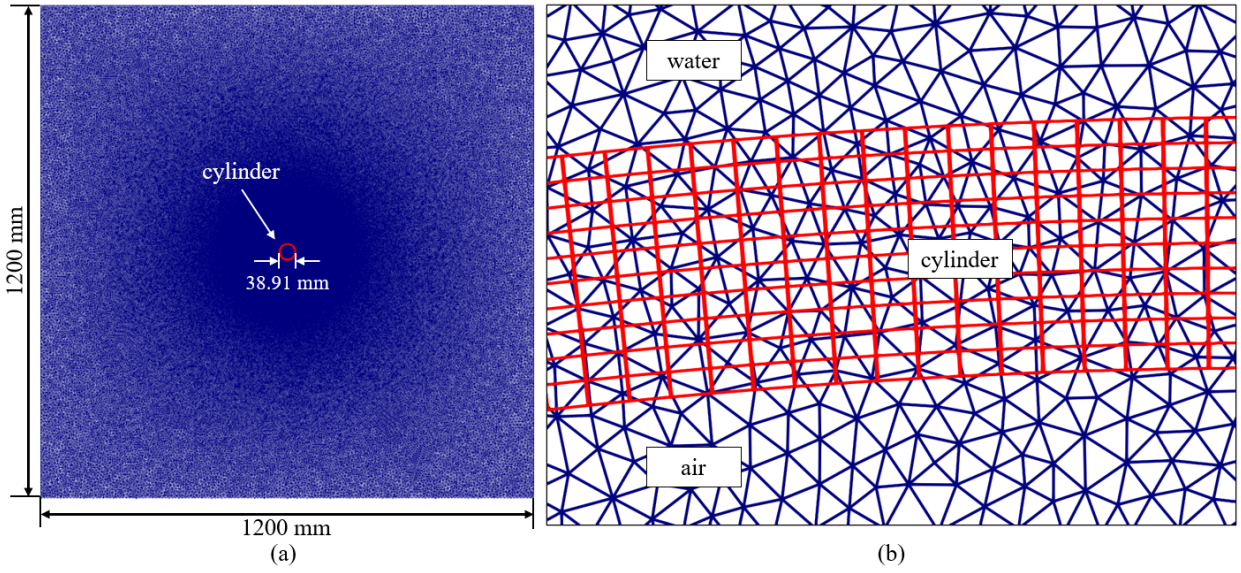

Figure 4.5: Example fluid and structural meshes (Pair 8): the entire computational domain (a) and a zoom-in snapshot around the fluid-structure interface (b).

($t = 0.706$ ms) is taken at a time shortly after the bubble reaches its maximum size. The third snapshot ($t = 3.259$ ms) is taken after the bubble has gone through two cycles of oscil-

lation (i.e. expansion and contraction). A liquid jet, which points away from the structure, penetrates the bubble's top surface. At this time instant, the structure has lost stability and undergone large deformation. Consequently, plastic strain occurs on the structure. It can be observed in the top image of Figure 4.6(c) that plastic deformation is concentrated at the left, right, top, and bottom portions of the cylinder. The last snapshot is taken at $t = 3.864$ ms, shortly after the structure has reached self-contact. The emission of a shock wave at the point of contact can be clearly observed. This type of *implosion* shock waves have been observed and investigated in the past in the context of hydrostatic collapse [11, 16, 38, 40]. Notably, in the final configuration, the two lobes of of the structure extends in the vertical direction, that is, in the propagation direction of the incident shock wave. The same behavior has been observed in a previous laboratory experiment reported in Ikeda [23](Figure 4.7). The cause of this mode of collapse will be discussed in Section 4.4 of this paper.

Figure 4.8 shows the convergence of the numerical results as the mesh gets refined. Two quantities of interest are examined, namely the structural displacement at the sensor location marked in Figure 4.6, and the bubble size. Both of them are measured at $t = 3.259$ ms. As the mesh gets refined, the convergence of these quantities are achieved. From mesh pairs 4 to 8, although the computational cost is increased by 30 times (in terms of core-hours), the result only changes 18.8% in sensor displacement and 12.2% in bubble size. Based on this analysis, mesh pair 6 is selected for the parametric study in the subsequent sections of the paper. The discrepancy between the solution obtained using mesh pair 6 and that using mesh pair 8 is only 0.76% in sensor displacement and 3.71% in bubble size.

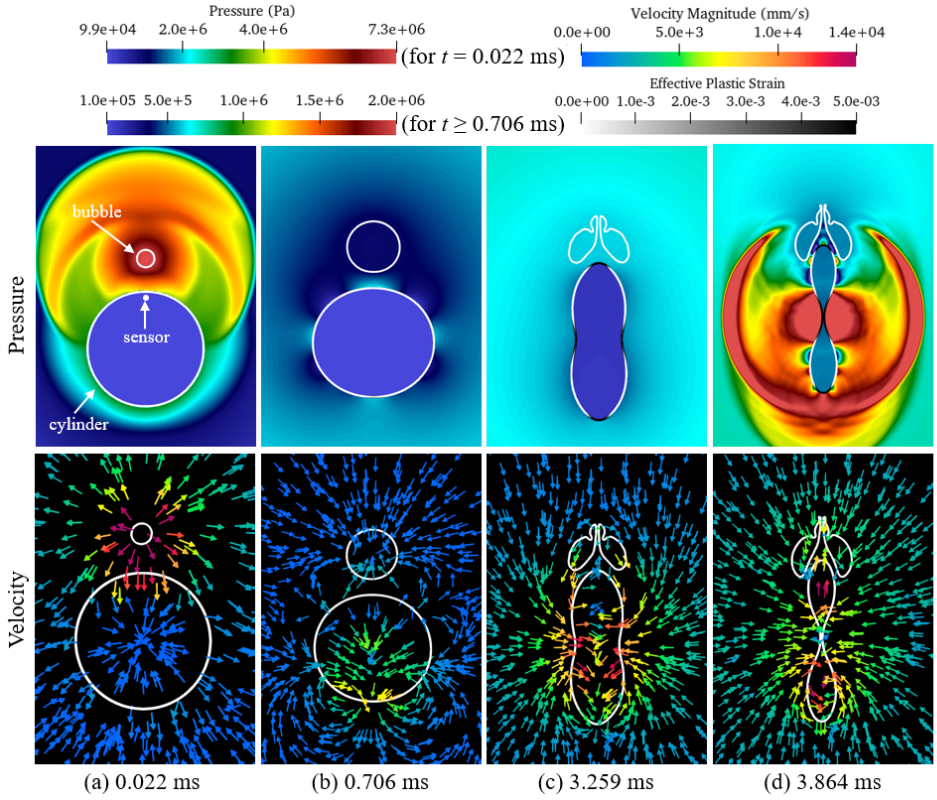

Figure 4.6: Results obtained using mesh pair 8 at four different time instants: The fluid pressure field and the plastic deformation of the structure (top row), and the fluid velocity field (bottom row).

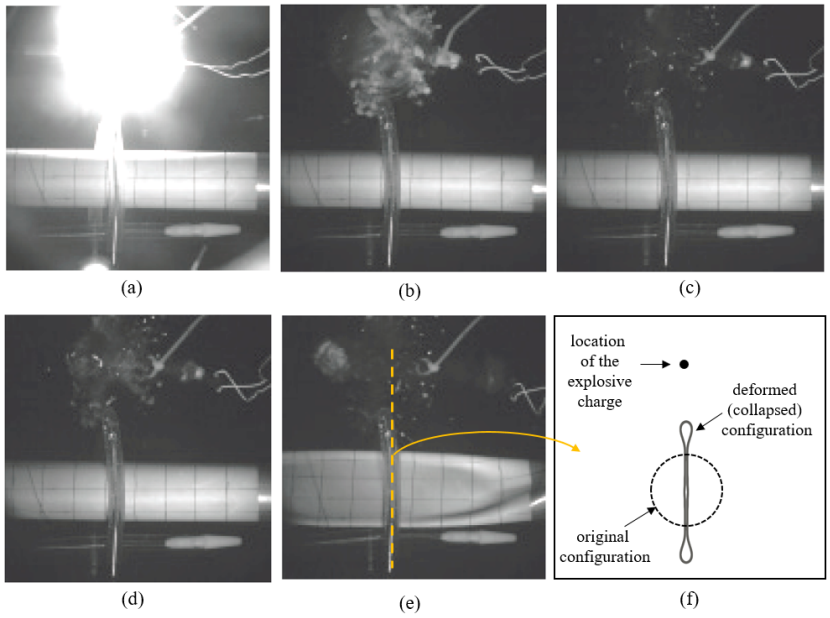

Figure 4.7: Experimental result of the collapse of an aluminum 6061 tube due to a near-field explosion (Ikeda [23], test AE05r01). (a)-(e) A sequence of images from the high-speed movie obtained from this test. (f) Schematic drawing of the collapsed cylinder (a cross-sectional view).

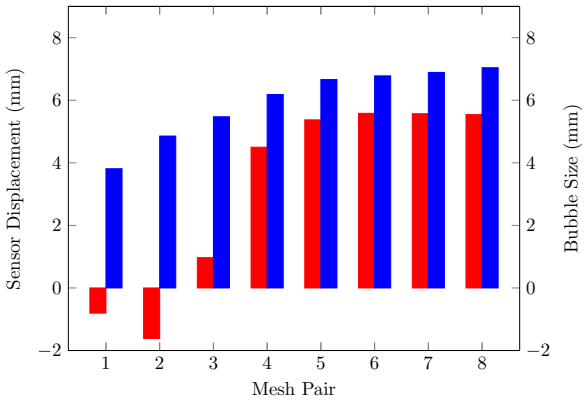

Figure 4.8: Mesh convergence analysis: Vertical displacement at the sensor marked in Figure 4.6 (red) and bubble size (radius equivalent, blue) at 3.259 ms, obtained using different pairs of meshes. (Pair 1: coarsest, Pair 8: finest)

4.4 Bubble-structure interaction and different collapse modes

To elucidate the dynamic bubble-fluid-structure interaction and the impact of this interaction on the structure's collapse, a parametric study was conducted with initial pressure inside the bubble (denoted by p_0) varied from 1 MPa to 100 MPa in different test cases, while all other parameters remained fixed. It was observed that the dynamics of the bubble and the structure do not evolve monotonically with respect to the variation of p_0. In this section, we present five (5) representative cases that exhibit dramatically different modes, whereas the transition among these modes is discussed in Section 4.5.

4.4.1 $p_0 = 8.0$ MPa (enthalpy: 0.5498 J/mm)

In this case, the pressure load created by the bubble is not high enough to make the cylinder collapse. The dynamic process features the cyclic expansion and contraction of the bubble, coupled with the oscillation of the cylinder. Figure 4.9 presents a series of solution snapshots that show the evolution of the bubble, the cylinder, and the fluid pressure and velocity fields. Furthermore, the structural deformation is characterized by the distance between the cylinder's top and bottom points and the distance between its left and right points, as shown in Figure 4.10(a). The time histories of bubble size and fluid pressure at a sensor location (P1 in Figure 4.4) are shown in Figure 4.10(b).

In Figure 4.9, the first snapshot (sub-figure ①) is taken at $t = 0.022$ ms, shortly after the incident shock wave generated by the bubble reaches the surface of the cylinder. The bubble is impacted by the reflection of the incident shock wave against the cylinder, which is the first evidence of a two-way coupling between bubble and structural dynamics. The expanding

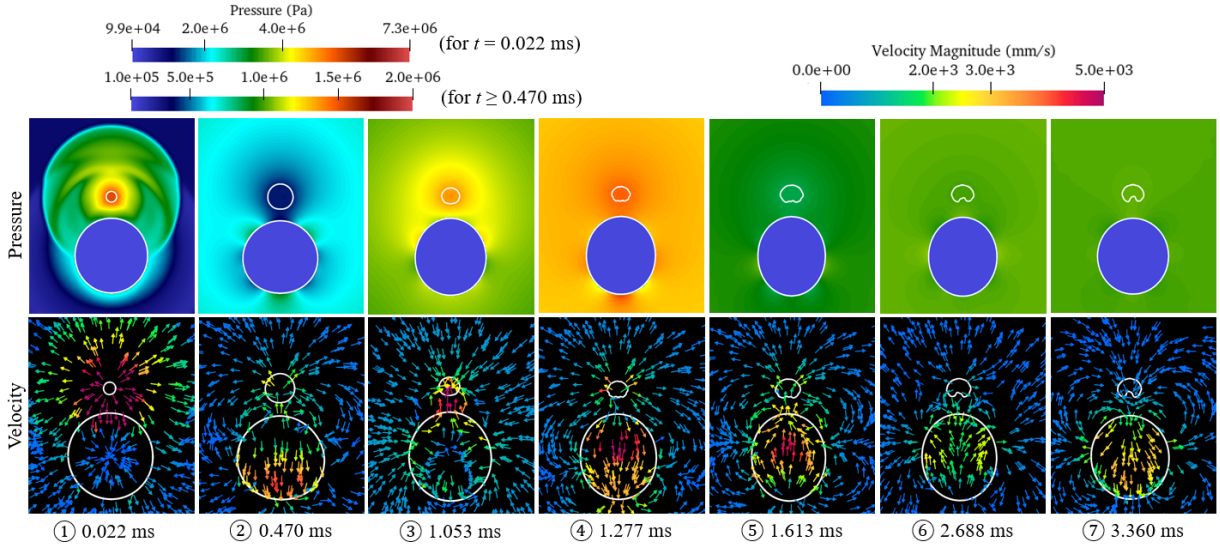

Figure 4.9: Snapshots of the fluid and structural results in the case of $p_0 = 8.0$ MPa.

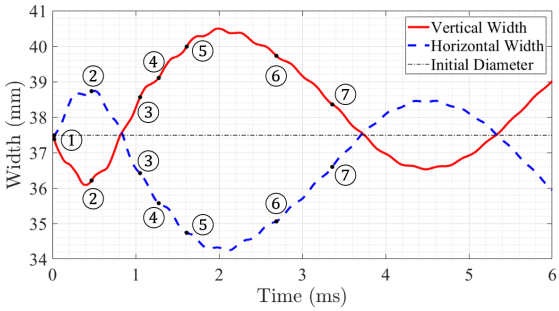

(a)

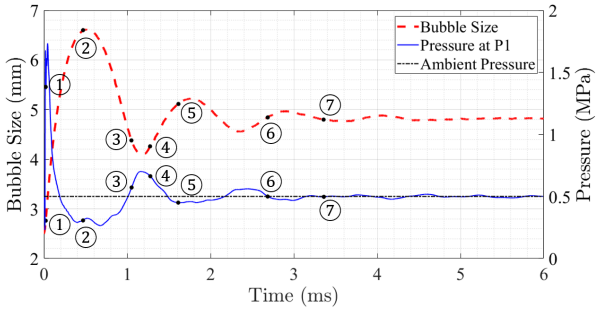

(b)

Figure 4.10: Time history of selected quantities of interest in the case of $p_0 = 8.0$ MPa. (a) The distances between the top and bottom points (i.e. vertical width)and the left and right points (i.e. horizontal width) of the cylinder. (b) The bubble size (radius equivalent) and the fluid pressure at a sensor location. The time instants shown in Figure 4.9 are marked on these curves.

bubble pushes the surrounding water. Therefore, the top portion of the cylinder is impacted by both a pressure load from the incident shock wave and a momentum from the water flow. As a result, the cylinder is compressed vertically. Around $t = 0.470$ ms (Figure 4.9 ②), the bubble is about to reach its maximum size. As the speed of its expansion decreases, the pressure of the surrounding water also decreases. At this time, the cylinder starts to bounce back from the vertical compression, which drives the volume of water above it to move towards the bubble. This again indicates that the bubble dynamics is affected by the transient structural deformation. After $t = 0.528$ ms, the bubble starts to contract. In accordance with the vertical stretch of the cylinder, a high pressure region occurs between the bubble and the structure at around 0.65 ms, which causes an increased vertical pressure gradient that accelerates the upward water flow at the bubble's bottom surface. Although this vertical pressure gradient gradually decreases and reverses direction at around 1 ms, the accelerated contraction of the bubble's bottom surface continues due to the inertia of water. Sub-figure ③ is taken at $t = 1.053$ ms, when the bubble is about to reach its minimum size.From the velocity field, the faster contraction of the bubble's bottom surface can still be observed. Sub-figure ③ also shows that as the bubble's contraction slows down, the local pressure increases. This increase is captured by sensor P1 as a pressure pulse around 1.2 ms (Figure 4.10(b)). At $t = 1.193$ ms, the bubble contracts to its first minimum size and begins to expand again. Sub-figure ④ is taken at $t = 1.277$ ms. From this time onward, the bubble's shape becomes clearly non-spherical. The last three sub-figures are taken during the second and third cycles of bubble oscillation (i.e. expansion and contraction). The pressure variation becomes smaller both in time and in space. A dent gradually develops at the bottom of the bubble, which can be attributed to both the reflection of the incident shock wave against the structural surface and the accelerated upward water flow generated by the high vertical pressure gradient between the bubble and the cylinder.

In this test case, the structural deformation is relatively small. Yielding only occurs on the outer and inner surfaces of the top, bottom, left, and right points of the cylinder, with the maximum value of effective plastic strain less than 2.0×10^{-3}. Figure 4.10(a) shows that although some higher frequency vibration modes are activated by the non-uniform hydrodynamic loads, the structural deformation is dominated by the first asymmetric breathing mode, which features alternative compression and expansion in vertical and horizontal directions [2, 27]. This figure also indicates that both the mean configuration of the cylinder and the configuration with the largest deformation (at around 2.0 ms) have an ellipsoidal shape, with the primary (longer) axis in the vertical direction. In other words, the result indicates a tendency of collapsing into a horizontally compressed configuration.

4.4.2 $p_0 = 12.5$ MPa (enthalpy 0.8590 J/mm)

When the initial pressure inside the bubble is increased to 12.5 MPa, the cylinder collapses in an orientation that features vertical extension and horizontal compression, as indicated by the previous case. This case has been briefly discussed in Section 4.3 to demonstrate mesh convergence. Figure 4.11 shows six (6) solution snapshots, which illustrates the evolution of the bubble, the cylinder, and the fluid pressure and velocity fields. The cylinder's effective plastic strain is also visualized in the upper-row images. Again, the cylinder's horizontal and vertical widths are calculated to characterize its deformation (Figure 4.12(a)). The time histories of bubble size and fluid pressure at a sensor location (P1 in Figure 4.4) are shown in Figure 4.12(b).

In Figure 4.11, the first snapshot is taken at $t = 0.022$ ms, the same time as Figure 4.9①. From the pressure field, it can be observed that the incident shock wave and its reflection both have a higher magnitude compared to the previous case ($p_0 = 8.0$ MPa). Again, the

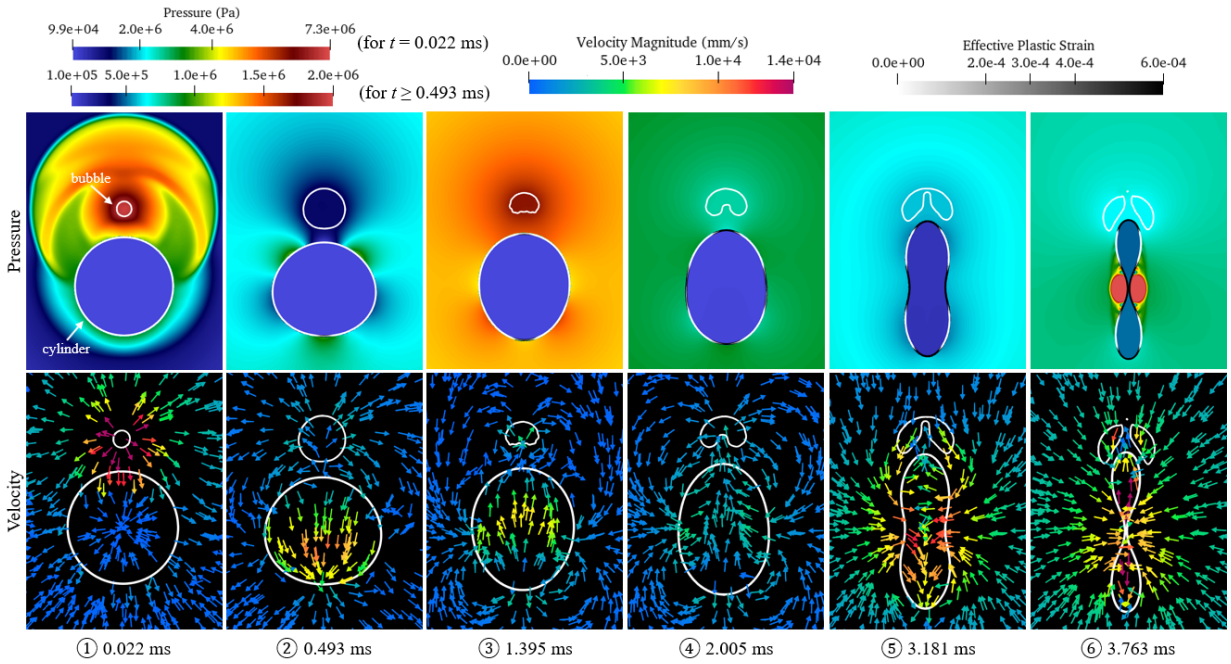

Figure 4.11: Snapshots of the fluid and structural results in the case of $p_0 = 12.5$ MPa.

cylinder is compressed in the vertical direction due to both the shock load and the water flow generated by the expanding bubble. The compression stops at around 0.4 ms, before the bubble reaches its maximum size (Figure 4.12). Sub-figure ② is taken at $t = 0.493$ ms, when the structure is bouncing back in the vertical direction, while the bubble is still expanding. As a result, the downward expansion of the bubble is hindered by the structure. Unlike the previous case, a small amount of plastic deformation (effective plastic strain: 1.34×10^{-3}) has already developed at this time at the bottom of the cylinder.

The bubble reaches its maximum size at $t = 0.569$ ms. Then, it starts to contract. Figure 4.11③ is taken at $t = 1.395$ ms, when the bubble reaches its minimum size. Again, a pressure pulse is generated by the bubble, which elevates the pressure around the cylinder (also see Figure 4.12(b)). At this time, the cylinder is still stretched in the vertical direction and compressed in the horizontal direction (Figure 4.12(a)). The elevated pressure field enhances its horizontal compression. Afterwards, the cylinder continues to deform in the

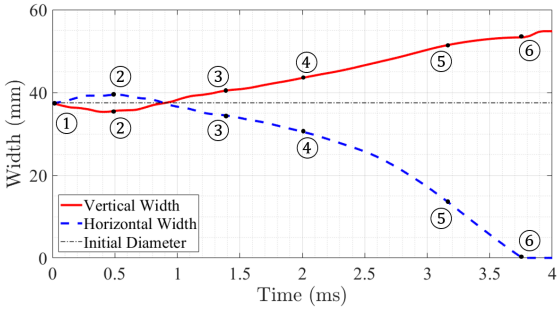

(a)

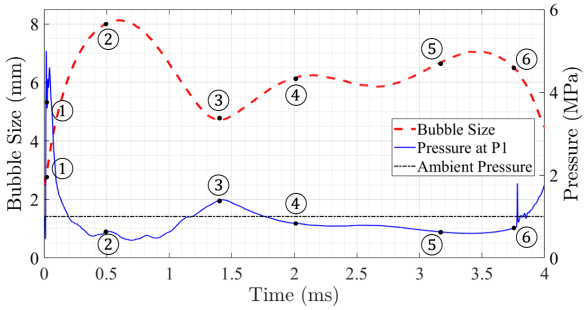

(b)

Figure 4.12: Time history of selected quantities of interest in the case of $p_0 = 12.5$ MPa. (a) The distances between the top and bottom points and the left and right points of the cylinder. (b) The bubble size (radius equivalent) and the fluid pressure at a sensor location. The time instants shown in Figure 4.11 are marked on these curves.

same mode, instead of bouncing back as in the previous case. Sub-figures ③④⑤ illustrate this process. Therefore, the result suggests that the second pressure pulse generated by the contraction of the bubble have a significant impact on the cylinder's mode of collapse.

Besides changing the collapse behavior of the cylinder, the increased initial pressure also influences the bubble dynamics through a complex dynamical interaction between the bubble and the cylinder. Like in the previous case, a dent forms at the bubble's bottom surface. In the present case, this dent gradually evolves into a liquid "jet" during the process of the cylinder's collapse. The jet penetrates the upper surface of the bubble at 3.46 ms (see Figure 4.11, Sub-figures ⑤ and ⑥). In the literature of cavitation, it is well-known that a bubble collapsing near a *rigid* surface often generates a liquid jet towards the surface, which

can be an important mechanism of material damage [4, 5, 32, 42, 48]. It should be noted that the jet observed in the current simulation is in the opposite direction, and its formation is closely related to the deformation of the cylinder. This type of "counter jet" has also been observed previously in experiments that involve underwater explosion near an elastic solid body [31].

Figure 4.12(a) shows that starting at around 1.2 ms, the speed of the cylinder's horizontal compression keeps increasing. The collapse of the cylinder pulls the surrounding water towards it, which can be observed in the fluid velocity field in Figure 4.11, Sub-figures ⑤ and ⑥. At $t = 3.763$ ms, the cylinder reaches self-contact. An implosion shock wave is emitted at the point of contact because the inward motion of the surrounding water is suddenly stopped. This shock wave is also captured at sensor P1 (Figure 4.12(b)).

A comparison between Figures 4.12(b) and 4.10(b) reveals that as p_0 increases, the bubble's period of oscillation also increases. For example, the time when the bubble reaches the second maximum size is approximately 2.15 ms in the current case, compared to 1.76 ms in the previous case. This trend is consistent with simplified bubble dynamics models that assume spherical symmetry (e.g. [3, 8]).

4.4.3 $p_0 = 25.0$ MPa (enthalpy 1.7181 J/mm)

The initial pressure inside the bubble is increased further to 25.0 MPa in this case. Figure 4.13 presents six (6) solution snapshots. Figure 4.14 shows the time histories of the cylinder's deformation, the bubble size, and the fluid pressure at the same sensor location. It is found that the cylinder collapses in an orientation that is perpendicular to the one observed previously in the case of 12.5 MPa.

Due to the higher initial pressure inside the bubble, both the incident and the reflected shock

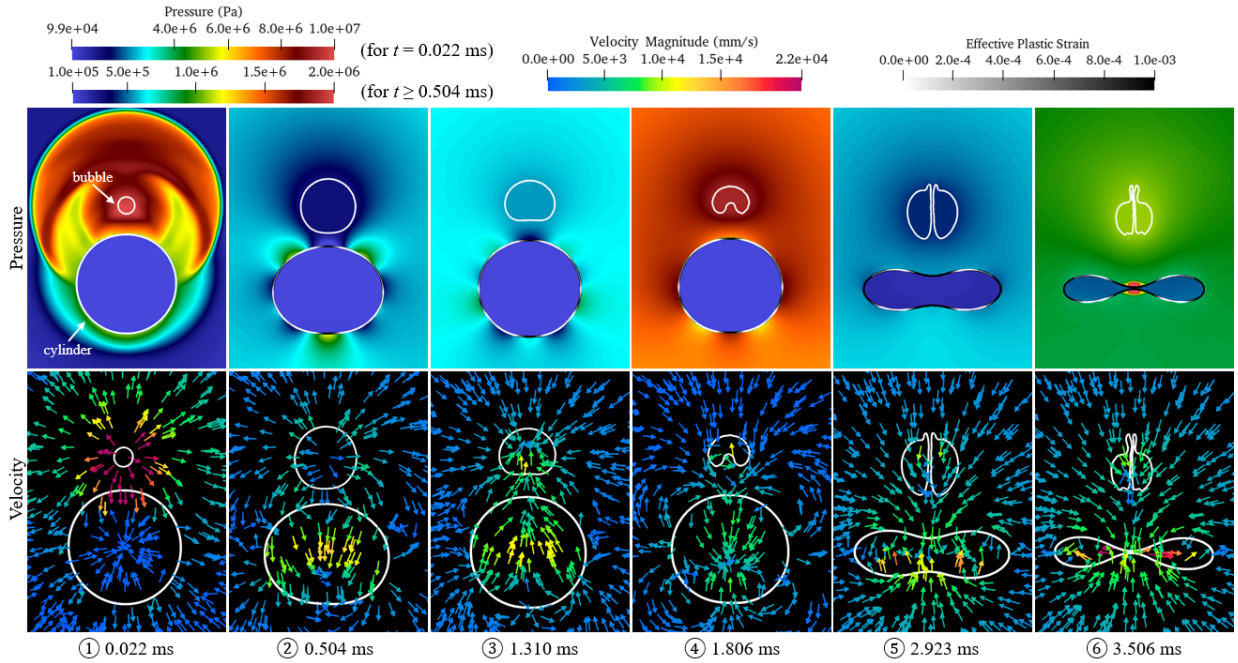

Figure 4.13: Snapshots of the fluid and structural results in the case of $p_0 = 25.0$ MPa.

waves have a higher magnitude (Figure 4.13①). Sub-figure ② is taken at $t = 0.504$ ms, when the bubble is expanding and the cylinder being compressed in the vertical direction. At this time, plastic deformation has already developed at the top, bottom, left, and right points of the cylinder, which can be observed from the visualization of effective plastic strain. The cylinder's vertical compression stops at $t = 0.68$ ms, before the bubble reaches its maximum size. Then, the cylinder starts to bounce back. Unlike all the previous cases, in this case the cylinder cannot recover its original circular configuration, because of the developed plastic deformation. This is evident in Figure 4.14(a), as the two curves never cross after $t = 0$ ms. Figure 4.13③ is taken at $t = 1.310$ ms, when the cylinder is expanding vertically while the bubble is contracting. It can be seen that the bottom of the bubble is flattened by the flow induced by the cylinder's vertical expansion. The vertical expansion and horizontal contraction of the cylinder stop at 1.445 ms. Then, the cylinder starts to deform in the opposite way.

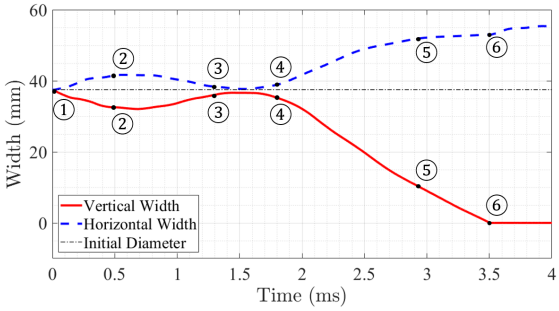

(a)

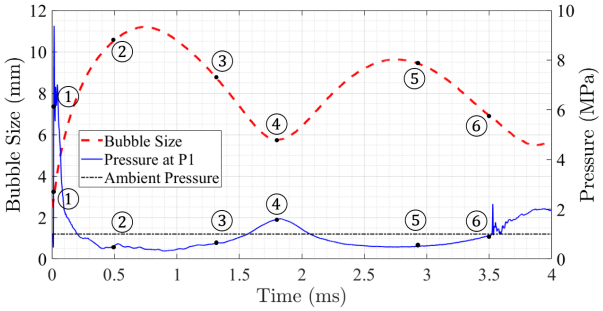

(b)

Figure 4.14: Time history of selected quantities of interest in the case of $p_0 = 25.0$ MPa. (a) The distances between the top and bottom points and the left and right points of the cylinder. (b) The bubble size (radius equivalent) and the fluid pressure at a sensor location. The time instants shown in Figure 4.13 are marked on these curves.

Because of the increased initial pressure (p_0), the bubble's period of oscillation increases. It is at $t = 1.806$ ms that the bubble contracts to its minimum size, compared to $t = 1.395$ ms in the previous case. Sub-figure ④ in Figure 4.13 is taken at this time. Same as the previous cases, the contraction of the bubble generates a pressure pulse that elevates the pressure field around the cylinder. Nonetheless, in this case the delayed pressure pulse meets a cylinder that has a different configuration, that is, vertically compressed and horizontally stretched. As a result, the pressure pulse promotes the vertical compression of the cylinder. After this time, the cylinder loses stability and starts to collapse. Sub-figures ⑤ and ⑥ are taken during this process.

In this case, the bubble also produces a counter jet pointing away from the cylinder. This

liquid jet keeps growing as the cylinder collapses, and it penetrates the upper surface of the bubble at $t = 2.509$ ms. Compared to the previous case, the jet is narrower and longer. When the cylinder is compressed vertically during the bubble's expansion phase after 1.806 ms, the bubble's lower surface expands faster than other regions, which elongates the bubble downwards. Sub-figure ⑥ in Figure 4.13 is taken at the instant that the cylinder reaches self-contact. Again, the emission of an implosion shock wave can be clearly observed from the pressure field. It is notable that the collapsed configuration of the cylinder is symmetric with respect to its horizontal mid-plane (i.e. the middle x-z plane), despite that the external load is highly asymmetric.

In addition, the cylinder collapses into a configuration that features vertical compression and horizontal expansion. Although this is a different mode compared to the previous case of $p_0 = 12.5$ MPa, the result shows that in both cases, the mode of collapse is determined at the time the bubble reaches its minimum size. The difference in collapse mode can be explained by the different configurations of the cylinder at this time. Specifically, in this case, the cylinder is vertically compressed and horizontally stretched, whereas in the case with $p_0 = 12.5$ MPa, it is vertically stretched and horizontally compressed. Furthermore, the result suggests that the difference in the cylinder's configuration at the arrival of the pressure pulse is related to both the increase of the bubble's period of oscillation and the cylinder's plastic deformation.

4.4.4 $p_0 = 50.0$ MPa (enthalpy 3.4361 J/mm)

In this case, the cylinder collapses into another shape that is noticeably different from those observed in the cases of $p_0 = 12.5$ MPa and $p_0 = 25$ MPa. The same set of results are extracted and presented in Figures 4.15 and 4.16.

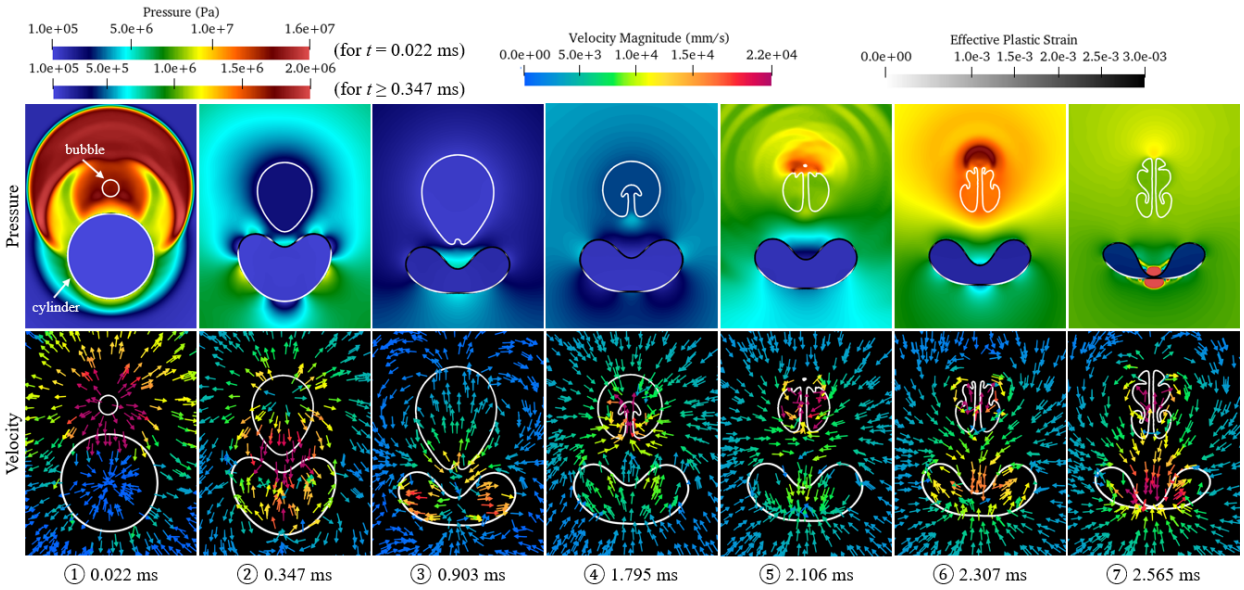

Figure 4.15: Snapshots of the fluid and structural results in the case of $p_0 = 50.0$ MPa.

In Figure 4.15, sub-figure ① is taken at the same time as in the previous cases, which highlights the initial loads from the bubble including a shock wave with pressure of the order of 20 MPa and a water flow with velocity of the order of 4×10^4 mm/s. At $t = 0.347$ ms (Sub-figure ②), the result is already very different from the previous cases. Both the bubble and the cylinder are no longer symmetric with respect to their horizontal mid-planes (i.e. the middle x-z plane). The top region of the cylinder is collapsing, while the bottom region has much smaller, elastic deformation. Despite a higher initial pressure (p_0) compared to the previous case, yielding in the bottom region of the cylinder is delayed. Sub-figure ② also shows that the bubble deforms into an oval shape, as its bottom region is pulled by a downward velocity field that is in accordance with the collapse of the cylinder.

Sub-figure ③ is taken at $t = 0.903$ ms. Around this time, the collapse of the cylinder stops, despite that its vertical width has dropped by over 70% compared to the original configuration (Figure 4.16(a)). Figure 4.16(b) shows that this is the time when the bubble has reached its maximum size and starts to contract. The contraction of the bubble is an

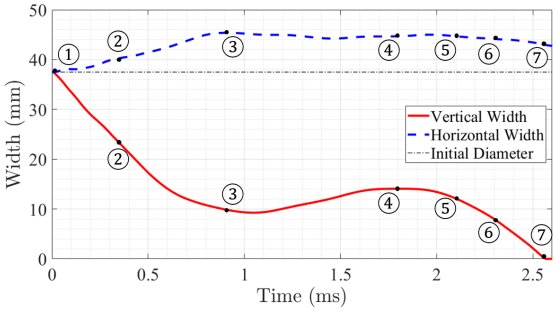

(a)

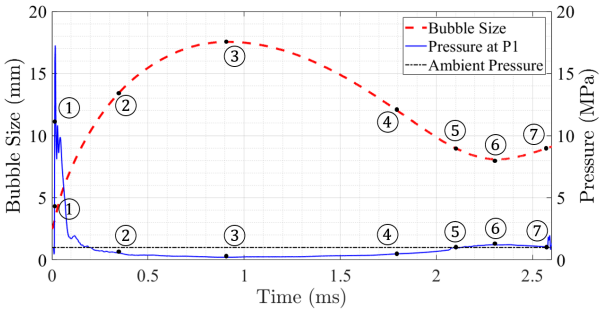

(b)

Figure 4.16: Time history of selected quantities of interest in the case of $p_0 = 50.0$ MPa. (a) The distances between the top and bottom points and the left and right points of the cylinder. (b) The bubble size (radius equivalent) and the fluid pressure at a sensor location. The time instants shown in Figure 4.15 are marked on these curves.

inertial effect, caused by the continuous decrease of the internal pressure during the bubble's expansion. It pulls the surrounding water towards it, thereby facilitating a velocity field that stops the downward collapse of the cylinder. Similar to the previous cases, a dent can be observed at the bottom of the bubble, which gradually evolves into an upward liquid jet. Sub-figure ④ is taken at $t = 1.795$ ms, when the collapse of the cylinder resumes. As the cylinder collapses, the liquid jet continues penetrating the bubble. Sub-figure ⑤ is taken at $t = 2.106$ ms, shortly after the jet penetrates the top surface of the bubble. At $t = 2.307$ ms, the bubble contracts to its minimum size (Sub-figure ⑥). Finally, at $t = 2.565$ ms, the cylinder reaches self-contact (Sub-figure ⑦). Again, an implosion shock wave is generated at the point of contact.

In summary, because of the higher initial pressure (p_0), the collapse of the cylinder starts at an earlier time compared to the previous two cases (12.5 MPa and 25 MPa), and it starts only in the top region, which is close to the bubble. In addition, the collapse of the cylinder does not progress in a monotonic fashion. Instead, it is temporarily pulled back as the bubble contracts, which again indicates a strong coupling between the bubble dynamics and the cylinder's transient deformation. At the end, when the cylinder reaches self-contact, its configuration is clearly different from the shape observed in the case of $p_0 = 25$ MPa in that it is no longer symmetric with respect to the horizontal mid-plane (i.e. the middle x-z plane).

4.4.5 $p_0 = 100.0$ MPa (enthalpy 6.8722 J/mm)

In this case, the cylinder collapses into a configuration similar to the one observed in the previous case. The main difference is that the collapse progresses monotonically, and is not interrupted by the bubble. The results are presented in Figures 4.17 and 4.18.

In Figure 4.17, Sub-figure ① is taken at 0.022 ms, the same time instant as in the previous cases. At this time, yielding has started not only in the top region of the cylinder, but also in its bottom region. The pressure field shows that the incident shock wave (i.e. the region that has red color and a crescent shape) has not reached the bottom of cylinder through water. Therefore, the yielding of the bottom region should be attributed to the convergence of the stress waves propagating downward along the two sides of the cylinder. Sub-figure ② is taken at $t = 0.034$ ms, when the reflected shock wave has just passed the sensor location P1. This reflection is captured by the sensor as the second, smaller pressure spike (Figure 4.18(b)). At this time, plastic deformation has already developed around the entire circumference of the cylinder. Sub-figure ③ is taken at 0.202 ms. At this time, the top region of the cylinder is

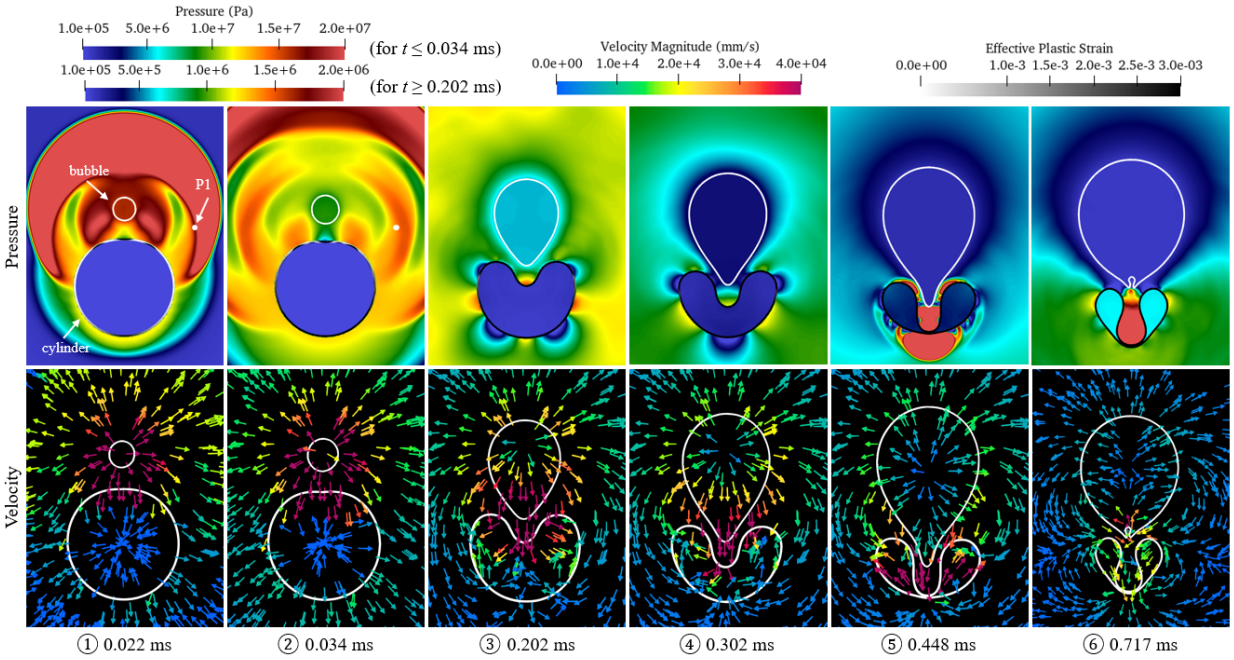

Figure 4.17: Snapshots of the fluid and structural results in the case of $p_0 = 100.0$ MPa. The sensor location P1 is marked in the first two sub-figures.

highly concave. Again, the bottom region of the bubble is pulled by the downward velocity field facilitated by the collapsing cylinder. As a result, it deforms into an oval shape. Sub-figure ④ is taken at 0.302 ms. From Figure 4.18(a) it can be observed that until this time, the horizontal width of the cylinder has largely remained constant. Afterwards, it starts to decrease, as the two lobes of the cylinder fold towards each other. This is different from the last two cases ($p_0 = 25$ MPa and 50 MPa) as in those cases, the horizontal width increases as the cylinder collapses. At $t = 0.448$ ms (sub-figure ⑤), the cylinder reaches self-contact and emits an implosion shock wave. The bubble is still expanding at this time instant. Lastly, Sub-figure ⑥ is taken at $t = 0.717$ ms. Again, a liquid jet forms at the bottom of the bubble, and it will gradually penetrate the bubble.

In this case, the cylinder collapses within 0.5 ms, a time interval that is much shorter than the previous cases. On the other hand, the bubble's period of oscillation is longer because of the higher initial pressure (p_0). As a result of these changes, the bubble keeps expanding during

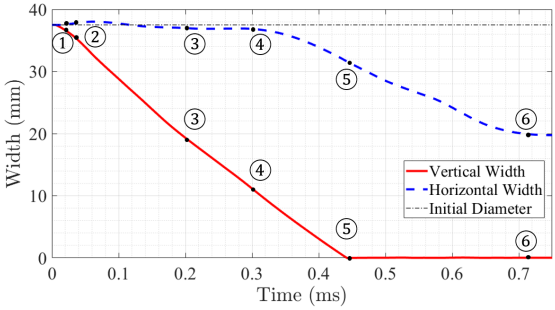

(a)

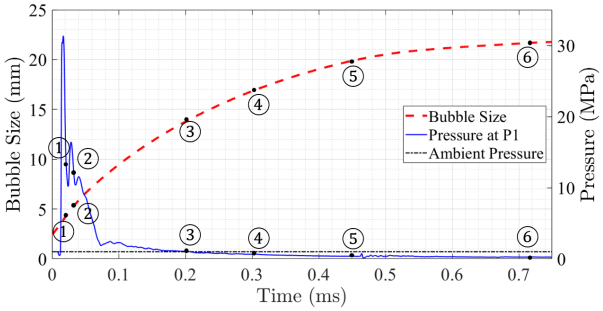

(b)

Figure 4.18: Time history of selected quantities of interest in the case of $p_0 = 100.0$ MPa. (a) The distances between the top and bottom points and the left and right points of the cylinder. (b) The bubble size (radius equivalent) and the fluid pressure at a sensor location. The time instants shown in Figure 4.17 are marked on these curves.

the entire collapsing process of the cylinder (Figure 4.18(b)). Since bubble contraction does not happen during the collapse of the cylinder, the cylinder does not rebound like in the previous case ($p_0 = 50$ MPa).

4.4.6 Summary

We have discussed five (5) representative cases with different initial pressure inside the bubble (p_0). The results show that the collapse behavior of the cylinder can be drastically different as p_0 varies, while all the other parameters remain fixed. Figure 4.19 presents a comparison of all the five cases in terms of structural deformation and bubble dynamics. In this figure,

the time axis is synchronized among all the cases. For each case, the ticks on the time axis mark the start and end times of the bubble's half cycles, i.e. the expansion and contraction phases. One image is presented within each time interval, in which the bubble and the cylinder's configuration at different time instants are superimposed. The time evolution is shown using opacity. Specifically, a darker line corresponds to a result at a later time. The time interval between adjacent time instants is fixed within each image. The dashed curly brackets along the time axis represent the time span of each image.

In the first case ($p_0 = 8.0$ MPa), due to the low pressure inside the bubble, the cylinder vibrates without collapsing. As p_0 increases, in the second case ($p_0 = 12.5$ MPa) the cylinder collapses into a configuration that features horizontal compression and vertical extension. The top of the cylinder, which is closest to the bubble, is found to move towards the bubble. In the third case ($p_0 = 25.0$ MPa), the cylinder collapses into a configuration that features vertical compression and horizontal extension, that is, a configuration perpendicular to that observed in the second case. Notably, in both cases, the collapsed configuration is symmetric with respect to the cylinder's horizontal mid-plane (i.e. the middle x-z plane), despite the fact that the loading is clearly asymmetric. In the fourth case ($p_0 = 50.0$ MPa), the cylinder is still vertically compressed after collapsing but the aforementioned symmetry is lost. The deformation mostly occurs at the top region of the cylinder. Moreover, the cylinder does not collapse monotonically. It is pulled back by the bubble during a short period of time when bubble is contracting. In the last case ($p_0 = 100.0$ MPa), the cylinder collapses monotonically within a very short period of time. It reaches self-contact before the bubble completes the first expansion phase.

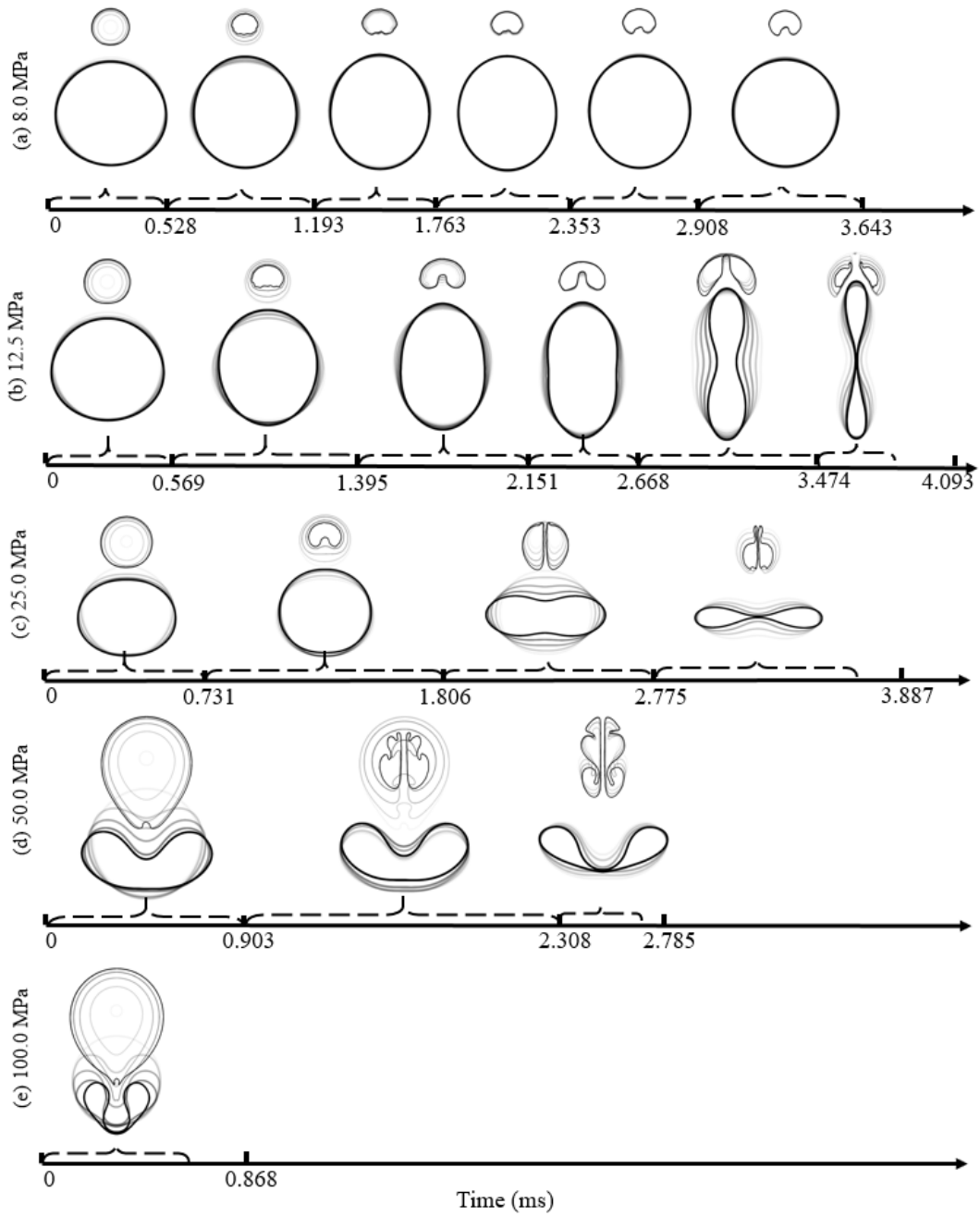

Figure 4.19: Comparison of the evolution of the bubble and the cylinder in the five (5) representative cases. One image is generated for each half cycle (expansion or contraction) of the bubble. Within each image, results at different time instants are superimposed, and the increase of opacity indicates the time evolution.

4.5 Transition of collapse modes

In this section, we discuss the different types of collapse behaviors using a bigger data set that consists of 15 simulations in which p_0 is varied from 1.0 MPa to 100.0 MPa. The transition among different modes of collapse are investigated.

4.5.1 Different collapse behaviors

Figure 4.20 summarizes the different collapse behaviors observed in this parametric study. In the remainder of this paper, the mode of collapse that features symmetric horizontal compression is referred to as Mode 2A. The mode of collapse that features symmetric vertical compression is referred to as Mode 2B. The asymmetric collapse with vertical compression is referred to as Mode 2C. Here, the number 2 refers to the fact that the collapsed configuration contains two lobes. In addition, Figure 4.21 presents the mode of collapse observed in each test case, as well as the time it takes for the cylinder to reach self-contact, denoted by t_{co}.

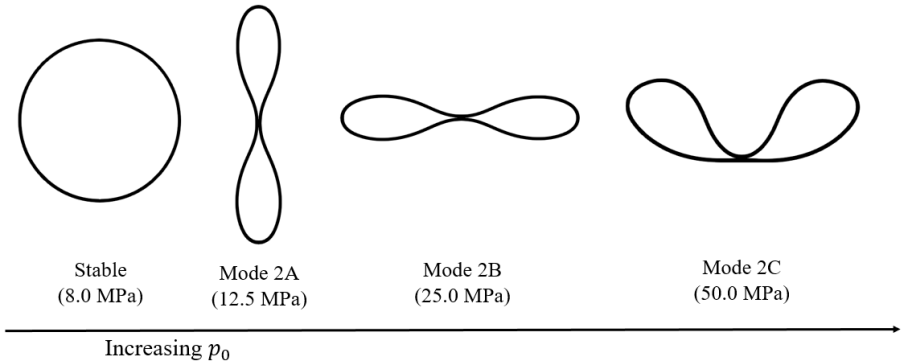

Figure 4.20: The transition of collapse modes as p_0 increases from 1 MPa to 100 MPa.

A few findings from this parametric study are noteworthy.

(1) As pressure p_0 increases, the first collapse mode (Mode 2A) features horizontal compression and vertical extension.

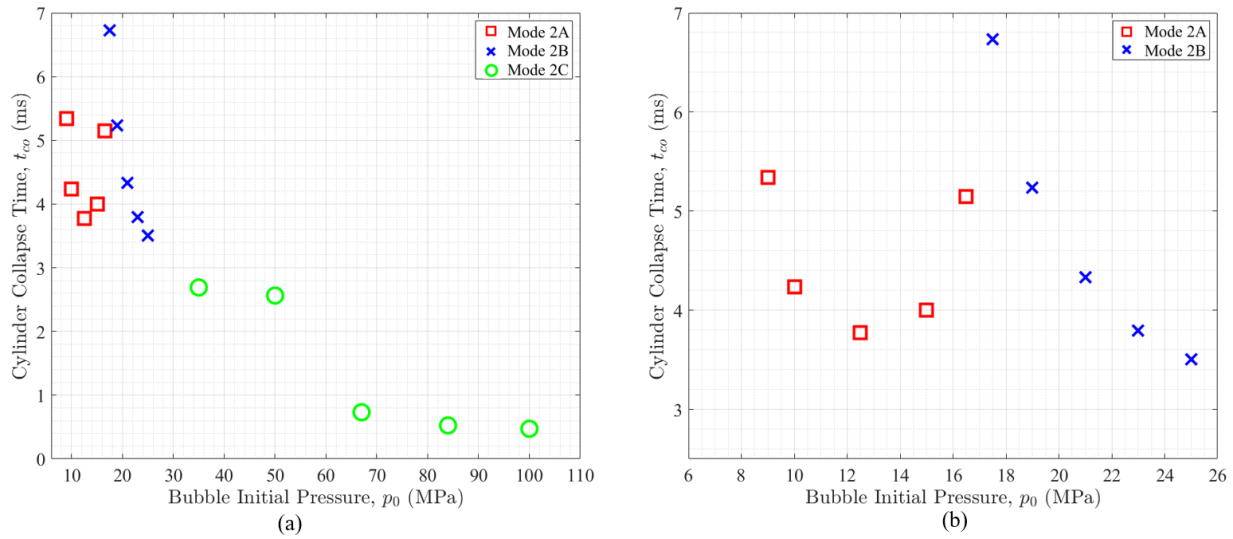

Figure 4.21: The time to collapse (t_{co}) for (a) 8 MPa $<$ p_0 $\leq$ 100.0 MPa and (b) 8 MPa $<$ $p_0 \leq$ 25 MPa.

(2) The time to collapse, t_{co}, is not a monotonically decreasing function of p_0, despite that a larger p_0 generally means a stronger load.

(3) As p_0 increases beyond 16.5 MPa, a change of collapse mode (from Mode 2A to Mode 2B) is observed.

4.5.2 Discussion

To explain the findings mentioned above, it is helpful to examine the time history of plastic strain in the cylinder. Figure 4.22 presents the effective plastic strain measured at the top and bottom points of the cylinder's inside wall. From Figure 4.22(a), it is clear that Mode 2A collapse is not induced directly by the initial loads, i.e. the incident shock wave and the water flow caused by the bubble's initial expansion. For example, in the cases of $p_0 = 12.5$ MPa and 15.0 MPa, the effective plastic strain remains zero (or nearly zero) until 1 ms, when the initial loads have long passed. In both cases, plastic strain starts to develop after 1.5 ms, when the surrounding water pressure is elevated due to the bubble's contraction

(cf. Figures 4.11 and 4.12). Therefore, the first collapse mode is induced mainly by the first contraction phase of the bubble and the resulting pressure pulse. Around this time, the cylinder happens to be in a configuration of vertical extension and horizontal compression, which determines the shape of Mode 2A collapse.

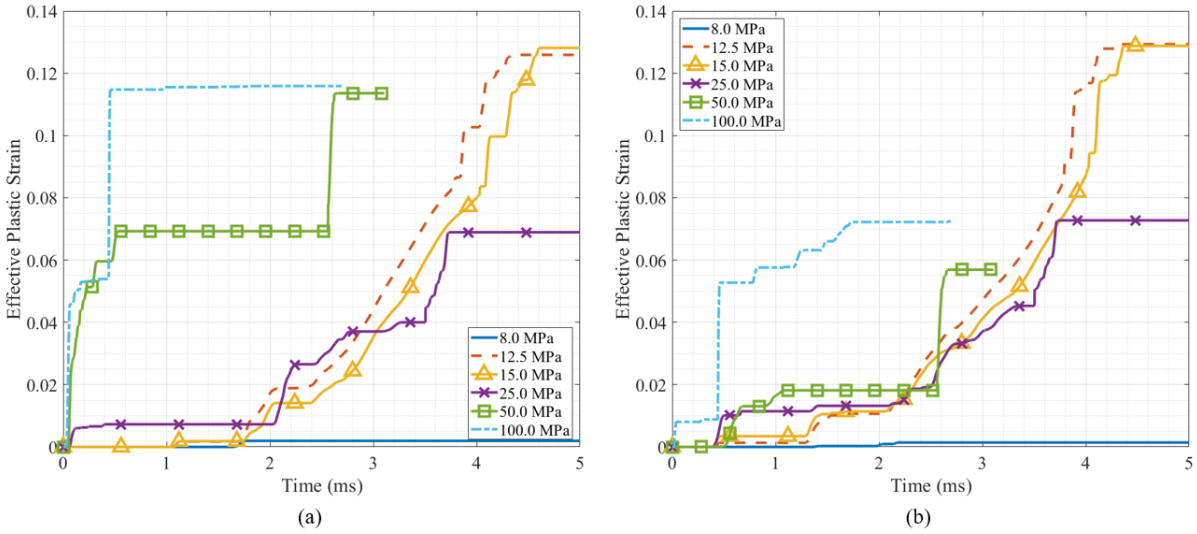

Figure 4.22: Effective plastic strain at the (a) top point and (b) bottom point of the cylinder's inside wall.

Figure 4.21(b) shows that for the cases that result in Mode 2A collapse, the time to collapse (t_{co}) does not decrease monotonically as p_0 increases. Specifically, when p_0 is increased from 12.5 MPa to 15.0 MPa, the cylinder collapses slower. This phenomenon is related to the plastic deformation caused by the initial loads. Figure 4.22(b) shows that, in the cases of $p_0 = 12.5$ MPa and $p_0 = 15.0$ MPa, there is a small amount of plastic deformation at the bottom of the cylinder around 0.5 ms. Around this time, the cylinder's vertical width reaches a minimum value. In other words, the cylinder has just completed the first half-cycle of vibration, which results directly from the initial loads (cf. Figure 4.12(a)). Figure 4.23 provides a cross comparison of the plastic deformation induced by the initial loads among all the test cases. It is clear that as p_0 increases, the effective plastic strain also increases. As discussed in Section 4.4.3, such plastic deformation tends to hinder Mode 2A collapse.

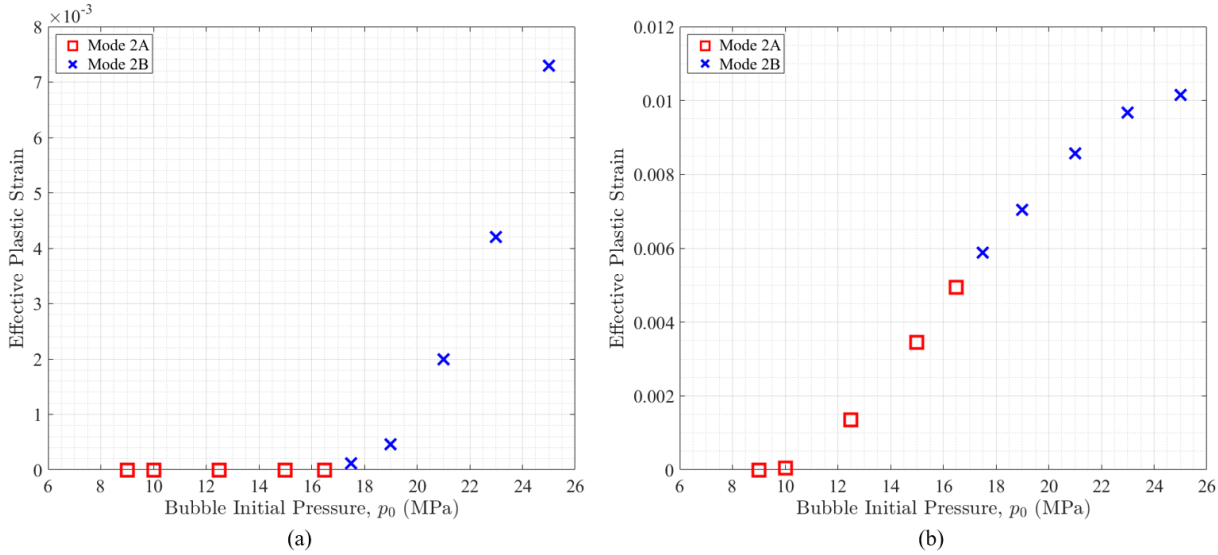

Figure 4.23: Effective plastic strain at the cylinder inside wall's (a) top and (b) bottom points when the cylinder's vertical width reaches minimum for the first time (i.e. when the cylinder completes the first half-cycle of vibration).

Therefore, the result shows that the increased plastic deformation due to stronger initial loads is a factor that increases the cylinder's time to collapse (t_{co}) in Mode 2A.

The increase of plastic deformation caused by the initial loads also leads to the fact that when the cylinder completes its first cycle of vibration, it can no longer recover the initial configuration. Instead, it is vertically compressed and horizontally stretched. Figure 4.24 shows that as p_0 further increases beyond 12.5 MPa, the vertical width of the cylinder decreases monotonically. As described in Section 4.4, when the cylinder completes its first cycle of vibration, it is subjected to a pressure pulse that results from the contraction of the bubble. This pressure pulse drives the cylinder to collapse in the vertical direction. In summary, the results suggest that Mode 2B collapse is triggered by the initial loads and facilitated by the bubble's dynamics, particularly its first contraction phase that generates the second pressure pulse.

In addition of the findings listed in Section 4.5.1, in Figure 4.21, it can be seen that when

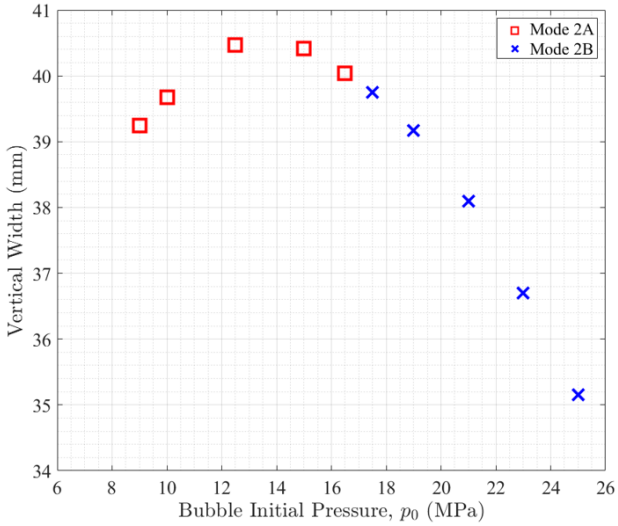

Figure 4.24: Vertical width of the cylinder when the bubble contracts to its minimum size.

the cylinder collapses in Mode 2C, there is a sudden decrease of t_{co} between $p_0 = 50.0$ MPa and 67.0 MPa. This behavior is related to the time sequence of cylinder collapse and bubble contraction, as discussed in Section 4.4.4 and Section 4.4.5.

4.6 Conclusion

The collapse of an underwater aluminum cylinder due to a near-field explosion is investigated in this work using fluid-structure coupled simulations. Previous studies suggest that the dynamics of the explosion bubble may have a substantial effect in this type of events. Nonetheless, knowledge about this effect is very limited. Therefore, a specific objective of this study is to capture and explain the two-way interaction between the explosion bubble and the structure, using a two-dimensional model problem.

The computational model employed in this study combines a multiphase compressible fluid dynamics solver with a nonlinear structural dynamics solver. It has been verified and validated for several problems that are closely related to the current work, including the collapse

of aluminum cylinders due to hydrostatic pressure, and the pulsation of bubbles in free field and near solid materials. In this work, we start with a mesh convergence analysis in which the fluid and structural meshes are progressively refined until convergence is achieved. Afterwards, a parametric study is conducted, in which the initial pressure inside the explosion bubble (p_0) is varied by two orders of magnitude. The interaction of the bubble, the surrounding liquid water, and the aluminum cylinder is investigated by inspecting the fluid pressure and velocity fields, the bubble dynamics, and the transient structural deformation and stresses.

It is found that as p_0 varies, the final configuration of the cylinder can be substantially different. Results from five representative cases (p_0 = 8 MPa, 12.5 MPa, 25 MPa, 50 MPa, 100 MPa) are discussed in detail. In these cases, the structural dynamics varies from a cyclic elastic vibration without collapse (p_0 = 8 MPa) to an immediate collapse without vibration (p_0 = 100 MPa). Three different types of collapse behaviors are observed, which are categorized as Mode 2A, Mode 2B, and Mode 2C (Figure 4.20). As p_0 increases, the mode of collapse changes from 2A to 2B, and then from 2B to 2C. The mode transitions are discussed using additional test cases in the parametric study.

The mechanisms of the three collapse modes are summarized below. Mode 2A is caused by a coincidence between the bubble's first contraction phase and the cylinder's horizontal compression. As the bubble contracts, it emits a pressure pulse that elevates the pressure around the entire cylinder. When this bubble pulse arrives at the horizontally compressed cylinder, it facilitates its compression, leading to an horizontal collapse that has been observed earlier in a laboratory experiment [23]. Mode 2B is related to the plastic deformation induced by the initial loads, i.e., the initial shock wave and the water flow caused by the bubble's initial expansion. This plastic deformation suppresses the vertical extension and horizontal compression of the cylinder. As a result, when the aforementioned bubble pulse

arrives at the cylinder, the cylinder is compressed in vertical direction. The bubble pulse facilitates this compression, leading to collapse mode 2B. For Mode 2C collapse, the result suggests that the cylinder's collapse is directly induced by the incident shock wave from the explosion. Clearly, the dynamics of the explosion bubble has a significant effect in collapse Modes 2A and 2B. In both cases, the plastic deformation remains relatively small long after the initial loads have passed. The collapse of the cylinder starts only after the bubble contracts to its first minimum size and emits a pressure pulse.

The time that the cylinder takes to completely collapse does not decrease monotonically as p_0 increases (cf. Figure 4.21). When the cylinder collapses in Mode 2A, increasing p_0 may cause the cylinder to take more time to reach self-contact. This phenomenon is caused by the increased amount of plastic deformation induced by the initial loads from the explosion.

The simulation result also reveals that the dynamics of an explosion bubble near a vibrating or collapsing cylinder is significantly different from the dynamics of bubbles in free field or near a rigid wall. In other words, the transient structural deformation has a clear effect on the bubble dynamics. In particular, in the cases with $p_0 \geq 8$ MPa, a counter-jet that points away from the structural surface is observed. It forms as a result of a complex interaction between the bubble and the vibrating and collapsing cylinder. This type of counter-jets has been observed previously in bubbles expanding near an elastic solid body. Compared to the liquid jets produced by bubbles collapsing near a rigid wall, this counter-jet is in the opposite direction.

Declaration of competing interest

The authors have no relevant financial or non-financial competing interests.

Acknowledgement

W.M., X.Z., and K.W. gratefully acknowledge the support of the Office of Naval Research (ONR) under Awards N00014-19-1-2102, and the support of the National Science Foundation (NSF) under Awards CBET-1751487. C.G. gratefully acknowledges ONR N00014-10-C-0108 and Prof. James H. Duncan from the University of Maryland.

Bibliography

[1] J R Blake and D C Gibson. Cavitation bubbles near boundaries. *Annual Review of Fluid Mechanics*, 19(1):99–123, 1987.

[2] R. Blevins. *Formulas for natural frequency and mode shape*. Van Nostrand Reinhold Company, 1979.

[3] Christopher Earls Brennen. *Cavitation and bubble dynamics*. Cambridge University Press, 2013.

[4] Emil-Alexandru Brujan, Tatsuya Noda, Atsushi Ishigami, Toshiyuki Ogasawara, and Hiroyuki Takahira. Dynamics of laser-induced cavitation bubbles near two perpendicular rigid walls. *Journal of Fluid Mechanics*, 841:28–49, 2018.

[5] S. Cao, G. Wang, O. Coutier-Delgosha, and K. Wang. Shock-induced bubble collapse near solid materials: effect of acoustic impedance. *Journal of Fluid Mechanics*, 907: A17, 2021.

[6] Shunxiang Cao, Alex Main, and Kevin G. Wang. Robin-neumann transmission conditions for fluid-structure coupling: Embedded boundary implementation and parameter

analysis. *International Journal for Numerical Methods in Engineering*, 115(5):578–603, 2018.

[7] Shunxiang Cao, Ying Zhang, Defei Liao, Pei Zhong, and Kevin G Wang. Shock-induced damage and dynamic fracture in cylindrical bodies submerged in liquid. *International journal of solids and structures*, 169:55–71, 2019.

[8] RH Cole. *Underwater explosions*. Princeton University Press, 1948.

[9] James H. Duncan and S. Zhang. On the interaction of a collapsing cavity and a compliant wall. *Journal of Fluid Mechanics*, 226:401–423, 1991.

[10] C. Farhat, A. Rallu, K. Wang, and T. Belytschko. Robust and provably second-order explicit–explicit and implicit–explicit staggered time-integrators for highly non-linear compressible fluid–structure interaction problems. *International Journal for Numerical Methods in Engineering*, 84(1):73–107, 2010.

[11] C. Farhat, K.G. Wang, A. Main, S. Kyriakides, L.-H. Lee, K. Ravi-Chandar, and T. Belytschko. Dynamic implosion of underwater cylindrical shells: experiments and computations. *International Journal of Solids and Structures*, 50(19):2943–2961, 2013. ISSN 0020-7683.

[12] Charbel Farhat, Arthur Rallu, and Sriram Shankaran. A higher-order generalized ghost fluid method for the poor for the three-dimensional two-phase flow computation of underwater implosions. *Journal of Computational Physics*, 227(16):7674–7700, 2008. ISSN 0021-9991.

[13] Charbel Farhat, Jean-Frédéric Gerbeau, and Arthur Rallu. Fiver: A finite volume method based on exact two-phase riemann problems and sparse grids for multi-material

flows with large density jumps. *Journal of Computational Physics*, 231(19):6360–6379, 2012. ISSN 0021-9991.

[14] DC Gibson. Cavitation adjacent to plane boundaries. In *Proceedings of 3rd Australasian Conference on Hydraulics and Fluid Mechanics*, pages 210–214, Sydney, Australia, 1968.

[15] DC Gisbon and JR Blake. Growth and collapse of cavitation bubbles near flexible boundaries. In *Proceedings of 7th Australasian Conference on Hydraulics and Fluid Mechanics*, pages 283–286, Brisbane, Australia, 1980.

[16] Sachin Gupta, James M. LeBlanc, and Arun Shukla. Mechanics of the implosion of cylindrical shells in a confining tube. *International Journal of Solids and Structures*, 51 (23):3996–4014, 2014. ISSN 0020-7683.

[17] Sachin Gupta, Helio Matos, James M LeBlanc, and Arun Shukla. Shock initiated instabilities in underwater cylindrical structures. *Journal of the Mechanics and Physics of Solids*, 95:188–212, 2016.

[18] Emily L Guzas, Sachin Gupta, Joseph M Ambrico, James M LeBlanc, and Arun Shukla. Computational modeling of dynamically initiated instabilities and implosion of underwater cylindrical structures in a confined environment. *Journal of Applied Mechanics*, 86(2), 2019.

[19] Daniel Z. Huang, Dante De Santis, and Charbel Farhat. A family of position- and orientation-independent embedded boundary methods for viscous flow and fluid–structure interaction problems. *Journal of Computational Physics*, 365:74–104, 2018. ISSN 0021-9991.

[20] S. Iakovlev. Interaction between a submerged evacuated cylindrical shell and a shock

wave—part i: Diffraction–radiation analysis. *Journal of Fluids and Structures*, 24(7): 1077–1097, 2008. ISSN 0889-9746.

[21] S. Iakovlev. Interaction between a submerged evacuated cylindrical shell and a shock wave—part ii: Numerical aspects of the solution. *Journal of Fluids and Structures*, 24 (7):1098–1119, 2008. ISSN 0889-9746.

[22] S. Iakovlev. Interaction between an external shock wave and a cylindrical shell filled with and submerged into different fluids. *Journal of Sound and Vibration*, 322(1):401–437, 2009. ISSN 0022-460X.

[23] C. Ikeda. *Fluid-structure interactions: implosions of shell structures and wave impact on a flat plate*. PhD thesis, University of Maryland, College Park, 2012.

[24] CM Ikeda, J Wilkerling, and JH Duncan. The implosion of cylindrical shell structures in a high-pressure water environment. *Proceedings of the Royal Society A: Mathematical, Physical and Engineering Sciences*, 469(2160):20130443, 2013.

[25] Carlos Javier, Michael Galuska, Michael Papa, James LeBlanc, Helio Matos, and Arun Shukla. Underwater explosive bubble interaction with an adjacent submerged structure. *Journal of Fluids and Structures*, 100:103189, 2021.

[26] Shyamal Kishore, P Naik Parrikar, Nicholas DeNardo, and Arun Shukla. Underwater dynamic collapse of sandwich composite structures. *Experimental Mechanics*, 59(5): 583–598, 2019.

[27] Y.W. Kwon and P.K. Fox. Underwater shock response of a cylinder subjected to a side-on explosion. *Computers & Structures*, 48(4):637–646, 1993. ISSN 0045-7949.

[28] Stelios Kyriakides and Edmundo Corona. *Mechanics of offshore pipelines: volume 1 buckling and collapse*, volume 1. Elsevier, 2007.

[29] James LeBlanc, Christopher Shillings, Erin Gauch, Frank Livolsi, and Arun Shukla. Near field underwater explosion response of polyurea coated composite plates. *Experimental Mechanics*, 56(4):569–581, 2016.

[30] C. Leblond and J.-F. Sigrist. A versatile approach to the study of the transient response of a submerged thin shell. *Journal of Sound and Vibration*, 329(1):56–71, 2010. ISSN 0022-460X.

[31] Shuai Li, A-Man Zhang, and Rui Han. Letter: Counter-jet formation of an expanding bubble near a curved elastic boundary. *Physics of Fluids*, 30(12):121703, 2018.

[32] L. T. Liu, X. L. Yao, A. M. Zhang, and Y. Y. Chen. Numerical analysis of the jet stage of bubble near a solid wall using a front tracking method. *Physics of Fluids*, 29(1): 012105, 2017.

[33] Zhanke Liu and Yin L Young. Transient response of submerged plates subject to underwater shock loading: an analytical perspective. *Journal of applied mechanics*, 75(4), 2008.

[34] Wentao Ma, Xuning Zhao, and Kevin Wang. A fluid-structure coupled computational model for the certification of shock-resistant elastomer coatings. In *Proceedings of 39th International Conference on Offshore Mechanics and Arctic Engineering*, volume 2A: Structures, Safety, and Reliability. ASME, 08 2020. V02AT02A024.

[35] Alex Main and Charbel Farhat. A second-order time-accurate implicit finite volume method with exact two-phase riemann problems for compressible multi-phase fluid and fluid–structure problems. *Journal of Computational Physics*, 258:613–633, 2014. ISSN 0021-9991.

[36] Alex Main, Xianyi Zeng, Philip Avery, and Charbel Farhat. An enhanced FIVER

method for multi-material flow problems with second-order convergence rate. *Journal of Computational Physics*, 329:141–172, January 2017.

[37] Ajai Kurian Mathew. Modeling underwater explosion (undex) shock effects for vulnerability assessment in early stage ship design. Master's thesis, Virginia Tech, 2018.

[38] Teguh Muttaqie, Sang Hyun Park, Jung Min Sohn, Sang-Rai Cho, In Sik Nho, Soonhung Han, Phill-Seung Lee, and Yoon Sik Cho. Experimental investigations on the implosion characteristics of thin cylindrical aluminium-alloy tubes. *International Journal of Solids and Structures*, 200-201:64–82, 2020. ISSN 0020-7683.

[39] P.L Roe. Approximate riemann solvers, parameter vectors, and difference schemes. *Journal of Computational Physics*, 43(2):357–372, 1981. ISSN 0021-9991.

[40] Christopher J. Salazar and Arun Shukla. Hydrostatic implosion of composite cylinders in an open-ended confining structure. *Composites Part B: Engineering*, 192:107993, 2020. ISSN 1359-8368.

[41] Michael M Swisdak Jr. Explosion effects and properties. part ii. explosion effects in water. Technical report, Naval Surface Weapons Center White Oak Lab, Silver Spring, MD, 1978.

[42] C. K. Turangan, G. J. Ball, A. R. Jamaluddin, and T. G. Leighton. Numerical studies of cavitation erosion on an elastic-plastic material caused by shock-induced bubble collapse. *Proceedings of the Royal Society A: Mathematical, Physical and Engineering Sciences*, 473(2205):20170315, 2017.

[43] Stephen E Turner and Joseph M Ambrico. Underwater implosion of cylindrical metal tubes. *Journal of Applied Mechanics*, 80(1), 2013.

[44] Bram van Leer. Towards the ultimate conservative difference scheme. v. a second-order sequel to godunov's method. *Journal of Computational Physics*, 32(1):101–136, 1979.

[45] K. Wang, Jon Gretarsson, A. Main, and C. Farhat. Computational algorithms for tracking dynamic fluid–structure interfaces in embedded boundary methods. *International Journal for Numerical Methods in Fluids*, 70:515–535, 2012.

[46] K. G. Wang, P. Lea, and C. Farhat. A computational framework for the simulation of high-speed multi-material fluid–structure interaction problems with dynamic fracture. *International Journal for Numerical Methods in Engineering*, 104(7):585–623, 2015.

[47] Kevin Wang, Arthur Rallu, Jean-Frédéric Gerbeau, and Charbel Farhat. Algorithms for interface treatment and load computation in embedded boundary methods for fluid and fluid-structure interaction problems. *International Journal for Numerical Methods in Fluids*, 67(9):1175–1206, 2011.

[48] Kevin G. Wang. Multiphase fluid-solid coupled analysis of shock-bubble-stone interaction in shockwave lithotripsy. *International Journal for Numerical Methods in Biomedical Engineering*, 33(10):e2855, 2017.

[49] Kevin G Wang. Multiphase fluid-solid coupled analysis of shock-bubble-stone interaction in shockwave lithotripsy. *International journal for numerical methods in biomedical engineering*, 33(10):e2855, 2017.

[50] Kevin G. Wang, Patrick Lea, Alex Main, Owen McGarity, and Charbel Farhat. Predictive simulation of underwater implosion: coupling multi-material compressible fluids with cracking structures. In *Proceedings of 33rd International Conference on Offshore Mechanics and Arctic Engineering*, volume 8A: Ocean Engineering. ASME, 06 2014. V08AT06A028.

[51] Gaoming Xiang, Xiaojian Ma, Cosima Liang, Hongyang Yu, Defei Liao, Georgy Sankin, Shunxiang Cao, Kevin Wang, and Pei Zhong. Variations of stress field and stone fracture produced at different lateral locations in a shockwave lithotripter field. *The Journal of the Acoustical Society of America*, 150(2):1013–1029, 2021.

Chapter 5

Efficient Solution of Bimaterial Riemann Problems for Compressible Multi-Material Flow Simulations

(Submitted to *Journal of Computational Physics*, under review.)

W. Ma[a], X. Zhao[a], S. Islam[a], A. Narkhede[a], K. Wang[a]

[a] Department of Aerospace and Ocean Engineering, Virginia Tech

Blacksburg, VA 24061, United States

Abstract

When solving compressible multi-material flow problems, an unresolved challenge is the computation of advective fluxes across material interfaces that separate drastically different thermodynamic states and relations. A popular idea in this regard is to locally construct bimaterial Riemann problems, and to apply their exact solutions in flux computation. For general equations of state, however, finding the exact solution of a Riemann problem is expensive as it requires nested loops. Multiplied by the large number of Riemann problems constructed during a simulation, the computational cost often becomes prohibitive. The work presented in this paper aims to accelerate the solution of bimaterial Riemann problems without introducing approximations or offline precomputation tasks. The basic idea is to exploit some special properties of the Riemann problem equations, and to recycle previous solutions as much as possible. Following this idea, four acceleration methods are developed, including (1) a change of integration variable through rarefaction fans, (2) storing and reusing integration trajectory data, (3) step size adaptation, and (4) constructing an R-tree on the fly to generate initial guesses. The performance of these acceleration methods is assessed using four example problems in underwater explosion, laser-induced cavitation, and hypervelocity impact. These problems exhibit strong shock waves, large interface deformation, contact of multiple (> 2) interfaces, and interaction between gases and condensed matters. For all the problems, the acceleration methods are able to significantly reduce the computational cost without affecting solver robustness or solution accuracy. In different cases, the solution of bimaterial Riemann problems is accelerated by 37 to 87 times. As a result, the total cost of advective flux computation, which includes the exact Riemann problem solution at material interfaces and the numerical flux calculation over the entire computational domain, is accelerated by 18 to 81 times.

Keywords

Multiphase flow, Multi-material flow, Riemann problem, Equation of state, Compressible flow

5.1 Introduction

Fluid flows involving multiple materials or phases arise in many scientific and engineering disciplines. In this paper, we consider a class of problems in which different materials (or phases) are separated by sharp interfaces, and the flow needs to be treated as being compressible. Many fluid dynamics problems involving bubbles, droplets, phase transitions, and chemical reactions fall into this category (e.g., [25, 64, 66]). Some problems in solid and soft matter mechanics also belong to this category, when the material behaves like a compressible fluid due to some special loading condition (e.g., [28, 34]). Because of compressibility, the physical model typically involves a thermodynamic equation of state (EOS) for each material. Across a material interface, discontinuity arises not only in some state variables (e.g. density, internal energy), but also in the EOS. These discontinuities can be quite significant, if the interface separates gaseous and condensed phases.

Different numerical methods have been developed to represent material interfaces. In Lagrangian [59, 60] and Arbitrary Lagrangian-Eulerian (ALE) [38, 43] frameworks, the computational mesh is updated to conform to the material interface. In the Eulerian framework, the material interface is tracked using numerical methods such as interface capturing [5, 32], level set [21], volume of fluid [6], and front tracking [57]. Regardless of the method used to represent interfaces, the spatial discretization of the governing equations (e.g. Navier-Stokes equations) at an interface presents new challenges not encountered in single-phase flow sim-

ulations. Many popular numerical flux functions (e.g. Roe, HLLC, HLLE) assume a single EOS. Therefore, they cannot be directly applied at material interfaces. It is also well known that spurious oscillations often occur near material interfaces, even if the applied numerical scheme performs well for single-phase flows (e.g., [30, 37]). For example, Brummelen *et al.* showed that when an interface capturing method is used, spurious pressure oscillation may occur due to the loss of pressure-invariance property in discretization [58]. Fedkiw *et al.* developed the ghost fluid method, in which ghost states on both sides of a material interface are constructed [19]. In order to suppress an "overheating" phenomenon, one needs to apply the "isobaric fixing" technique that requires solving another auxiliary partial differential equation [18, 19]. Some authors have also reported that the original ghost fluid method may produce inaccurate results when an interface is hit by a shock wave, or the density or EOS jumps significantly across it [36, 37, 51].

In the past two decades, many authors have proposed the idea of constructing bimaterial Riemann problems across material interfaces, and applying their exact solutions in flux computation [4, 7, 13, 16, 17, 25, 27, 29, 32, 37, 51, 55, 61]. For example, Liu *et al.* incorporated exact Riemann solvers in their ghost fluid method, in order to correctly predict the double rarefaction waves in nearly cavitating flow conditions [37]. Later, Wang *et al.* used the exact Riemann solutions to populate not only ghost cells but also the real fluid cells near material interfaces, thereby eliminating the need of isobaric fix [61]. Cocchi and Saurel developed a prediction-correction scheme in which the solutions of exact Riemann problems are used to correct flow states near contact discontinuities [13]. Igra and Takayama modified this method to make it work in conjunction with the level-set method [27]. Also, Kitamura *et al.* conducted a comparative study of the AUSM (Advection Upstream Splitting Method) family of schemes, and found that when combined with the exact Riemann problem solver, AUSM schemes are applicable to more challenging problems with larger pressure

ratios [32]. Recently, Farhat *et al.* developed the FIVER (FInite Volume method with Exact multiphase Riemann solvers) method, in which the exact solutions of bimaterial Riemann problems are used directly to compute advective fluxes, instead of populating ghost or real fluid cells [16, 17, 24, 41, 62]. FIVER has been applied to study several shock-dominated multiphase flow and fluid-structure interaction problems, including underwater explosion and implosion [15, 39], pipeline explosion [62], cavitation erosion [8, 9, 63, 65], laser-induced vaporization [66], and hypervelocity impact [28]. Furthermore, some authors have proposed to extend exact Riemann problem solvers to account for additional interfacial physics, such as surface tension and phase transition [7, 25, 29].

A unique advantage of the constructed bimaterial Riemann problems is that they account for not only the discontinuity of state variables (e.g. density, internal energy) across a material interface, but also the change of thermodynamic EOS. With this in mind, one may expect this idea to be more impactful for problems that require sophisticated, highly nonlinear EOS. In reality, however, most of the efforts reviewed above deal with simple EOS, such as perfect and stiffened gases. For general EOS, computational cost becomes a major issue, as finding the exact solution of a Riemann problem requires nested loops [31, 56]. In particular, when the solution contains a rarefaction fan, each iteration in the outer loop requires numerically integrating two state variables through the fan, with the upper bound of the integral being an unknown variable [31]. As a result, finding the exact solution of a Riemann problem often requires evaluating the EOS thousands of times. In contrast, approximate Riemann solvers (e.g. Roe, HLLC) only call the EOS a few times. Therefore, although the exact Riemann problem solver is only applied within a lower-dimensional subset (i.e., material interfaces) of the computational domain, its cost can be much higher than the approximate Riemann solver that is applied in the entire domain. This dramatic increase of computational cost often makes the simulation unfeasible.

In this work, our objective is to accelerate the solution of bimaterial Riemann problems without introducing approximations or requiring additional precomputation. Our basic idea is to exploit some special properties of the Riemann problem equations, and to recycle previous solutions (obtained during the same simulation) as much as possible. Following this idea, we present four acceleration methods that can be used either in combination or separately. Three of the four methods are designed to accelerate the numerical integration through rarefaction fans, as it is the most expensive part of the solution procedure. We show that through a change of integration variable, the upper bound of the integral can be determined. We also show that the integral curve (i.e., isentrope) is uniquely determined by the inputs of each constructed Riemann problem. Therefore, the numerical integration performed within each iteration of the solution procedure is along the same curve, only with a different end point. In light of this observation, we present a method that eliminates repeated calculations by storing and reusing previous integration trajectories. The conventional solution procedure uses a fixed integration step size. We show that the nonlinearity of the EOS and the high degree of automation needed here allow us to benefit from step size adaptation. Furthermore, the cost of the exact Riemann problem solver also depends on the quality of the initial guesses. The fourth acceleration method is designed to generate better initial guesses, by storing previous Riemann solutions in a five-dimensional R-tree [22, 42] and finding initial guesses through nearest-neighbor search. To assess the performance of these acceleration methods, we solve four example problems in underwater explosion, laser-induced cavitation, and hypervelocity impact. These problems exhibit strong shock waves, large interface deformation, contact of multiple (> 2) interfaces, and interaction between gases and condensed matters. The robustness, accuracy, and computational efficiency of the acceleration methods are put to the test.

A major difference between the current work and previous acceleration efforts (e.g., [14,

17, 37, 47]) is that here we do not introduce approximations or require any offline precomputation. Previously, Colella and Glaz accelerated single-material Riemann problem solvers by developing a local parametrization for the EOS [14]. This method assumes slow variation of the thermodynamic state, which may not be true in challenging multi-material flow problems. Liu *et al.* found that their ghost fluid method equipped with a specifically designed approximate two-phase Riemann problem solver cannot provide correct solutions under nearly cavitating flow conditions [37]. Exact solutions of Riemann problems were thus employed to address the two strong rarefaction waves in this situation. Farhat *et al.* avoided online numerical integration by tabulating and interpolating the Riemann invariants on sparse grids [17, 47]. For the problem they considered, which involves the stiffened gas EOS and the Jones-Wilkins-Lee (JWL) EOS, only one two-dimensional sparse grid needs to be constructed. But for arbitrary EOS, two three-dimensional sparse grids need to be constructed for each material. This offline precomputation can be expensive. It also requires a high level of expertise from the user, who is expected to specify, before the simulation, the resolution of the sparse grids as well as the lower and upper bounds of each tabulated variable. These complexities motivated us to pursue a different path, that is, to accelerate the Riemann solver without introducing approximations or requiring offline precomputation.

The remainder of this paper is organized as follows. In Sec. 5.2, we present the governing compressible Navier-Stokes equations and the bimaterial Riemann problem with general convex and smooth EOS. We also briefly describe the aforementioned FIVER method, which is adopted in this work to perform numerical tests. In Sec. 5.3, we discuss the computational efficiency of the exact Riemann problem solver in detail. The acceleration methods mentioned above are presented. In Sec. 5.4, we present the numerical tests and discuss the performance of the acceleration methods. Finally, we provide a summary in Sec. 5.5.

5.2 Governing equations and solution framework

5.2.1 Navier-Stokes equations with general equations of state

In general, the dynamics of compressible multi-material flows are governed by Navier-Stokes equations, which enforce the conservation of mass, momentum, and energy. In the literature, the exact solutions of bimaterial Riemann problems are used mostly to compute the advective fluxes (e.g., [17, 25]). Therefore, we write the Navier-Stokes equations as

$$\frac{\partial \boldsymbol{U}}{\partial t} + \nabla \cdot \mathcal{F}(\boldsymbol{U}) = \boldsymbol{\mathcal{S}}, \qquad \text{in } \Omega \times (0,\ t_{\max}], \tag{5.1}$$

which emphasizes the advective fluxes $\mathcal{F}(\boldsymbol{U})$. Here, $\boldsymbol{U}$ denotes the conservative state vector. t denotes time, and $\boldsymbol{\mathcal{S}}$ represents collectively the additional terms that may need to be included in the conservation laws, depending on the specific flow being analyzed. Examples include viscous fluxes, heat diffusion fluxes, heat sources, and body forces. Because bimaterial Riemann problems are neither constructed based on these terms nor used to evaluate them, we do not formulate $\boldsymbol{\mathcal{S}}$ explicitly. Ω denotes the spatial domain of the flow, and $t_{\max}$ the maximum physical time of interest. $\boldsymbol{U}$ and $\mathcal{F}(\boldsymbol{U})$ are given by

$$\boldsymbol{U} = \begin{bmatrix} \rho \\ \rho \boldsymbol{u} \\ \rho e_t \end{bmatrix}, \quad \mathcal{F}(\boldsymbol{U}) = \begin{bmatrix} \rho \boldsymbol{u}^T \\ \rho \boldsymbol{u} \otimes \boldsymbol{u} + p\boldsymbol{I} \\ (\rho e_t + p)\boldsymbol{u}^T \end{bmatrix}, \tag{5.2}$$

where ρ, e_t, and p denote the density, total energy per unit mass, and pressure, respectively. $\boldsymbol{u} = [u, v, w]^T$ is the velocity vector. $\boldsymbol{I}$ denotes the 3×3 identity matrix. In addition,

$$e_t = e + \frac{1}{2}|\boldsymbol{u}|^2, \tag{5.3}$$

where e is the internal energy per unit mass.

We assume that the fluid domain Ω consists of multiple non-overlapping open sets (i.e. subdomains) occupied by different materials, i.e.,

$$\Omega = \bigcup_{m=1}^{M} \mathrm{cl}(\Omega_m), \quad \Omega_m \cap \Omega_n = \emptyset, \ \forall m, \ n \ (m \neq n), \tag{5.4}$$

where $\mathrm{cl}(\Omega_m)$ denotes the closure of Ω_m. Within each subdomain Ω_m, a thermodynamic equation of state (EOS) of the form

$$p = p(\rho, e) \tag{5.5}$$

is needed to close the governing equations. The speed of sound, c, is given by

$$c = \sqrt{\frac{\partial p}{\partial \rho}\Big|_e + \frac{p}{\rho^2}\frac{\partial p}{\partial e}\Big|_\rho}. \tag{5.6}$$

Here, we introduce a few specific examples that are used in the numerical tests in Sec. 5.4. Nonetheless, the algorithms presented in this paper are designed to be applicable to general convex and smooth equations of state in the form of (5.5).

As a generalization of perfect gas, the noble-Abel stiffened gas equation of state [35] is given by

$$p = (\gamma - 1)\frac{\rho(e - e_c)}{1 - \rho b} - \gamma p_c, \tag{5.7}$$

where γ, e_c, b, and p_c are constant parameters. The sound speed is given by

$$c\,(p, \rho) = \sqrt{\frac{\gamma(p + p_c)}{\rho - \rho^2 b}}. \tag{5.8}$$

The Jones-Wilkins-Lee (JWL) equation of state is widely used to model the thermodynamics of detonation products [44]. It has the expression

$$p = \omega\rho e + f(\rho), \tag{5.9}$$

where

$$f(\rho) = A_1\left(1 - \frac{\omega\rho}{R_1\rho_0}\right)\exp\Big(-\frac{R_1\rho_0}{\rho}\Big) + A_2\left(1 - \frac{\omega\rho}{R_2\rho_0}\right)\exp\Big(-\frac{R_2\rho_0}{\rho}\Big), \tag{5.10}$$

Here, ρ_0, ω, A_1, A_2, R_1, and R_2 are constant parameters. The sound speed is given by

$$c(p,\rho) = \sqrt{\frac{\gamma p - f(\rho) + \rho f'(\rho)}{\rho}}. \tag{5.11}$$

The Mie-Grüneisen equation of state is often used to model solids and liquids under high pressure. In this work, we adopt the formulation given in [48], i.e.,

$$p = \frac{\rho_0 c_0^2 \eta}{(1 - s\eta)^2}\Big(1 - \frac{1}{2}\Gamma_0\eta\Big) + \rho_0\Gamma_0 e, \tag{5.12}$$

with $\eta = 1 - \rho_0/\rho$. ρ_0 and c_0 denote the density and bulk speed of sound in the ambient condition. s is the slope of the Hugoniot curve. Γ_0 is the Grüneisen parameter in the ambient condition. In this case, the sound speed is given by

$$c(p,\rho) = \sqrt{\frac{\rho_0^2 c_0^2}{\rho^2}\frac{1 + (s - \Gamma_0)\eta}{(1 - s\eta)^3} + \frac{p}{\rho^2}\Gamma_0\rho_0}. \tag{5.13}$$

For these examples, both e and c can be evaluated analytically in closed-form. There are more complicated EOS for which one or both of them can only be evaluated through numerical iteration (e.g. [52]). As a result, the computational cost may increase drastically.

If the term $\boldsymbol{\mathcal{S}}$ in (5.1) involves temperature, a temperature law is also needed for each material. However, the temperature law is not involved in the construction and solution of exact Riemann problems. Therefore, additional details are omitted for the sake of conciseness.

5.2.2 Formulation of bimaterial Riemann problems at material interfaces

At the interface between two adjacent material subdomains, normal velocity and pressure are assumed to be continuous, i.e.,

$$\begin{aligned} (\boldsymbol{u}_l - \boldsymbol{u}_r) \cdot \boldsymbol{n} &= 0, \\ p_l - p_r &= 0, \end{aligned} \qquad \text{on } \partial\Omega_l \cap \partial\Omega_r, \tag{5.14}$$

where $\boldsymbol{n}$ denotes the unit normal to the material interface, and the subscripts l and r indicate the one-sided limits of the state variable ($\boldsymbol{u}$ or p) obtained within the two subdomains. At each point on the interface, the bimaterial Riemann problem is defined as the 1D Euler equations [4, 13, 16, 17, 27, 32, 37, 51, 55],

$$\frac{\partial \boldsymbol{q}}{\partial \tau} + \frac{\partial \mathcal{F}(\boldsymbol{q})}{\partial \xi} = 0, \tag{5.15}$$

with a piecewise constant initial condition obtained from the original 2D or 3D flow field (Fig. 5.1). Here, τ is a fictitious time coordinate, ξ is the spatial coordinate, which in principle is along the direction of $\boldsymbol{n}$. The initial condition, which features a discontinuity at the material interface, is given by

$$\boldsymbol{q}(\xi, 0) = \begin{cases} \boldsymbol{q}_l, & \text{if } \xi \leq 0, \\ \boldsymbol{q}_r, & \text{if } \xi > 0, \end{cases} \tag{5.16}$$

with

$$\boldsymbol{q}_l \equiv \begin{bmatrix} \rho_l \\ \rho_l u_l \\ \rho_l e_{tl} \end{bmatrix} = \begin{bmatrix} \rho_l \\ \rho_l \left(\boldsymbol{u}_l \cdot \boldsymbol{n}\right) \\ \rho_l e_l + \frac{1}{2}\rho_l \left(\boldsymbol{u}_l \cdot \boldsymbol{n}\right)^2 \end{bmatrix}, \quad \boldsymbol{q}_r \equiv \begin{bmatrix} \rho_r \\ \rho_r u_r \\ \rho_r e_{tr} \end{bmatrix} = \begin{bmatrix} \rho_r \\ \rho_r \left(\boldsymbol{u}_r \cdot \boldsymbol{n}\right) \\ \rho_r e_r + \frac{1}{2}\rho_r \left(\boldsymbol{u}_r \cdot \boldsymbol{n}\right)^2 \end{bmatrix}. \tag{5.17}$$

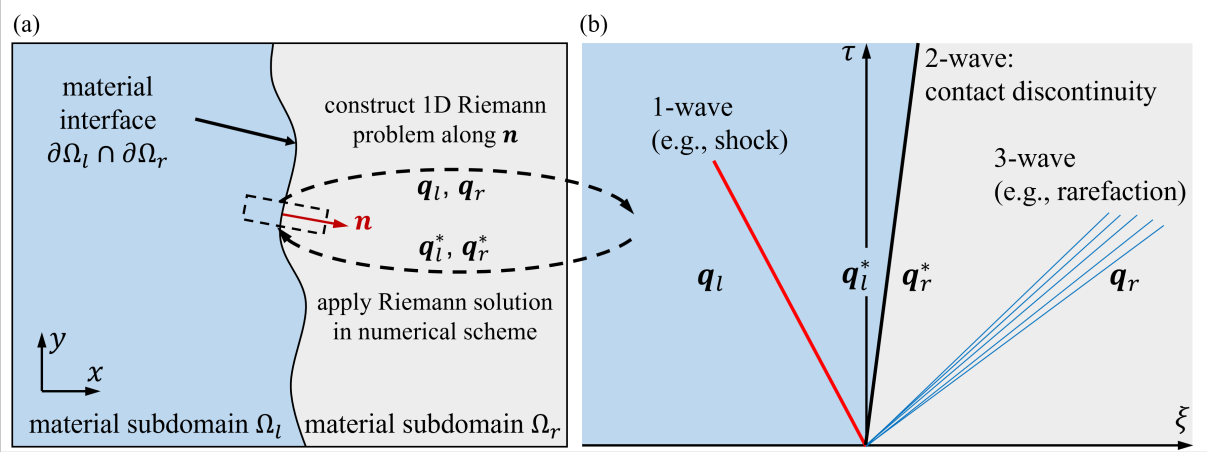

Figure 5.1: Construction and solution of a bimaterial Riemann problem at material interface.

Solving the Riemann problem exactly generally means finding a weak entropy solution that consists of three waves, as illustrated in Fig. 5.1(b). The one in the middle (i.e., the 2-wave) is a contact discontinuity that tracks the motion of the material interface. It separates the two material subdomains in which different EOS should be applied. Each of the other two waves can be either a shock wave or a rarefaction fan. These three waves divide the ξ-τ space into four regions, plus the interior of any rarefaction fan. The outer two regions have not been affected by the shock and/or rarefaction yet, so the initial fluid states $\boldsymbol{q}_l$ and $\boldsymbol{q}_r$ sill hold there (Fig. 5.1(b)). The state variables in the two middle regions next to the material interface are unknowns that need to be solved for. Following the convention in the literature ("star states"), these variables are identified by a superscript $*$. It should be noted that the aforementioned three-wave solution structure requires the EOS to be convex and smooth [45].

Given the convexity and smoothness of the EOS, the Riemann solution is unique if the EOS in the meantime satisfies the "medium condition" in [45].

Across the contact discontinuity, pressure and velocity are continuous, i.e.,

$$\begin{aligned} p_l^* &= p_r^*, \\ u_l^* &= u_r^*. \end{aligned} \tag{5.18}$$

Therefore, the solution of the exact Riemann problem automatically satisfies the interface conditions (5.14).

Across a shock wave, the Rankine-Hugoniot jump conditions can be derived from (5.15). After some algebraic manipulations, we get the following two equations.

$$e_K(p_K^*, \rho_K^*) - e_K(p_K, \rho_K) + \frac{1}{2}(p_K + p_K^*)\Big(\frac{1}{\rho_K^*} - \frac{1}{\rho_K}\Big) = 0 \tag{5.19}$$

and

$$u_K^* = u_K \mp \sqrt{-\big(p_K^* - p_K\big)\Big(\frac{1}{\rho_K^*} - \frac{1}{\rho_K}\Big)}, \tag{5.20}$$

where $K = l, r$. Equation (5.19) only involves the thermodynamic variables, and is known as the Hugoniot equation. The function $e_K(p, \rho)$ evaluates internal energy using the EOS that holds in material subdomain Ω_K. In (5.20), the minus sign holds for $K = l$, and the plus sign holds for $K = r$.

Through a rarefaction fan, two Riemann invariants can be derived from the 1D Euler equations (5.15). They are

$$s - s_K = 0 \tag{5.21}$$

and

$$u - u_K \pm \int_{\rho_K}^{\rho} \frac{c_K(s_K, \rho)}{\rho} d\rho = 0, \tag{5.22}$$

where s, u, ρ denote the entropy, velocity, and density evaluated at any point within a rarefaction fan, including its boundaries. In (5.22), the plus sign applies to the 1-wave (i.e., $K = l$), and the minus sign applies to the 3-wave (i.e., $K = r$). The first Riemann invariant (5.21) indicates that entropy is constant through a rarefaction fan. Therefore, the sound speed can be evaluated from $c^2 = \left.\frac{\partial p}{\partial \rho}\right|_s$. Integrating this relation through the rarefaction fan, i.e., from the ambient state to the star state, gives

$$p_K^* = p_K + \int_{\rho_K}^{\rho_K^*} c_K^2(s_K, \rho) d\rho, \tag{5.23}$$

where the function $c_K(s, \rho)$ evaluates the sound speed using the EOS for material K. Similarly, substituting $\rho = \rho_K^*$ and $u = u_K^*$ into (5.22) yields

$$u_K^* = u_K \mp \int_{\rho_K}^{\rho_K^*} \frac{c_K(s_K, \rho)}{\rho} d\rho, \tag{5.24}$$

where the minus sign applies to the 1-wave (i.e., $K = l$) and the plus sign applies to the 3-wave (i.e., $K = r$). Although these two equations involve entropy in the evaluation of sound speed, the actual computation does not necessarily need it. We can write the sound speed c as a function of p and ρ, as given in equations (5.8), (5.11), and (5.13).

To determine whether each of the 1 and 3 waves is a shock or a rarefaction, we enforce an entropy condition. Each of the two waves is determined to be a shock wave if and only if $p_K^* > p_K$, where $K = l$ for the 1-wave, and $K = r$ for the 3-wave.

In summary, the solution of the exact Riemann problem, $\boldsymbol{q}_l^*$ and $\boldsymbol{q}_r^*$, is determined by Eqs. (5.18), (5.19), (5.20), (5.23), (5.24), and the above entropy condition. The shock speed, u_s, and the state variables through any rarefaction fan can be easily derived based on $\boldsymbol{q}_l^*$ and $\boldsymbol{q}_r^*$. For a general equation of state, the exact Riemann problem cannot be solved analytically. The numerical solution methods are presented in Sec. 5.3 in detail.

5.2.3 Interface tracking and discretization of governing equations

We briefly describe the interface tracking and spatial discretization methods adopted in this work, thereby providing a clear context for the construction and solution of bimaterial Riemann problems. Nonetheless, the algorithms for solving the Riemann problems — to be introduced in Sec. 5.3 — are not restricted to these methods.

For a problem that involves M (≥ 2) materials, there can be as many as $C_2^M = M(M-1)/2$ material interfaces. Instead of tracking each one of them explicitly, we solve $M-1$ level set equations, i.e.

$$\frac{\partial \phi^{(m)}(\boldsymbol{x},t)}{\partial t} + \boldsymbol{u}\cdot\nabla\phi^{(m)} = 0, \quad m = 1,2,\cdots M-1, \tag{5.25}$$

to track the boundaries of the first $M-1$ subdomains (Fig. 5.2). Here, $\phi^{(m)}(\boldsymbol{x},t)$ denotes a level set function, initialized to be the signed shortest distance from $\boldsymbol{x}$ to $\partial\Omega_m$. Any point $\boldsymbol{x}\in\Omega$ is within subdomain Ω_m ($m = 1,2,\cdots M-1$) at time t if and only if $\phi^{(m)}(\boldsymbol{x},t) < 0$. The last subdomain is simply

$$\Omega_M = \Omega \setminus \Big(\bigcup_{m=1}^{M-1} \mathrm{cl}(\Omega_m) \Big). \tag{5.26}$$

Notably, all the level set equations share the same velocity field $\boldsymbol{u}$, which prevents spurious overlapping and separation of subdomains. The interface between each pair of materials — e.g. m and n ($1 \leq m < n \leq M$) — is simply given by

$$\partial\Omega_m \cap \partial\Omega_n = \begin{cases} \Big\{ \boldsymbol{x}\in\Omega, \quad \phi^{(m)}(\boldsymbol{x},t) = \phi^{(n)}(\boldsymbol{x},t) = 0 \Big\}, & n < M, \\ \Big\{ \boldsymbol{x}\in\Omega, \quad \phi^{(k)}(\boldsymbol{x},t) = 0 \ \text{ iff } \ k = m \Big\}, & n = M. \end{cases} \tag{5.27}$$

We discretize the governing equations (5.1) using the FIVER method [40, 66]. Applying a

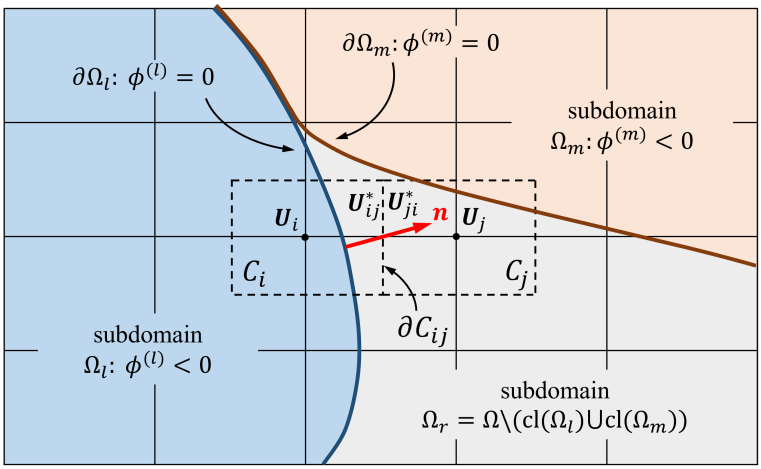

Figure 5.2: Interface tracking and discretization of governing equations: The level set method and FIVER.

standard finite volume method to the left hand side of (5.1) yields

$$\frac{\partial \boldsymbol{U}_i}{\partial t} + \frac{1}{\|C_i\|} \sum_{j \in N(i)} \int_{\partial C_{ij}} \mathcal{F}(\boldsymbol{U}) \cdot \boldsymbol{n_{ij}} dS = \boldsymbol{\mathcal{S}}^h, \tag{5.28}$$

where C_i denotes a control volume in Ω, $\|C_i\|$ being its volume. $\boldsymbol{U}_i$ denotes the cell-average of $\boldsymbol{U}$. $N(i)$ is the set of nodes that are connected to node i by an edge. $\partial C_{ij} = \partial C_i \cap \partial C_j$ is the cell interface between C_i and C_j. $\boldsymbol{\mathcal{S}}^h$ represents a numerical approximation of $\boldsymbol{\mathcal{S}}$, which does not need to be based on the same finite volume method. Between cell C_i and each neighboring cell C_j, a numerical advective flux is computed to approximate the surface integral in (5.28). If i and j belong to the same material subdomain, a conventional flux function (e.g. local Lax-Friedrichs (LLF), Roe, HLLC) is directly applied. If they belong to different material subdomains (e.g. Ω_l and Ω_r in Fig. 5.2), a 1D bimaterial Riemann problem is constructed using the method described in Sec. 5.2.2. Its solution, $\boldsymbol{q}^*_l$ and $\boldsymbol{q}^*_r$, are mapped back to 2D or 3D, generating interface states U^*_{ij} and U^*_{ji}. Then, the advective fluxes on the

two sides of ∂C_{ij} are computed as

$$\begin{aligned} F_{ij} &= \|\partial C_{ij}\| \, \Phi \left(\boldsymbol{U}_{ij}, \boldsymbol{U}^*_{ij}, n_{ij}, \mathrm{EOS}(\Omega_l) \right) \\ F_{ji} &= \|\partial C_{ij}\| \, \Phi \left(\boldsymbol{U}_{ji}, \boldsymbol{U}^*_{ji}, n_{ji}, \mathrm{EOS}(\Omega_r) \right), \end{aligned} \tag{5.29}$$

where $\|\partial C_{ij}\|$ is the area of ∂C_{ij}, and Φ denotes a conventional numerical flux function. $\boldsymbol{U}_{ij}$ and $\boldsymbol{U}_{ji}$ are interface states reconstructed using the MUSCL (monotonic upwinding scheme for conservation laws) method and a slope limiter. Additional details about FIVER can be found in [40, 66].

5.3 Efficient solution of bimaterial Riemann problems

5.3.1 Conventional solution procedure and its efficiency issues

We start with summarizing the conventional method for solving Riemann problems (e.g., [31, 56]), while at the same time, emphasizing its high computational cost. This cost may not be a practical issue if the user only needs to solve one or a few Riemann problems. Nonetheless, it can dominate the entire simulation cost, when bimaterial Riemann problems are constructed and solved along each edge in the mesh that penetrates a material interface, although the union of all the interfaces is still a lower-dimensional subset of the computational domain.

The equations that govern the three-wave entropy solution of the Riemann problem are Eqs. (5.18) to (5.24), together with the entropy condition described in Sec. 5.2.2. The unknowns are p^* $(= p^*_l = p^*_r)$, u^* $(= u^*_l = u^*_r)$, ρ^*_l, and ρ^*_r. We define function $f(p)$ as

$$f(p) = u^*_l(p;\ \rho_l, u_l, p_l, \mathrm{EOS}_l) - u^*_r(p;\ \rho_r, u_r, p_r, \mathrm{EOS}_r), \tag{5.30}$$

where the subscripts l and r indicate the material subdomains separated by the interface. For an arbitrary input p, the first term of $f(p)$ evaluates the interface velocity u_l^* that complies with an interface pressure $p^* = p$, and the left ambient state ρ_l, u_l, and p_l. Specifically, the entropy condition is first examined to determine whether the 1-wave is a shock or a rarefaction. If it is a shock, Eqs. (5.19) and (5.20) are solved for u_l^*, with $K = l$ and $p_K^* = p$. If it is a rarefaction, Eqs. (5.23) and (5.24) are solved for u_l^*, also with $K = l$ and $p_K^* = p$. Similarly, the second term of $f(p)$ evaluates the interface velocity u_r^* that complies with an interface pressure $p^* = p$, and the right ambient state ρ_r, u_r, and p_r. Again, it starts with enforcing the entropy condition, followed by the solution of either (5.19) and (5.20), or (5.23) and (5.24), depending on whether the 3-wave is a shock or a rarefaction. Because of (5.18), the true solution of interface pressure, p^*, is a root of $f(p)$, i.e.

$$f(p^*) = 0. \tag{5.31}$$

Equation (5.31) is nonlinear, and for general equations of state it cannot be solved analytically. The standard method is to solve it numerically through an iterative procedure, such as the one illustrated in Fig. 5.3. Starting with an initial guess of p^*, in each iteration, we first apply the entropy condition to determine whether each of the 1 and 3 waves is a shock or a rarefaction. If it is a shock wave, ρ_K^* can be first obtained by solving Eq. (5.19) using an iterative method (e.g. the secant method). Then, u_K^* can be obtained using Eq. (5.20).

If it is a rarefaction fan, u_K^* and ρ_K^* are computed from Eqs. (5.23) and (5.24). For simple equations of state such as perfect gas, the integrals therein can be evaluated analytically in closed-form (e.g. see [17]). However, for an arbitrary equation of state, the two integrals need to be evaluated using a numerical integration method. For example, using the fourth-order

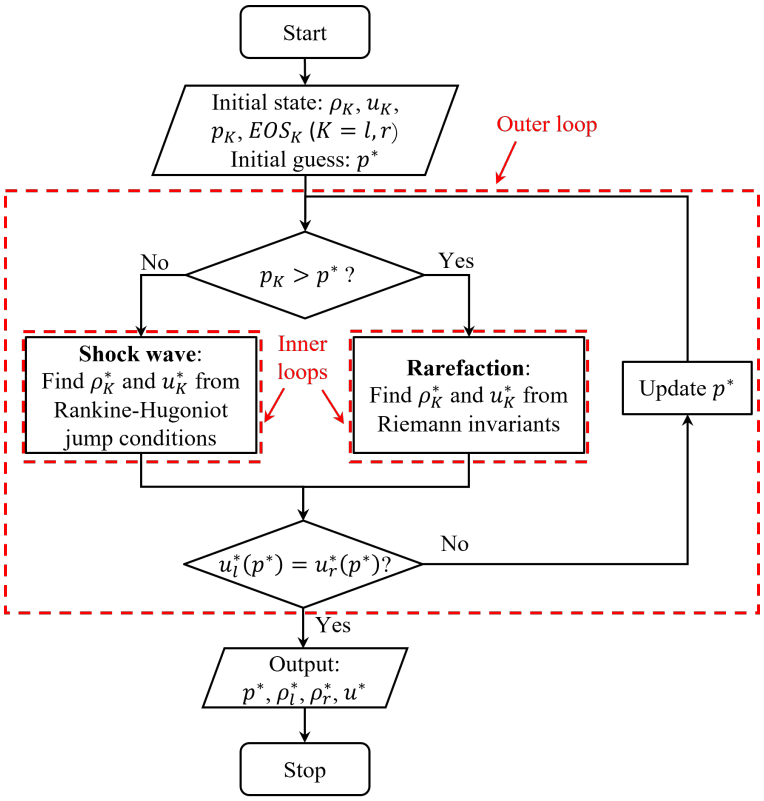

Figure 5.3: The conventional procedure for solving bimaterial Riemann problems.

Runge-Kutta method, in each step, the pressure and velocity are evaluated as

$$p^{(i+1)} = p^{(i)} + \frac{1}{6}\left[\hat{c}_1^2 + 2\left(\hat{c}_2^2 + \hat{c}_3^2\right) + \hat{c}_4^2\right]\Delta\rho, \tag{5.32}$$

$$u^{(i+1)} = u^{(i)} \mp \frac{1}{6}\left[\frac{\hat{c}_1}{\hat{\rho}_1} + 2\left(\frac{\hat{c}_2}{\hat{\rho}_2} + \frac{\hat{c}_3}{\hat{\rho}_3}\right) + \frac{\hat{c}_4}{\hat{\rho}_4}\right]\Delta\rho, \tag{5.33}$$

where $p^{(i)}$ and $u^{(i)}$ are the pressure and density evaluated from the previous step. In the second equation, the minus sign applies to the 1-wave, and the plus sign applies to the 3-wave. $\hat{c}_i$ and $\hat{\rho}_i$ $(i = 1, 2, 3, 4)$ are sound speed and density evaluated at intermediate stages

within the step, specifically,

$$\begin{aligned}
\hat{c}_1 &= c_K\left(p^{(i)},\ \hat{\rho}_1\right),\ \text{with}\ \hat{\rho}_1 =\ \rho^{(i)},\\
\hat{c}_2 &= c_K\left(p^{(i)} + 0.5\Delta\rho\hat{c}_1^2,\ \hat{\rho}_2\right),\ \text{with}\ \hat{\rho}_2 =\ \rho^{(i)} + 0.5\Delta\rho,\\
\hat{c}_3 &= c_K\left(p^{(i)} + 0.5\Delta\rho\hat{c}_2^2,\ \hat{\rho}_3\right),\ \text{with}\ \hat{\rho}_3 =\ \rho^{(i)} + 0.5\Delta\rho,\\
\hat{c}_4 &= c_K\left(p^{(i)} + \Delta\rho\hat{c}_3^2,\ \hat{\rho}_4\right),\ \text{with}\ \hat{\rho}_4 =\ \rho^{(i)} + \Delta\rho.
\end{aligned}$$

It should be noted that in Eq. (5.23), the unknown variable is the integral's upper bound, ρ_K^*, while the integration result (p^*) on the left hand side is given. In order to find ρ_K^* that yields the given p^*, a trial-and-error procedure is needed. For example, Kamm [31] proposed an iterative procedure to find a constant $\Delta\rho$ that would allow the numerical integration to end at p_K^*. In each iteration, the entire course of integration is repeated with an updated $\Delta\rho$. A more efficient method is to update $\Delta\rho$ in each step of the numerical integration process, based on the difference between the current pressure $p^{(i)}$ and the given p^*[1]. Either way, the computational cost is higher than standard numerical integration, where the lower and upper bounds of the integral are both given.

If the computed interface velocities, u_l^* and u_r^*, satisfy

$$|u_l^*(p^*) - u_r^*(p^*)| < \epsilon_u, \tag{5.34}$$

an approximate solution of p^* has been obtained. Here, ϵ_u denotes the error tolerance. ρ_l^* and ρ_r^* have also been obtained through the solution of the Hugoniot equation (5.19) and/or the Riemann invariant (5.23). u^* can be set by

$$u^* = \frac{1}{2}\left(u_l^* + u_r^*\right). \tag{5.35}$$

[1]This method is adopted in the baseline simulations presented in Sec. 5.4.

The propagation speed of any shock wave can be calculated easily using the Rankine-Hugoniot jump conditions. If needed, the solution of ρ, u, and p within any rarefaction fan can be obtained from the numerical integration procedure as a byproduct.

If (5.34) is not satisfied, the nonlinear equation solver (i.e., the outer loop in Fig. 5.3) enters the next iteration with an updated guess of p^*, which can be obtained using the secant method.

Compared to approximate Riemann problem solvers, such as LLF [50], Roe and HLLC [26], the cost of the exact Riemann problem solver presented above is significantly higher, as it involves nested loops (Fig. 5.3). This difference can be examined by counting and comparing the number of times the EOS are evaluated. For the exact Riemann problem solver, let N_{out} denote the number of iterations in the outer loop. Let N_{sh} be the average number of iterations in the inner loop for solving the shock Hugoniot equation. Let N_{rf} be the number of integration steps required to go through any rarefaction fan. The number of EOS evaluations — including the evaluation of c, e, and p — is 2 within each step of the shock Hugoniot equation solver, and 4 within each integration step. Therefore, executing the algorithm shown in Fig. 5.3 requires at least

$$N_{\text{exact}} = N_{\text{out}}(2N_{\text{sh}} + 4N_{\text{rf}}) \tag{5.36}$$

calls to the EOS, if we assume the solution structure consists of one shock wave and one rarefaction fan. In comparison, the LLF, Roe, and HLLC solvers require 4, 3, and 5 calls to the EOS, respectively. Table 5.1 shows a typical scenario with $N_{\text{out}} = N_{\text{sh}} = 5$ and $N_{\text{rf}} = 200$, in which the cost of the exact Riemann problem solver is roughly 1000 times that of approximate Riemann problem solvers, in terms of the number of EOS evaluations.

Table 5.1: Number of EOS evaluations required by exact and approximate Riemann problem solvers.

	Exact Riemann solver	Approx. Riemann solver		
		LLF	Roe	HLLC
Shock ($= 2N_{\text{out}}N_{\text{sh}}$)	50	-	-	-
Rarefaction ($= 4N_{\text{out}}N_{\text{rf}}$)	4000	-	-	-
Total*	4050	4	3	5

* Assuming one shock wave and one rarefaction fan in the solution structure (Fig. 5.1(b))

The exact Riemann problem solver is only applied across or near material interfaces, which is a lower-dimensional subset of the computational domain. In comparison, approximate Riemann solvers are generally applied within the entire domain. Although the number of times the exact Riemann problem solver is used is smaller, its cost can still dominate the entire simulation cost. As an example, consider a square domain in 2D, discretized uniformly into n elements in both directions. The total number of edges along which numerical fluxes need to be computed is roughly $2n^2$. Let us assume that $2n$ of them penetrate material interfaces. In this case, the ratio between the number of approximate Riemann problems and that of exact Riemann problems is approximately n. Based on the statistics shown in Table 5.1, for $n = 200$, exact Riemann problem solutions account for more than 80% of the computational cost, measured by the number of EOS evaluations.

In numerical tests, we have found that during flux calculations, over 95% of the computation time can be consumed by the exact Riemann problem solver. This number is higher than the estimate obtained above, for at least two reasons. First, in some cases, the numerical integration procedure requires more than 200 steps (i.e., $N_{rf} > 200$) to reach a sufficient degree of accuracy (e.g. see Fig. 5.24 in Sec. 5.4.4). Second, in parallel computations, the mesh is usually partitioned without knowledge of the location of material interfaces, which results in load imbalance. Some processors may need to solve a larger number of exact Riemann problems, if the subdomain assigned to it covers a larger fraction of material

interface. For the most burdened processor, the ratio of approximate to exact Riemann problems is often lower than 200, which was assumed in the above estimation.

Next, we propose several techniques that can significantly reduce the computational cost of the exact Riemann problem solver, without sacrificing accuracy or introducing precomputation efforts (e.g. sparse-grid tabulation [17]).

5.3.2 Change of integration variable

As mentioned in Sec. 5.3.1, when evaluating the integrals in (5.23) and (5.24), the upper bound ρ_K^* is unknown. A trial-and-error procedure is required to find the correct ρ_K^* that makes Eq. (5.23) hold for the given p^*. We show that this trial-and-error procedure can be eliminated by rewriting (5.23) and (5.24) in an alternative form, in which the integration variable is p instead of ρ. Then, the upper bound of the integral becomes p^*, which is specified within the outer loop.

The two Riemann invariants, (5.23) and (5.24), can be expressed in a differential form,

$$\begin{cases} \dfrac{dp}{d\rho} &= c_K^2(s_K,\rho), \\ \dfrac{du}{d\rho} &= \mp\dfrac{c_K(s_K,\rho)}{\rho}, \\ p(\rho_K) &= p_K, \\ u(\rho_K) &= u_K, \end{cases} \tag{5.37}$$

for all $\rho \in [\rho^*, \rho_K]$ and $p \in [p^*, p_K]$. In the second equation, the minus sign applies to the 1-wave ($K = l$), and the plus sign applies to the 3-wave ($K = r$). Through the rarefaction fan, entropy does not change, so pressure $p(s_K, \rho)$ is essentially a single variable function of density, i.e., $p(\rho)$. Also, the first equation in (5.37) indicates that $p(\rho)$ increases mono-

tonically with respect to ρ since its derivative is $c^2(s_K, \rho)$. Therefore, the function $p(\rho)$ has an inverse function $\rho(p)$. Its derivative, $\frac{d\rho}{dp}$, can be obtained easily from the first equation of (5.37), i.e.,

$$\frac{d\rho}{dp} = \frac{1}{dp/d\rho} = \frac{1}{c_K^2(s_K, \rho(p))} = \frac{1}{c_K^2(s_K, p)}. \tag{5.38}$$

Then, $\frac{du}{dp}$ can be derived from the second equation in (5.37) and (5.38) using the chain rule, i.e.,

$$\frac{du}{dp} = \frac{du}{d\rho}\frac{d\rho}{dp} = \mp\frac{c_K(s_K, p)}{\rho(p)}\frac{1}{c_K^2(s_K, p)} = \mp\frac{1}{c_K(s_K, p)\rho(p)}. \tag{5.39}$$

Using (5.38) and (5.39), (5.37) can be rewritten as

$$\begin{cases} \dfrac{d\rho}{dp} &= \dfrac{1}{c_K^2(s_K, p)}, \\ \dfrac{du}{dp} &= \mp\dfrac{1}{c_K(s_K, p)\rho(p)}, \\ \rho(p_K) &= \rho_K, \\ u(p_K) &= u_K, \end{cases} \tag{5.40}$$

for all $\rho \in [\rho^*, \rho_K]$ and $p \in [p^*, p_K]$. Integrating the ODEs in (5.40) from p_K to p^* yields

$$\rho_K^* = \rho_K + \int_{p_K}^{p^*} \frac{1}{c_K^2(s_K, p)} dp, \tag{5.41}$$

$$u_K^* = u_K \mp \int_{p_K}^{p^*} \frac{1}{c_K(s_K, p)\rho(p)} dp. \tag{5.42}$$

Again, we can express sound speed c as a function of p and ρ. Hence, a closed-form formulation of entropy is not needed. We use (5.41) and (5.42) to replace (5.23) and (5.24). In this way, the integration interval is fixed, and the computational overhead associated with the aforementioned trial-and-error procedure is eliminated.

5.3.3 Storing and reusing integration trajectory data

We show that the integrations needed to resolve rarefaction fans, i.e. (5.41) and (5.42), can be accelerated by storing and reusing previous results. Our idea is based on the following two observations.

(1) Although the iterative solution of exact Riemann problems (i.e., the outer loop in Fig. 5.3) requires repeated evaluation of (5.41) and (5.42), the initial state of the integration is always the same, namely, $\{p_K, \rho_K, u_K\}$. Only p^* varies from one iteration to the next.

(2) Once p_K, ρ_K, and u_K are fixed, the integrands in (5.41) and (5.42) are both single variable functions of p.

(1) is true because the initial state, $\{p_K, \rho_K, u_K\}$, is determined by the construction of the Riemann problem, and the iterative solution procedure does not change it. (2) is true because entropy is constant through a rarefaction fan, and its value is determined uniquely by the initial state, $\{p_K, \rho_K, u_K\}$.

Indeed, throughout the solution procedure (i.e., the outer loop), we always integrate along the same isentrope, defined by the initial state, and characterized by a single variable, p. Only the final state varies in different iterations. Therefore, from one iteration to the next, the "overlapped" part of the integration trajectory is first evaluated, then discarded, and then re-evaluated again.

This redundancy can be shown clearly using an example problem. We consider a Riemann

problem (i.e., (5.15)) with initial condition

$$(\rho, u, p, \text{EOS}) = \begin{cases} (1.2 \times 10^{-6}\ \text{g/mm}^3, 0.0\ \text{mm/s}, 1.0 \times 10^5\ \text{Pa}, \text{stiffened gas}) & \text{if} \quad \xi < 0\ \text{mm} \\ (2.204 \times 10^{-3}\ \text{g/mm}^3, 4.0 \times 10^5\ \text{mm/s}, 1.0 \times 10^5\ \text{Pa}, \text{Mie-Grüneisen}) & \text{if} \quad \xi > 0\ \text{mm}. \end{cases} \tag{5.43}$$

The parameters in the stiffened gas EOS are given by $\gamma = 1.4$, $e_c = 0$, $b = 0$, and $p_c = 0$. Therefore, it degenerates to a perfect gas. The parameters in the Mie-Grüneisen EOS are given by $p_0 = 2.204 \times 10^{-3}$ g/mm^3, $c_0 = 2.22 \times 10^6$ mm/s, $s = 1.61$, and $\Gamma_0 = 0.65$. The solution has a double-rarefaction wave structure. 200 steps are specified for the numerical integration.

Figure 5.4 shows the integration trajectories through the 1-wave, obtained in 3 successive iterations in the outer loop. Clearly, these curves all start from the same point at $p = 1.0 \times 10^5$ Pa (the right end). They follow the same trajectory, only end at different points. It can be observed that the trajectory traversed in the first iteration is the same as that in the next two iterations. In iterations 2 and 3, only the last point (i.e., the end point) really needs to be evaluated. Nonetheless, the algorithm recalculates the entire trajectory from the right end. Therefore, the vast majority of the computations performed in iterations 2 and 3 are redundant and unnecessary. To eliminate this redundancy, we propose to store and reuse the numerically obtained integration trajectory. Let $\boldsymbol{\chi}$ denote this trajectory, which is a discrete sequence of state variables $\{p, \rho, u\}$ on the isentrope. At the beginning of the outer loop (see Fig. 5.3), $\boldsymbol{\chi}$ is initialized to contain only the start point, $\{p_K, \rho_K, u_K\}$. In each iteration of the outer loop, the standard numerical integration procedure is replaced by Algorithm 1.

Algorithm 1 has two main steps. In Step 1, we find the point in $\boldsymbol{\chi}$ that is closest to the given p^*, but bigger. We start the numerical integration from this point, thereby avoiding

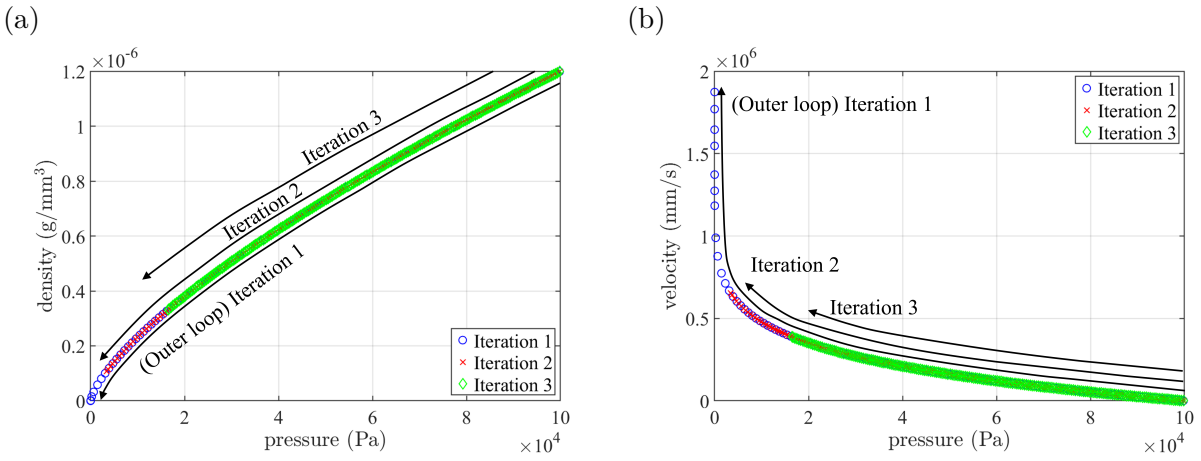

Figure 5.4: Integration trajectories through the 1-wave of the example Riemann problem in three successive outer loop iterations.

Algorithm 1: Numerical integration of (5.41) and (5.42) with a stored trajectory.

Input: Start point $\{p_K, \rho_K, u_K\}$, end point $p^* < p_K$, and step size Δp.
Stored trajectory $\boldsymbol{\chi}$, with N denoting its size.

Step 1: Reset the start point based on the stored trajectory $\boldsymbol{\chi}$:
for $s = N,\ N-1,\ \cdots,\ 1$ **do**
  if $p^* \le p_s$ **then**
    $\{p^{(0)}, \rho^{(0)}, u^{(0)}\} \leftarrow \{p_s, \rho_s, u_s\}$ ▷ reuse the stored trajectory
    $\Delta p \leftarrow \min(\Delta p, p_s - p^*)$
    break
  end
end
Step 2: Integrate, and update the stored trajectory
$i \leftarrow 0$
while $p^{(i)} > p^*$ **do**
  $\Delta p \leftarrow \min(\Delta p,\ p^{(i)} - p^*)$
  $\left\{p^{(i+1)}, \rho^{(i+1)}, u^{(i+1)}\right\} \leftarrow \mathcal{I}\left(\left\{p^{(i)}, \rho^{(i)}, u^{(i)}\right\}, \Delta p\right)$ ▷ integrate one step by RK4
  if $p^{(i+1)} < p_N$ **then**
    $N \leftarrow N + 1$
    $\{p_N, \rho_N, u_N\} \leftarrow \left\{p^{(i+1)}, \rho^{(i+1)}, u^{(i+1)}\right\}$ ▷ add new point to $\boldsymbol{\chi}$
  end
  $i \leftarrow i + 1$
end
Output: $\rho_K^* = \rho^{(i)}$, $u_K^* = u^{(i)}$, and $\boldsymbol{\chi}$

redundant calculations as much as possible. In Step 2, we perform the numerical integration, and expand $\boldsymbol{\chi}$ with new points obtained on the isentrope.

It is possible that both the 1-wave and the 3-wave are rarefactions. Therefore, two separate trajectories, namely $\boldsymbol{\chi}_l$ and $\boldsymbol{\chi}_r$, should be constructed.

Consider the same example problem shown in Fig. 5.4. If we apply Algorithm 1, iterations 2 and 3 can be completed in one integration step (Fig. 5.5), as opposed to hundreds. This leads to a significant reduction of computational cost.

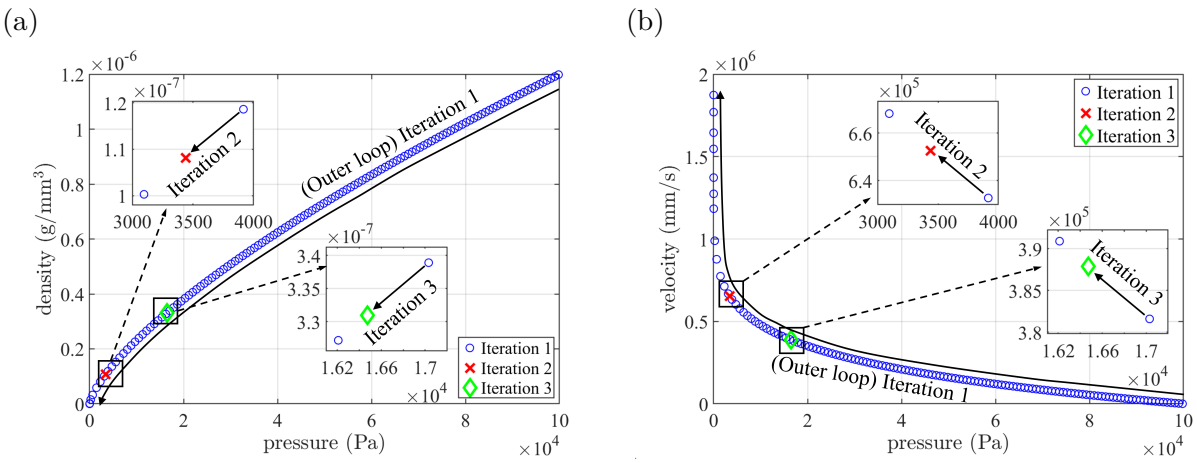

Figure 5.5: Integration trajectories in three successive outer loop iterations, with Algorithm 1.

5.3.4 Adaptive step size

The accuracy and cost of the numerical integration performed in Step 2 of Algorithm 1 depend heavily on the step size, Δp. When a user solves a small number of Riemann problems one by one, it may be possible to specify an appropriate step size for each problem based on the user's experience. Nonetheless, when exact Riemann problems are constructed and solved in 2D and 3D multi-material simulations, manually specifying an integration step size for each Riemann problem is impossible. A common practice is to specify a fixed

number of integration steps for all the exact Riemann problems constructed throughout the simulation (e.g., [17, 28, 66]). Clearly, this is not optimal from both accuracy and efficiency standpoints. For different Riemann problems, the number of integration steps required to achieve a certain degree of accuracy varies with the EOS and the integration interval. Moreover, for each Riemann problem, applying a constant Δp through the entire rarefaction fan is also problematic, as $\rho(p)$ and $u(p)$ are often highly nonlinear. Their slopes may change rapidly through a rarefaction. For example, in the case shown in Fig. 5.4(b), the slope of $u(p)$ varies by 6 orders of magnitude — from -2 mm/(s Pa) to -4×10^6 mm/(s Pa) — along the trajectory.

To resolve this issue, we propose to apply the adaptive Runge-Kutta methods, which automatically adjust the step size based on the local, single-step error of the integration. This method (Algorithm 2) is described in Fig. 5.6 in the form of a flowchart. Here, we apply the Runge-Kutta-Fehlberg method [20] as an example, which embeds a fourth-order formulation inside a fifth-order one. The difference between the fourth- and fifth-order results serves as an approximation of the local error. Applying this method to (5.41) and (5.42), the fourth-order integration formulas for density and velocity are given by

$$\rho^{(i+1)}_{\text{4th order}} = \rho^{(i)} + \left(\frac{2825}{27,648}\frac{1}{\hat{c}_1^2} + \frac{18,575}{48,384}\frac{1}{\hat{c}_3^2} + \frac{13,525}{55,296}\frac{1}{\hat{c}_4^2} + \frac{277}{14,336}\frac{1}{\hat{c}_5^2} + \frac{1}{4}\frac{1}{\hat{c}_6^2}\right)\Delta p^{(i)}, \tag{5.44}$$

$$u^{(i+1)}_{\text{4th order}} = u^{(i)} \mp \left(\frac{2825}{27,648}\frac{1}{\hat{\rho}_1\hat{c}_1} + \frac{18,575}{48,384}\frac{1}{\hat{\rho}_3\hat{c}_3} + \frac{13,525}{55,296}\frac{1}{\hat{\rho}_4\hat{c}_4} + \frac{277}{14,336}\frac{1}{\hat{\rho}_5\hat{c}_5} + \frac{1}{4}\frac{1}{\hat{\rho}_6\hat{c}_6}\right)\Delta p^{(i)}. \tag{5.45}$$

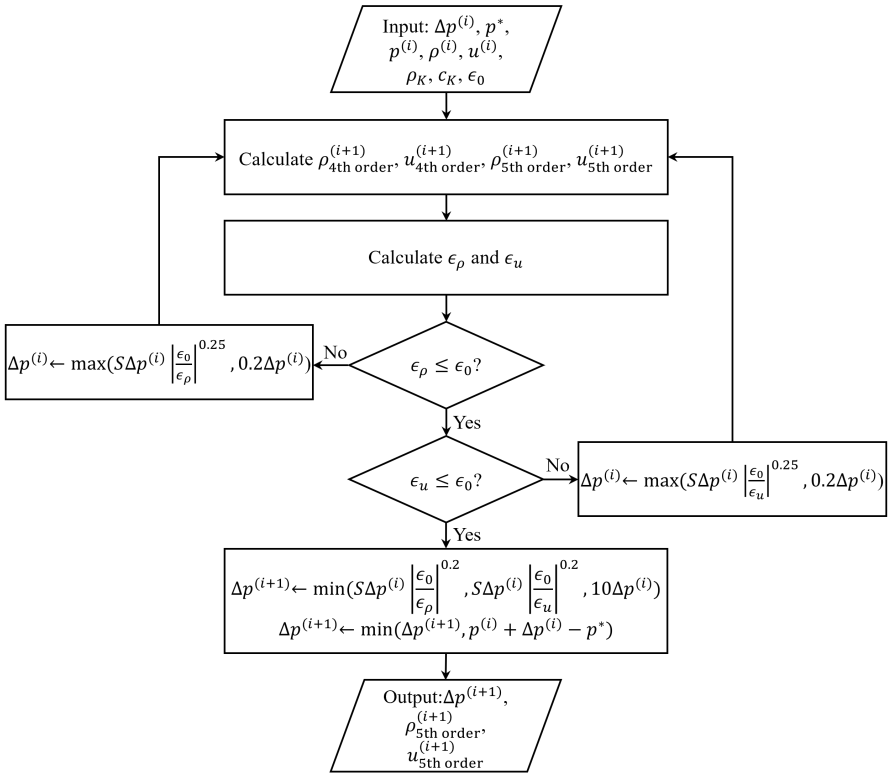

Figure 5.6: Algorithm 2: One step of numerical integration through a rarefaction fan with adaptive step size.

Similarly, the fifth-order integration formulas are given by

$$\rho^{(i+1)}_{\text{5th order}} = \rho^{(i)} + \left(\frac{37}{378}\frac{1}{\hat{c}_1^2} + \frac{250}{621}\frac{1}{\hat{c}_3^2} + \frac{125}{594}\frac{1}{\hat{c}_4^2} + \frac{512}{1771}\frac{1}{\hat{c}_6^2}\right)\Delta p^{(i)}, \tag{5.46}$$

$$u^{(i+1)}_{\text{5th order}} = u^{(i)} \mp \left(\frac{37}{378}\frac{1}{\hat{\rho}_1\hat{c}_1} + \frac{250}{621}\frac{1}{\hat{\rho}_3\hat{c}_3} + \frac{125}{594}\frac{1}{\hat{\rho}_4\hat{c}_4} + \frac{512}{1771}\frac{1}{\hat{\rho}_6\hat{c}_6}\right)\Delta p^{(i)}. \tag{5.47}$$

In (5.45) and (5.47), the minus sign applies to the 1-wave, and the plus sign applies to the 3-wave. $\hat{c}_i$ and $\hat{\rho}_i$ $(i = 1, 2, \cdots, 6)$ are sound speed and density evaluated at intermediate

stages, specifically,

$$
\begin{aligned}
\hat{c}_1 &= c_K\left(p^{(i)},\ \hat{\rho}_1\right),\ \text{with } \hat{\rho}_1 = \ \rho^{(i)},\\
\hat{c}_2 &= c_K\left(p^{(i)}+\frac{1}{5}\Delta p^{(i)},\ \hat{\rho}_2\right),\ \text{with } \hat{\rho}_2 = \ \rho^{(i)}+\frac{1}{5}\frac{1}{\hat{c}_1^2}\Delta p^{(i)},\\
\hat{c}_3 &= c_K\left(p^{(i)}+\frac{3}{10}\Delta p^{(i)},\ \hat{\rho}_3\right),\ \text{with } \hat{\rho}_3 = \ \rho^{(i)}+\frac{3}{40}\frac{1}{\hat{c}_1^2}\Delta p^{(i)}+\frac{9}{40}\frac{1}{\hat{c}_2^2}\Delta p^{(i)},\\
\hat{c}_4 &= c_K\left(p^{(i)}+\frac{3}{5}\Delta p^{(i)},\ \hat{\rho}_4\right),\ \text{with } \hat{\rho}_4 = \ \rho^{(i)}+\frac{3}{10}\frac{1}{\hat{c}_1^2}\Delta p^{(i)}-\frac{9}{10}\frac{1}{\hat{c}_2^2}\Delta p^{(i)}+\frac{6}{5}\frac{1}{\hat{c}_3^2}\Delta p^{(i)},\\
\hat{c}_5 &= c_K\left(p^{(i)}+\Delta p^{(i)},\ \hat{\rho}_5\right),\ \text{with } \hat{\rho}_5 = \ \rho^{(i)}-\frac{11}{54}\frac{1}{\hat{c}_1^2}\Delta p^{(i)}+\frac{5}{2}\frac{1}{\hat{c}_2^2}\Delta p^{(i)}-\frac{70}{27}\frac{1}{\hat{c}_3^2}\Delta p^{(i)}+\frac{35}{27}\frac{1}{\hat{c}_4^2}\Delta p^{(i)},\\
\hat{c}_6 &= c_K\left(p^{(i)}+\frac{7}{8}\Delta p^{(i)},\ \hat{\rho}_6\right),\ \text{with } \hat{\rho}_6 = \ \rho^{(i)}+\frac{1631}{55,296}\frac{1}{\hat{c}_1^2}\Delta p^{(i)}+\frac{175}{512}\frac{1}{\hat{c}_2^2}\Delta p^{(i)}+\frac{575}{13,824}\frac{1}{\hat{c}_3^2}\Delta p^{(i)}+\\
&\quad \frac{44,275}{110,592}\frac{1}{\hat{c}_4^2}\Delta p^{(i)}+\frac{253}{4096}\frac{1}{\hat{c}_5^2}\Delta p^{(i)}.
\end{aligned}
\tag{5.48}
$$

The coefficients utilized in the above formulas were developed by Cash and Karp [10]. They allow the intermediate stages involved in the fourth-order formula to be re-used in the fifth-order one.

We normalize the errors in density and velocity using the initial state, i.e.,

$$\epsilon_\rho = \left|\frac{\rho^{(i+1)}_{\text{4th order}}-\rho^{(i+1)}_{\text{5th order}}}{\rho_K}\right|+\tilde{\epsilon}, \tag{5.49}$$

$$\epsilon_u = \left|\frac{u^{(i+1)}_{\text{4th order}}-u^{(i+1)}_{\text{5th order}}}{c_K}\right|+\tilde{\epsilon}, \tag{5.50}$$

where ρ_K and c_K are density and sound speed in the initial state. Because ϵ_ρ and ϵ_ρ will appear in the denominator, a small positive number, $\tilde{\epsilon}$, is added to avoid division by zero. In all the numerical tests presented in this paper, it is set to 1×10^{-30}. Then, the integration step size Δp is adjusted according to the two errors and an error tolerance ϵ_0. For example,

a new step size, Δp^*, can be calculated based on the density error, ϵ_ρ, by

$$\Delta p^* = S \cdot \Delta p^{(i)} \cdot \left(\frac{\epsilon_0}{\epsilon_\rho}\right)^\alpha. \tag{5.51}$$

Here, $S \in (0, 1)$ is introduced as a safety factor, because ϵ_ρ is only an estimate of the true error. In this work, we set $S = 0.9$, following [11]. α is set to 0.2 if $\epsilon_\rho \leq \epsilon_0$, and 0.25 otherwise [11].

If $\epsilon_\rho \leq \epsilon_0$, we set

$$\Delta p^{(i+1)} = \Delta p^*, \tag{5.52}$$

and move on to examine the error in velocity (Fig. 5.6). If $\epsilon_\rho > \epsilon_0$, we repeat step i with a smaller step size, i.e.

$$\Delta p^{(i)} = \Delta p^*. \tag{5.53}$$

Following [46], we cap the variation of Δp within one step at a factor of 10 for increase, and a factor of 5 for decrease. Next, the same procedure is applied to update Δp using the velocity error ϵ_u, as shown in Fig. 5.6.

To apply the adaptive step size within Algorithm 1, we note that the input Δp in Algorithm 1 becomes $\Delta p^{(0)}$. It does not need to be determined precisely, as the actual step size will be calculated automatically in each integration step. In practice, we set $\Delta p^{(0)}$ to be a small number to avoid the repetition of the first integration step (i.e., $i = 0$). Because of step size adaptation, every point (i.e., $\{p_s \mid s \in [1, N]\}$) stored on the integration trajectory $\boldsymbol{\chi}$ is quality checked in terms of accuracy. The stored step sizes (e.g., $p_s - p_{s+1}$) automatically satisfy the requirement on local accuracy. This fact can be utilized to determine the new initial step size $\Delta p^{(0)}$ when we reset the integration start point. If the new start point p_s is not the last stored point on $\boldsymbol{\chi}$, the inequality $p_s > p^* > p_{s+1}$ must hold. This means the

new initial step size $\Delta p^{(0)}$ can be set by

$$\Delta p^{(0)} \leftarrow p_s - p^*. \tag{5.54}$$

In this way, the new integration is completed in only one step while satisfying accuracy requirements. If the new start point p_s is the last stored point on $\boldsymbol{\chi}$, we set the new initial step size to

$$\Delta p^{(0)} \leftarrow \min\left(p_{s-1} - p_s, p_s - p^*\right). \tag{5.55}$$

Therefore, (5.54) and (5.55) are used to replace line 5 in Algorithm 1 when adaptive step size is applied.

Repeating the solution of the Riemann problem given in (5.43) with adaptive integration step size gives Fig. 5.7. Comparing with the result shown in Fig. 5.4, the advantage brought by the adaptive step size is clear. Smaller step sizes are applied near the left end, where the slopes of $\rho(p)$ and $u(p)$ vary rapidly. At the right end, although the starting step size, $\Delta p^{(0)}$ is small, the algorithm is able to quickly increase its value to adapt to the slow variation of slopes.

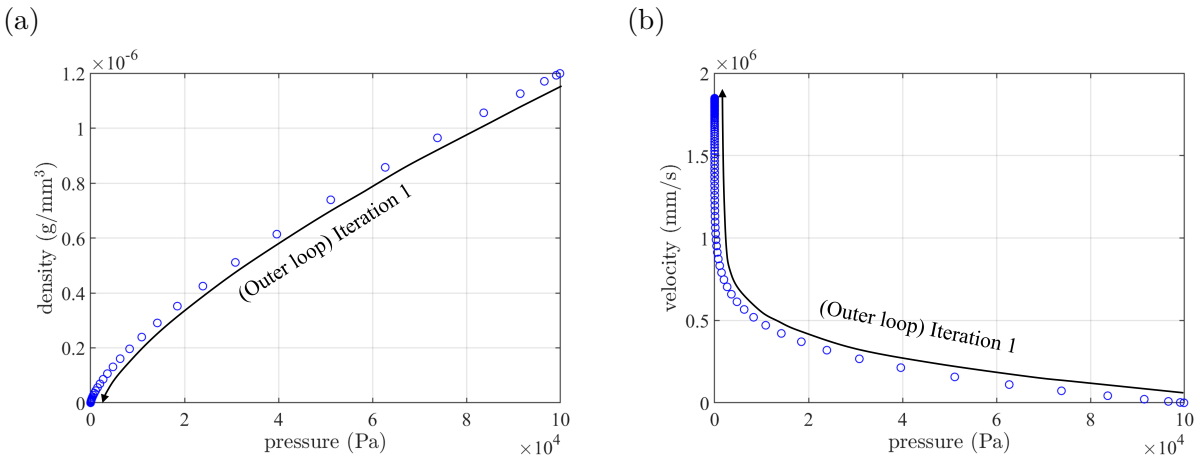

Figure 5.7: Repetition of iteration 1 in Fig. 5.4 with adaptive step size.

5.3.5 Obtaining initial guesses using R-tree data structure

The computational cost of exact Riemann problem solution depends on the number of iterations performed in the outer loop (Fig. 5.3). When the error tolerance is fixed, the number of iterations is largely determined by the quality of the initial guesses. A popular method to specify initial guesses is to apply the linear acoustic theory [31]. Assuming that two initial guesses are needed, such as in the Secant method, the first one, $p^{*(0)}$, is given by

$$p^{*(0)} = \left[C_r p_l + C_l p_r + C_l C_r \left(u_l - u_r\right)\right] / \left(C_l + C_r\right), \tag{5.56}$$

where l and r refer to the two materials, c denotes the sound speed, and $C = \rho c$. The second initial guess, $p^{*(1)}$, is obtained by applying a different sound speed. Specifically,

$$p^{*(1)} = \left[\overline{C}_r p_l + \overline{C}_l p_r + \overline{C}_l \overline{C}_r \left(u_l - u_r\right)\right] / \left(\overline{C}_l + \overline{C}_r\right), \tag{5.57}$$

where $\overline{C}_K$ $(K = l, r)$ is given by

$$\overline{C}_K = \begin{cases} \left|p^{*(0)} - p_K\right| / \left|u_K^{*(0)} - u_K\right| & \text{if} \quad u_K^{*(0)} \neq u_K, \\ \rho_K c_K & \text{if} \quad u_K^{*(0)} = u_K. \end{cases} \tag{5.58}$$

Here, $u_K^{*(0)}$ denotes the velocity obtained with pressure $p^{*(0)}$.

When the Riemann problem is highly nonlinear, the initial guesses obtained using the linear acoustic theory may not be close to the true solution. To mitigate this issue, we introduce another method based on storing and reusing the solutions of previously solved Riemann problems. The motivation of this data-based method is that in the course of a multi-material simulation, a large number of bimaterial Riemann problems are constructed and solved. Some of them may have similar inputs, hence similar solutions. As an example, Fig. 5.8

visualizes the Riemann problems solved in the simulation presented in Sec. 5.4.3, within 10 time steps. Some clusters can be easily identified in this data set. Our basic idea is to store the solutions of solved exact Riemann problems using an efficient data structure, and to generate the initial guesses for a new problem through nearest neighbor search.

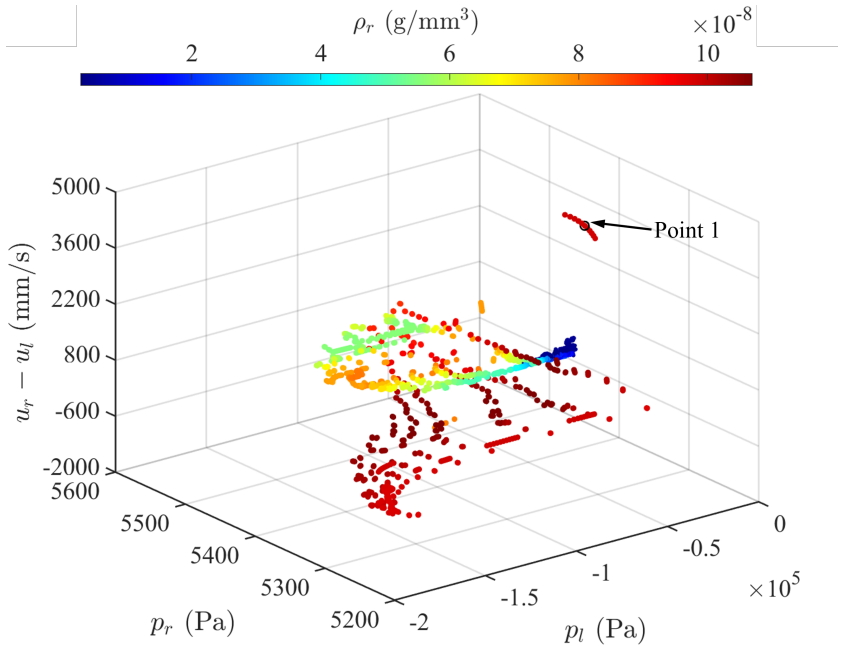

Figure 5.8: Visualization of the bimaterial Riemann problems solved in the simulation presented in Sec. 5.4.3 during 10 time steps. This 5D data set is displayed with p_l, p_r, and $u_r - u_l$ as the three spatial coordinates. The color of each data point indicates the value of ρ_r, and the size of the point indicates the value of ρ_l. "Point 1" is used to demonstrate the initial guess improvement from the nearest neighbor search.

Notably, the bimaterial Riemann problem is 5D, with $(\rho_l, p_l, \rho_r, p_r, u_r - u_l)$ as the independent variables. Also, this data set needs to be frequently updated and accessed. For these reasons, we adopt the R-tree data structure, which is specifically designed for efficient indexing and searching of multidimensional data [22, 42].

Unlike the idea of constructing a sparse grid before each simulation [17], the R-tree data set is designed to be constructed during the simulation (i.e., "on the fly"). Specifically, this method involves three components.

- **Construction of R-tree.** In the course of a simulation, after solving each bimaterial Riemann problem, we pair the solution p^* with the corresponding 5D inputs, and insert the pair into the R-tree.

- **Normalization of the five (5) coordinates.** The 5 coordinates of the database represent density, pressure, and velocity. Their numerical values often differ by several orders of magnitudes, depending on their units (e.g., see Fig. 5.8). Directly performing nearest-neighbor search on these dimensional coordinates is problematic, as the evaluation of distance would be biased towards coordinates with larger numerical values. Therefore, we normalize the 5 coordinates using a lower bound and an upper bound, so that each normalized, non-dimensional coordinate varies between 0 and 1.

- **Nearest-neighbor search.** Once a new Riemann problem is constructed, we apply a bounding-box based nearest-neighbor search algorithm [12, 49] to find the data point in the R-tree whose inputs are closest to the new Riemann problem. Its solution, p^*, is taken as the first initial guess for solving the new Riemann problem. The second initial guess, if needed, can be obtained either by Eq. (5.57) or by applying a perturbation to the first initial guess.

Consider the same example problem shown in Fig. 5.8. In this figure, Point 1 marks a new Riemann problem that is constructed during the simulation. Table 5.2 shows the state variables — including both the 5 inputs and the solution p^* — at this point and its nearest neighbor in the existing R-tree. Clearly, the two points are close to each other. Using the solution at the nearest neighbor as the first initial guess, it takes only 1 iteration to solve the new Riemann problem at Point 1. In comparison, it takes 8 iterations to converge to the same error tolerance, if the first initial guess is generated using the linear acoustic theory, i.e., by (5.56).

Table 5.2: Comparison of the state variables at Point 1 in Fig. 5.8 and its nearest neighbor in the R-tree.

	ρ_l (g/mm^3)	p_l (Pa)	ρ_r (g/mm^3)	p_r (Pa)	$u_r - u_l$ (mm/s)	p^* (Pa)
Point 1	9.9628×10^{-4}	-4.4378×10^4	9.8425×10^{-8}	5.3338×10^3	4.3761×10^3	5.21797×10^3
Nearest neighbor	9.9628×10^{-4}	-4.4266×10^4	9.8425×10^{-8}	5.3338×10^3	4.3757×10^3	5.21798×10^3

This work utilizes the R-tree data structure implemented in the widely used Boost Generic Geometry Library [1]. In particular, the insertion of data points, query of the nearest neighbor, and searching of the lower and upper bounds for normalization are performed by built-in functions in the Boost library. More details about the creating, modifying and using R-tree data structure in Boost library can be found in [1]. For the numerical experiments in Sec. 5.4, we store the Riemann problems solved in the previous time step, and perform the normalization at the beginning of each time step.

In summary, Fig. 5.9 presents the new algorithm for solving an exact bimaterial Riemann problem, which incorporates the acceleration methods presented in Sec. 5.3.2, 5.3.3, 5.3.4, and 5.3.5.

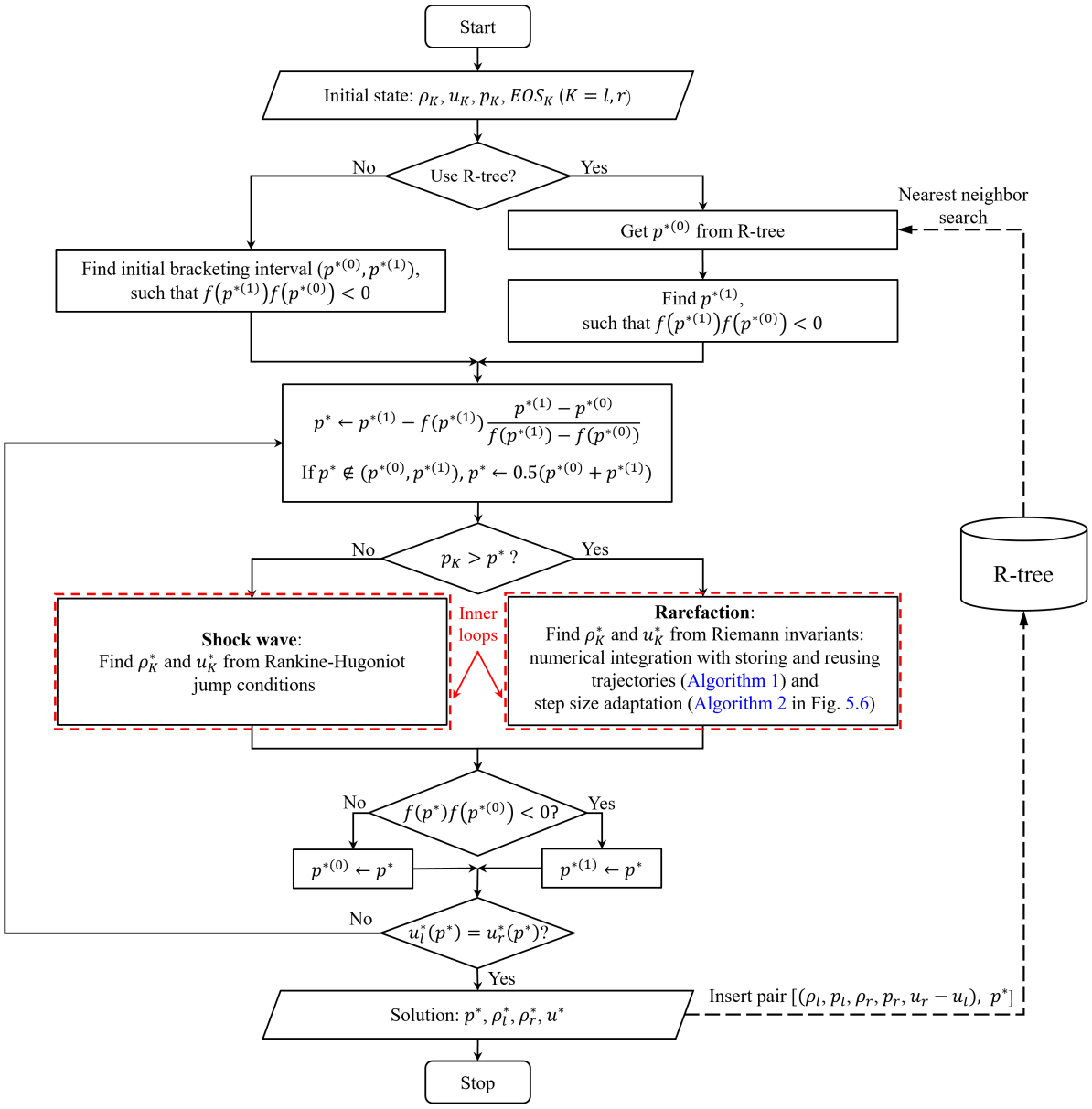

Figure 5.9: Improved solution procedure for bimaterial Riemann problems in multi-material flow simulaitons.

5.4 Numerical experiments

We assess the performance of the acceleration methods presented in Sec. 5.3.2 - 5.3.5 using four example problems that involve multiple (2 or 3) materials and significant discontinuities

across their interfaces. For conciseness, the four acceleration methods are referred to as Methods 1 to 4 in this section.

- Method 1: Change of integration variable (Sec. 5.3.2).
- Method 2: Storing and reusing integration trajectory data (Sec. 5.3.3).
- Method 3: Adaptive step size (Sec. 5.3.4).
- Method 4: Obtaining initial guesses using R-tree data structure (Sec. 5.3.5).

The simulations presented in this section are performed using the M2C (Multiphysics Modeling and Computation) solver [2] and the Tinkercliffs computer cluster at Virginia Tech. A standalone version of the exact Riemann problem solver is available at [3].

5.4.1 One-dimensional benchmark problem

The 1D bimaterial Riemann problem defined by (5.43) is solved numerically using the FIVER method described in Sec. 5.2.3. This problem models a condensed phase (soda lime glass) moving away from a gas (air) at high speed (400 m/s). The exact solution is used to verify the numerical solver. At any time $t > 0$, density jumps by 4 orders of magnitude across the material interface, from 0.3 kg/m^3 to 2203.98 kg/m^3. Therefore, this example problem also challenges the robustness of the solver.

To separate the effects of different acceleration methods, we perform four simulations in which the exact Riemann problems constructed during the simulation are solved using different methods.

- Simulation (i): using the baseline method presented in Sec. 5.3.1;

- Simulation (ii): with acceleration Methods (1) and (2);
- Simulation (iii): with acceleration Methods (1), (2), and (3); and
- Simulation (iv): with acceleration Methods (1), (2), (3), and (4).

The computational domain extends from $x = 0$ to 1.0 mm. The material interface is initially at $x = 0.2$ mm. 200 rectangular elements are used to discretize the domain. In Simulations (iii) and (iv), the error tolerance for controlling the adaptive step size (Eqs. (5.49) and (5.50)) is set to 1.0×10^{-9}. In Simulations (i) and (ii), we need to specify a fixed number of integration steps. To have a fair comparison in terms of solution accuracy, we set the number of integration steps to be the maximum integration steps required in (iii) to reach the error tolerance, which is $5,307$.

The density, pressure, and velocity results obtained from Simulation (iv) at $t = 0.15$ μs are shown in Fig. 5.10, in comparison with the exact solution. For all the three variables, the simulation result matches closely the exact solution. The results obtained from Simulations (i), (ii), and (iii) are essentially the same as that from Simulation (iv), as the acceleration methods do not introduce new approximations. Therefore, their results are not shown separately. Figure 5.11 compares the computational cost of the four simulations up to $t = 0.15$ μs. Here, we measure the computation time for evaluating the advective fluxes, which includes two parts: the time spent on solving the exact Riemann problems at the material interface, and the time spent on evaluating the numerical flux functions (LLF in this case) over the entire domain. The effect of the acceleration methods is found to be significant. When all the four methods are adopted (i.e., in Simulation (iv)), the time consumed by the exact Riemann solver is reduced by a factor of 37.6 compared to the baseline simulation (from 4.32 s to 0.123 s) . The total computation time for evaluating the advective fluxes is also significantly reduced, by a factor of 17.8 (from 4.46 s to 0.26 s). Comparing the computation

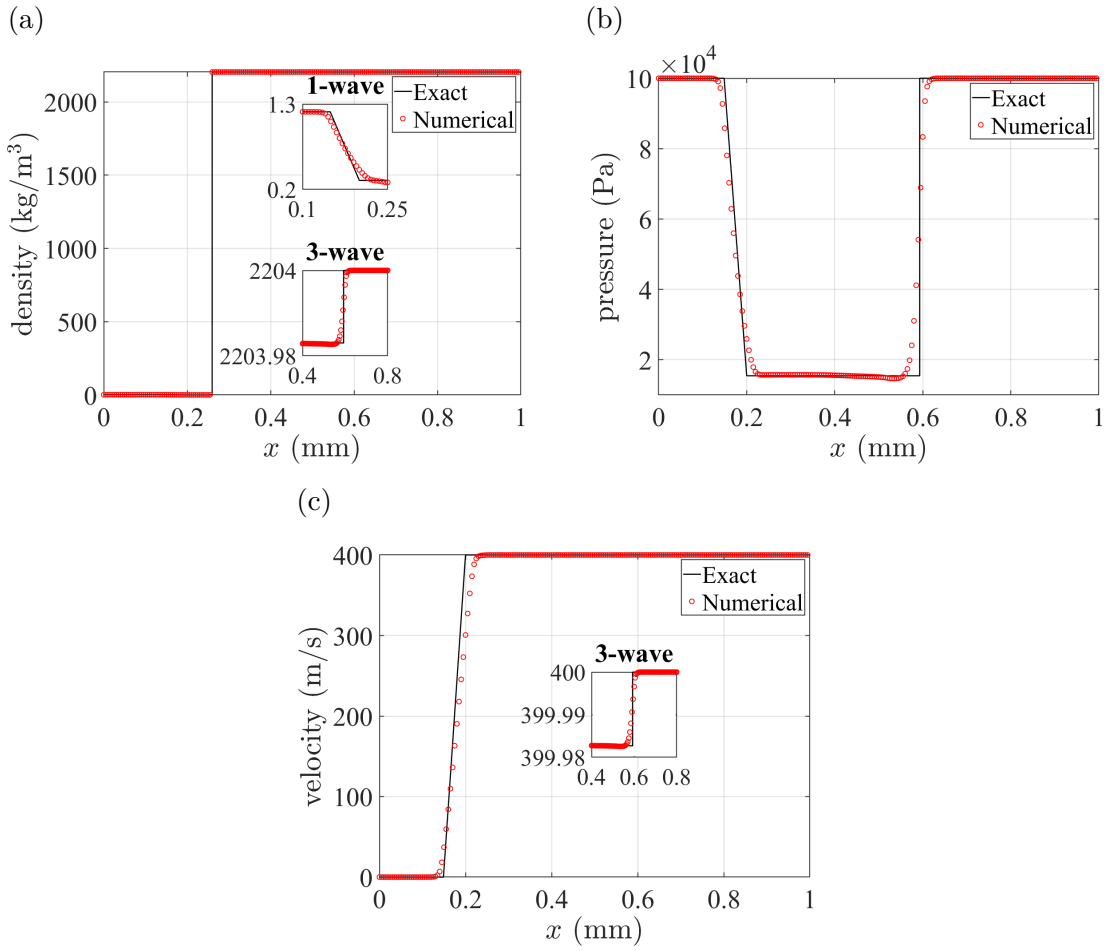

Figure 5.10: A 1D bimaterial Riemann problem: Density, pressure, and velocity distributions at $t = 0.15$ μs.

times of Simulations (iii) and (iv), it can be observed that searching for the initial guesses from the R-tree reduces the cost of exact Riemann problem solutions by about 70%. This reduction can be explained by Fig. 5.12, which shows the number of integration steps in the first 200 time steps. At each time step, because the initial guesses provided by the R-tree are closer to the true solution, the integration interval is shorter in Simulation (iv), which leads to a smaller number of integration steps. The computational overhead associated with updating, normalizing, and accessing the R-tree is found to be less than 10% of the time spent on solving the exact Riemann problems. This overhead is acceptable, as expected.

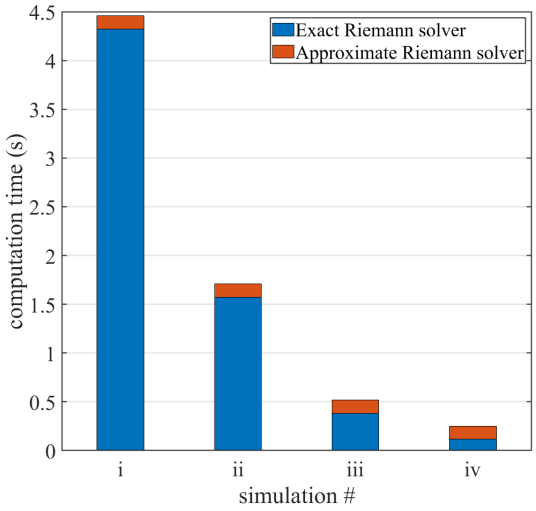

Figure 5.11: A 1D bimaterial Riemann problem: Comparison of the flux computation time of different simulations.

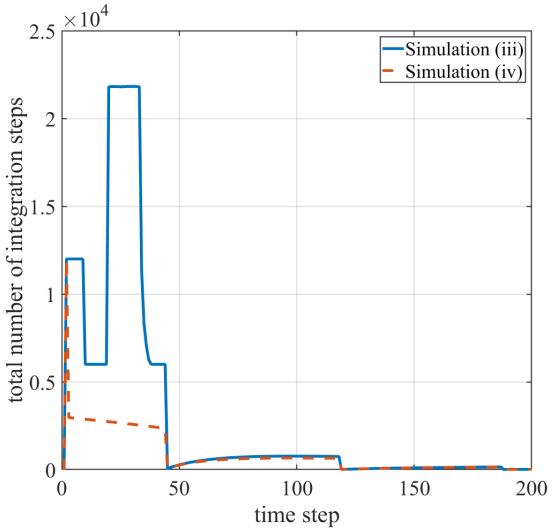

Figure 5.12: A 1D bimaterial Riemann problem: Effect of R-tree on the total number of integration steps.

5.4.2 Underwater explosion

We simulate the expansion of a high-pressure gas bubble in a liquid, which can be viewed as a model problem for underwater explosion. Following [53], we specify a bubble with radius $r = 0.2$ at $t = 0$. The (non-dimensional) initial conditions inside and outside the bubble are

given by

$$(\rho, u, p, EOS) = \begin{cases} (0.991, 0, 3.059 \times 10^{-4}, \text{stiffend gas}) & \text{liquid phase, outside the bubble,} \\ (1.241, 0, 2.753, \text{stiffened gas}) & \text{gas phase, inside the bubble.} \end{cases} \tag{5.59}$$

The parameters in the stiffened gas EOS, i.e., Eq. (5.7), are $\gamma = 5.5$, $e_c = 0$, $b = 0$ and $p_c = 1.505$ for the liquid phase, and $\gamma = 1.4$, $e_c = 0$, $b = 0$, and $p_c = 0$ for the gas phase. The Euler equations are solved, which means in Eq. (5.1), $\boldsymbol{\mathcal{S}} = \mathbf{0}$. The computational domain is 2D, extending from 0.0 to 1.0 in both x and y directions. It is discretized by a uniform, 500×500 grid. The Roe's flux function is adopted to compute the advective fluxes. Again, the four simulations designed in Sec. 5.4.1 are performed for this problem. All the simulations are parallelized to run on 256 CPU cores. Same as in the previous case, the error tolerance for adaptive step size control is set to 1.0×10^{-9} in Simulations (iii) and (iv). Reaching this tolerance requires up to $1,092$ integration steps. This number is then specified as the fixed number of integration steps in Simulations (i) and (ii), in order to ensure the same level of accuracy.

The results obtained from the four simulations are essentially the same, as the acceleration methods do not introduce new approximations. As an example, Fig. 5.13 shows the result of Simulation (iv) at $t = 0.058$. In this figure, Subfigures (a) and (b) visualize the density and pressure fields. Subfigures (c) and (d) plot the same solution fields along the horizontal centerline of the computational domain, in comparison with the results given in [53]. For both density and pressure, the present result is in close agreement with the reference. The liquid-gas interface, the outgoing shock wave, and the incoming rarefaction fan are all captured accurately. Figure 5.14 shows the computational cost of exact Riemann problem solutions within the first 200 time steps, when the exact Riemann problems are highly nonlinear. After storing and reusing the integration trajectories (i.e., Simulation (ii)), the cost of

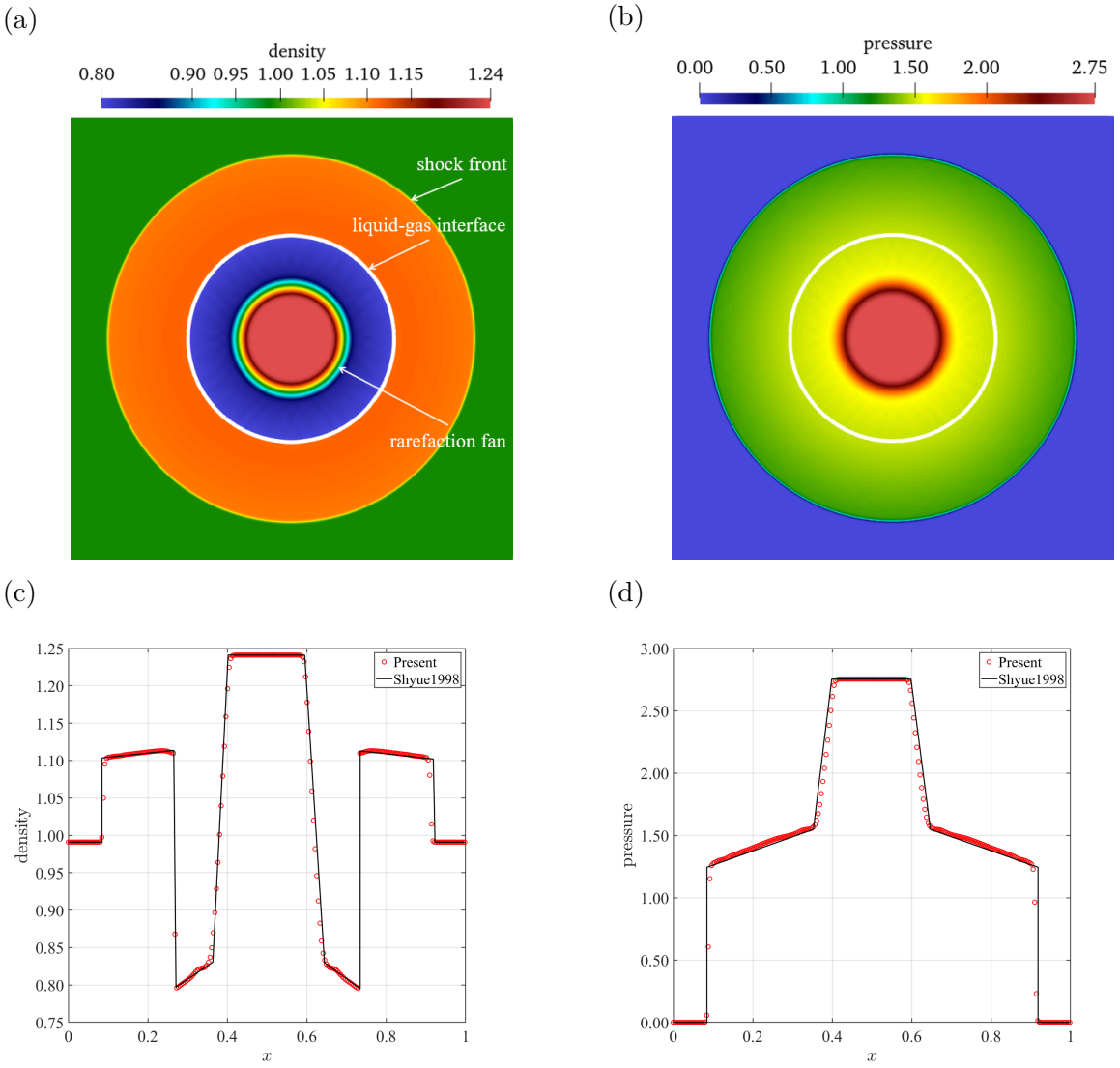

Figure 5.13: Underwater explosion: simulation results at $t = 0.058$. (a) density filed, (b) pressure filed, (c) density along the horizontal symmetric axis, (d) pressure along the horizontal symmetric axis.

numerical integration becomes trivial after the first iteration in the outer loop. As a result, the computation time is reduced by a factor of 3 (9 s vs. 29 s), compared to the baseline Simulation (i). After adopting step size adaptation (i.e., Simulation (iii)), the computation time is further reduced by 34%, because fewer integration steps are needed. Comparing the costs of Simulations (iii) and (i), it is found that the first three acceleration methods, when

combined together, provides a 5-fold cost reduction. By obtaining the initial guesses from R-tree (i.e., Simulation (iv)), however, the computational cost increases slightly by 0.86% compared to Simulation (iii). This is because the reduction in Riemann problem solution time is offset by the computational overhead associated with updating and maintaining the R-tree. Specifically, the Riemann problem solution time is reduced by 10.35% compared to Simulation (iii), but the computational overhead amounts to 11.21%. The benefit brought by the R-tree is less significant than in the previous case. This can be attributed to the fact that the density jump across the material interface is less than a factor of 2 in this case, while it was 4 orders of magnitude in the previous case. Overall, we have found that unless the density and EOS across the material interface are extremely different, the initial guesses provided by the R-tree may not be significantly better than those obtained by the linear acoustic theory. For this reason, Simulation (iv) is excluded from the subsequent test cases, except one in Sec. 5.4.4, where the R-tree's benefits overtake its cost due to the significant discontinuity across the material interface. Furthermore, Fig. 5.15 compares the computa-

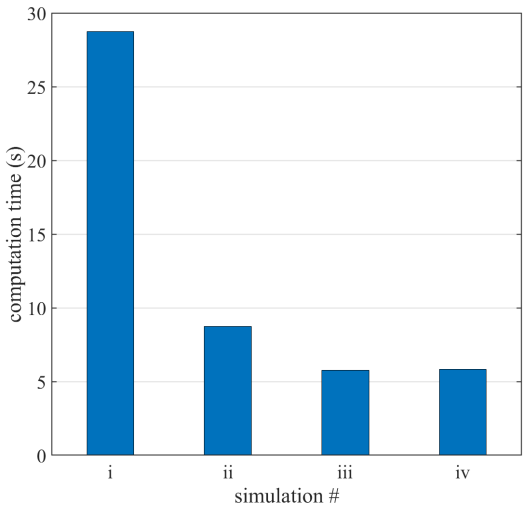

Figure 5.14: Underwater explosion: Computational cost of exact Riemann problem solutions in the first 200 time steps.

tion time of Simulations (i)(ii)(iii) up to $t = 0.058$, or $13,029$ time steps. It can be observed

that when acceleration Methods (1), (2), and (3) are applied, the solution of exact Riemann problems is accelerated by 45 times (from 808 s to 18 s). The total time on advective flux computation is reduced by a factor of 22 (from 822 s to 37 s).

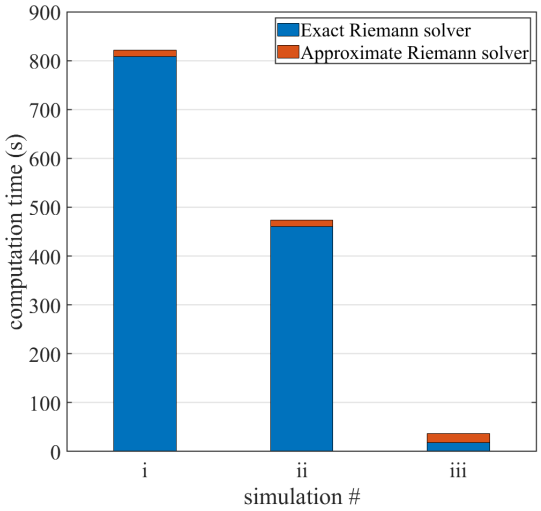

Figure 5.15: Underwater explosion: Comparison of the flux computation time of different simulations.

In the aforementioned simulations, the gas inside the bubble is modeled using the stiffened gas EOS, following the example problem described in [53]. In general, the thermodynamics of gaseous explosion products can be better described using the JWL EOS (5.9). Compared to stiffened gas, the JWL EOS is highly nonlinear as it involves exponential functions. Also, ρ can no longer be solved analytically from p and e. Instead, an iterative numerical method is needed. To further assess the performance of the acceleration methods, we perform another set of simulations in which the gas inside the bubble is modeled using the JWL EOS. Its parameters are set by $\omega = 0.28$, $A_1 = 37.12$, $A_2 = 0.323$, $R_1 = 4.15$, $R_2 = 0.95$, and $\rho_0 = 1.241$, so that the results are comparable with those obtained using the stiffened gas EOS. Figure 5.16 shows the density and pressure distributions at $t = 0.058$ along the horizontal centerline of the computational domain. Figure 5.17 shows the performance of the accelerated

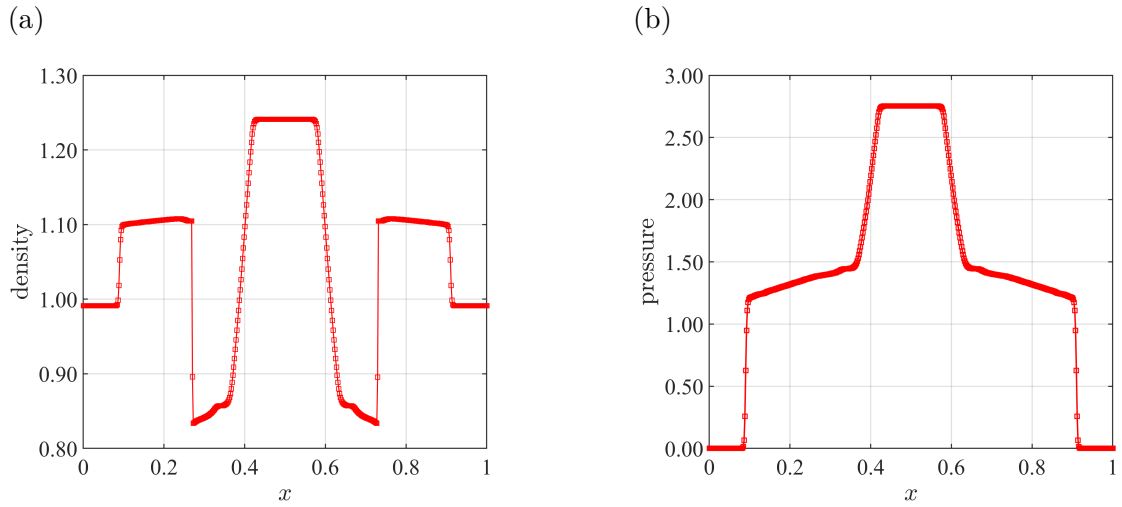

Figure 5.16: Underwater explosion with the JWL EOS: Simulation result at $t = 0.058$, along the horizontal centerline of the computational domain.

Riemann problem solver, in the presence of the JWL EOS. Again, the computation time is calculated up to $t = 0.058$. Comparing with Fig. 5.15, it is clear that the JWL EOS leads to a higher computational cost. The effect of the acceleration methods is even more significant. When Methods (1), (2), and (3) are combined (i.e., Simulation (iii)), the solution of exact Riemann problems is accelerated by 76 times (39 s vs. $2,963$ s). As a result, the total cost of flux computation is reduced by a factor of 38 (80 s vs. $2,994$ s).

5.4.3 Laser-induced cavitation

Next, we assess the performance of the acceleration methods using an example problem of cavitation induced by a long-pulse laser, first presented in [66]. A Holmium:YAG laser with a 2.12×10^{-3} mm wavelength, a 10.2 μs pulse duration, and a peak power of 2.854 kW is considered. The cylindrical laser fiber has a radius of 0.1825 mm, and is placed within a water tank. The energy of the laser pulse is high enough to vaporize a small volume of liquid water in front of the laser fiber, thereby generating a vapor bubble. The two-phase

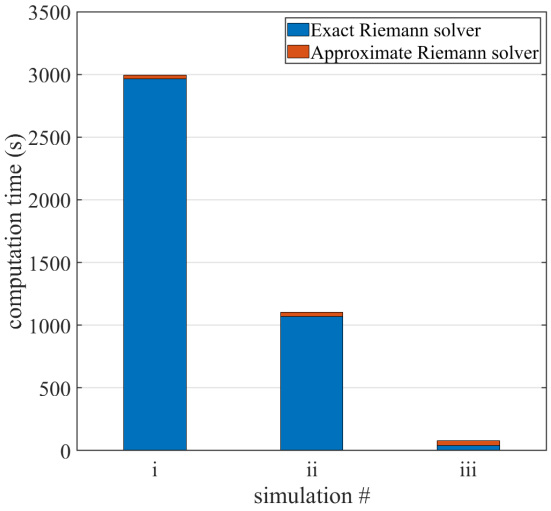

Figure 5.17: Underwater explosion with the JWL EOS: Comparison of the flux computation time of different simulations.

liquid-vapor flow is modeled as a compressible and inviscid flow. A radiative heat source is added to the energy conservation equation. Therefore, the term $\boldsymbol{\mathcal{S}}$ in (5.1) has the form

$$\boldsymbol{\mathcal{S}} = \begin{bmatrix} 0 \\ \mathbf{0} \\ -\nabla \cdot \boldsymbol{q}_r \end{bmatrix}, \tag{5.60}$$

where $\boldsymbol{q}_r$ denotes the radiative heat flux, given by

$$\boldsymbol{q}_r = L\boldsymbol{s}. \tag{5.61}$$

Here, $L = L(\boldsymbol{x})$ denotes laser radiance at position $\boldsymbol{x}$. It characterizes the laser intensity at that position. $\boldsymbol{s}$ denotes the propagation direction of the laser light. It is also a function of $\boldsymbol{x}$ because the laser beam simulated here has a 7.5° diverging angle. L is governed by the

following laser radiation equation that enforces conservation of energy.

$$\nabla \cdot (L\boldsymbol{s}) = \nabla L \cdot \boldsymbol{s} + (\nabla \cdot \boldsymbol{s})L = -\mu_\alpha L. \tag{5.62}$$

Here, μ_α is the laser absorption coefficient, which depends on the laser wavelength, the fluid material, and the fluid temperature. Same as in [66], the method of latent heat reservoir is applied to model the phase transition (i.e., vaporization). In addition, the cylindrical symmetry of the fluid flow with respect to the central axis of the laser fiber is leveraged to allow simulations on 2D grids.

Both the liquid and vapor phases are modeled by the stiffened gas EOS. The parameters are $\gamma = 6.12$, $e_c = 0$, $b = 0$, and $p_c = 343$ MPa for the liquid phase, and $\gamma = 1.34$, $e_c = 0$, $b = 0$, and $p_c = 0$ for the vapor. In the latter case, the stiffened gas degenerates to the perfect gas. Additional details about this problem — including its background, novelty, the model equations, and the numerical methods — can be found in [66].

The computational domain is 2D, discretized by a non-uniform Cartesian grid with approximately $338,000$ elements. In the most refined region, the element size is around 2.5×10^{-3} mm. Simulations (i), (ii), and (iii) defined in Sec. 5.4.1 are performed for this example problem, on 256 CPU cores. Again, the error tolerance for integration step adaptation is set to 1.0×10^{-9} in Simulation (iii), which translates to 841 integration steps for Simulations (i) and (ii).

Figure 5.18 presents the laser radiance and fluid velocity fields obtained from Simulation (iii). The solutions obtained from the other two simulations are the same. Initially, the entire fluid domain is occupied by the liquid phase. The laser source power rapidly grows from 0 to its peak value during the first 0.2 μs. Then, it stays at the peak value until $t = 10.0$ μs. At around 4.8 μs, the simulation predicts the formation of a vapor bubble

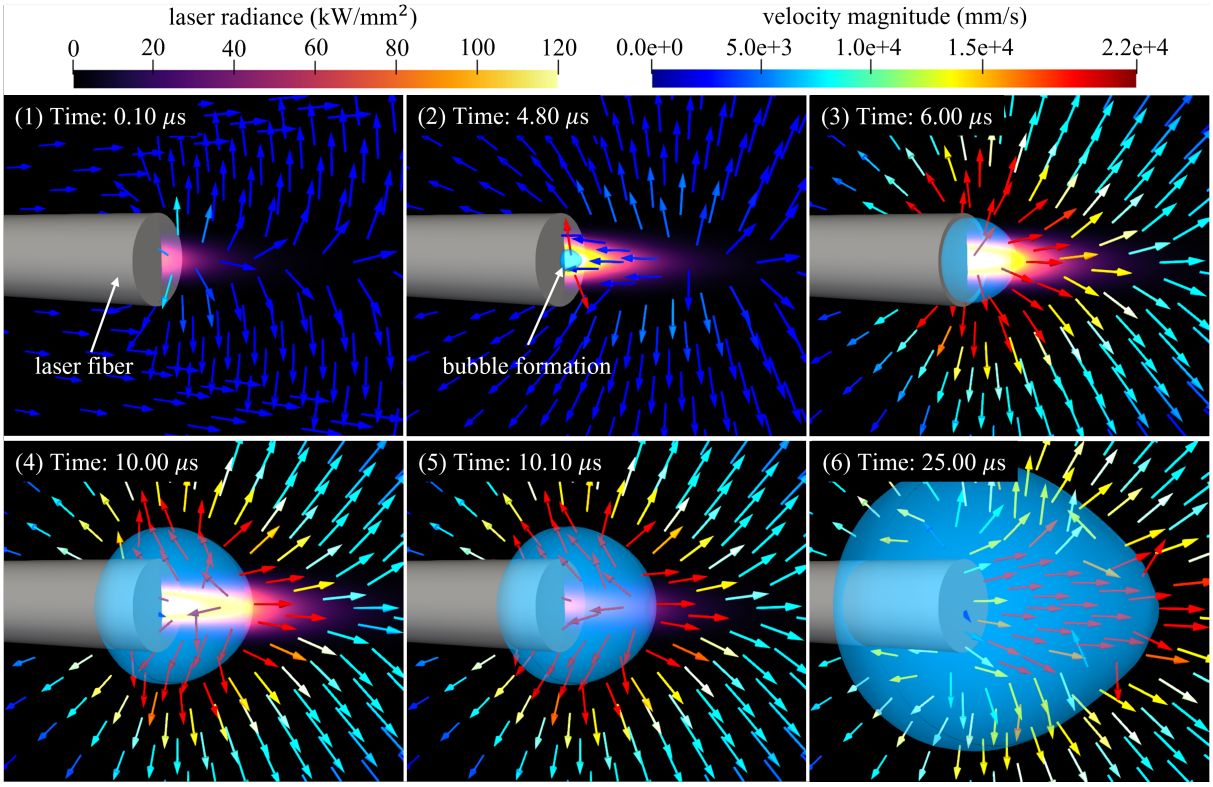

Figure 5.18: Laser-induced cavitation: Laser radiation, bubble formation, and the fluid velocity field.

right in front of the laser fiber tip. Phase transition lasted around 0.025 μs. Afterwards, the main flow features are the expansion of the bubble, the propagation of vaporization-induced acoustic waves, and laser heating. Figure 5.19 presents the fluid pressure field at six time instances. Subfigures (1) and (2) show the acoustic waves induced by the sudden increase of the fluid's internal energy due to laser radiation. Subfigures (3) and (4) demonstrate the formation and expansion of the vapor bubble, as well as the associated acoustic waves. The laser power vanishes at $t = 10.2$ μs. Afterwards, the bubble continues to grow and gradually deforms into a teardrop shape, which is shown in Subfigures (5) and (6). The same shape has been observed in laboratory experiments using the same type of laser [23]. This type of non-spherical, beam dependent bubbles is a unique feature of long-pulse laser-induced cavitation.

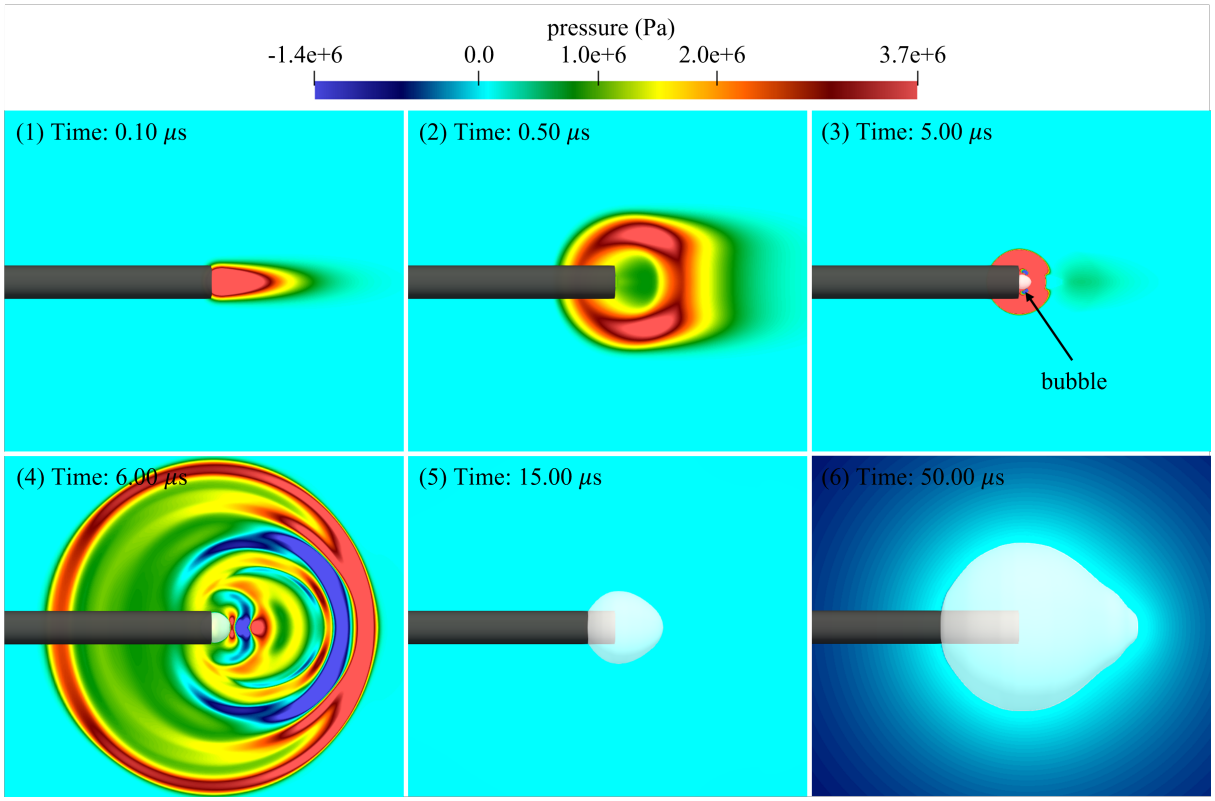

Figure 5.19: Laser-induced cavitation: The pressure field.

Figure 5.20 compares the computation times of Simulations (i)(ii)(iii) up to $t = 50$ μs. The advective fluxes are evaluated using the LLF numerical flux function. It can be observed that the solution of exact Riemann problems is accelerated by 51 times (350 s vs. 17,899 s), when Methods (1), (2), and (3) are used. In the baseline Simulation (i), over 95% of the flux computation time is spent on solving the exact Riemann problems. As a result, after the acceleration, the total flux computation time is reduced by a factor of 26 (from 18,233 s to 696 s).

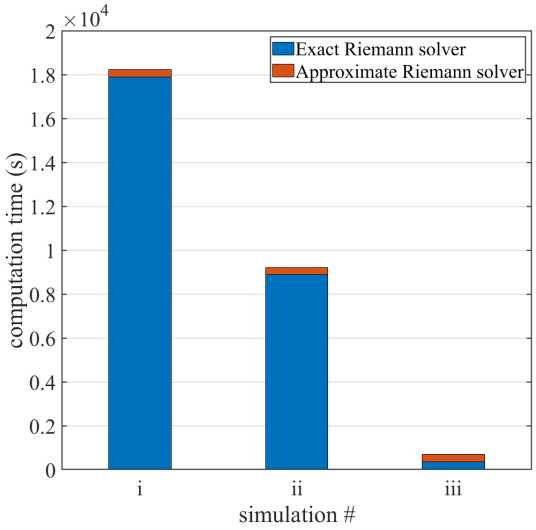

Figure 5.20: Laser-induced cavitation: Comparison of the flux computation time of different simulations.

5.4.4 Hypervelocity impact in a fluid environment

Finally, we consider an example problem of hypervelocity impact, first presented in [28]. In this problem, a copper projectile impacts onto a soda lime glass (SLG) target in a neon gas environment. If the projectile's velocity is sufficiently high, the peak pressure inside the projectile and the target can be much higher than the material's Hugoniot elastic limit. In this scenario, the solid materials can be modeled as compressible fluids. Unlike conventional impact simulations that consider only the projectile and the target, we perform a fluid-solid coupled analysis that includes the ambient neon gas as a material subdomain. Therefore, this problem involves three material subdomains, and three material interfaces (neon-copper, copper-SLG, and SLG-neon). Two level set equations are solved to track the boundaries of the copper and SLG subdomains, using the method described in Sec. 5.2.3. This problem also challenges the robustness of the solver as it exhibits extreme mechanical and thermodynamic states, and the EOS vary significantly across the fluid-solid interfaces.

Following [28], the effects of viscosity and heat diffusion are neglected. The impact problem

is analyzed in two stages, namely the flight of the projectile in the fluid medium, followed by the collision of the projectile onto the target. The first stage produces a bow shock that reaches the target before the projectile. This flow field can be obtained by either a conventional body-fitted CFD analysis ([28]), or a multi-material simulation in which the projectile surface is tracked using the level set method. To demonstrate the accelerated Riemann problem solver, we first present a simulation that employs the second approach. The copper projectile is a cylinder with a spherical leading edge. Its thermodynamics is modeled using the Mie-Grüneisen EOS (i.e., Eq. (5.12)), with parameters $c_0 = 3.93$ km/s, $s = 1.5$, $\rho_0 = 8,960$ kg/m^3, and $\Gamma_0 = 2.12$ [28]. The neon gas is modeled as a perfect gas, with $\gamma = 1.667$. The initial pressure within the copper projectile and neon gas are both 1.0×10^5 Pa. The copper projectile has an initial density of $8,960$ kg/m^3 and neon gas 0.82 kg/m^3. Therefore, the density ratio across the projectile surface reaches 4 orders of magnitude.

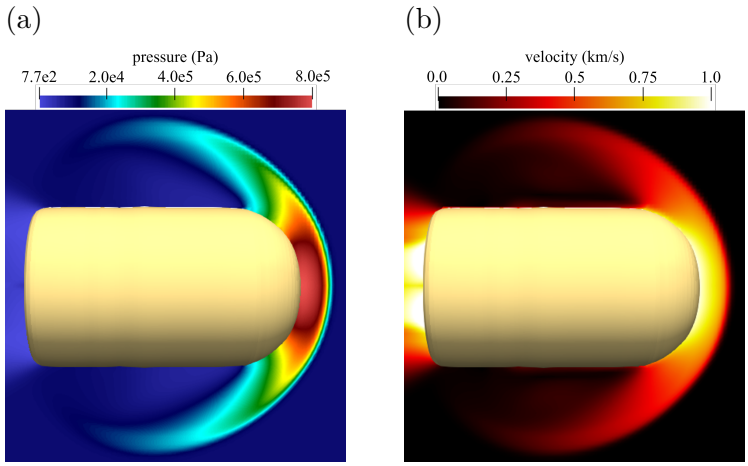

Figure 5.21: Simulation of flow around a copper projectile before collision: Pressure and velocity fields at $t = 8.87$ μs. Velocity of projectile: 1 km/s.

Leveraging the cylindrical symmetry of the problem, we use a 2D non-uniform Cartesian mesh. In the most refined region, the element size is around 0.25 mm. Simulations (i), (ii), (iii), and (iv) defined in Sec. 5.4.1 are performed, each one using 256 CPU cores. The

number of integration steps in Simulations (i) and (ii) is set to $8,915$, which is determined by the step size adaptation of Simulation (iii), to achieve an error tolerance of 1.0×10^{-9}. This number of integration steps is greater than those in previous test cases, because of the significant discontinuity across the material interface and the extreme physical conditions.

Figure 5.21 presents the pressure and velocity fields obtained from the simulation at $t = 8.87$ μs. As expected, a bow shock appears in front of the projectile, and rarefaction waves are generated at the projectile's back surface. The computation times of the four simulations up to $t = 40.2$ μs are presented in Fig. 5.22. The solution of exact Riemann problems is accelerated by 87 times (from $1,970.5$ s to 22.7 s), after applying the four methods. In the baseline simulation, over 99% of the flux computation time is spent on solving the exact Riemann problems. As a result, the total advective flux computation time is reduced by a factor of 81.3, when the four acceleration methods are applied. In particular, after using the initial guesses searched from R-tree, the flux computation time further drops by 58.7% (from 58.7 s to 24.2 s). The computational time spent on updating, normalizing, and accessing the R-tree is only 1.08 s. Therefore, in this test case with very significant discontinuity across the projectile surface, the benefits of Method 4 far overtake its cost.

Next, we present a simulation of the second stage of the impact problem. The projectile's velocity is set to 4 km/s. A body-fitted CFD analysis is performed to generate the initial flow field, following [28]. In this case, the projectile is a long copper cylinder with a spherical leading edge. Its radius is 5 mm. The material properties of the copper projectile and the neon gas are identical to the previous test case. The SLG target is modeled using the stiffened gas EOS (i.e., Eq. (5.7)), with $\gamma = 3.9$, $e_c = 0$, $b = 0$, and $p_c = 2.62$ GPa. Additional details about this test case can be found in [28].

The 2D computational domain is discretized by a non-uniform Cartesian grid with approximately $240,000$ elements. In the most refined region, the grid size is around 0.1 mm.

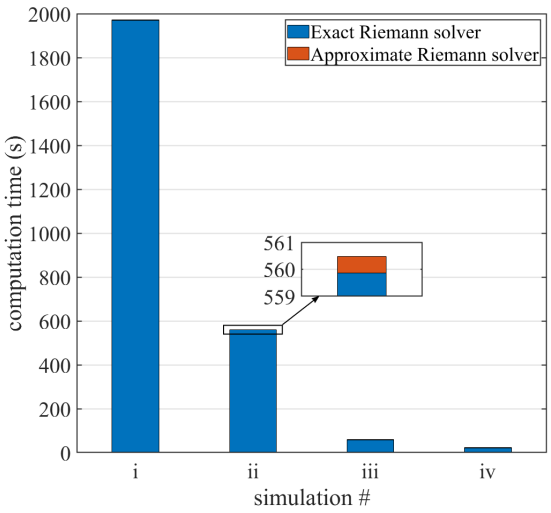

Figure 5.22: Simulation of flow around a copper projectile before collision: Comparison of the flux computation time.

Simulations (i), (ii), and (iii) defined in Sec. 5.4.1 are performed on 256 CPU cores. The number of integration steps in Simulations (i) and (ii) is set to $8,596$, which is determined by the step size adaptation of Simulation (iii), to achieve an error tolerance of 1.0×10^{-9}. The number of integration steps is greater than those in previous sections, because of the extreme physical conditions generated by the impact.

Figure 5.23 presents the pressure, velocity, and temperature fields at four different time instances. The surfaces of the copper projectile and the SLG target are obtained by extracting the zero level set of the two level set functions. At $t = 0.75$ μs, a time instance shortly after the contact of the two objects, two shock waves propagate in the projectile and the target. The pressure behind the shocks exceeds 20 GPa. Similar pressure magnitudes were observed in previous experiments [33], also using SLG as the target. In the velocity and temperature fields, the bow shock attached to the projectile is formed due to its hypersonic flight. It is not visible in the pressure field because the scale is selected to highlight the much higher pressure in the solid materials. Because of the impact, the neon gas between the target

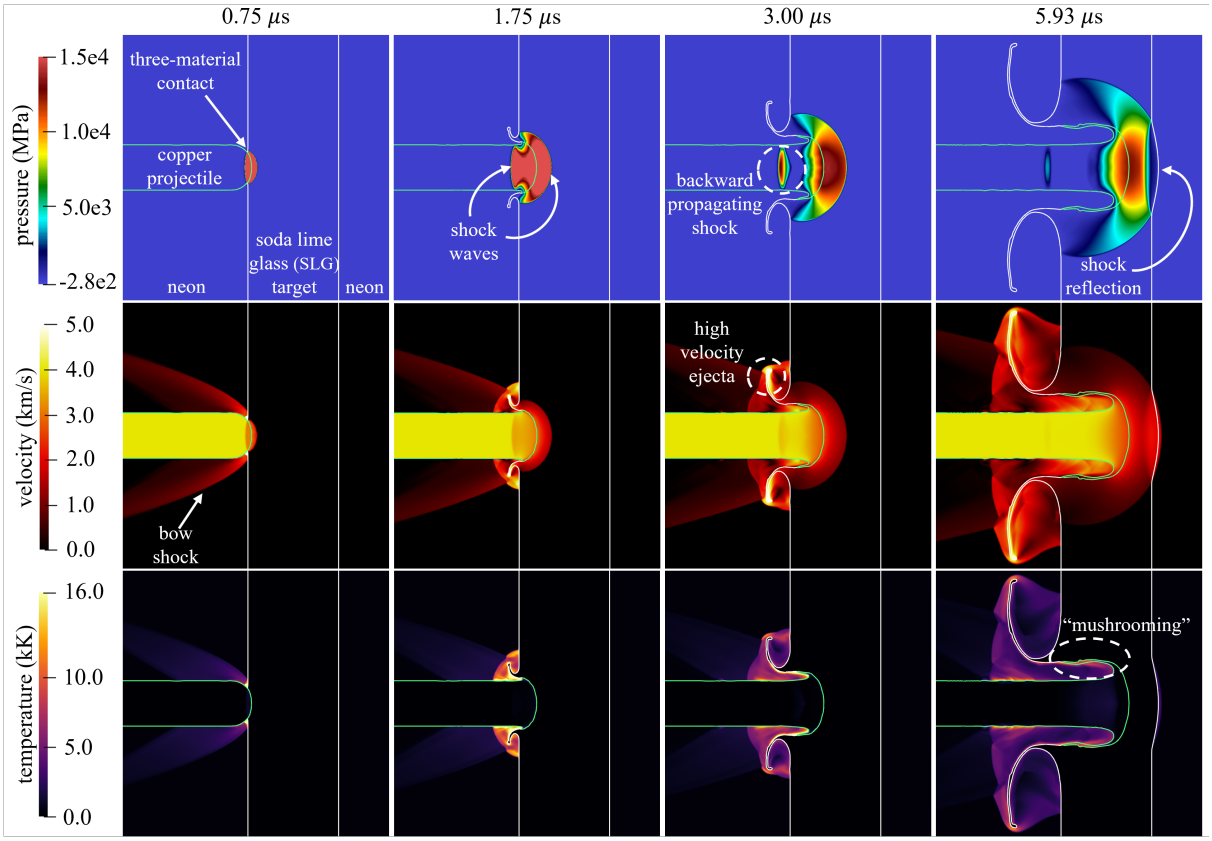

Figure 5.23: Hypervelocity impact in a fluid environment: pressure, velocity, and temperature fields. Velocity of projectile: 4 km/s.

and the projectile are compressed rapidly, resulting in a region of high pressure and high temperature. As time advances, a crater is formed in the target. The SLG material from the rim of the crater is ejected in the neon gas, at a high velocity that amounts to the impact velocity. At $t = 5.93$ μs, the back wall of the target deforms under the impact of the shock wave. In the meantime, the compressive shock wave is reflected as a tensile wave, interfering with the incident shock wave. In the projectile, its leading edge morphs into a "mushroom head" shape, due to the rapid deceleration caused by the initially static target. This type of deformation has been observed in previous studies [54].

In Fig. 5.24, the pressure time history at a sensor location is plotted. Specifically, we have performed Simulation (iii) with different error tolerances (ϵ_0) for step adaptation. For

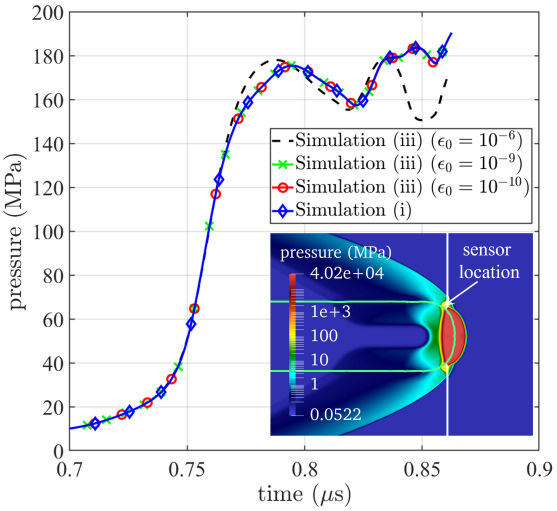

Figure 5.24: Hypervelocity impact in a fluid environment: the time history of the pressure at the marked sensor location. The pressure field is from $t = 0.825$ μs.

comparison, the result from Simulation (i) with $8,596$ integration steps is also shown. Except for the one with $\epsilon_0 = 10^{-6}$, all the other results match perfectly. This indicates that the flow field predictions can be affected by the error tolerance in the exact Riemann solver; and in certain cases, a very small tolerance — such as 10^{-9} in this case — is needed.

The computation times of Simulations (i)(ii)(iii) up to $t = 0.87$ μs are presented in Fig. 5.25. After applying Methods (1), (2), and (3), the solution of exact Riemann problems is accelerated by 83 times (from $8,956$ s to 108 s). The total advective flux computation time is reduced by a factor of 79.

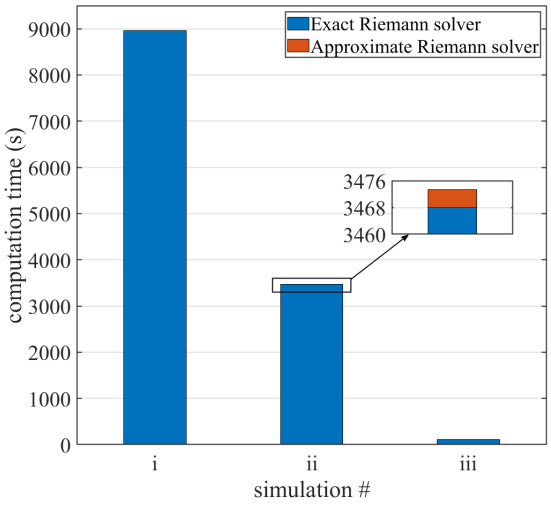

Figure 5.25: Hypervelocity impact in a fluid environment: Comparison of the flux computation time of different simulations.

5.5 Summary

We consider the numerical solution of compressible multi-material flow problems with sharp interfaces and significant discontinuities. In this context, the advective flux calculator can be viewed as the engine of the solver. Within the engine, the calculation of interfacial fluxes is arguably the most important (yet tricky) part. The idea of locally constructing and solving bimaterial Riemann problems across interfaces has gained popularity in the past two decades. It has a unique advantage in that the discontinuity of both state variables and the thermodynamic EOS are naturally accounted for. This idea entails solving a large number — up to 10^8 in the test cases presented in Sec. 5.4 — of bimaterial Riemann problems on the fly. On the other hand, the off-the-shelf method for solving Riemann problems (Sec. 5.3.1) was developed earlier to solve individual problems on a case-by-case basis, and therefore not optimized for computational efficiency. As a result, applying it in multi-material flow solvers leads to a drastic — sometimes prohibitive — increase of computational cost, especially when complicated EOS are involved.

In this paper, we presented four methods to accelerate the solution of bimaterial Riemann problems. The main idea behind these methods is to exploit some special properties of the Riemann problem equations (Sec. 5.3.2, 5.3.3, and 5.3.4), and to store and reuse previous solutions as much as possible (Sec. 5.3.3 and 5.3.5). The most expensive part of the solution procedure is the numerical integration of state variables through rarefaction fans. Three of the four methods were designed to accelerate this part, exploiting a change of integration variable (Sec. 5.3.2), the recycle of integration trajectories (Sec. 5.3.3), and the adoption of adaptive step size (Sec. 5.3.4). The computational cost also depends heavily on the quality of the initial guess. In this regard, the fourth acceleration method (Sec. 5.3.5) stores previous inputs and solutions in a 5D R-tree, and performs a nearest-neighbor search to generate the initial guess for the next Riemann problem to be solved. Compared to previous efforts on the acceleration of Riemann solvers, the four methods presented in this paper do not introduce new approximations, nor do they require additional pre-processing work. Also, they do not depend on or conflict with each other. These methods have been implemented in a standalone Riemann problem solver [3] and a 3D multi-material flow solver [2], both of which are open source and under the GPL (Version 3) license.

We presented four example problems to demonstrate and assess these acceleration methods (Sec. 5.4). These problems represent different application areas including underwater explosion (Sec. 5.4.2), laser-induced cavitation (Sec. 5.4.3), and hypervelocity impact (Sec. 5.4.1 and 5.4.4). They involve some major computational challenges such as large interface motion and deformation, multiple (> 2) interfaces in contact, drastically different thermodynamic relations, and significant jumps of state variables across interfaces. For two example problems (Sec. 5.4.1 and 5.4.2), the proposed numerical methods are verified against reference solutions. For all the problems, the speedup obtained by the proposed acceleration methods was found to be significant. The time spent on solving exact Riemann problems was reduced

by a factor of 37 to 87. As a result, the total time spent on calculating advective fluxes was also reduced by a factor of 18 to 81. Among the four acceleration methods, the first three were found to be effective in all the test cases. The last one (presented in Sec. 5.3.5) was found to be effective when the local density jump across the material interface is significant. While the simulations presented in this paper were performed using a specific solver that implements the FIVER method, the proposed acceleration methods were not tailored for this solver. They are generally applicable to multi-material and multiphase flow solvers that utilize the exact solution of Riemann problems; and similar acceleration effects can be expected.

Declaration of competing interest

The authors declare that they have no known competing financial interests or personal relationships that could have appeared to influence the work reported in this paper.

Acknowledgement

The authors gratefully acknowledge the support of the National Science Foundation (NSF) under Award CBET-1751487, the support of the Office of Naval Research (ONR) under Award N00014-19-1-2102, and the support of the National Institutes of Health (NIH) under Award 2R01-DK052985-24A1. W.M. and K.W. also acknowledge the support of U.S. Department of Transportation (DOT) Pipeline and Hazardous Materials Safety Administration under contract number 693JK32250007CAAP.

Bibliography

[1] Boost Generic Geometry Library. URL https://www.boost.org/doc/libs/1_82_0/libs/geometry/doc/html/index.html.

[2] *M2C solver*. Github. URL https://github.com/kevinwgy/m2c. Accessed: 2023-02-17.

[3] *One-dimensional two-phase Riemann problem solver*. Github. URL https://github.com/kevinwgy/riemann. Accessed: 2023-02-17.

[4] Tariq D. Aslam. A level set algorithm for tracking discontinuities in hyperbolic conservation laws ii: Systems of equations. *Journal of Scientific Computing*, 19(1-3):37 – 62, 2003.

[5] J.W. Banks, D.W. Schwendeman, A.K. Kapila, and W.D. Henshaw. A high-resolution godunov method for compressible multi-material flow on overlapping grids. *Journal of Computational Physics*, 223(1):262–297, 2007. ISSN 0021-9991.

[6] David J Benson. Volume of fluid interface reconstruction methods for multi-material problems. *Applied Mechanics Reviews*, 55(2):151–165, 04 2002. ISSN 0003-6900.

[7] Wurigen Bo, Xingtao Liu, James Glimm, and Xiaolin Li. A robust front tracking method: Verification and application to simulation of the primary breakup of a liquid jet. *SIAM Journal on Scientific Computing*, 33(4):1505–1524, 2011.

[8] S Cao, G Wang, O Coutier-Delgosha, and K Wang. Shock-induced bubble collapse near solid materials: Effect of acoustic impedance. *Journal of Fluid Mechanics*, 907, 2021.

[9] Shunxiang Cao, Ying Zhang, Defei Liao, Pei Zhong, and Kevin G Wang. Shock-induced damage and dynamic fracture in cylindrical bodies submerged in liquid. *International journal of solids and structures*, 169:55–71, 2019.

[10] J. R. Cash and Alan H. Karp. A variable order runge-kutta method for initial value problems with rapidly varying right-hand sides. *ACM Trans. Math. Softw.*, 16(3):201–222, sep 1990. ISSN 0098-3500.

[11] S.C. Chapra and R.P. Canale. *Numerical Methods for Engineers*. McGraw-Hill Higher Education, New York, NY, 7 edition, 2015.

[12] King Lum Cheung and Ada Wai-Chee Fu. Enhanced nearest neighbour search on the r-tree. *SIGMOD Rec.*, 27(3):16–21, sep 1998. ISSN 0163-5808.

[13] Jean-Pierre Cocchi and Richard Saurel. A Riemann problem based method for the resolution of compressible multimaterial flows. *Journal of Computational Physics*, 137 (2):265–298, 1997. ISSN 0021-9991.

[14] Phillip Colella and Harland M Glaz. Efficient solution algorithms for the riemann problem for real gases. *Journal of Computational Physics*, 59(2):264–289, 1985. ISSN 0021-9991.

[15] C. Farhat, K.G. Wang, A. Main, S. Kyriakides, L.-H. Lee, K. Ravi-Chandar, and T. Belytschko. Dynamic implosion of underwater cylindrical shells: Experiments and computations. *International Journal of Solids and Structures*, 50(19):2943–2961, 2013.

[16] Charbel Farhat, Arthur Rallu, and Sriram Shankaran. A higher-order generalized ghost fluid method for the poor for the three-dimensional two-phase flow computation of underwater implosions. *Journal of Computational Physics*, 227(16):7674–7700, 2008. ISSN 0021-9991.

[17] Charbel Farhat, Jean-Frédéric Gerbeau, and Arthur Rallu. Fiver: A finite volume method based on exact two-phase riemann problems and sparse grids for multi-material

flows with large density jumps. *Journal of Computational Physics*, 231(19):6360–6379, 2012. ISSN 0021-9991.

[18] Ronald Fedkiw, Antonio Marquina, and Barry Merriman. An isobaric fix for the overheating problem in multimaterial compressible flows. *Journal of Computational Physics*, 148:545–578, 1999.

[19] Ronald P Fedkiw, Tariq Aslam, Barry Merriman, and Stanley Osher. A non-oscillatory eulerian approach to interfaces in multimaterial flows (the ghost fluid method). *Journal of Computational Physics*, 152(2):457–492, 1999.

[20] E. Fehlberg. Low-order classical runge-kutta formulas with stepsize control and their application to some heat transfer problems. Technical report, National Aeronautics and Space Administration.(NASA), Washington, D.C, (United States), 1969.

[21] Frederic Gibou, Ronald Fedkiw, and Stanley Osher. A review of level-set methods and some recent applications. *Journal of Computational Physics*, 353:82–109, 2018. ISSN 0021-9991.

[22] Antonin Guttman. R-trees: a dynamic index structure for spatial searching. In *ACM SIGMOD Conference*, 1984.

[23] Derek S. Ho, Dominick Scialabba, Russell S. Terry, Xiaojian Ma, Junqin Chen, Georgy N. Sankin, Gaoming Xiang, Robert Qi, Glenn M. Preminger, Michael E. Lipkin, and Pei Zhong. The role of cavitation in energy delivery and stone damage during laser lithotripsy. *Journal of Endourology*, 35(6):860–870, 2021.

[24] Jonathan Ho and Charbel Farhat. Discrete embedded boundary method with smooth dependence on the evolution of a fluid-structure interface. *International Journal for Numerical Methods in Engineering*, 122(19):5353–5383, 2021.

[25] Ryan W. Houim and Kenneth K. Kuo. A ghost fluid method for compressible reacting flows with phase change. *Journal of Computational Physics*, 235:865–900, 2013. ISSN 0021-9991.

[26] XY Hu, Nikolaus A Adams, and Gianluca Iaccarino. On the hllc riemann solver for interface interaction in compressible multi-fluid flow. *Journal of Computational Physics*, 228(17):6572–6589, 2009.

[27] D. Igra and K. Takayama. A high resolution upwind scheme for multi-component flows. *International Journal for Numerical Methods in Fluids*, 38(10):985–1007, 2002.

[28] Shafquat T. Islam, Wentao Ma, John G. Michopoulos, and Kevin Wang. Plasma formation in ambient fluid from hypervelocity impacts. *Extreme Mechanics Letters*, 58: 101927, 2023. ISSN 2352-4316.

[29] Ali Jafarian and Ahmadreza Pishevar. An exact multiphase riemann solver for compressible cavitating flows. *International Journal of Multiphase Flow*, 88:152–166, 2017. ISSN 0301-9322.

[30] Eric Johnsen and Frank Ham. Preventing numerical errors generated by interface-capturing schemes in compressible multi-material flows. *Journal of Computational Physics*, 231(17):5705–5717, 2012. ISSN 0021-9991.

[31] James Russell Kamm. An exact, compressible one-dimensional riemann solver for general, convex equations of state. Technical report, Los Alamos National Lab.(LANL), Los Alamos, NM (United States), 2015.

[32] Keiichi Kitamura, Meng-Sing Liou, and Chih-Hao Chang. Extension and comparative study of ausm-family schemes for compressible multiphase flow simulations. *Communications in Computational Physics*, 16(3):632–674, 2014.

[33] T. Kobayashi, T. Sekine, O.V. Fat'yanov, E. Takazawa, and Q.Y. Zhu. Radiation temperatures of soda-lime glass in its shock-compressed liquid state. *Journal of Applied Physics*, 83(3):1711 – 1716, 1998.

[34] Jeff Krimmel, Tim Colonius, and Michel Tanguay. Simulation of the effects of cavitation and anatomy in the shock path of model lithotripters. *Urological research*, 38:505–518, 2010.

[35] O Le Métayer and Richard Saurel. The Noble-Abel Stiffened-Gas equation of state. *Physics of Fluids*, 28:046102, 2016. doi: 10.1063/1.4945981.

[36] T.G. Liu, B.C. Khoo, and K.S. Yeo. Ghost fluid method for strong shock impacting on material interface. *Journal of Computational Physics*, 190(2):651–681, 2003. ISSN 0021-9991.

[37] T.G. Liu, B.C. Khoo, and C.W. Wang. The ghost fluid method for compressible gas–water simulation. *Journal of Computational Physics*, 204(1):193–221, 2005. ISSN 0021-9991.

[38] Raphaël Loubère, Pierre-Henri Maire, Mikhail Shashkov, Jérôme Breil, and Stéphane Galera. Reale: A reconnection-based arbitrary-lagrangian–eulerian method. *Journal of Computational Physics*, 229(12):4724–4761, 2010. ISSN 0021-9991.

[39] Wentao Ma, Xuning Zhao, Christine Gilbert, and Kevin Wang. Computational analysis of bubble–structure interactions in near-field underwater explosion. *International Journal of Solids and Structures*, 242:111527, 2022.

[40] Alex Main, Xianyi Zeng, Philip Avery, and Charbel Farhat. An enhanced FIVER method for multi-material flow problems with second-order convergence rate. *Journal of Computational Physics*, 329:141–172, January 2017.

[41] Alex Main, Xianyi Zeng, Philip Avery, and Charbel Farhat. An enhanced fiver method for multi-material flow problems with second-order convergence rate. *Journal of Computational Physics*, 329:141–172, 2017.

[42] Yannis Manolopoulos, Alexandros Nanopoulos, Apostolos N. Papadopoulos, and Yannis Theodoridis. *R-Trees: Theory and Applications*. Springer London, 1 edition, 2006.

[43] Alexis Marbœuf, Alexandra Claisse, and Patrick Le Tallec. Conservative and entropy controlled remap for multi-material ale simulations with space-staggered schemes. *Journal of Computational Physics*, 390:66–92, 2019. ISSN 0021-9991.

[44] Ralph Menikoff. JWL equation of state. Technical report, Los Alamos National Lab.(LANL), Los Alamos, NM (United States), 2015.

[45] Ralph Menikoff and Bradley J. Plohr. The riemann problem for fluid flow of real materials. *Rev. Mod. Phys.*, 61:75–130, Jan 1989.

[46] William H. Press, Saul A. Teukolsky, William T. Vetterling, and Brian P. Flannery. *Numerical Recipes 3rd Edition: The Art of Scientific Computing*. Cambridge University Press, 3 edition, 2007.

[47] Arthur Rallu. *A multiphase fluid-structure computational framework for underwater imploison problems*. PhD thesis, Stanford University, 2009.

[48] Allen C Robinson. The mie-gruneisen power equation of state. Technical report, Sandia National Lab.(SNL-NM), Albuquerque, NM (United States), 2019.

[49] Nick Roussopoulos, Stephen Kelley, and Frédéric Vincent. Nearest neighbor queries. *SIGMOD Rec.*, 24(2):71–79, may 1995. ISSN 0163-5808.

[50] VV Rusanov. On difference schemes of third order accuracy for nonlinear hyperbolic systems. *Journal of Computational Physics*, 5(3):507–516, 1970.

[51] Shiv Kumar Sambasivan and H. S. UdayKumar. Ghost fluid method for strong shock interactions part 1: Fluid-fluid interfaces. *AIAA Journal*, 47(12):2907–2922, 2009.

[52] J.J. Sanchez. Inelastic equation of state for solids. *Computer Methods in Applied Mechanics and Engineering*, 375:113622, 2021. ISSN 0045-7825.

[53] Keh-Ming Shyue. An efficient shock-capturing algorithm for compressible multicomponent problems. *Journal of Computational Physics*, 142(1):208–242, 1998. ISSN 0021-9991.

[54] Yunhou Sun, Cuncheng Shi, Zheng Liu, and Desheng Wen. Theoretical research progress in high-velocity/hypervelocity impact on semi-infinite targets. *Shock and Vibration*, 2015:1–15, 2015. doi: 10.1155/2015/265321.

[55] Hiroshi Terashima and Grétar Tryggvason. A front-tracking method with projected interface conditions for compressible multi-fluid flows. *Computers & Fluids*, 39(10): 1804–1814, 2010. ISSN 0045-7930.

[56] Eleuterio F Toro. *Riemann solvers and numerical methods for fluid dynamics: a practical introduction*. Springer Science & Business Media, 2013.

[57] G. Tryggvason, B. Bunner, A. Esmaeeli, D. Juric, N. Al-Rawahi, W. Tauber, J. Han, S. Nas, and Y.-J. Jan. A front-tracking method for the computations of multiphase flow. *Journal of Computational Physics*, 169(2):708–759, 2001. ISSN 0021-9991.

[58] E.H. van Brummelen and B. Koren. A pressure-invariant conservative godunov-type method for barotropic two-fluid flows. *Journal of Computational Physics*, 185(1):289–308, 2003. ISSN 0021-9991.

[59] François Vilar, Chi-Wang Shu, and Pierre-Henri Maire. Positivity-preserving cell-centered lagrangian schemes for multi-material compressible flows: From first-order

to high-orders. part ii: The two-dimensional case. *Journal of Computational Physics*, 312:416–442, 2016. ISSN 0021-9991.

[60] J. VonNeumann and R. D. Richtmyer. A Method for the Numerical Calculation of Hydrodynamic Shocks. *Journal of Applied Physics*, 21(3):232–237, 04 1950. ISSN 0021-8979.

[61] C. W. Wang, T. G. Liu, and B. C. Khoo. A real ghost fluid method for the simulation of multimedium compressible flow. *SIAM Journal on Scientific Computing*, 28(1):278–302, 2006.

[62] K. G. Wang, P. Lea, and C. Farhat. A computational framework for the simulation of high-speed multi-material fluid-structure interaction problems with dynamic fracture. *International Journal for Numerical Methods in Engineering*, 104(7):585–623, 2015.

[63] Kevin G. Wang. Multiphase fluid-solid coupled analysis of shock-bubble-stone interaction in shockwave lithotripsy. *International Journal for Numerical Methods in Biomedical Engineering*, 33(10), 2017. doi: 10.1002/cnm.2855.

[64] Gaoming Xiang and Bing Wang. Numerical study of a planar shock interacting with a cylindrical water column embedded with an air cavity. *Journal of Fluid Mechanics*, 825:825–852, 2017.

[65] Gaoming Xiang, Xiaojian Ma, Cosima Liang, Hongyang Yu, Defei Liao, Georgy Sankin, Shunxiang Cao, Kevin Wang, and Pei Zhong. Variations of stress field and stone fracture produced at different lateral locations in a shockwave lithotripter field. *The Journal of the Acoustical Society of America*, 150(2):1013–1029, 2021. doi: 10.1121/10.0005823.

[66] Xuning Zhao, Wentao Ma, and Kevin Wang. Simulating laser-fluid coupling and laser-

induced cavitation using embedded boundary and level set methods. *Journal of Computational Physics*, 472:111656, 2023. ISSN 0021-9991.

Chapter 6

Conclusions and Perspectives for Future Work

6.1 Conclusion

This dissertation investigates multiphase fluid-material interaction problems featuring strong discontinuity across the material interface, large deformation, shock waves, and extreme loading conditions.

The dissertation starts with investigating the interactions between an underwater structure, the ambient liquid water, and the gas bubble generated by a near-field underwater explosion. In particular, the first part of the dissertation developed a fluid-structure coupled computational framework to certify the shock-resistant performance of elastomer coating materials (e.g., polyurea). This work is motivated by recent studies that reveal their excellent mechanical behaviors under high pressure, high strain-rate loading, such as in the scenarios of underwater and aerial explosions. The computational model employed in this study combines a multiphase compressible fluid dynamics solver and a nonlinear structural dynamics solver. In particular, the mass, momentum, and energy conservation across the fluid-fluid and fluid-solid interfaces are enforced by constructing local bimaterial Riemann problems and solving them exactly. Across material interfaces, strong discontinuities generated by explosive loading conditions can be accommodated naturally by this method. By adopting and

implementing recently developed constitutive models of polyurea, the hyper-elasticity and viscoelasticiy of the coating material are included in the aforementioned high-fidelity fluid-structure coupled computational framework. Then, the extended computational framework is applied to model the dynamics of a bilayer coating–substrate system including a thin-walled aluminum cylinder and polyurea coating. Various loading conditions are studied. In particular, the observed two-way coupling between the structure and the bubble in near-field underwater explosion motivates the work presented in the next part of this dissertation.

In the second part of this dissertation, the collapse of an underwater aluminum cylinder due to a near-field explosion is investigated using fluid-structure coupled simulations. Previous studies suggest that the dynamics of the explosion bubble may have a substantial effect in this type of events. Nonetheless, knowledge about this effect is very limited. Therefore, a specific objective of this study is to capture and explain the two-way interaction between the explosion bubble and the structure. In particular, a parametric study is conducted, in which the initial pressure inside the explosion bubble (p_0) is varied by two orders of magnitude.

It is found that as p_0 varies, the final configuration of the cylinder can be substantially different. Results from five representative cases ($p_0 = 8$ MPa, 12.5 MPa, 25 MPa, 50 MPa, 100 MPa) are discussed in detail. In these cases, the structural dynamics varies from a cyclic elastic vibration without collapse ($p_0 = 8$ MPa) to an immediate collapse without vibration ($p_0 = 100$ MPa). Three different types of collapse behaviors are observed, which are categorized as Mode 2A, Mode 2B, and Mode 2C (Figure 4.20). As p_0 increases, the mode of collapse changes from 2A to 2B, and then from 2B to 2C. The mode transitions are discussed using additional test cases in the parametric study.

The mechanisms of the three collapse modes are summarized below. Mode 2A is caused by a coincidence between the bubble's first contraction phase and the cylinder's horizontal com-

pression. As the bubble contracts, it emits a pressure pulse that elevates the pressure around the entire cylinder. When this bubble pulse arrives at the horizontally compressed cylinder, it facilitates its compression, leading to an horizontal collapse that has been observed earlier in a laboratory experiment. Mode 2B is related to the plastic deformation induced by the initial loads, i.e., the initial shock wave and the water flow caused by the bubble's initial expansion. This plastic deformation suppresses the vertical extension and horizontal compression of the cylinder. As a result, when the aforementioned bubble pulse arrives at the cylinder, the cylinder is compressed in vertical direction. The bubble pulse facilitates this compression, leading to collapse mode 2B. For Mode 2C collapse, the result suggests that the cylinder's collapse is directly induced by the incident shock wave from the explosion. Clearly, the dynamics of the explosion bubble has a significant effect in collapse Modes 2A and 2B. In both cases, the plastic deformation remains relatively small long after the initial loads have passed. The collapse of the cylinder starts only after the bubble contracts to its first minimum size and emits a pressure pulse.

The time that the cylinder takes to completely collapse does not decrease monotonically as p_0 increases (see Figure 4.21). When the cylinder collapses in Mode 2A, increasing p_0 may cause the cylinder to take more time to reach self-contact. This phenomenon is caused by the increased amount of plastic deformation induced by the initial loads from the explosion.

The third part of the dissertation develops numerical algorithms that significantly improve the computational efficiency of compressible multi-material flow simulations, including those performed in the first two parts of this dissertation. When numerically solving compressible multi-material flow problems with sharp interfaces and significant discontinuities, the advective flux calculator can be viewed as the engine of the solver. Within the engine, the calculation of interfacial fluxes is arguably the most important (yet tricky) part. The

idea of locally constructing and solving bimaterial Riemann problems across interfaces has gained popularity in the past two decades. It has a unique advantage in that the discontinuity of both state variables and the thermodynamic equations of state (EOS) are naturally accounted for. This idea entails solving a large number — up to 10^8 in the test cases presented in Sec. 5.4 — of bimaterial Riemann problems on the fly. On the other hand, the off-the-shelf method for solving Riemann problems (Sec. 5.3.1) was developed earlier to solve individual problems on a case-by-case basis, and therefore not optimized for computational efficiency. As a result, applying it in multi-material flow solvers leads to a drastic — sometimes prohibitive — increase of computational cost, especially when complicated EOS are involved.

This dissertation presents four methods to accelerate the solution of bimaterial Riemann problems. The main idea behind these methods is to exploit some special properties of the Riemann problem equations (Sec. 5.3.2, 5.3.3, and 5.3.4), and to store and reuse previous solutions as much as possible (Sec. 5.3.3 and 5.3.5). The most expensive part of the solution procedure is the numerical integration of state variables through rarefaction fans. Three of the four methods were designed to accelerate this part, exploiting a change of integration variable (Sec. 5.3.2), the recycle of integration trajectories (Sec. 5.3.3), and the adoption of adaptive step size (Sec. 5.3.4). The computational cost also depends heavily on the quality of the initial guess. In this regard, the fourth acceleration method (Sec. 5.3.5) stores previous inputs and solutions in a 5D R-tree, and performs a nearest-neighbor search to generate the initial guess for the next Riemann problem to be solved. Compared to previous efforts on the acceleration of Riemann solvers, the four methods presented in this dissertation do not introduce new approximations, nor do they require additional pre-processing work. Also, they do not depend on or conflict with each other.

Four example problems are presented to demonstrate and assess these acceleration methods

(Sec. 5.4). These problems represent different application areas including underwater explosion (Sec. 5.4.2), laser-induced cavitation (Sec. 5.4.3), and hypervelocity impact (Sec. 5.4.1 and 5.4.4). They involve some major computational challenges such as large interface motion and deformation, multiple (> 2) interfaces in contact, drastically different thermodynamic relations, and significant jumps of state variables across interfaces. For two example problems (Sec. 5.4.1 and 5.4.2), the proposed numerical methods are verified against reference solutions. For all the problems, the speedup obtained by the proposed acceleration methods was found to be significant. The time spent on solving exact Riemann problems was reduced by a factor of 37 to 87. As a result, the total time spent on calculating advective fluxes was also reduced by a factor of 18 to 81. Among the four acceleration methods, the first three were found to be effective in all the test cases. The last one (presented in Sec. 5.3.5) was found to be effective when the local density jump across the material interface is significant. While the simulations presented in this dissertation were performed using a specific solver that implements the FIVER method, the proposed acceleration methods were not tailored for this solver. They are generally applicable to multi-material and multiphase flow solvers that utilize the exact solution of Riemann problems; and similar acceleration effects can be expected.

6.2 Perspectives for future work

The work in this dissertation illustrates the advantages of constructing and solving bimaterial Riemann problems in the solution of challenging multi-material flow problems. However, currently this method has neglected surface tension and interfacial mass transport, which can be crucial in predicting interface dynamics, such as the evolution of the interface shape, as well as the surrounding pressure and temperature fields. Future studies may consider

these physical phenomena by extending the bimaterial Riemann problem solver. This can be achieved by the incorporation of interface jump conditions derived from physical principles describing surface tension and mass transport across a material interface. Consequently, the exact solution to the interface Riemann problems will be updated.

Second, the shock-resistant effect of polyurea coating can be further studied. Utilizing the fluid-structure coupled computational framework developed in Chapter 2, well-designed numerical experiments can be performed to study the dynamic interaction among the elastomer coating, the solid substrate, and the surrounding fluid. From the analysis of the simulation results, the shock-mitigation mechanism and performance of elastomer coating materials can be better understood in realistic fluid-structure coupled settings. In addition, parametric studies regarding the thickness, location, and the shape of coating material can be designed and performed, with the goal of providing design guidance to real-world applications.